An Investigation of Stimulated Emission Processes in Thin-film Molecular Materials and Structures



Yiren Xia

Lincoln College

University of Oxford

A thesis submitted for the degree of Doctor of Philosophy

Trinity Term 2019

Declaration

The work described in this thesis is original and was carried out at Imperial College London (2014-2016) and University of Oxford (2016-2019) under the supervision of Professor Paul N. Stavrinou and Professor Donal D. C. Bradley. It has not been submitted previously for a degree. Except where specific reference is given, this thesis is the product of my own work.

Acknowledgements

First, I would like to express my deepest gratitude to my supervisors Prof. Paul Stavrinou and Prof. Donal Bradley for their abundant knowledge, continuous guidance and utmost encouragement through the years from Imperial to Oxford. Their scientific vision and enthusiasm for my project helped me overcome numerous difficulties in my research. I am also greatly appreciative to Prof. Kok Wai Cheah at Hong Kong Baptist University for his valuable advice and generous financial support.

Special thanks to Dr. Xuhua Wang for her tremendous kindness and patience in laboratory trainings. I would also like to thank my fellow graduates at Imperial, Dr. Nathan Cheetham and Dr. Matthew Dyson, for their help with experiments and useful discussions. I am grateful to Dr. Yi Jiang for the collaborations and organic materials provided.

Finally, I would like to thank my family for their boundless love and entire support, which make me feel at home wherever I am.

Abstract

Molecular semiconductor materials are highly attractive as gain media for solid state lasers and amplifiers. Devices based on thin-film structures show great potential in miniaturised, tunable and flexible lasing applications at a low cost. The ultimate aim in this context is the realisation of electrically pumped organic semiconductor lasers. One of the main challenges is understanding the relationship between material properties and stimulated-device performance, i.e. identifying generally applicable molecular structures that facilitate amplified spontaneous emission (ASE) or lasing.

This thesis comprehensively investigates stimulated emission processes in thin-film molecular materials and structures by numerical modelling and experimental characterisation on amorphous and glassy spin-coated samples. Absorption and emission spectroscopies are used to obtain material properties in photo-physics, and excited state lifetime is extracted from transient photoluminescence measurement. A 2-level spatial-temporal model reveals some of the key material and structure parameters for ASE in planar thin-films, which is guided by nonuniformly distributed modal gain. Meanwhile, a semi-automated ASE measurement set-up is introduced, followed by a reliable gain characterisation based on a modified single-pass travelling wave approach with homogeneous saturation. New metrics, ‘gain versus pump’ and ‘gain length product’, are proposed to evaluate gain media independent of measurement conditions. Furthermore, resonance energy transfer in molecular blends is studied systematically. Results from a set of samples with varying donor-acceptor concentration ratios unambiguously link photoluminescence quantum efficiency and excited state lifetime to ASE performance, which opens the door to tailor-made materials for organic semiconductor lasers.

Contents

1 Introduction 11

1.1 Historical Background 11

1.1.1 Amplification of Light 11

1.1.2 Applications and Demands 12

1.2 Molecular Semiconductor Materials 13

1.2.1 Molecular Structures and Optoelectronic Properties of Conjugated Polymers 13

1.2.2 Advances in Material Processing and Device Fabrication 16

1.2.3 Recent Progress in Organic Semiconductor Lasers 17

1.2.4 Organic Semiconductor Gain Characterisation 19

1.2.5 Challenges in Organic Semiconductor Lasers 20

1.3 Thesis Outline 21

References 23

2 Experimental Techniques and Material Characterisation 29

2.1 Introduction 29

2.2 Thin-film Preparation and Characterisation 29

2.3 Photo-physics Characterisation 30

2.3.1 UV-Vis Spectroscopy 31

2.3.2 Photoluminescence Spectroscopy 33

2.3.3 Photoluminescence Quantum Efficiency 35

2.4 Photoluminescence Lifetime Characterisation 37

2.4.1 Streak Camera Operating Principle 37

2.4.2 Experimental Set-up and Data Collection 38

2.4.3 Data Analysis 41

2.4.4 Error Analysis 44

2.4.5 Extracting Lifetimes and Distributions 46

2.5 Summary 57

References 58
3 Amplified Spontaneous Emission in Thin-film Structures 60
3.1 Introduction 60
3.2 Rate Equations for Molecular Semiconductor Materials 60
3.2.1 From 4-Level Model to 2-Level Model 60
3.2.2 Model Simulation and Validation 64
3.2.3 Identifying Key Material Parameters for Amplified Spontaneous Emission 67
3.3 Modelling Thin Film Structures 69
3.3.1 Modal Property of Thin-film Planar Structures 69
3.3.2 Spatial Dependence of State Density and Photon Density 71
3.3.3 Effect of Gain Saturation 75
3.3.4 Further Considerations 77
3.4 Summary 78
References 79
4 Measurements of Amplified Spontaneous Emission 81
4.1 Introduction 81
4.2 Experimental Set-up 82
4.2.1 Calibration and Measurement Procedures 82
4.2.2 Experimental Error and Reliability 85
4.3 Characterisation of Amplified Spontaneous Emission 87
4.3.1 ASE Threshold and Modal Effect 87
4.3.2 Simplified Gain Equation – Limitations and Applicability 91
4.3.3 Gain Extraction (gm) not including Saturation 93
4.3.4 Gain Extraction ($g0$) including Saturation 96
4.4 New Metrics for ASE in Thin-film Structures 99
4.4.1 Material Aspect – Gain versus Pump 99
4.4.2 Device Aspect – Gain Length Product 101
4.5 Material Comparison and Discussion 103

4.5.1 Materials 103
4.5.2 Blue Polyfluorenes F8DP2, SC5A, PFO glassy 106
4.5.3 Green-yellow F8BT 108
4.6 Summary 111
References 112
5 Energy Transfer and Blend Study 115
5.1 Motivation 115
5.2 Energy Transfer Modelling 116
5.2.1 Donor-acceptor Energy Transfer 116
5.2.2 Rate Equation Model – 2-Level System 118
5.2.3 Donor-Acceptor Resonance Energy Transfer Analytical Solution 120
5.3 Photo-physics and Energy Transfer of Polymer Blends 121
5.3.1 Sample Preparation 121
5.3.2 Photo-physics Characterisation 123
5.3.3 Photoluminescence Lifetime Characterisation 127
5.3.4 Energy Transfer Rate 131
5.4 ASE and Gain Characterisation of Polymer Blends SC5A:SpL 133
5.4.1 ASE Energy Response 133
5.4.2 Optical Gain Characterisation 137
5.4.3 Linking ASE/lasing and Photo-physics 141
5.5 Summary 143
References 144
6 Conclusions 146
6.1 Thesis Summary 146
6.2 Outlook for Future Work 149
References 151
Appendices 152

List of Abbreviations

AFM	Atomic force microscope
ASE	Amplified spontaneous emission
CCD	Charge-coupled device
DFB	Distributed feedback
FRET	Förster resonance energy transfer
FWHM	Full width at half maximum
HOMO	Highest occupied molecular orbital
LASER	Light amplification by stimulated emission radiation
LUMO	Lowest unoccupied molecular orbital
NA	Numerical aperture
ND	Neutral density
OFET	Organic field-effect transistor
OLED	Organic light-emitting diode
OPV	Organic photovoltaic
OSL	Organic semiconductor laser
PC	Personal computer
PL	Photoluminescence
PLE	Photoluminescence excitation
PLQE	Photoluminescence quantum efficiency
PLQY	Photoluminescence quantum yield
TADF	Thermally activated delayed fluorescence
TE	Transverse electric
TM	Transverse magnetic
UV-Vis	Ultraviolet-visible spectroscopy
YAG	Yttrium aluminium garnet

List of Symbols

α	Absorption coefficient $[m^{-1}]$
α_{lo}	Re-absorption loss coefficient $[m^{-1}]$
α_{ex}	Photon cavity loss coefficient $[m^{-1}]$
β	Spontaneous emission factor
$\Gamma, \Gamma_{TE}, \Gamma_{TM}$	Waveguide confinement factor
η	PLQE
λ	Wavelength $[m]$
σ	Gaussian pulse width
σ_p, σ_e	Absorption and stimulated cross-section $[m^2]$
τ, τ_i	Excited state lifetime $[s]$
$\Psi(t)$	Probability a photon is emitted at time t
ν	Vibronic electronic energy level
Ω	Solid angle
A, A_i	Fitting constant
A_{DA}	Energy transfer rate
A_{PL}	Rate of PL component in ASE $[m^{-3}s^{-1}]$
A	Absorbance
$A\%$	Absorption [%]
b	Background noise
c	Fitting constant in compressed hyperbola
c	Speed of light in vacuum $[ms^{-1}]$
d	Film thickness $[m]$
E, E_i, E_f	Energy $[J]$
E_x, E_y, E_z	Electric field strength $[Vm^{-1}]$
$f(t)$	Decay function
$g(t)$	Excitation function

g, g_0, g_m	Gain coefficient $[m^{-1}]$
h	Planck constant $[Js]$
H_x, H_y, H_z	Magnetic field strength $[Am^{-1}]$
I, I_s	Photon intensity per area $[m^{-2}s^{-1}]$
I_p, I_{max}	Pump energy per pulse per area $[Jm^{-2}]$
I_{th}	ASE threshold energy per pulse per area $[Jm^{-2}]$
J	Cost function to minimise
k, k_{ij}	Electronic transition rate $[s^{-1}]$
L, L_{min}, L_{max}	Excitation stripe length $[m]$
L_{PL}, L_{th}, L_s	Excitation Stripe length for PL, ASE threshold and saturation $[m]$
n, n_{eff}	Refractive index, effective index
N, N_i	Electronic state density $[m^{-3}]$
$P(\tau)$	Normalised probability the excited state has lifetime τ
r	Distance separating donor and acceptor chromophores $[m]$
R	Configuration coordinate of molecular materials
R, R_{af}, R_{ff}	Reflectance [%]
R_0	Förster distance $[m]$
$R_p, R_{lo}, R_{sp}, R_{se}$	Rate of pump, loss, spontaneous and stimulated emission $[m^{-3}s^{-1}]$
S, S_{PL}	Photon density $[m^{-3}]$
S_0, S_1, S_2	Singlet electronic state energy manifolds
t, t_0	Time $[s]$
T, T_0	Transmittance [%]
T_1	Triplet electronic state energy manifold
u_p	Pump intensity per area $[m^{-2}s^{-1}]$
v_g	Group velocity $[ms^{-1}]$
W	Excitation stripe width $[m]$

1 Introduction

1.1 Historical Background

1.1.1 Amplification of Light

Laser, an acronym for ‘light amplification by stimulated emission radiation’, is a device that generates or amplifies coherent radiation at frequencies in the infrared, visible or ultraviolet regions of the electromagnetic spectrum [1]. Since the first demonstration of ruby lasers in 1960, lasers have changed the scope of light amplification and coherent electronics thanks to the remarkable beam properties of directionality, spectral purity and intensity [1]. Today, lasers as a tool have helped to understand the physical world through light-matter interaction, and laser related applications can be found in almost every corner of daily life. While lasers come in great variety of forms, there are three essential elements – a laser medium, an optical feedback structure and a pump [1,2]. The laser medium, also called gain media, is responsible for the amplification of light by stimulated emission. The optical feedback structure is carefully designed to proactively control light oscillation inside the structure and maintain a balanced gain/loss in order to meet specific requirement of coherence and intensity. The pump excites atoms/molecules in the laser medium into higher energy levels for optical emission. In general terms, the pump activates the laser medium, which radiates emission; the optical feedback structure traps the majority of light and aids stimulated processes in the gain medium, while the remaining minority exits the structure as laser output. On the other hand, devices with amplified spontaneous emission (ASE), also called ‘mirrorless laser’, do not have a feedback structure as the amplification is already strong enough [1,2]. ASE consists of both spontaneous

emission and amplified emission (i.e. stimulated emission) although the ratio of the two varies in different devices [1]. It is, therefore, stimulated emission that is the key to amplification of light.

The stimulated emission process is defined as the radiative decay of an excited state stimulated by an incoming photon [1-3]. The new photon has the same phase, frequency, polarisation and direction of travel as the incoming photon. This is in contrast to spontaneous emission whose emission properties are independent of the ambient electromagnetic field. The rate of stimulated emission depends on the number of incoming photons, the stimulated emission cross-section of the emitting species, and the excessive amount of available excited states (i.e. population inversion) [3]. In practice, although devices with feedback structures are usually sought, amplified spontaneous emission is favoured to characterise the stimulated emission in materials as it eliminates designing factors [4-6].

1.1.2 Applications and Demands

There are a wide range of applications involving the amplification of light [7]. Lasers and amplifiers are the core devices for transmitting and reading information in a fast and accurate way, from fibre-optic communication to optical disc storage. Lasers are widely used in manufacturing as a ‘mechanical’ drill as a small laser spot can carry high optical densities. Laser projection displays containing RGB sources are beneficial when large screen dimension, high resolution and colour saturation are required. Lasers are also used as a means of sensors in research due to the excellent beam quality and spectral purity. Recently, following the miniaturisation and integration of photonic components, small, tunable and flexible lasers are attractive for new application areas [8,9]. For example, miniaturised lasers that are also

biocompatible and implantable, have broad capability in medical imaging and sensing [10,11]. Meeting all the requirements is too challenging for inorganic lasers as they are generally brittle, non-flexible, made from toxic materials with intrinsic emission only at several fixed wavelengths [6]. On the contrary, molecular semiconductor materials are interesting candidates since carbon-based structures have better biocompatibility; their chemical versality and broad emission enables large tunability; organic materials are mechanically flexible by nature and compatible with a large variety of feedback structures; the large absorption coefficient has the potential for large optical gain [6,9,12-14].

1.2 Molecular Semiconductor Materials

1.2.1 Molecular Structures and Optoelectronic Properties of Conjugated Polymers

Molecular semiconductor materials are a fascinating class of materials for optoelectronic applications, thanks to their unique molecular structures and properties. In contrast to inorganic semiconductors band structures, molecular semiconductor materials are based on linked carbon chains or rings, which introduces infinite possibilities in chemical structures. In particular, conjugated polymers, also called linear macromolecules, have attracted great interests due to their tunable and efficient optical and electrical properties since conjugated polymers were electrically realised in 1977 [15]. As a definition, conjugated polymers are carbon-based macromolecules characterised by a backbone chain of alternating single (σ) and double ($\sigma + \pi$) bonds [16]. Each sp^2 hybridised carbon electron configuration consists of three σ bonds and a π bond. The former connects each carbon with three neighbours, while the latter contributes to a shared electron orbital along the chain [16,17]. These overlapping π orbitals

delocalise electrons over the length of conjugation (subject to distortion of polymer chains), where π^* anti-bonding orbitals have higher potential energy than π bonding orbitals, resulting in different electronic energy levels [16,17]. In contrast to valence and conduction bands of inorganic materials, the two electronic energy bands in π conjugated systems are named highest occupied molecular orbital π (HOMO) and lowest unoccupied molecular orbital π^* (LUMO) [16,17]. Each electronic energy level is further divided into a series of vibrational levels determined by vibrational wavefunctions [16,17]. Figure 1.1 is the Jablonski diagram showing the main photo-physical processes in conjugated polymers [18]. Once electrons are excited from the lowest ground state, bound states (i.e. excitons) of electron-hole pairs are formed at different vibrational levels of excited states, through internal relaxation, part of which (in singlet manifolds) then follow fluorescent decay back to the ground state [19]. Note the emission has lower energy than absorption (Stokes shift) [19]. Also note that absorption and internal relaxations are usually much faster than emission.

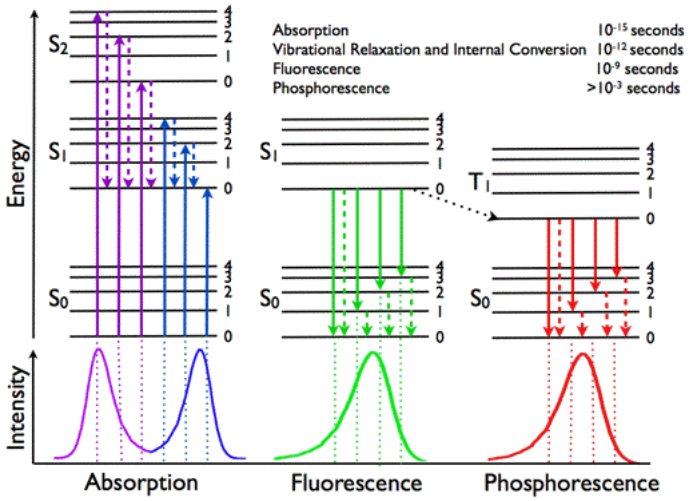


Figure 1.1 – The Jablonski diagram showing energy diagram of ground state S_0, singlet excited state S_1, S_2 and triplet state T_1. Photo-physical processes in conjugated polymers are illustrated, namely absorption (solid violet and blue), internal relaxation (dashed), fluorescence (solid green) and phosphorescence (solid red), of which the transition rate is in the descending order. Adapted from [18].

In general, conjugated polymers have a high absorption coefficient, and typically only $100-200\ nm$ thick thin-films can absorb more than 90% of light around the absorption peak, which is ideal for ultrathin flexible optoelectronic devices [5]. In terms of fluorescence, conjugated materials can also have high photoluminescence quantum efficiency [20]. Furthermore, charge transport in conjugated polymers can also be enhanced by orientation and packing of the molecules [21]. Combined with chemical versatility and broad tunable spectral range, conjugated polymers have great flexibility in optoelectronic properties [5,6]. Figure 1.2 shows a strategic material design that BBEHBO-PPV features the best attributes of MEH-PPV and BBEHP-PPV – high PLQY and short lifetime for visible light communications [22]. Therefore, tailor-made conjugated polymers prioritising certain properties have accommodated a large range of applications; organic light-emitting diodes (OLEDs), organic photovoltaics (OPVs), organic field-effect transistors (OFETs) are either commercialised or on track for large-area fabrication, and their superiority over inorganic counterparts include optical and electrical tunability, mechanical flexibility, and cost-effective high-volume production [23-25].

Fundamentally, conjugated polymers are also potentially good gain media for lasers and amplifiers, as the large absorption cross-section indicates a large stimulated emission cross-section and broad emission spectrum suggests spectrally tunable gain [4-6]. Although organic semiconductor lasers (OSLs) have been under extensive research in the hope of realising small, flexible, tunable and cost-effective lasers, electrically pumped OSLs have not yet been confirmed [26].

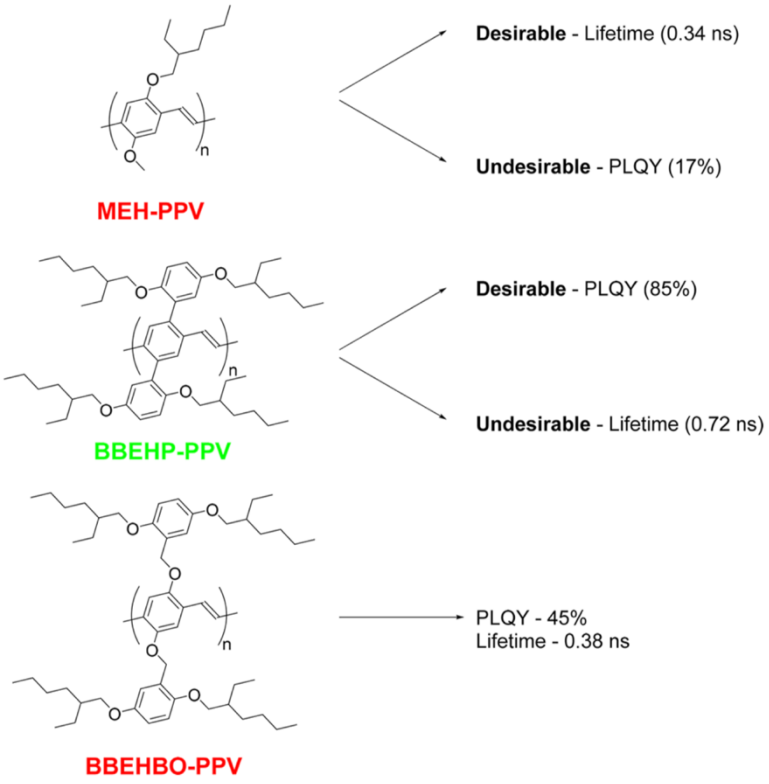


Figure 1.2 – A new PPV derivative (BBEHBO-PPV) for visible light communications combines high PLQY and short lifetime from two constituents, showing that optoelectronic properties can be strategically tuned in conjugated polymers. Adapted from [22].

1.2.2 Advances in Material Processing and Device Fabrication

One of the main advantages of molecular semiconductor materials is the ease of material processing and solid-state device fabrication at room temperature. In particular, conjugated polymers, which exhibit superior mechanical property, can be conveniently processed in solution and form thin-film multi-layer structures by spin-coating or ink-jet printing (for example), which opens the door to large-scale devices at a low cost [27]. More importantly, those devices have controllable variety of morphologies, ranging from amorphous to crystalline [6]. Amorphous samples are preferred in optical characteristics as glassy surface and uniform film quality suppress scattering/loss, while crystalline sample's high charge

carrier mobility is beneficial in electronic devices. For OSLs, device fabrication is more complicated as lasers require feedback structures. Although conventional lithography and etching processes cannot be applied to organic semiconductors, there are alternative attractive techniques to define wavelength-scale photonic microstructures required for lasing resonators [28]. One solution is to prepare a substrate with gratings or patterns, which could be done by electron beam lithography or nanoimprinting, before making semiconductor devices [29,30]. On the other hand, structure formation can be achieved when depositing organic materials via self-assembly [31]. Moreover, spatial patterning is also possible after polymer thin-films are coated by introducing conformation change via masked solvent vapor exposure [32]. It is worth mentioning that most molecular semiconductor devices have vertical thin-film structures around $0.1 - 1\ \mu m$ thick and are relatively flexible with surface areas [23-25]. However, gain characterisation often involves photon propagation lengths of multiple mm and thus very sensitive to the overall film quality [33]. Similarly, encapsulation is also more demanding for organic gain media in thin-film structures, even in research labs. Since samples are intensely pumped by an inorganic laser, oxidation, thermal degradation and laser ablation are unavoidable, but can be significantly reduced by simple encapsulation [34].

1.2.3 Recent Progress in Organic Semiconductor Lasers

Despite the early organic dye lasers discovered in the 1960s, the first solid-state optically pumped OSL was only realised 30 years later following the wave of organic electronics opened up by OLED research [35,36]. Since then, optically pumped OSLs have attracted extensive research and devices are mostly based on OLED materials as emission layer but with added resonators [4-6,37]. For a material study, photopumping can be convenient to study stimulated emission and gain properties without the complications induced by current injection, charge

transport and electrode incorporation [4]. Optically pumped OSLs have been demonstrated in a large variety of materials including small molecules, star-shaped and dendritic oligomers and linear conjugated polymers [22,33,34]. In conjugated polymers, two classes of materials are most widely used as gain media – polyfluorenes and poly(phenylenevinylenes) (PPV) – both were first reported as OLED materials, which have high fluorescence but low charge carrier mobility [38-41]. In addition to the typical OLED material strategy to raise quantum efficiency and reduce quenching, other improvements have been made to enhance stimulated emission [42]. For example, changing the side chains to the backbone of polyfluorenes could increase carrier mobility by introducing more interchain effective hopping sites [43]; morphologies and phases in polyfluorenes can be controlled by deposition conditions (e.g. solvent quality) and post treatment (e.g. thermal and/or vapor annealing) – the structural conformation change may result in increased crystallinity and distinct narrowed emission spectrum [20,44]; aligning the polymer chains of MEH-PPV in parallel can reduce ASE threshold by 20 times with polarised emission [45]. Donor-acceptor blends are also one of the solutions to combine the required fluorescence and mobility in a single active medium – 85%F8BT:15%P3HT blend achieved confluence of efficient optical gain and conducive charge injection/transport [46,47]. More recently, some significant progresses towards electrically pumped OSLs have emerged. Organic light-emitting field-effect transistor (OLEFET) with vertical microcavity was demonstrated to show superior optical resonance under electroluminescence [48]. Encapsulated devices using high PLQE material BSBCz as active medium, incorporating a mixed order (distributed feedback) DFB grating, not only operated at high repetition rate of 80 MHz or long pulse duration of 30 ms under optical pumping but also showed narrowed emission in current-injection OSL diodes, which opened up the opportunity for continuous-

wave operation and electrical pumping [26,34]. As an alternative to electrical pumping, OSLs can be optically pumped by small and compact excitation sources, such as microchip laser or light-emitting diode [49,50]. Apart from OSLs, conjugated polymers, as gain media, have also been used in other devices such as optical amplifier and chemical sensors [51,52]. Besides, in a broader view of materials, perovskite-based organic/inorganic hybrid lasing devices (optically pumped), utilising high absorption coefficient and high charge carrier mobility, were recently reported [53,54]. Devices with advanced concepts such as exciton-polariton condensation or colloidal quantum dots could also become potential small and flexible alternatives to OSLs [55,56].

1.2.4 Organic Semiconductor Gain Characterisation

The main method for gain characterisation for organic materials used to be pump-probe transient absorption spectroscopy, where samples are pumped by an ultrafast pulse of intense laser light and transient absorption is probed by another weak pulse of light at different time delays [4,5]. The probe beam will be amplified if gain is present in the material. Due to the complication of pump-probe measurement, a much easier method – ASE measurement – has been widely adapted to characterise organic gain media as the ‘probing’ photons are internally created by spontaneous emission [4]. On the other hand, the disadvantage of ASE measurement is that only gain at a spectral peak can be observed as ‘probing’ photons are fixed although the material gain can be spectrally much broader (Appendix 4F) [4]. It is also relatively straightforward to prepare samples for ASE measurement – a uniform thin-film that is thick enough to support a guided mode in the planar waveguide (air/thin-film/substrate) (Chapter 3.3.1) [4]. The sample is excited in a stripe surface area, and emission is recorded from the film edge at varying pump energies and stripe lengths. Several methods have been adapted

from inorganics and used to characterise organic gain media, namely variable pump intensity (VPI), variable stripe length (VSL) and shifting excitation spot (SES) [40,57,58]. VPI and VSL are for optical gain characterisation, and SES measures the waveguide loss. However, the widely used methods have already brought doubts and concerns on their applicability and reliability, especially for the most popular VSL method [59-61]. Firstly, the extracted net gain is found to be dependent on excitation density and pulse duration, which makes it impossible to compare 'maximum gain values' without quoting pump energy [63-65]. Secondly, the choice of stripe length range also affects the extracted gain, as VSL is only valid in 'small-signal' regime without any gain saturation [65,66]. Thirdly, the ASE measurement is subject to waveguide geometry (i.e. thin-film thickness), and all extracted gain/loss are modal values – not material properties [67-69]. As a result, although a large variety of organic gain media have been reported, their gain properties are often inconsistent and incomparable under different measurement conditions. Therefore, a standard approach to characterise ASE is greatly needed.

1.2.5 Challenges in Organic Semiconductor Lasers

To date, the most significant gap of knowledge in electrically pumped OSLs fall in the underlying material physics – the general relationship between molecular structures and ASE/lasing performance has not yet been found [6]. There has not been a definitive answer to determines the ideal material for OSLs. Unfortunately, materials for OSLs are still mainly based on (somehow extended) knowledge and experience from other devices (e.g. OLEDs, OPVs, OFETs), and very few materials are specially designed for lasing [4-6]. Furthermore, although there have been doubts and concerns about the applicability and reliability of characterisation methods, the research community has not yet adapted a standardised

characterisation methodology for organic gain media, which results in inconsistent, incomparable and even mistaken claims [70]. This thesis tackles the challenges by presenting a comprehensive investigation of stimulated emission processes in molecular thin-film structures with emphasis in conjugated polymers. The aim is to propose a reliable and practical way to characterise gain media in thin-film format and reveal some of the links between the well-understood photo-physics parameters and desired ASE performance.

1.3 Thesis Outline

Chapter 2 starts from sample preparation and standard photo-physics characterisation with detailed step-by-step description. Once solution processed thin-film structures are presented, non-destructive measurements including UV-Vis spectroscopy, photoluminescence (PL) spectroscopy, photoluminescence quantum efficiency (PLQE) are discussed, followed by the introduction of photoluminescence lifetime characterisation by streak camera. Its operating principle and experimental set-up are outlined, and more importantly, data analysis and error analysis are explained in detail, which help to extract accurate fluorescent lifetime and dynamics by non-linear curve fitting.

Chapter 3 establishes a rate equation model to describe ASE in thin-film structures. 4-level and 2-level models are compared in both temporal evolution and steady-state energy response. Model parameters and assumptions are discussed in detail, and experimental data are used to validate the model. Emphasise is made on waveguide modal properties in thin-film planar structures, and the modified spatial-temporal model reveals significant distribution of gain and photon density, subject to travelling wave conditions, which are often not considered in ASE.

Chapter 4 focuses on ASE measurement and gain characterisation of polymer thin-films. Experimental set-up is described in detail and measures are taken to improve calibration and reliability. Data from a blue polyfluorenes (F8DP2) is presented as an example for characterisation. ASE threshold is defined and assessed, and modal effect are shown in measurement. Based on a modified single-pass travelling wave equation, a new procedure to extract net modal gain is introduced – fitting to data in PL, ASE, saturation regions separately and extracting one parameter at a time. In particular, the effect of gain saturation is examined thoroughly including the comparison between homogeneous and inhomogeneous saturation. Moreover, new metrics are derived and proposed to evaluate material and device gain properties independent of measurement conditions. A set of fluorene-based materials are characterised and show comparable results.

Chapter 5 investigates resonance energy transfer in donor-acceptor blends, in the hope of utilising the best of optical and electrical properties from both constituents. Temporal evolution of donor and acceptor is calculated numerically (rate equation model from Chapter 3) and analytically (convolution). Experimentally, two complete sets of thin-film samples (F8BT:RedF and SC5A:SpL) are prepared and characterised through photo-physics measurements in Chapter 2. Efficient resonance energy transfer is observed quantitatively in transient PL measurement. Furthermore, a comprehensive ASE and gain characterisation (from Chapter 4) of SC5A:SpL is discussed in detail and the new metrics reveal clear evidence of relationships between material properties and device ASE performance, which is also consistent with the rate equation model.

Finally, Chapter 6 summarises the work reported in this thesis and proposes some future outlooks on developing electrically pumped organic lasers.

References

[1] Siegman, A. E. (1986). Lasers. *University Science Books.*

[2] Svelto, O. (2010). Principles of lasers, 5th edition. *Springer.*

[3] Paschotta, R. (2008). Article on 'stimulated emission' in the Encyclopedia of Laser Physics and Technology, 1. *Wiley-VCH,* ISBN 978-3-527-40828-3

[4] McGehee, M. D., & Heeger, A. J. (2000). Semiconducting (conjugated) polymers as materials for solid-state lasers. *Advanced Materials, 12*(22), 1655–1668.

[5] Samuel, I. D. W., & Turnbull, G. A. (2007). Organic semiconductor lasers. *Chemical Reviews, 25*(7), 1272–1295.

[6] Kuehne, A. J. C., & Gather, M. C. (2016). Organic Lasers: Recent Developments on Materials, Device Geometries, and Fabrication Techniques. *Chemical Reviews, 116*(21), 12823–12864.

[7] Paschotta, R. (2008). Article on 'laser applications' in the Encyclopedia of Laser Physics and Technology, 1. *Wiley-VCH,* ISBN 978-3-527-40828-3

[8] Hill, M. T., & Gather, M. C. (2014). Advances in small lasers. *Nature Photonics, 8*(12), 908–918.

[9] Zhang, W., Yao, J., & Zhao, Y. S. (2016). Organic Micro/Nanoscale Lasers. *Accounts of Chemical Research, 49*(9), 1691–1700.

[10] Gather, M. C., & Yun, S. H. (2011). Single-cell biological lasers. *Nature Photonics, 5*(7), 406–410.

[11] Kim, T., McCall, J. G., Jung, Y. H., Huang, X., Siuda, E. R., Li, Y., … Bruchas, M. R. (2013). Injectable, cellular-scale optoelectronics with applications for wireless optogenetics. *Science, 340*(6129), 211–216.

[12] Samuel, I. D. W., & Turnbull, G. A. (2004). Polymer lasers: Recent advances. *Materials Today, 7*(9), 28–35.

[13] Menard, E., Meitl, M. A., Sun, Y., Park, J. U., Shir, D. J. L., Nam, Y. S., … Rogers, J. A. (2007). Micro- and nanopatterning techniques for organic electronic and optoelectronic systems. *Chemical Reviews, 107*(4), 1117–1160.

[14] Karl, M., Glackin, J. M. E., Schubert, M., Kronenberg, N. M., Turnbull, G. A., Samuel, I. D. W., & Gather, M. C. (2018). Flexible and ultra-lightweight polymer membrane lasers. *Nature Communications, 9*(1), 1525.

[15] Chiang, C. K., Fincher, C. R., Park, Y. W., Heeger, A. J., Shirakawa, H., Louis, E. J., … MacDiarmid, A. G. (1977). Electrical Conductivity in Doped Polyacetylene. *Physical Review Letters, 39*(17), 1098–1101.

[16] Patrick, G. L. (2003). Organic chemistry, 2nd edition. *Taylor & Franics.*

[17] Wade, L. G. (2013). Organic chemistry, 8th edition. *Pearson.*

[18] Visser, A. J. W. G., & Rolinski, O. J. (2010). Basic Photophysics. *Photobiological Science Online.*

[19] Lakowicz, J. R. (2006). Principles of fluorescence spectroscopy, 3rd edition. *Springer.*

[20] Perevedentsev, A., Chander, N., Kim, J. S., & Bradley, D. D. C. (2016). Spectroscopic properties of poly(9,9-dioctylfluorene) thin films possessing varied fractions of β-phase chain segments: enhanced photoluminescence efficiency via conformation structuring. *Journal of Polymer Science, Part B: Polymer Physics, 54*(19), 1995–2006.

[21] Feng, X., Marcon, V., Pisula, W., Hansen, M. R., Kirkpatrick, J., Grozema, F., … Müllen, K. (2009). Towards high charge-carrier mobilities by rational design of the shape and periphery of discotics. *Nature Materials, 8*(5), 421–426.

[22] Kanibolotsky, A. L., Laurand, N., Dawson, M. D., Turnbull, G. A., Samuel, I. D. W., & Skabara, P. J. (2019). Design of Linear and Star-Shaped Macromolecular Organic Semiconductors for Photonic Applications. *Accounts of Chemical Research, 52*(6), 1665–1674.

[23] Friend, R. H., Gymer, R. W., Holmes, A. B., Burroughes, J. H., Marks, R. N., Taliani, C., … Salaneck, W. R. (1999). Electroluminescence in conjugated polymers. *Nature, 397*(6715), 121–128.

[24] Günes, S., Neugebauer, H., & Sariciftci, N. S. (2007). Conjugated polymer-based organic solar cells. *Chemical Reviews, 107*(4), 1324–1338.

[25] Dimitrakopoulos, C. D., & Malenfant, P. R. L. (2002). Organic Thin Film Transistors for Large Area Electronics. *Advanced Materials, 14*(2), 99–117.

[26] Sandanayaka, A. S. D., Matsushima, T., Bencheikh, F., Terakawa, S., Potscavage, W. J., Qin, C., … Adachi, C. (2019). Indication of current-injection lasing from an organic semiconductor. *Applied Physics Express, 12*(6), 061010.

[27] Voss, D. (2000). Cheap and cheerful circuits. *Nature, 407*, 442–444.

[28] Clark, J., & Lanzani, G. (2010). Organic photonics for communications. *Nature Photonics, 4*(7), 438–446.

[29] Lawrence, J. R., Turnbull, G. A., & Samuel, I. D. W. (2003). Polymer laser fabricated by a simple micromolding process. *Applied Physics Letters, 82*(23), 4023–4025.

[30] Tsiminis, G., Wang, Y., Kanibolotsky, A. L., Inigo, A. R., Skabara, P. J., Samuel, I. D. W., & Turnbull, G. A. (2013). Nanoimprinted organic semiconductor laser pumped by a light-emitting diode. *Advanced Materials, 25*(20), 2826–2830.

[31] Furumi, S. (2012). Recent advances in polymer colloidal crystal lasers. *Nanoscale, 4*(18), 5564.

[32] Perevedentsev, A., Sonnefraud, Y., Belton, C. R., Sharma, S., Cass, A. E. G., Maier, S. A., … Bradley, D. D. C. (2015). Dip-pen patterning of poly(9,9-dioctylfluorene) chain-conformation-based nano-photonic elements. *Nature Communications, 6*, 5977.

[33] Xia, R., Heliotis, G., Hou, Y., & Bradley, D. D. C. (2003). Fluorene-based conjugated polymer optical gain media. *Organic Electronics, 4*(2–3), 165–177.

[34] Sandanayaka, A. S. D., Matsushima, T., Bencheikh, F., Yoshida, K., Inoue, M., Fujihara, T., … Adachi, C. (2017). Toward continuous-wave operation of organic semiconductor lasers. *Science Advances, 3*(4), e1602570.

[35] Tessler, N., Denton, G. J., & Friend, R. H. (1996). Lasing from conjugated-polymer microcavities. *Nature, 382*(6593), 695–697.

[36] Hide, F., Díaz-García, M. A., Schwartz, B. J., Andersson, M. R., Pei, Q., & Heeger, A. J. (1996). Semiconducting Polymers: A New Class of Solid-State Laser Materials. *Science, 273*(5283), 1833 LP – 1836.

[37] Barnes, W. L., Samuel, I. D. W., Turnbull, G. A., & Andrew, P. (2003). Photonic mode dispersion of a two-dimensional distributed feedback polymer laser. *Physical Review B - Condensed Matter and Materials Physics, 67*(16), 1–8.

[38] Burroughes, J. H., Bradley, D. D. C., Brown, A. R., Marks, R. N., Mackay, K., Friend, R. H., … Holmes, A. B. (1990). Light-emitting diodes based on conjugated polymers. *Nature, 347*(6293), 539–541.

[39] Grell, M., Bradley, D. D. C., Inbasekaran, M., & Woo, E. P. (1997). A glass-forming conjugated main-chain liquid crystal polymer for polarised electroluminescence applications. *Advanced Materials, 9*(10), 798–802.

[40] McGehee, M. D., Gupta, R., Veenstra, S., Miller, E. K., Díaz-García, M. A., & Heeger, A. J. (1998). Amplified spontaneous emission from photopumped films of a conjugated polymer. *Physical Review B - Condensed Matter and Materials Physics, 58*(11), 7035–7039.

[41] Heliotis, G., Bradley, D. D. C., Turnbull, G. A., & Samuel, I. D. W. (2002). Light amplification and gain in polyfluorene waveguides. *Applied Physics Letters, 81*(3), 415–417.

[42] Aimono, T., Kawamura, Y., Goushi, K., Yamamoto, H., Sasabe, H., & Adachi, C. (2005). 100% fluorescence efficiency of 4, 4′ -bis[(N-carbazole)styryl] biphenyl in a solid film and the very low amplified spontaneous emission threshold. *Applied Physics Letters, 86*(7), 071110.

[43] Yap, B. K., Xia, R., Campoy-Quiles, M., Stavrinou, P. N., & Bradley, D. D. C. (2008). Simultaneous optimisation of charge-carrier mobility and optical gain in semiconducting polymer films. *Nature Materials, 7*(5), 376–380.

[44] Stavrinou, P. N., Ryu, G., Campoy-Quiles, M., & Bradley, D. D. C. (2007). The change in refractive index of poly(9,9-dioctylfluorene) due to the adoption of the β-phase chain conformation. *Journal of Physics: Condensed Matter, 19*(46), 466107.

[45] Martini, I. B., Craig, I. M., Molenkamp, W. C., Miyata, H., Tolbert, S. H., & Schwartz, B. J. (2007). Controlling optical gain in semiconducting polymers with nanoscale chain positioning and alignment. *Nature Nanotechnology, 2*(10), 647–652.

[46] Xia, R., Stavrinou, P. N., Bradley, D. D. C., & Kim, Y. (2012). Efficient optical gain media comprising binary blends of poly(3-hexylthiophene) and poly(9,9-dioctylfluorene-co-benzothiadiazole). *Journal of Applied Physics, 111*(12), 123107.

[47] Zhang, Q., Wei, Q., Guo, X., Hai, G., Sun, H., Li, J., … Cabanillas-Gonzalez, J. (2019). Concurrent Optical Gain Optimisation and Electrical Tuning in Novel Oligomer: Polymer Blends with Yellow-Green Laser Emission. *Advanced Science, 6*, 1801455.

[48] Hu, Y., Lin, J., Song, L., Lu, Q., Zhu, W., & Liu, X. (2016). Vertical Microcavity Organic Light-emitting Field-effect Transistors. *Scientific Reports, 6*, 23210.

[49] Turnbull, G. A., Andrew, P., Barnes, W. L., & Samuel, I. D. W. (2003). Operating characteristics of a semiconducting polymer laser pumped by a microchip laser. *Applied Physics Letters, 82*(3), 313–315.

[50] Yang, Y., Turnbull, G. A., & Samuel, I. D. W. (2008). Hybrid optoelectronics: A polymer laser pumped by a nitride light-emitting diode. *Applied Physics Letters, 92*(16), 163306.

[51] Amarasinghe, D., Ruseckas, A., Vasdekis, A. E., Turnbull, G. A., & Samuel, I. D. W. (2009). High-gain broadband solid-state optical amplifier using a semiconducting copolymer. *Advanced Materials, 21*(1), 107–110.

[52] Yang, Y., Turnbull, G. A., & Samuel, D. W. (2010). Sensitive explosive vapor detection with polyfluorene lasers. *Advanced Functional Materials, 20*(13), 2093–2097.

[53] Xing, G., Mathews, N., Lim, S. S., Yantara, N., Liu, X., Sabba, D., … Sum, T. C. (2014). Low-temperature solution-processed wavelength-tunable perovskites for lasing. *Nature Materials, 13*(5), 476–480.

[54] Li, Z., Moon, J., Gharajeh, A., Haroldson, R., Hawkins, R., Hu, W., … Gu, Q. (2018). Room-Temperature Continuous-Wave Operation of Organometal Halide Perovskite Lasers. *ACS Nano, 12*(11), 10968–10976.

[55] Samuel, I. (2018). Colloidal nanocrystals: Electrifying quantum dots for lasers. *Nature Materials, 17*(1), 9–10.

[56] Rajendran, S. K., Wei, M., Ohadi, H., Ruseckas, A., Turnbull, G. A., & Samuel, I. D. W. (2019). Low Threshold Polariton Lasing from a Solution-Processed Organic Semiconductor in a Planar Microcavity. *Advanced Optical Materials, 7*(12), 1801791.

[57] Tsiminis, G., Wang, Y., Shaw, P. E., Kanibolotsky, A. L., Perepichka, I. F., Dawson, M. D., … Samuel, I. D. W. (2009). Low-threshold organic laser based on an oligofluorene truxene with low optical losses. *Applied Physics Letters, 94*(24), 243304.

[58] Cerdán, L. (2020). Simultaneous retrieval of optical gains , losses , and threshold in active waveguides. *Optics and Laser Technology, 121*, 105814.

[59] Kobayashi, T., Flämmich, M., Jordan, G., D'Arcy, R., Rüther, M., Blau, W. J., … Kaino, T. (2006). Blue-green small-signal gain and saturation in a luminescent polymer gain medium. *Applied Physics Letters, 89*(13), 131119.

[60] Lange, C., Schwalm, M., Chatterjee, S., Rühle, W. W., Gerhardt, N. C., Johnson, S. R., … Zhang, Y. H. (2007). The variable stripe-length method revisited: Improved analysis. *Applied Physics Letters, 91*(19), 191107.

[61] Cerdán, L., Costela, A., & García-Moreno, I. (2010). On the characteristic lengths in the variable stripe length method for optical gain measurements. *Journal of the Optical Society of America B, 27*(9), 1874.

[62] Lange, C., Schwalm, M., Metzger, B., & Chatterjee, S. (2010). Carrier-depletion in the stripe-length method: Consequences for gain measurement. *Journal of Applied Physics, 108*(10), 103119.

[63] Lattante, S., De Giorgi, M. L., Pasini, M., & Anni, M. (2017). Low threshold Amplified Spontaneous Emission properties in deep blue of poly[(9,9-dioctylfluorene-2,7-dyil)-alt-p-phenylene] thin films. *Optical Materials, 72*, 765–768.

[64] Lampert, Z. E., Papanikolas, J. M., Lappi, S. E., & Reynolds, C. L. (2017). Intrinsic gain and gain degradation modulated by excitation pulse width in a semiconducting conjugated polymer. *Optics and Laser Technology, 94*, 77–85.

[65] Silvestre, I., Marques, P. W. B., Valadares, M., & Cury, L. A. (2008). Gain coefficient method for amplified spontaneous emission in thin waveguided film of a conjugated polymer. *Applied Physics Letters, 93*(16), 163307.

[66] Cerdán, L. (2017). Variable Stripe Length method: influence of stripe length choice on measured optical gain. *Optics Letters, 42*(24), 5258.

[67] Visser, T. D., Blok, H., Demeulenaere, B., & Lenstra, D. (1997). Confinement factors and gain in optical amplifiers. *IEEE Journal of Quantum Electronics, 33*(10), 1763–1766.

[68] Lahoz, F., Oton, C. J., Capuj, N., Ferrer-González, M., Cheylan, S., & Navarro-Urrios, D. (2009). Reduction of the amplified spontaneous emission threshold in semiconducting polymer waveguides on porous silica. *Optics Express, 17*(19), 16766–16775.

[69] Bourdakos, K. N., Cury, L. A., & Monkman, A. P. (2011). The dependence of the amplified spontaneous emission on the waveguide excitation length for high quantum efficiency conjugated polymers. *Organic Electronics, 12*(7), 1142–1145.

[70] Samuel, I. D. W., Namdas, E. B., & Turnbull, G. A. (2009). How to recognise lasing. *Nature Photonics*, *3*(10), 546–549.

2 Experimental Techniques and Material Characterisation

2.1 Introduction

This chapter discusses sample preparation and characterisation techniques used for molecular materials, mostly conjugated polymers, in this thesis. All samples were prepared in thin-film format by solution processing. Atomic force microscope (AFM) and surface profilometer (Dektak) were used to characterise the film roughness and thickness but were only performed after all other measurements (including photo-physics and ASE/gain measurements). On the other hand, UV-Vis spectroscopy provides non-destructive alternative to estimate film quality. While standard photoluminescence (PL) and photoluminescence quantum efficiency (PLQE) presents qualitative properties of light emitting materials, the main focus of this chapter is the transient PL measured using a streak camera, which quantitatively describes the decay mechanism in thin-film samples. Both experimental set-up and data analysis will be discussed in detail. The characterisation in this chapter extracts important material parameters for ASE/gain study.

2.2 Thin-film Preparation and Characterisation

All samples were made inside a fume hood in a high pressure semi-clean room by solution processed spin-coating technique. Materials were used as received in bottles and were weighed in pre-cleaned vials. Solutions were prepared by adding known volumes of solvents (typically Chlorobenzene) then stirred and heated (typically 100C, lower than solvent boiling point) overnight. Calibrated pipettes were used to ensure the volume of the solvents match the

required solution concentration. Quartz substrate were pre-cleaned with acetone and isopropyl alcohol in ultrasonic bath for 15 minutes each and were given an oxygen plasma treatment for 10 minutes before use. For spin-coating, the solution was cooled to room temperature and deposited onto the quartz substrate until fully covered. The substrate was locked in place by vacuum and spun at typically 2000rpm for 1 minute. The acceleration of the spin-coater per second is set to half of the maximum rpm. The spin-coating technique is capable of making reliable and homogeneous thin-films for characterisation, while film roughness and thickness depend on both solution (e.g. molecular weight, concentration, cohesion, adhesion) and spin speed [1]. All samples were not encapsulated but stored in a vacuum desiccator between measurements. The actual film thickness would only be measured after all other non-destructive measurements are performed. Atomic force microscope (AFM) and optical microscope images are used to check film morphology and roughness, especially for donor-acceptor blended samples, ensuring thin-films are amorphous and glassy. This will be discussed in detail in Chapter 5. Surface profilometer (Dektak) measures film thickness from scratched samples. Each sample to be measured has 3 scratches, each of which were measured at 10 different positions. The average value is used as measured thickness of the sample. Note that for extensively studied polymeric materials (e.g. absorption coefficient known), roughness and thickness of its neat thin-films can be estimated by UV-Vis spectroscopy discussed in Chapter 2.3.1.

2.3 Photo-physics Characterisation

Steady-state photo-physics characterisation is widely used to study optical properties of molecular materials. Absorption and emission spectra showing how materials interact with

excitation light can reveal underlying vibronic structures and energy levels [2]. As an example, Figure 2.1 plots absorption and photoluminescence (PL) emission measured from a SC5A thin-film sample. While its absorption has a broad peak, the emission spectrum, with Stokes shift, shows 3 vibronic peaks (0-0, 0-1, 0-2 with 0-0 the highest intensity). The spectra are also important for stimulated emission. The gain guided amplified spontaneous emission (ASE) comes from 0-1 peak as absorption overlaps with part of the 0-0 peak, which suffers from severe self-absorption in propagation. Details of ASE measurement will be discussed in Chapter 4.

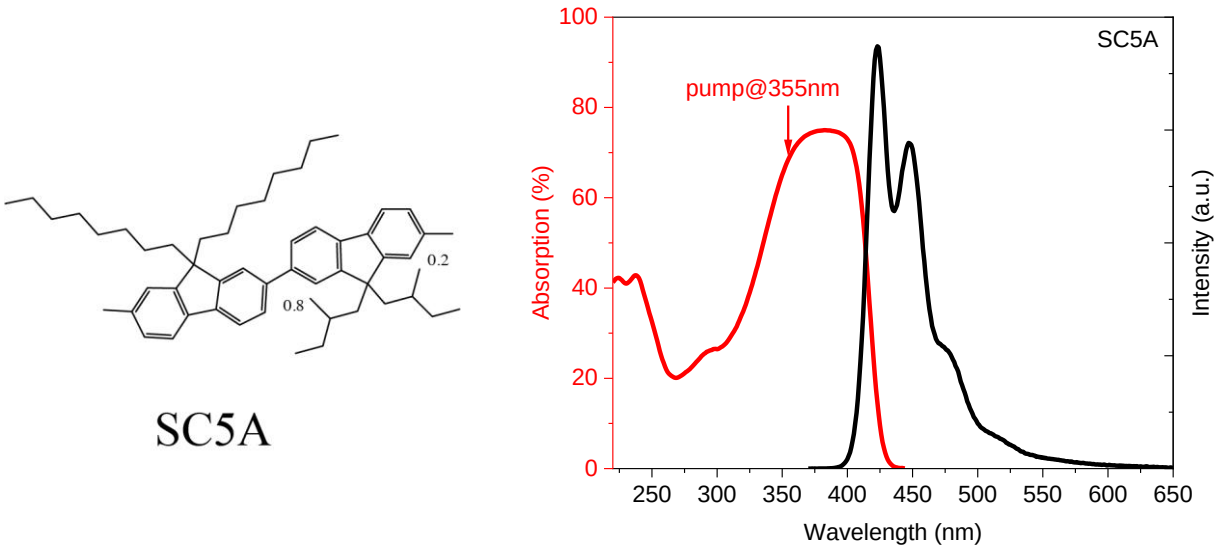


Figure 2.1 – SC5A molecular structure and its spectral response of UV-Vis absorption (red) and photoluminescence (PL) emission (black) in thin-film format. Absorption $A\%$ is calculated from measured transmittance T and specular reflectance R as $A\% = 100\% - T\% - R\%$. The sample here is SC5A with $130\ nm$ film thickness ($20\ mg/ml$ in P-xylene, 2000rpm).

2.3.1 UV-Vis Spectroscopy

UV-Vis spectroscopy is recorded from a Shimadzu UV-2600 [3]. Transmittance is measured using a direct method – simultaneously comparing transmitted photons from the sample and a

reference to determine the fraction transmitted (Figure 2.2(a)). In experiment, the reference is always left blank so that the baseline is 100%, and the minimum transmittance resolution is down to 0.01%. Alternatively, transmittance can be measured in an integrating sphere (Figure 2.2(b)), which also measures reflectance. This method can measure scattered transmittance. After measuring the reference, the sample is measured, thus its minimum resolution increases to 0.1%, and the signal would be saturated when measuring thick samples. The monochromator resolution is around $1nm$ for both methods. Since scattering is low in good quality neat polymer thin-films and reflectance does not have a major effect on characterisation, only direct transmittance is measured, from which absorbance A can be calculated by Beer-Lambert law.

$$A = -\log_{10}(T/T_0) \tag{2.1}$$

where $T_0 = 100\%$ in this case. Absorbance can be used to estimate film thickness d without the destructive Dektak measurement if the material has a known absorption coefficient α.

$$A = \alpha d/\ln 10 \tag{2.2}$$

UV-Vis transmittance can also assess the roughness of thin-films. Figure 2.3 plots an example of transmittance and absorbance spectra measured from SC5A film. The Fabry-Pérot oscillation due to internal reflections ($20\ mg/ml$) should just touch the transmittance of quartz for a good quality film. If not, this suggests the film is rough or suffers from scattering. This cannot be used on very thin films as the period of Fabry-Pérot oscillation is too long to be observed in the fixed wavelength range.

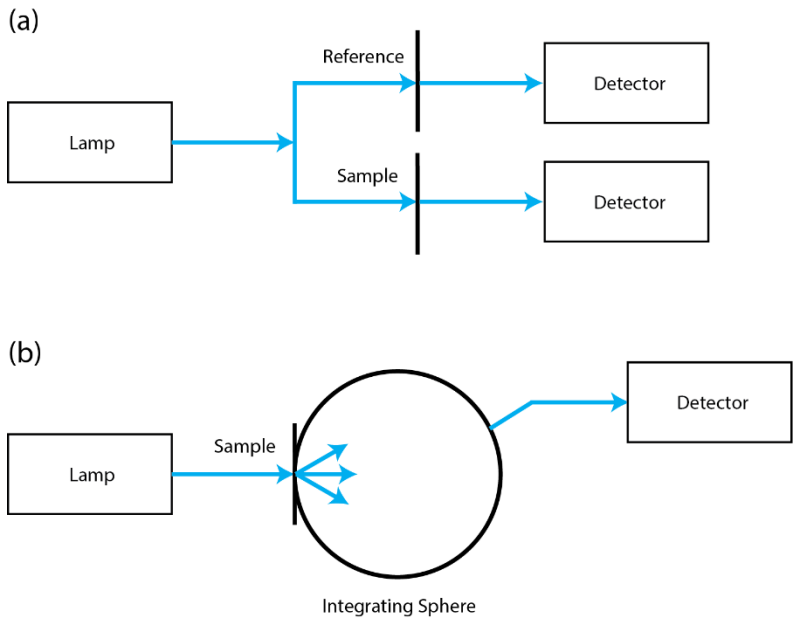


Figure 2.2 – Schematic diagram of UV-Vis transmittance measurement. (a) Direct method simultaneously measures transmitted photons through the sample and a reference. (b) Using an integrating sphere, the total transmittance (including direct and scattered) can be measured while a reference signal is taken before measuring the sample.

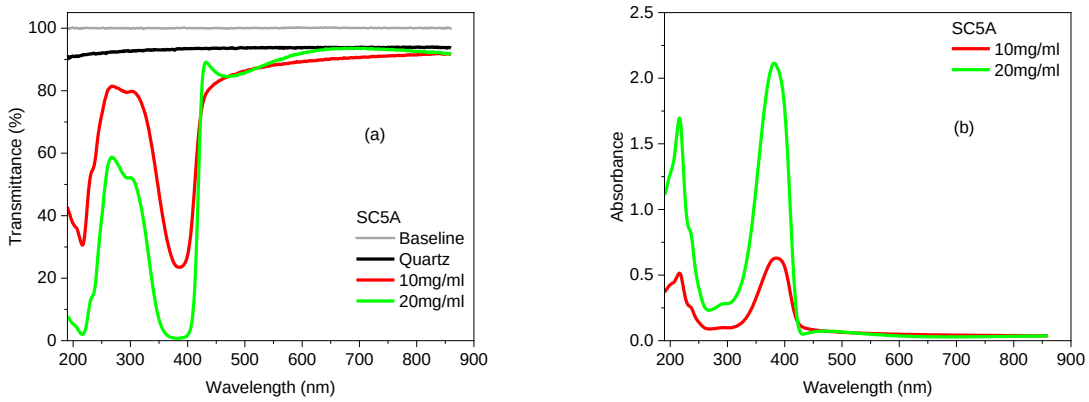


Figure 2.3 – (a) UV-Vis transmittance of SC5A thin-films in two thicknesses ($10, 20\ mg/ml$ in Chlorobenzene, 2000rpm). Baseline is measured as $100 \pm 0.5\%$ and transmittance of $1\ mm$ thick quartz substrate is about 93%. Thicker film ($20\ mg/ml$) has lower transmittance in absorbed region ($< 430\ nm$) and more periods of Fabry-Pérot oscillation at longer wavelength. (b) Calculated absorbance of SC5A thin-films by Equation (2.1). Film thickness is estimated to be $70\ nm$ for $10\ mg/ml$ and $190\ nm$ for $20\ mg/ml$ by Equation (2.2).

2.3.2 Photoluminescence Spectroscopy

Photoluminescence (PL) spectroscopy was performed using a Horiba FluoroMax-4 [4]. The

thin-film sample is pumped at 60 degrees incident angle while emission is collected at 30 degrees. There are two monochromators for the pump and emission spectra respectively, both of which typically have spectral resolution (monochromator slit width) of $1\,nm$. Pumping intensity is simultaneously measured with the emission so that spectral response can be calibrated. The spectrum is also corrected by a pre-set instrument response function. To compare different samples, spectra are area normalised by total number of photons collected.

$$\hat{I}(E) = \frac{I(E)}{S_{PL}} \tag{2.3}$$

where $S_{PL} = \int_{E_i}^{E_f} I(E)dE = \int_{\lambda_i}^{\lambda_f} I(\lambda)\frac{hc}{\lambda^2}d\lambda$ includes the Jacobian conversion from wavelength to energy.

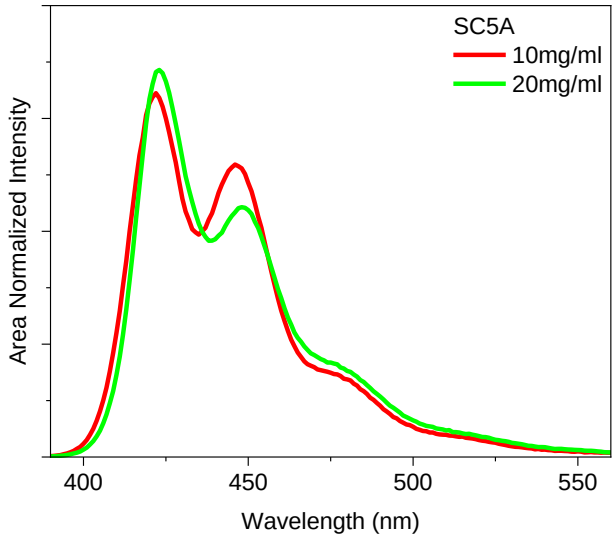


Figure 2.4 – Photoluminescence (PL) spectra of SC5A thin-films (as in Figure 2.3) pumped at $380nm$. The spectral response is area normalised by Equation (2.3) to show the same number of photons collected. Thicker film ($20\,mg/ml$) has slightly red-shifted vibronic peaks due to self-absorption (the spectral overlap at $400-450\,nm$ in Figure 2.1 between absorption and emission). Therefore, thinner films ($50-100\,nm$ thickness) are preferred for basic photo-physics characterisation providing the emission intensity is sufficient.

2.3.3 Photoluminescence Quantum Efficiency

Photoluminescence quantum efficiency (PLQE) is also measured using the Horiba FluoroMax-4 but with an integrating sphere, which has not been calibrated for spectral response thus PLQE results in this thesis are relative values. Following the de Mello method, three measurements are taken for each sample (Figure 2.5) – when a blank quartz substrate is placed inside the sphere ('Substrate'); when sample is placed inside the sphere, but excitation beam is directed to the sphere wall which then reflects the beam and pumps the sample indirectly ('Indirect Pump'); when sample is placed inside the sphere and is directly pumped ('Direct Pump') [5]. In order to measure the narrow and intense excitation spectrum, the monochromator slit width is reduced to $0.2\,nm$. The recorded spectra cover both excitation and emission wavelength range (Figure 2.6). For each spectrum, recorded excitation and emission photons are calculated by Equation (2.3). For excitation wavelength, the integration is within a $10\,nm$ window ($\pm 5\,nm$ excitation wavelength). For emission, the integration starts from excitation wavelength $+10\,nm$ but the end varies. As in Figure 2.6, PLQE of the SC5A thin-film is calculated as 36.8% for emission range $390-600\,nm$ and 37.0% for $390-700\,nm$. Therefore, it does not matter how to define the emission spectral range as long as the bold spectrum is visibly included. Generally, the PLQE measurement carries error of $\pm 5\%$. Figure 2.7 shows sample specific results from SC5A thin-films in different thicknesses and also the summary result of molecular materials used in this thesis.

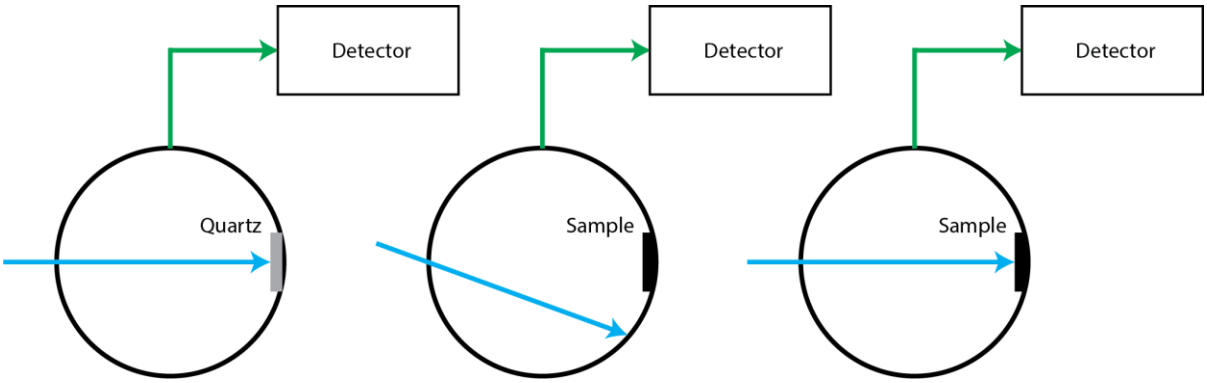


Figure 2.5 – Schematic diagram of photoluminescence quantum efficiency (PLQE) measurement using integrating sphere (de Mello method). Three spectral responses are recorded separately – when a blank quartz substrate is placed inside the sphere (left); when sample is placed inside the sphere, but excitation beam is directed to the sphere wall which then reflects the beam and pumps the sample indirectly (middle); when sample is placed inside the sphere and is directly pumped (right). The integrating sphere has not been calibrated for spectral response.

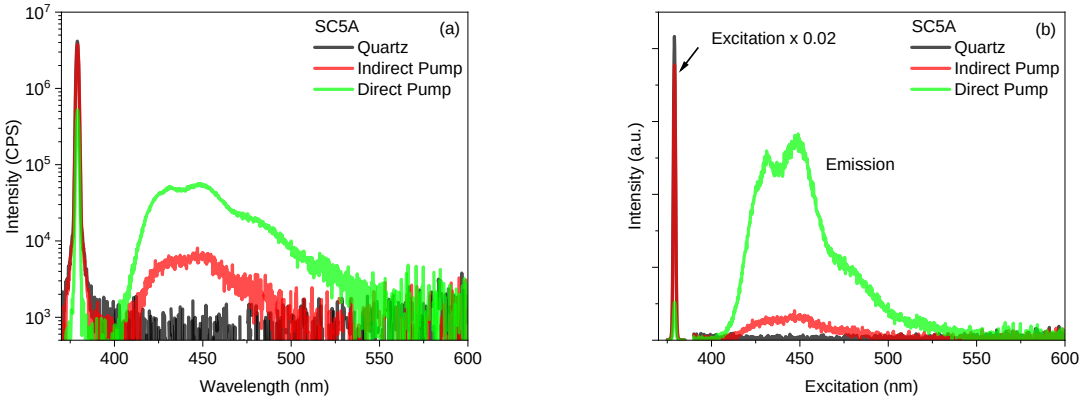


Figure 2.6 – photoluminescence quantum efficiency spectral response of SC5A thin-film ($20\ mg/ml$ in Chlorobenzene, 2000rpm) measured as in Figure 2.5 and plotted on a semi-log scale (a) and linear scale (b). Excitation spectrum is binned at $380 \pm 5\ nm$ and emission spectrum is cropped between $390 - 600\ nm$. Among the spectra, the more excitation photons are absorbed (less collected), the more emission photons are collected.

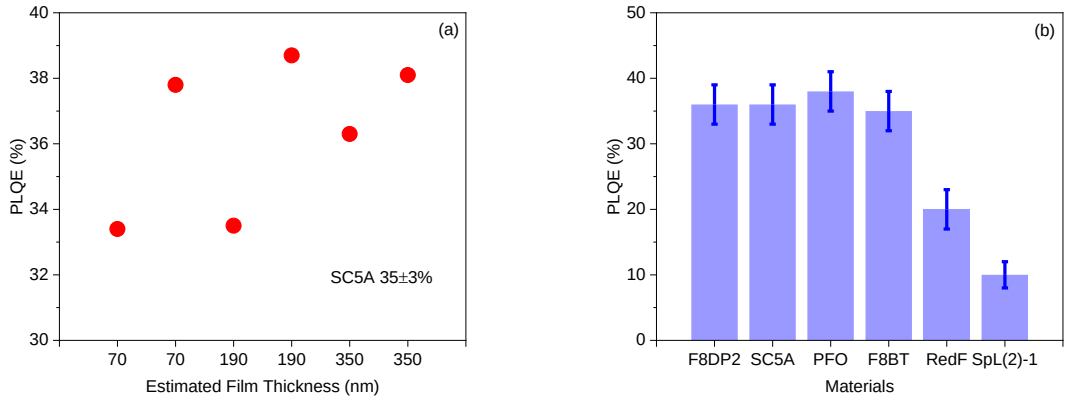


Figure 2.7 – (a) PLQE of SC5A thin-films in different thicknesses measured using the de Mello method as in Figure 2.5 – the values are consistent within 10% error. (b) PLQE summary of molecular materials used in this thesis. For each material, excitation wavelength is set at absorption peak. Although the set-up is not calibrated, the relative values can be compared and analysed.

2.4 Photoluminescence Lifetime Characterisation

2.4.1 Streak Camera Operating Principle

Streak camera is an important tool in measuring ultra-fast time-resolved spectroscopy, which assesses the lifetime of fluorophores in excited state before returning to ground state [2,6-9]. By converting time information into spatial information, streak camera can simultaneously measure spectral and temporal resolution of light-emitting molecular materials, delivering intensity vs. time and position (often wavelength) information [2]. This two-dimensional data is convenient to analyse the underlying mechanisms such as fluorescent decays and energy transfer [9]. Figure 2.8 shows the operating principle of streak camera [10,11]. It has a narrow rectangular entrance slit, which allows spectrally resolved light from monochromator. The photocathode converts incident light into a number of electrons proportional to photon intensity. A high voltage is then applied between a pair of sweep electrodes, which sweep the

electrons from top to bottom. The voltage is synchronised to the incident light and electrons arriving at different times are deflected in slightly different angles in the vertical direction, which results in different positions as they travel. Before being displayed on the phosphor screen, electrons are multiplied several thousands of times by MCP (micro-channel plate). Finally, the two-dimensional streak image is measured using a CCD. In this way, time information of incident light is converted into vertical spatial information, while the position in horizontal wavelength axis does not change in the whole process.

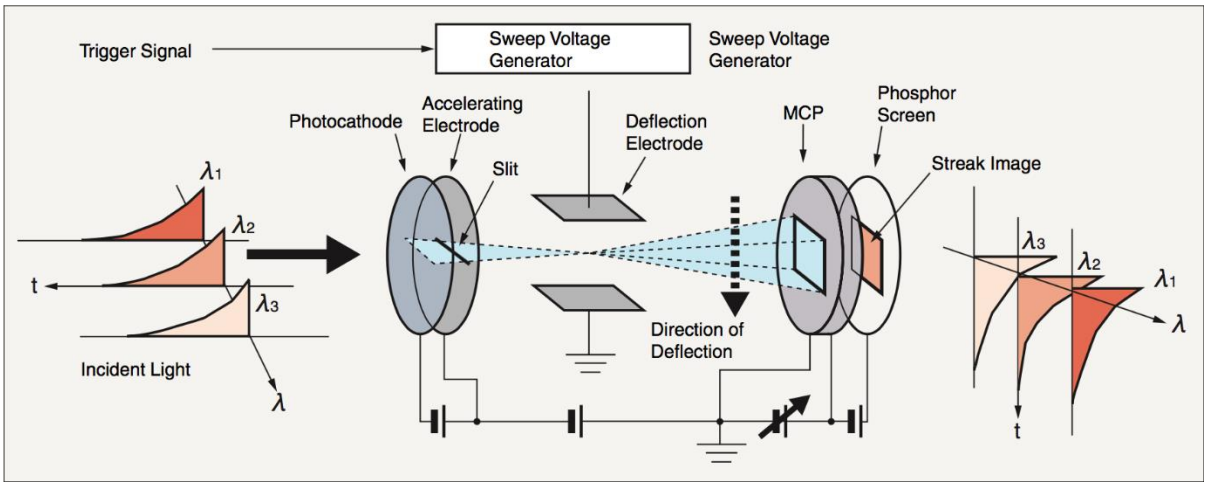


Figure 2.8 – Operating principle of streak camera assuming the incident light is from a monochromator thus horizontally positioned in wavelength. The photocathode converts the incoming photons into electrons, which are then applied a high sweep voltage at a synchronised timing. The electrons arriving at different times are deflected in slightly different angles thus displayed at different positions along vertical axis on the phosphor screen. Time information becomes physical spatial information. Adapted from [11].

2.4.2 Experimental Set-up and Data Collection

The full streak camera set-up consists of excitation, collection and synchronisation (Figure 2.9). An electrically triggered diode laser (Hamamatsu PLP-10) optically pumps sample surface. The generated photoluminescence is collected by a monochromator (Chromex 250is) through microscope objectives and an optical fibre. Then the spectrally resolved light is further resolved

in time axis by streak camera (Hamamatsu C4334-01). Both laser and streak camera are synchronised by synchronous delay generator (Hamamatsu C4792-01), which allow multiple pulses to be cumulatively collected. It is also used to adjust the delay of time axis so that expected signal can fall in the specific time window. A dichroic longpass filter is placed in optical path to prevent reflected excitation beam from saturating streak camera. In addition, a multi-mode fibre is used in collection optics to conveniently couple the emission into monochromator. All equipment is connected and controlled by a PC, where measurement is displayed in a 640 by 480 matrix with 640 data points for wavelength axis and 480 data points for time axis. Each data point represents photon intensity at certain wavelength and certain time. This set-up is capable of measuring photoluminescence in $220 - 850\ nm$ range with relatively high spectral response in $300 - 600\ nm$. However, the monochromator limits the spectral window of a single measurement down to $96/288\ nm$ depending on grating, which has resolution of $2/6\ nm$ respectively. For the time axis, the range is selected by the user from $1\ ns$ to $10\ \mu s$. The streak camera itself has a temporal resolution of $15\ ps$, however, the minimum resolution of the set-up is always higher due to electrical jitter and is also highly dependent on chosen time range. In practice, the laser usually operates at $1\ MHz$ and one measurement consists of hundreds of millions of exposures/pulses to achieve an ideal statistical average of photoluminescence decay. With good alignment and settings, the streak camera set-up should be capable of measuring signals with a dynamic range of $3 - 4$ orders of magnitude.

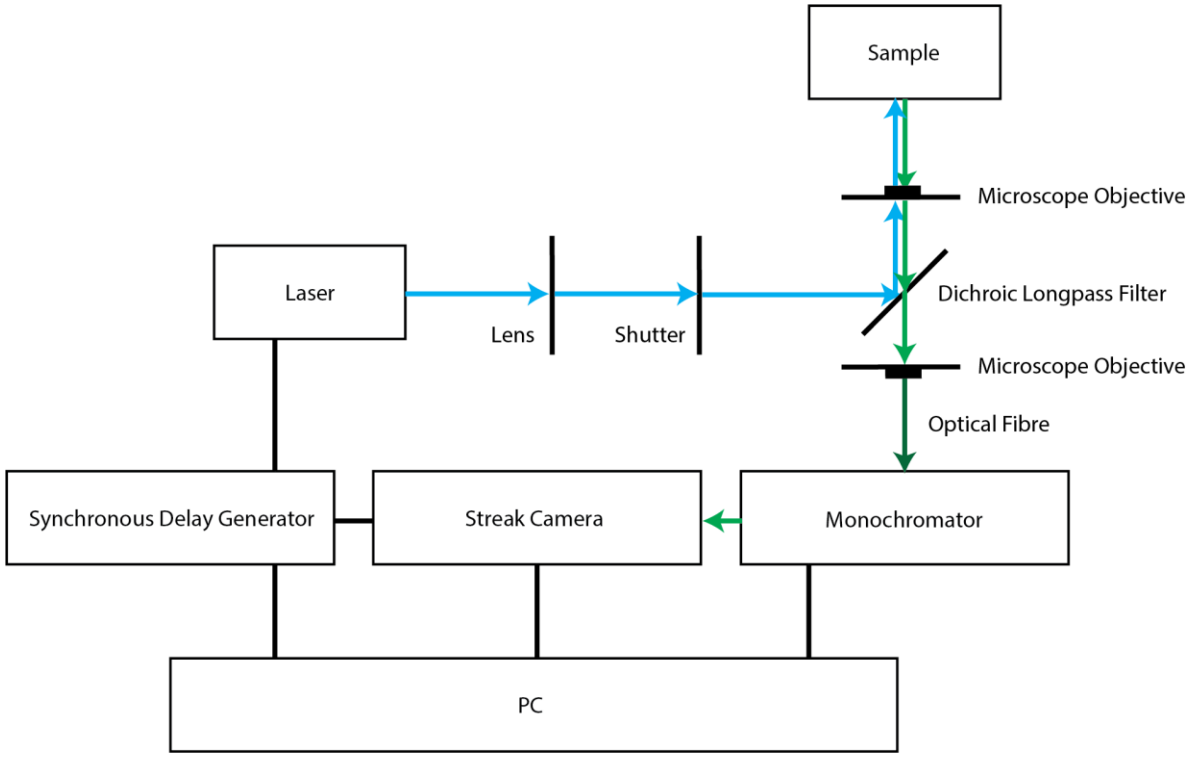


Figure 2.9 – Schematic diagram of streak camera set-up. A pulsed laser is focused onto the sample surface and photoluminescence is collected through an optical fibre into monochromator, which then passes the incident light to streak camera as in Figure 2.8. A dichroic longpass filter is used to eliminate excitation beam. The synchronous decay generator is used to sync excitation and emission for acquisition of multiple pulses.

Figure 2.10 shows a streak camera image in a linear contour plot. The sample here is F8BT thin-film, which was pumped by $379\,nm$ laser and measured in a $288\,nm$ spectral range centred at $550\,nm$. The laser is measured separately in a $288\,nm$ spectral range centred at $400\,nm$ by placing a blank quartz substrate on the sample holder. It is worth mentioning that the quartz is at normal incident to excitation beam when measuring the laser, while the thin-film sample is placed at a small angle (around 10 degrees) to ensure minimum excitation beam is reflected back. The time range for both sample and laser are $10\,ns$. The absolute value in time axis is arbitrary as the axis can be shifted by tuning synchronous delay generator. Steady-state spectrum $I(\lambda)$ can be obtained by integrating along time axis, while the transient response $I(t)$ is the integral along wavelength axis. For spectrum $I(\lambda)$, fast Fourier transform (FFT) can

be used to eliminate background noise and oscillations induced by fibre optics when necessary (Appendix 2A). The method is not applied in this thesis because vibronic peaks are recognisable and FFT of $I(\lambda)$ does not affect $I(t)$. Detailed transient data analysis will be discussed later, including choosing a suitable time range, controlling error and applying an appropriate decay model.

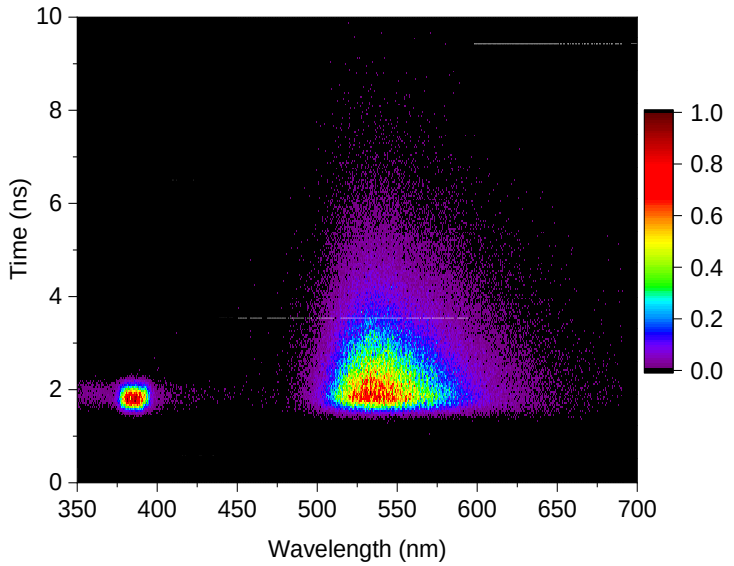


Figure 2.10 – Streak camera image of F8BT thin-film ($20\,mg/ml$ in Chlorobenzene, 2000rpm) pumped by $379\,nm$ laser at $1MHz$. Spectral range $288\,nm$ and time range $10\,ns$. Excitation and emission were measured separately.

2.4.3 Data Analysis

The methodology of post-measurement data analysis is important for transient spectroscopy. Once transient response (intensity vs. time) is obtained from streak camera image, extracting material properties and the underlying dynamics is not straightforward. In this thesis, the focus is on transient photoluminescence of molecular materials, where excited electrons decay both radiatively and non-radiatively.

$$\frac{dN(t)}{dt} = -(k_r + k_{nr})N(t) = -\frac{N(t)}{\tau} \tag{2.4}$$

where $N(t)$ is excited state density, k_r and k_{nr} are radiative decay rate and non-radiative decay rate respectively, τ is excited state lifetime. In experiment, instead of counting the number of excited states, photon intensity $k_r N(t)$ is observed, which is proportional to $N(t)$ [2]. Since streak camera measurement collects millions of independent photoluminescence, excited state lifetime is, statistically, the average amount of time before an excited state emits a photon and decays to ground state.

$$\langle \tau \rangle = \frac{\int_0^\infty t\Psi(t)dt}{\int_0^\infty \Psi(t)dt} \tag{2.5}$$

where $\Psi(t)$ is the probability a photon is emitted at time t. The expectation value $\langle \tau \rangle$ is a straightforward way to calculate expected lifetime. However, this method assumes instant excitation (delta function) while in fact laser pulses are Gaussian. As excitation takes time, this would overestimate lifetime. On the other hand, the measurement does not go to infinity but only takes a finite time range. A small fraction of photons emitted at longer times cannot be collected, which would underestimate lifetime. As a result, Equation (2.5) can be used as a quick check but is not capable of giving accurate excited state lifetime. To account for the full excitation-emission cycle, the convolution approach is implemented. The collected data is a convolution of pump and decay functions [12].

$$I(t) = \int_0^t g(t')f(t-t')dt' \tag{2.6}$$

where $g(t)$ is the excitation function depending on pump and $f(t)$ is the decay function

proportional to excited state density $N(t)$. $g(t)$ is proportional to the intensity of laser pulses and can either be measured from streak camera or defined as Gaussian function.

$$g(t) = \frac{1}{\sigma\sqrt{2\pi}} e^{-\frac{(t-t_0)^2}{2\sigma^2}} \tag{2.7}$$

where σ and t_0 are pulse width and peak position respectively. $f(t)$ has different form – the most common is single exponential. This is valid for materials with a single emitting species. The dynamics of excited state is in Equation (2.4), which can be solved as

$$f(t) = \mathrm{A}N(t) = \mathrm{A}e^{-\frac{t}{\tau}} \tag{2.8}$$

where A is constant for normalisation. Substitution of Equations (2.7) and (2.8) into Equation (2.6), the analytical solution of the convolution of $g(t)$ and $f(t)$ is (Appendix 2B)

$$\int_0^t g(t')f(t-t')dt' = \frac{1}{2}\mathrm{A}e^{\left(\frac{-2\tau t+\sigma^2+2\tau t_0}{2\tau^2}\right)}\left[erf\left(\frac{t\tau - t_0\tau - \sigma^2}{\sqrt{2}\sigma\tau}\right) - erf\left(\frac{-t_0\tau - \sigma^2}{\sqrt{2}\sigma\tau}\right)\right] \tag{2.9}$$

In practice, curve fitting is performed numerically by Equation (2.6). A least square approach is used to find optimal parameters (fitting algorithm 'lsqnonlin' in Matlab).

$$J = minimize \sum \left(\ln I_{fit}(t) - \ln I(t)\right)^2 \tag{2.10}$$

For all curve fitting, a background is included as additional parameter to account for the background during measurement. Upper and lower constraints are set for each fitting parameter. For lifetime τ, the statistical expectation in Equation (2.5) provides an initial guess. To confirm the validity of curve fitting result, residual and autocorrelation of $I_{fit}(t)$ and $I(t)$ are

calculated.

2.4.4 Error Analysis

There are a number of limitations in streak camera measurement, which would induce errors in data analysis [13]. Fundamentally, the minimum resolution of the streak camera image in time axis is governed by the response function of the instruments in Figure 2.8, which is about $15\ ps$. However, this resolution can never be achieved in the set-up. To study the temporal resolution, pulses from $379/405/465\ nm$ lasers are measured and FWHM of transient response is plotted against different time range settings in Figure 2.11. For time range $\geq 100\ ns$, the laser transient FWHM increases linearly with the time range as temporal resolution is limited by the 480 data points in time axis. However, for shorter time ranges, the FWHM does not decreases proportionally as temporal resolution is limited by the pump. The pulsed laser in use consists of different laser heads and an electrically triggered controller, which has electric jitter. Although the laser heads are capable of producing $60\ ps$ pulses, the minimum pulse width achievable in experiment is $120\ ps$. As a result, for time range $< 100\ ns$, laser pulses are always measured and used as $g(t)$ in Equation (2.6), while Gaussian function in Equation (2.7) may be used for longer time ranges.

There are also limitations in spectral response. As mentioned in Chapter 2.4.2, the monochromator has two gratings with different spectral ranges and resolutions listed in Table 2.1. Grating 2 is used in this thesis as molecular thin-films typically have photoluminescence range broader than the $96\ nm$ range of grating 1. The $6\ nm$ resolution of grating 2 is also sufficient to measure the vibronic peaks, which normally have $> 20\ nm$ FWHM. Instead of streak camera, samples requiring accurate spectral analysis should be measured using the

photoluminescence set-up as mentioned in Chapter 2.3.2.

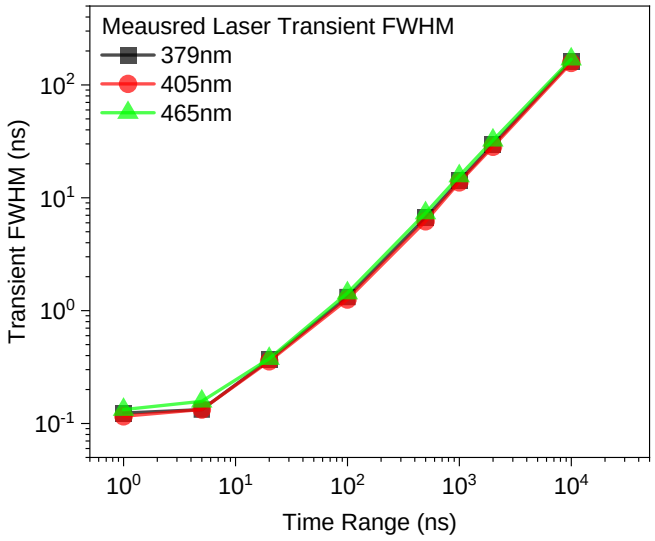


Figure 2.11 – $379/405/465\ nm$ laser pulses were measured using the streak camera in different time ranges. FWHM of the transient response is plotted to study the change of temporal resolution, which is linear when time range $\geq 100\ ns$.

Table 2.1 – The monochromator connected to streak camera has two gratings. Grating 2 is more suitable to measure the photoluminescence from molecular thin-films.

Monochromator Setting	Spectral Range	Spectral Resolution
Grating 1	$96\ nm$	$2\ nm$
Grating 2	$288\ nm$	$6\ nm$

Apart from pump and collection, error also arises from the optical path in between – the fibre-coupled design could seriously limit the temporal resolution due to wavelength dependent group delay and intermodal dispersion [14]. The $200\ \mu m$ diameter multi-mode fibre used may cause wavelength dependent group delay, which is also called group velocity dispersion, while intermodal dispersion is negligible in a set-up with $2\ m$ fibre and $> 100\ ps$ resolution. The group velocity dispersion would delay wavelength bins in time and is significant when time range is short. Figure 2.12 shows streak camera image of SC5A thin-film ($20\ mg/ml$ in

Chlorobenzene, 2000rpm) measured in 2 ns time range. Looking at the onset defined as 10% of the maximum intensity for each wavelength bin, the raw data has a group delay linear to wavelength. To correct the chirp, data is shifted in time axis accordingly to achieve same onset time independent of wavelength. The chirp corrected data has faster rise time, which fits better to the measured laser pulses. In this thesis, chirp correction is performed when time range is $\leq 20\ ns$ as the $0.2\ ns$ chirp will not affect longer time ranges.

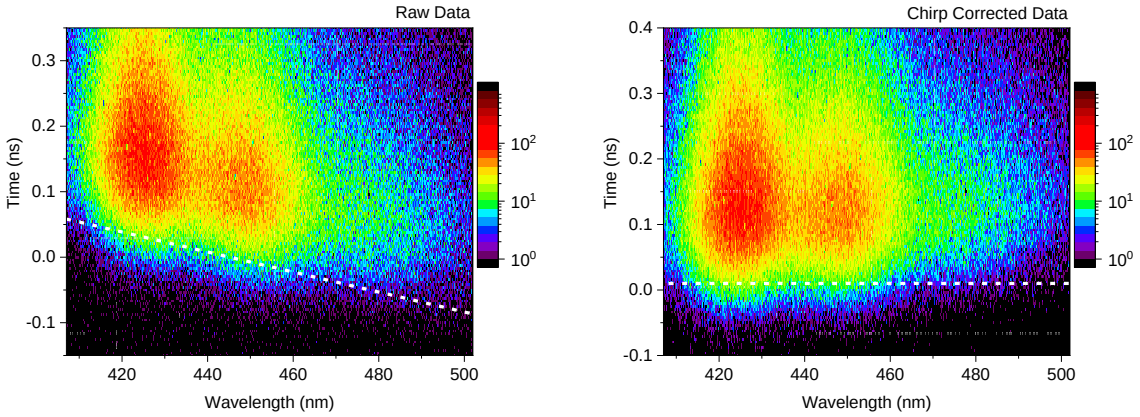


Figure 2.12 – Streak image of SC5A thin-film ($20\ mg/ml$ in Chlorobenzene, 2000rpm) pumped by 379 nm laser and measured in 2 ns time range. Raw data has onset time linearly dependent on wavelength due to group velocity dispersion in optical fibre. After chirp correction, each wavelength bin has the same onset time

2.4.5 Extracting Lifetimes and Distributions

This section showcases some examples of extracting photoluminescence lifetime from streak camera data. The methodology is to fit transient response $I(t)$ by Equation (2.6). The key is to determine $f(t)$ – which type of decay is suitable for the sample. Two basic decays – single exponential (Equation (2.8)) and biexponential (Equation (2.11)) – will be discussed in detail.

$$f(t) = \mathrm{A}_1 e^{-\frac{t}{\tau_1}} + \mathrm{A}_2 e^{-\frac{t}{\tau_2}} \tag{2.10}$$

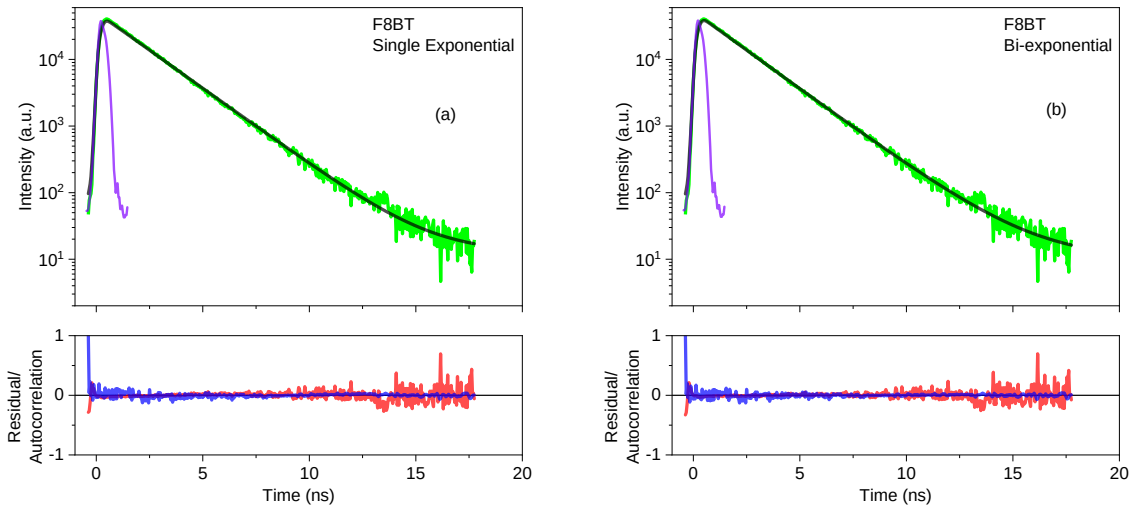


Figure 2.13 – Single exponential fit (a) and biexponential fit (b) of F8BT thin-film ($20\ mg/ml$ in Chlorobenzene, 2000rpm) pumped by $379\ nm$ laser and measured in $20ns$ time range. Measured transient response $I(t)$ is plotted in green, measured laser pulses in purple, fitted curve in black, residual in red and autocorrelation in blue. Both methods fit equally well.

Figure 2.13 plots curve fitting of F8BT thin-film ($20mg/ml$ in Chlorobenzene, 2000rpm) transient response by both single exponential and biexponential. The pulsed laser is $379\ nm$ and streak camera time range is $20\ ns$. Both types of decay fit the data well as residual and autocorrelation are close to zero. Looking at results in Table 2.2, both methods have similar extracted lifetime (for 97.3% photons in case of biexponential). To further determine which type of decay is applicable to F8BT, spectra from binned wavelengths and binned emission time window are plotted in Figure 2.14. Statistical expectation is used to estimate lifetime of each wavelength bin as curve fitting is less reliable for the reduced intensity in each bin. It is observed that photons emitted into different wavelength have similar lifetime. In addition, the binned time window shows that spectrum is unchanged against time. Therefore, F8BT can be considered as a material with single emitting species and single exponential decay should be used. Although biexponential would fit every single exponential data, there is no physical meaning to do so.

Table 2.2 – Extracted F8BT lifetime by single exponential and biexponential as in Figure 2.13. The ratio is the percentage of photons emitted in the corresponding lifetime. The single exponential lifetime 1.90 ns is very similar to the lifetime 1.85 ns that 97.3% photons have in biexponential fit.

Decay	Single Exponential	Biexponential
Equation	$f(t) = \mathrm{A}e^{-\frac{t}{\tau}}$	$f(t) = \mathrm{A}_1 e^{-\frac{t}{\tau_1}} + \mathrm{A}_2 e^{-\frac{t}{\tau_2}}$
Extracted Lifetime	$\tau = 1.90\ ns$	$\tau_1 = 1.85\ ns, \tau_2 = 3.15\ ns$
Ratio	100%	97.3% / 2.7%

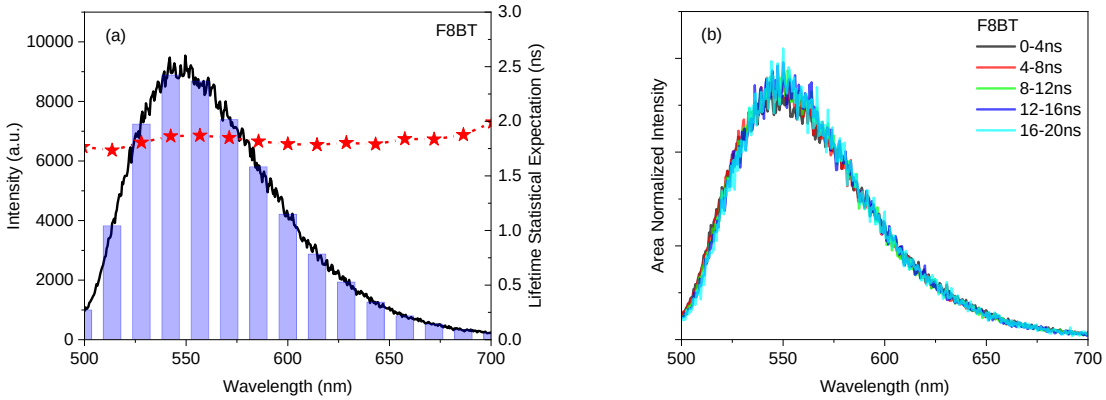


Figure 2.14 – (a) F8BT spectrum and lifetime statistical expectation of binned wavelengths showing that lifetime expectation is independent of wavelength. (b) F8BT spectra of binned emission time window showing that spectrum is independent of when it is emitted.

Streak camera data of SC5A thin-film (20 mg/ml in Chlorobenzene, 2000rpm) is also studied. Laser pulses remain at 379 nm but time range is reduced to 5ns to suit the short blue fluorescence. Transient response by both single exponential and biexponential is plotted in Figure 2.15. Unlike F8BT, SC5A data is fitted substantially better with biexponential decay. While residual and autocorrelation in biexponential fit stick with the zero baseline, the single exponential fit does not come close at all. It is also obvious in Table 2.3 that the single exponential lifetime is 40% longer than 97.9% photons in biexponential fit. Again, spectra from binned wavelengths and binned emission time window are analysed in Figure 2.16. Lifetime in the green wavelength region is significantly longer than in blue region, confirmed

by the spectral shift from narrow blue to broad green. SC5A is blue polyfluorene material (glassy phase only, no beta phase) with broad green-band emission with longer lifetime once the thin-film is oxidised. Since the measurement is taken in air, laser pulses may oxidise the un-encapsulated film. Even in a small fraction 2.1%, this green-band emission can be collected by streak camera. As a result, there are two emitting species in SC5A data and biexponential decay is the valid method.

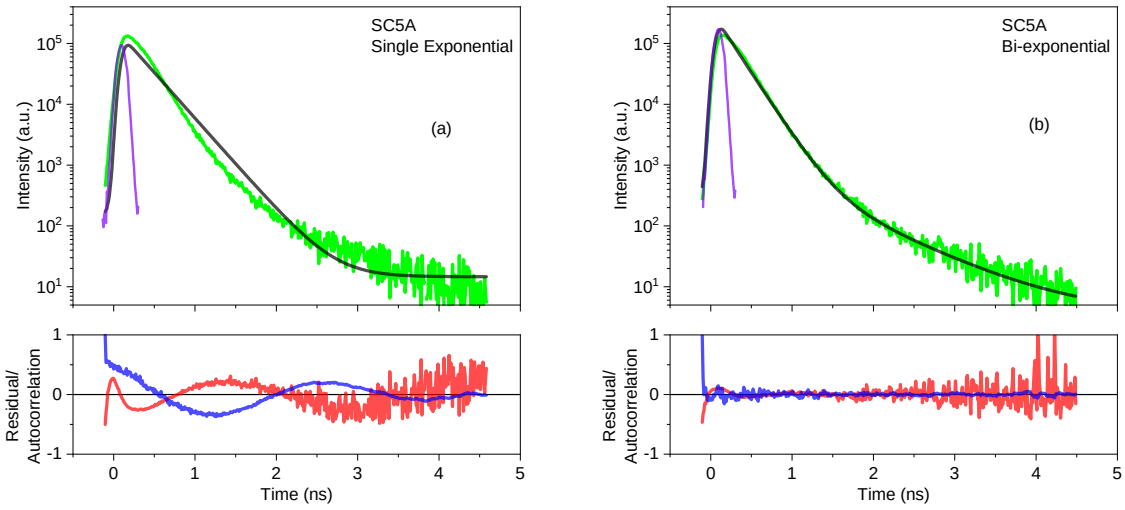


Figure 2.15 – Single exponential fit (a) and biexponential fit (b) of SC5A thin-film (20 mg/ml in Chlorobenzene, 2000rpm) pumped by 379 nm laser and measured in 20ns time range. Measured transient response $I(t)$ is plotted in green, measured laser pulses in purple, fitted curve in black, residual in red and autocorrelation in blue. Biexponential fit is substantially better than single exponential.

Table 2.3 – Extracted SC5A lifetime by single exponential and biexponential as in Figure 2.15. The ratio is the percentage of photons emitted in the corresponding lifetime. Single exponential fit has a lifetime that is 40% longer than 97.9% photons in biexponential fit.

Decay	Single Exponential	Biexponential
Equation	$f(t) = \mathrm{A}e^{-\frac{t}{\tau}}$	$f(t) = \mathrm{A}_1 e^{-\frac{t}{\tau_1}} + \mathrm{A}_2 e^{-\frac{t}{\tau_2}}$
Extracted Lifetime	$\tau = 0.29\ ns$	$\tau_1 = 0.21\ ns, \tau_2 = 0.71\ ns$
Ratio	100%	97.9% / 2.1%

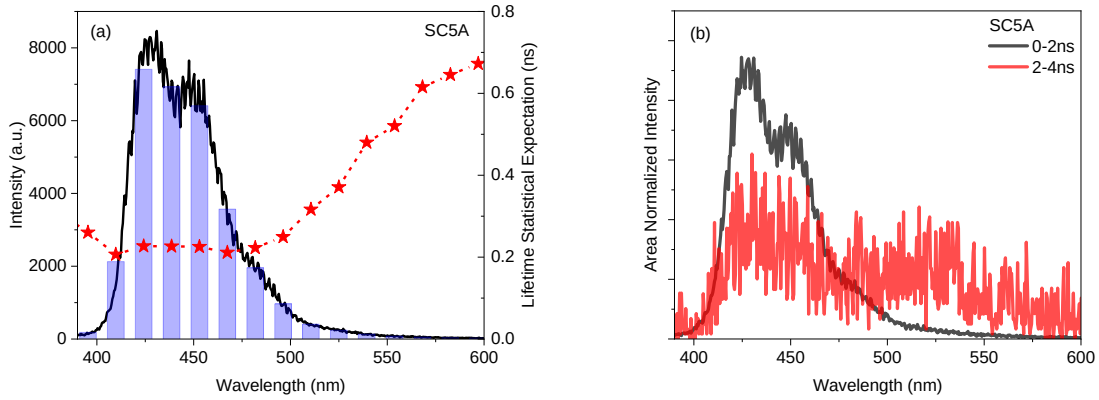


Figure 2.16 – (a) SC5A spectrum and lifetime statistical expectation of binned wavelengths showing lifetime expectation. Lifetime in green-band is significantly longer than blue fluorescence emission. (b) SC5A spectra of binned emission time window showing the changing spectrum against time. The change confirms that the broad green-band emission has longer lifetime than blue fluorescence.

The transient analysis was used to investigate the effect of *para* fluoro 'click' functionalisation, which can quantitatively tether nucleophiles to the polythiophene backbone [15]. The material introduces pentafluorobenzene (PFB) as a single end-group in a polythiophene derivative (P3OT), which is then tethered by a thiolated dye Coumarin$_{343}$-SH. Figure 2.17 compares the peak normalised absorption spectra of P3OT-PFB, P3OT-PFB-S-Coumarin$_{343}$ and the 9% dispersed dye in polystyrene, all of which in thin-film format. With the 'click' functionalisation, the absorption of P3OT-PFB-S- Coumarin$_{343}$ clearly indicates the additional contribution from dye moiety (the shaded region). Despite the differences in UV-Vis absorption, both P3OT-PFB and P3OT-PFB-S-Coumarin$_{343}$ thin-films display similar steady state photoluminescence spectra. Therefore, transient spectroscopy was employed to spot the differences (if any) of underlying dynamics in transient photoluminescence.

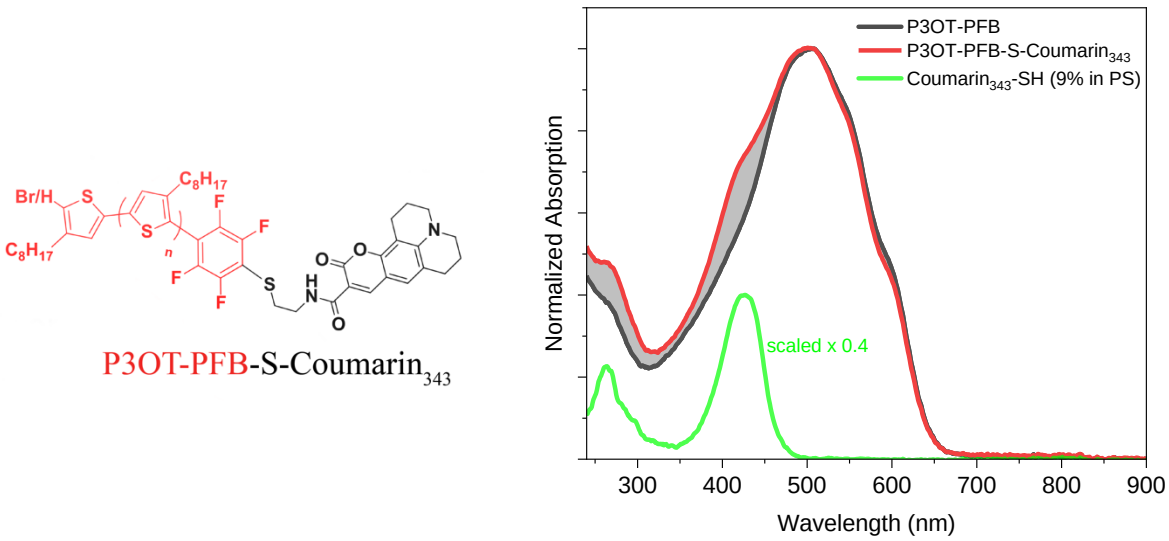


Figure 2.17 – Molecular structures and peak normalised thin-film UV-Vis spectra (obtained from recording both transmittance and specular reflectance as $A\% = 100\% - T\% - R\%$) for P3OT–PFB, P3OT–PFB–S–Coumarin343, and Coumarin343–SH dispersed in a polystyrene matrix (9 wt%). Films spun from 5 mg/ml THF solution.

Since polythiophenes have much lower PLQE than polyfluorenes and the streak camera set-up has poorer sensitivity (at least an order of magnitude down) in red region than in blue, all samples for streak camera measurements were drop-casted. The pump is at 405 nm laser as it excites both P3OT-PFB and the dye. Time range is set to 2 ns, which is enough to cover the emission from short-lived excited states in polythiophenes. Figure 2.18 plots P3OT-PFB-S-Coumarin$_{343}$ binned spectrum and lifetime statistical expectation, where no spectral or temporal contribution from the dye can be observed. It also shows there is no spectral difference between the two polymers. However, when comparing transient responses and extracting lifetime by single exponential decay, the excited state lifetime of the P3OT-PFB-S-Coumarin$_{343}$ system reduces by around 20% compared to the P3OT-PFB (Figure 2.19). The measurement was repeated for excitation at 465 nm and the result still holds, although the absolute values of the extracted lifetimes did increase with excitation wavelength (Table 2.4).

Note that there is less absorption for the dye at 465 nm than 405 nm. The non-radiative energy transfer mechanisms, such as Förster resonance energy transfer (FRET), are likely to be at play is evident from the consistent reduction of the lifetime for the polymer + dye system. The detailed nature of the processes, however, is not easily ascertained here but will be discussed in detail in Chapter 5 for polymer blends, which have more distinct emission for energy transfer analysis. In conclusion, streak camera set-up has shown its capability of studying the photoluminescence dynamics of mixed/modified system particularly on differentiating decays and transfers at different transient stages, which allows a more comprehensive understanding of material properties.

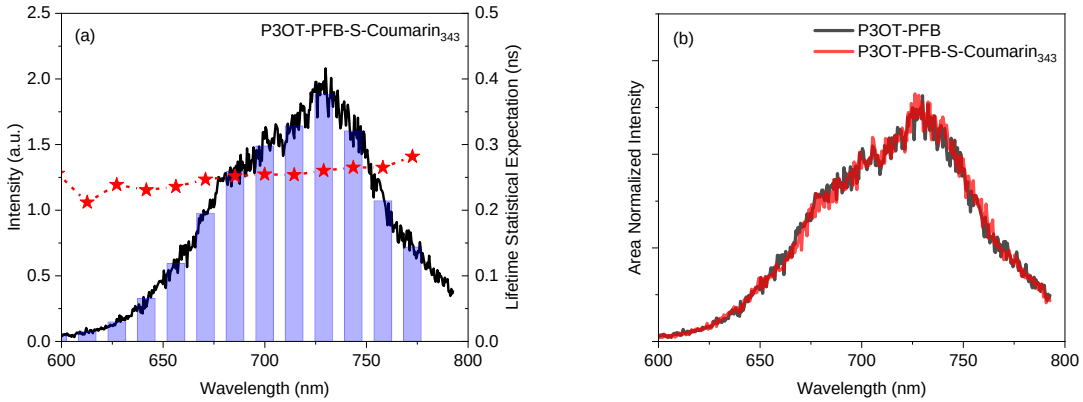


Figure 2.18 – (a) P3OT-PFB-S-Coumarin$_{343}$ spectrum and lifetime statistical expectation of binned wavelengths showing lifetime expectation similar to typical polythiophenes and independent of wavelength. (b) P3OT-PFB and P3OT-PFB-S-Coumarin$_{343}$ drop-casted samples show the same spectra when pumped by 405 nm laser. The spectra were acquired from 2 ns window, which is sufficient for polythiophenes.

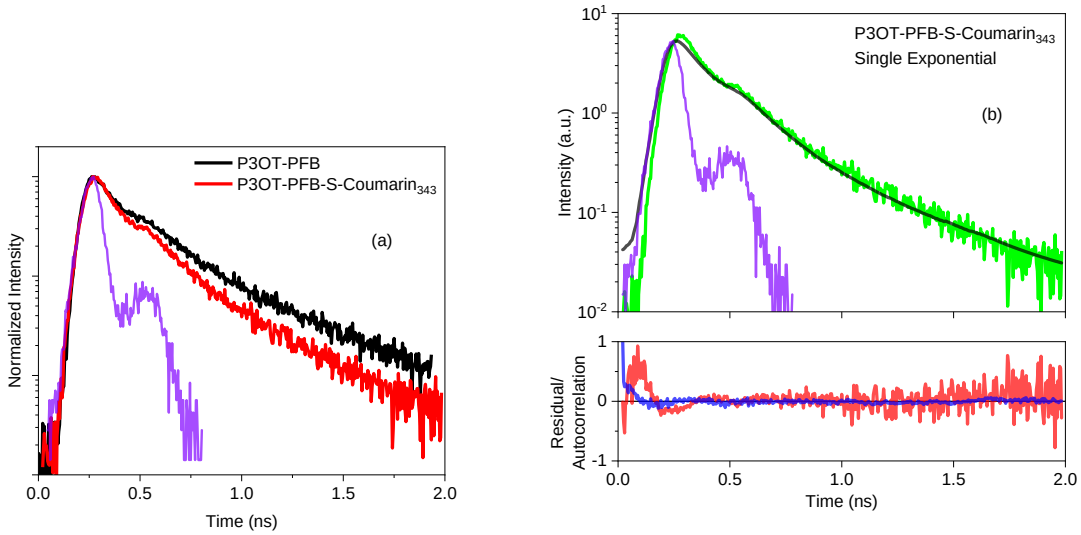


Figure 2.19 – (a) Transient responses of P3OT-PFB and P3OT-PFB-S-Coumarin$_{343}$ drop-casted samples pumped by $405\ nm$ laser pulses (plotted in purple) and measured in $2ns$ time range. The polymer + dye system shows 20% faster photoluminescence decay. Note the laser here has apparent electric jitter. (b) Single exponential fit of P3OT-PFB-SCoumarin$_{343}$. Measured transient response $I(t)$ is plotted in green, measured laser pulses in purple, fitted curve in black, residual in red and autocorrelation in blue. The convolution with measured laser pulses effectively eliminates the electric jitter.

Table 2.4 – Summary of extracted lifetimes (by single exponential decay) for drop-casted samples of P3OT-PFB and P3OT-PFB-S-Coumarin$_{343}$. The polymer + dye system consistently has shorter lifetime despite the absolute value increases with excitation wavelength.

Excitation Wavelength	P3OT-PFB	P3OT-PFB-S-Coumarin$_{343}$
$405\ nm$	$0.27\ ns$	$0.22\ ns$
$465\ nm$	$0.37\ ns$	$0.27\ ns$

It is worth mentioning that single and multi-exponential decays assume distinct and well-defined emitting species. In polymer materials, however, excited states are not identical and photoluminescence decay is dispersed in nature [16]. The actual lifetime is better described by a continuous probability distribution [16-17]. Statistically Equation (2.8) can be written as

$$f(t) = \int_0^\infty P(\tau)\, e^{-\frac{t}{\tau}} d\tau \tag{2.11}$$

where $P(\tau)$ is a normalised probability distribution of an excited state to have lifetime τ. Among various power-like distribution models (Appendix 2C), compressed hyperbola is suitable for molecular materials as it describes trapping and re-trapping processes when there are both localised and interactive luminescent centres [18,19]. Re-writing Equation (2.4) as

$$\frac{dN(t)}{dt} = -(k_r + k_{nr})N(t)^{1+\mathrm{c}} \tag{2.12}$$

where $0 < \mathrm{c} < 1$ describes how dispersive the system is. Solving Equation (2.12)

$$f(t) = \mathrm{A}N(t) = \mathrm{A}\left(1 + \mathrm{c}\frac{t}{\tau_0}\right)^{-\frac{1}{\mathrm{c}}} \tag{2.13}$$

$$\tau(t) = \tau_0 + \mathrm{c}t \tag{2.14}$$

where τ_0 is defined as the characteristic lifetime. The actual lifetime increases with time. To study this type of transient photoluminescence, a spin-coated thin-film of an undisclosed quantum dot material is measured [20] – excitation at $379\,nm$ and emission collected in $100\,ns$ time range. The transient response is plotted in Figure 2.20. The decay curve looks like bended single exponential but not as distinct as biexponential. To extract the lifetime, both biexponential and compressed hyperbola decay were used. Note that the pump is fitted Gaussian function as the shape laser pulses in $100\,ns$ time range is not affected by jittering. Figure 2.21 shows the extracted lifetime from curve fitting results. Although both methods obtained a good fit, only lifetime distribution can be physically explained for a material with single emitting species. This can be confirmed in Figure 2.22, as lifetime statistical expectation is increasing within a single emission peak. The associated longer lifetime and slightly red-shifted spectrum implies that some electrons are transferred to lower energy states, which takes

a significant amount of time, before emitting photons. In this way, compressed hyperbola and other lifetime distribution is useful to study the dispersed luminescent system. However, it has to be used with sufficient physical evidence as curve fitting may be less reliable with one more fitting parameter.

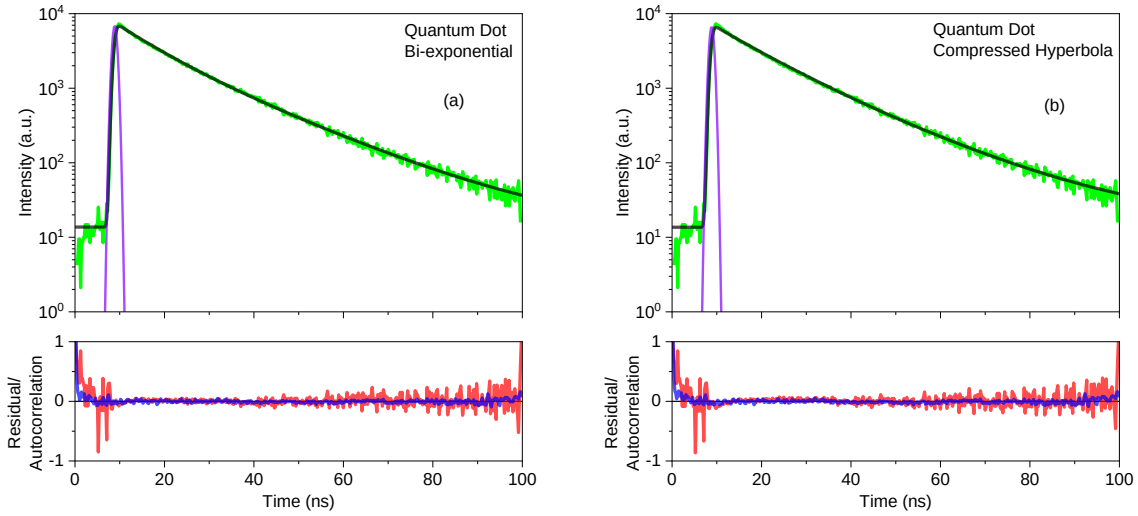


Figure 2.20 – Biexponential (a) and compressed hyperbola fit (b) of quantum dot thin-film pumped by 379 nm laser and measured in 100 ns time range. Measured transient response $I(t)$ is plotted in green, fitted Gaussian pulses in purple, fitted curve in black, residual in red and autocorrelation in blue. Both methods fit well to data.

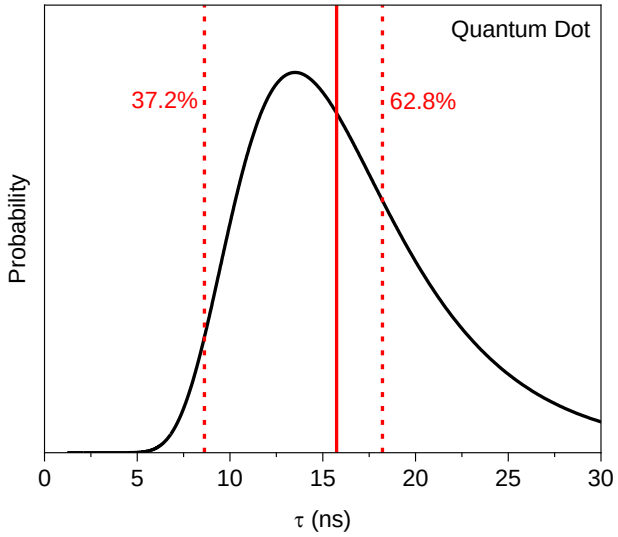


Figure 2.21 – Extracted lifetime of quantum dot material by single exponential (solid red, $15.8\,ns$), biexponential (dashed red, $8.62\,ns$ for 37.2% photons and $18.22\,ns$ for 62.8% photons) and compressed hyperbola (black, $\tau_0 = 12.29\,ns$, $c = 0.09$). Results from single exponential and biexponential are delta functions, while result from the compressed hyperbola is a probability distribution.

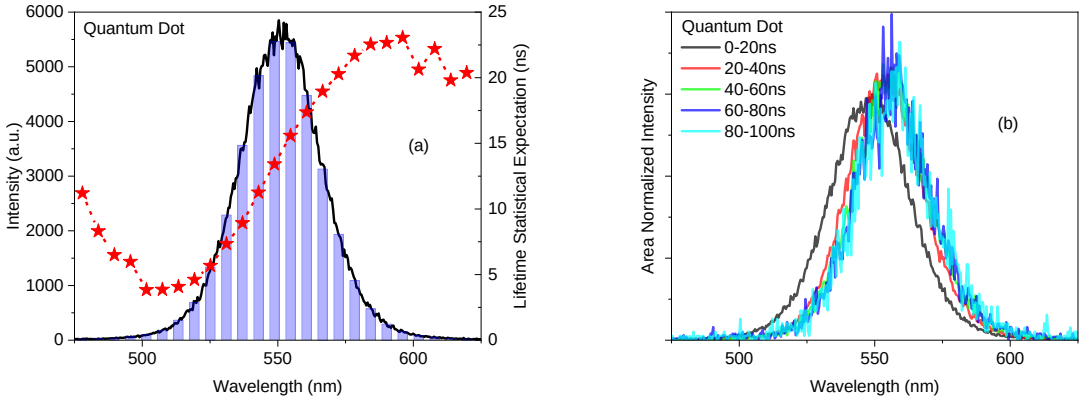


Figure 2.22 – (a) Quantum dot thin-film spectrum and lifetime statistical expectation of binned wavelengths showing that lifetime expectation is varying significantly in a narrow wavelength range. (b) Quantum dot thin-film spectra of binned emission time window showing that spectrum is slightly red-shifted, which implies some electrons being transferred to lower energy states before emission.

2.5 Summary

This chapter presented sample preparation and photo-physics characterisation of molecular thin-film structures. Materials were solution-processed and spin-coated on quartz to form thin films of $\sim 100\ nm$. Absorption and emission in steady state were characterised by UV-Vis spectroscopy, PL spectroscopy and PLQE measurement. To obtain PL lifetime and the associated dynamics of excited states, a streak camera pumped by pulsed diode lasers was introduced to measures transient PL in ps resolution, meanwhile still producing adequate spectrum. The two-dimensional data were analysed by nonlinear curve fitting, which extracts PL lifetime via a convolution of laser excitation and fluorescent decay. The method was proven to be robust and reliable for various kinds of PL lifetime – single exponential, biexponential and lifetime distributions.

References

[1] Schubert, D. W. (1997). Spin coating as a method for polymer molecular weight determination. *Polymer Bulletin*, *38*(2), 177–184.

[2] Lakowicz, J. R. (2006). Principles of Fluorescence Spectroscopy, 3rd edition. *Springer*.

[3] Shimadzu UV-VIS Spectrophotometer UV-2600 https://www.shimadzu.com/an/molecular_spectro/uv/uv2600_2700.html *accessed 20/03/19*

[4] Horiba FluoroMax-4 http://www.horiba.com/en_en/products/detail/action/show/Product/fluoromax-1576/ *accessed 20/03/19*

[5] de Mello, J. C., Wittmann, H. F., & Friend, R. H. (1997). An improved experimental determination of external photoluminescence quantum efficiency. *Advanced Materials*, *9*(3), 230–232.

[6] Bruice, D., & Miners, J. (1993). Use of a pulsed laser diode to measure picosecond fluorescence lifetimes. *Photochemistry and Photobiology*, *58*(3), 464–468.

[7] Suhling, K., French, M. W., & Phillips, D. (2005). Time-resolved fluorescence microscopy. *Photochemical & Photobiological Sciences*, *4*, 13–22.

[8] Tsai, H. M., Souris, J. S., Kim, H. J., Cheng, S. H., Chen, C. T., Lo, L. W., … Kao, C. M. (2017). Rapid measurement of fluorescence lifetimes using SIPM detection and waveform sampling. *Review of Scientific Instruments*, *88*, 096107.

[9] Kubicki, A. A., Bojarski, P., Grinberg, M., Sadownik, M., & Kukliński, B. (2006). Time-resolved streak camera system with solid state laser and optical parametric generator in different spectroscopic applications. *Optics Communications*, *263*(2), 275–280.

[10] Hamamatsu Streak Camera https://www.hamamatsu.com/eu/en/product/photometry-systems/streak-camera/operating-principle/index.html *accessed 20/03/19*

[11] Hamamatsu booklet. (2007). Picosecond Fluorescence Lifetime Measurement System C4780. *Hamamatsu Photonics K.K.*

[12] Ng, Y. K. (2010). PhD Thesis. *Imperial College London*.

[13] Wiessner, A., & Staerk, H. (1993). Optical design considerations and performance of a spectro-streak apparatus for time-resolved fluorescence spectroscopy. *Review of Scientific Instruments*, *64*(12), 3430–3439.

[14] Montgomery, D. S., & Johnson, R. P. (2001). Design considerations for fiber-coupled streaked optical spectroscopy. *Review of Scientific Instruments*, *72*(1), 979–982.

[15] Boufflet, P., Casey, A., Xia, Y., Stavrinou, P. N., & Heeney, M. (2017). Pentafluorobenzene end-group as a versatile handle for para fluoro “click” functionalisation of polythiophenes. *Chemical Science*, *8*(3), 2215–2225.

[16] Kierdaszuk, B. (2010). From discrete multi-exponential model to lifetime distribution model and power law fluorescence decay function. *Spectroscopy*, *24*(3–4), 399–407.

[17] Włodarczyk, J., & Kierdaszuk, B. (2003). Interpretation of fluorescence decays using a power-like model. *Biophysical Journal*, *85*(1), 589–598.

[18] Berberan-Santos, M. N., Bodunov, E. N., & Valeur, B. (2005). Mathematical functions for the analysis of luminescence decays with underlying distributions 1. Kohlrausch decay function (stretched exponential). *Chemical Physics*, *315*(1–2), 171–182.

[19] Berberan-Santos, M. N., Bodunov, E. N., & Valeur, B. (2005). Mathematical functions for the analysis of luminescence decays with underlying distributions: 2. Becquerel (compressed hyperbola) and related decay functions. *Chemical Physics*, *317*(1), 57–62.

[20] The undisclosed quantum dot material was received in solid form at Imperial college London. The material was then solution-processed and spin-coated by Dr. Nathan Cheetham.

3 Amplified Spontaneous Emission in Thin-film Structures

3.1 Introduction

Amplified spontaneous emission (ASE) in molecular semiconductor materials has been investigated intensively in recent years due to their spectral tunability and superior optical cross-section [1]. In practice, thin-film structures are widely used to accommodate the gain media as they are solution processable and highly flexible for various device applications [2]. Despite the progress in experiment, data measured in different conditions are often found difficult to compare and there are few reports about modelling of ASE in thin-film structures until recently [3]. In the early years of inorganic semiconductor and organic dye lasers, theories and models were studied systematically, which helped to understand key factors for stimulated emission [4-8]. This chapter implements a validated rate equation model specifically designed for thin-film structures. The model simulation results provide a better understanding of ASE process with emphasise on the effect of waveguiding dynamics. The model also categorises important material parameters for ASE and gives an insight of what to expect in ASE measurement and how to avoid misleading errors.

3.2 Rate Equations for Molecular Semiconductor Materials

3.2.1 From 4-Level Model to 2-Level Model

Rate equations are a straightforward way to describe the dynamics of electronic state populations in molecular semiconductor materials, especially for gain media [9,10]. These

differential equations are able to simulate the temporal evolution of populations in different energy levels under the influence of radiative and non-radiative transitions. In this chapter, a numerical model based on rate equations is established to study stimulated emission in molecular thin-film structures [11,12]. For simplicity, only singlet manifolds of ground state S_0 and the first excited state S_1 are considered and all non-linear processes other than stimulated emission (e.g. singlet-singlet annihilations) are neglected [13]. Figure 3.1 shows the schematic of energy levels and transitions in S_0 and S_1 vibrational manifolds, where the two most populated vibronic levels 0 and 1 of each manifold are converted to a 4-level rate equation model (Equation 3.1 – 3.5).

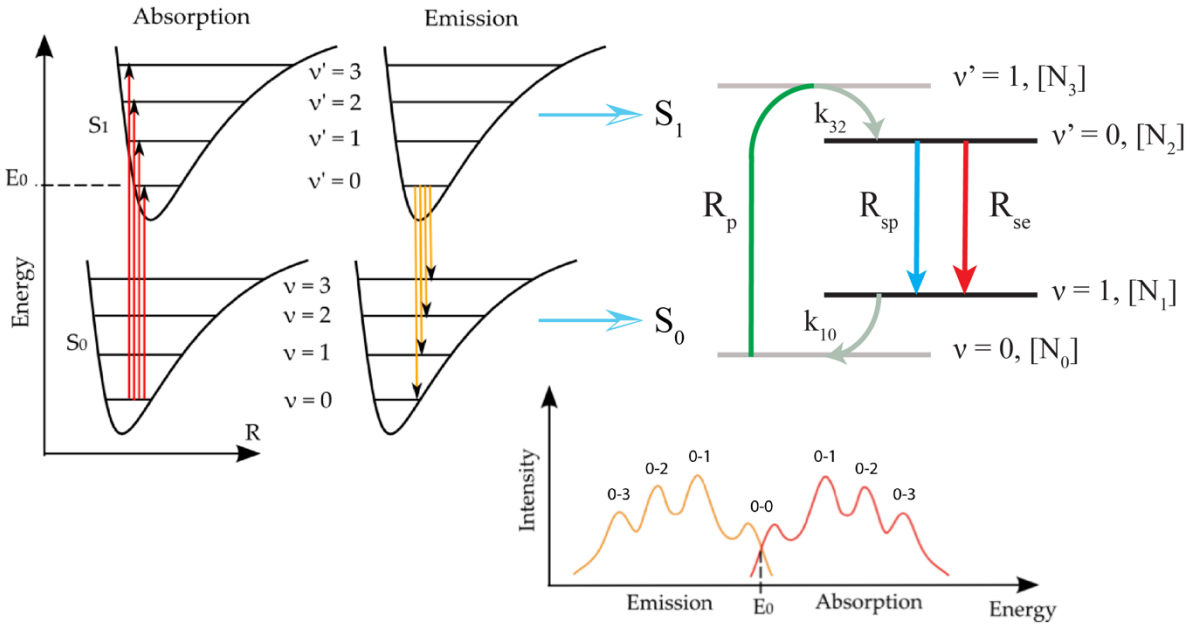


Figure 3.1 – Schematic of ground state and excited state manifolds with vibrational energy levels in typical molecular semiconductor materials. R is configuration coordinate (i.e. chemical bond length). The 4-level rate equation model describes the transitions in vibronic levels 0 and 1 including absorption, internal relaxation, spontaneous and stimulated emission. 0-1 peak is usually the ASE peak as population inversion happens between N_1 and N_2, which are the two energy levels in the simplified 2-level model.

$$\frac{dN_3(t)}{dt} = \sigma_p u_p N_0(t) - \frac{N_3(t)}{\tau_3} \tag{3.1}$$

$$\frac{dN_2(t)}{dt} = \frac{N_3(t)}{\tau_3} - \frac{N_2(t)}{\tau_2} - v_g\sigma_e\big(N_2(t) - N_1(t)\big)S(t) + v_g\alpha_{lo}S(t) \tag{3.2}$$

$$\frac{dN_1(t)}{dt} = -\frac{N_1(t)}{\tau_1} + \frac{N_2(t)}{\tau_2} + v_g\sigma_e\big(N_2(t) - N_1(t)\big)S(t) - v_g\alpha_{lo}S(t) \tag{3.3}$$

$$\frac{dN_0(t)}{dt} = \frac{N_1(t)}{\tau_1} - \sigma_p u_p N_0(t) \tag{3.4}$$

$$\frac{dS(t)}{dt} = \Gamma\left[\beta\frac{N_2(t)}{\tau_2} + v_g\sigma_e\big(N_2(t) - N_1(t)\big)S(t) - v_g(\alpha_{lo} + \alpha_{ex})S(t)\right] \tag{3.5}$$

The populations in each energy level (Equation (3.1 – 3.4)), also called state densities, are defined as N_0, N_1, N_2, N_3, where the transitions include ground state absorption R_p, excited state spontaneous emission R_{sp}, stimulated emission R_{se} and non-radiative internal relaxation k_{32} and k_{10}. Both R_{sp} and R_{se} are the decay from the $\nu = 0$ excited state manifold to $\nu = 1$ ground state manifold because most stimulated emission in molecular semiconductor materials is at the 0-1 vibronic peak as illustrated in Figure 3.1 [8,12]. The absorption process is determined by excitation intensity u_p and material absorption cross-section σ_p as $R_p = \sigma_p u_p N_0$ [12]. The spontaneous emission (radiative and non-radiative) has the rate $R_{sp} = N_2/\tau_2$, while stimulated emission rate $R_{se} = v_g\sigma_e(N_2 - N_1)S$ is subject to population inversion $(N_2 - N_1)$, stimulated emission cross-section σ_e, incoming photon density S and its group velocity v_g [8]. The internal relaxations from $\nu = 1$ to $\nu = 0$ have very fast transition rates as $\tau_3 \approx \tau_1 \approx 10^{-2}\tau_2$ [12]. There is also a loss term $R_{lo} = v_g\alpha_{lo}S$ to account the re-absorption loss. Finally, the photon equation (Equation (3.5)) connects the internal transitions

to the actual emitted photons, which can be measured in ASE experiment. Note that waveguide confinement factor Γ is included in the equation because thin-film sample prepared in Chapter 2.2 is actually an air/film/substrate slab waveguide (Chapter 3.3.1) and only photons in guided modes can propagate and amplifies the spontaneous emission. Similarly, a spontaneous emission factor $\beta = \Omega\eta$ represents the fraction (Ω for thin-film geometry and η for material quantum efficiency) of spontaneous emission that is collected at film edge (Chapter 4.2.1, Appendix 4C). It is also worth mentioning that the temporal model applies a self-feeding mechanism to simulate guided light propagations. As a result, an additional loss term α_{ex} in the photon equation compensates the photon cavity lifetime – the finite time a photon remains in a confined thin-film waveguide structure.

The 4-level rate equation model forms a closed transition loop as the sum of all state derivatives is always zero. Its complexity requires a longer time in numerical simulations, especially as ground state density is a large number and is hard to measure for molecular semiconductor materials. For example, ground state density of fluorene-based materials is estimated to be $N_0 \approx 10^{21}\ cm^{-3}$ as absorption cross-section $\sigma_p \approx \sigma_e \approx 10^{-16}\ cm^2$ and absorption coefficient $\alpha_p \approx 10^5\ cm^{-1}$ [14,15]. Therefore, a simplified 2-level model is often used, which assumes N_0 is sufficiently large that $dN_0/dt \to 0$ and internal relaxation is sufficiently fast that $\tau_3 \to 0$ [3,7]. By removing the differential equations for $N_0(t)$ and $N_3(t)$, the open loop 2-level rate equation model can be written as

$$\frac{dN_2(t)}{dt} = \sigma_p u_p N_0 - \frac{N_2(t)}{\tau_2} - v_g\sigma_e\big(N_2(t) - N_1(t)\big)S(t) + v_g\alpha_{lo}S(t) \tag{3.6}$$

$$\frac{dN_1(t)}{dt} = -\frac{N_1(t)}{\tau_1} + \frac{N_2(t)}{\tau_2} + v_g\sigma_e\big(N_2(t) - N_1(t)\big)S(t) - v_g\alpha_{lo}S(t) \tag{3.7}$$

$$\frac{dS(t)}{dt} = \Gamma\left[\beta\frac{N_2(t)}{\tau_2} + v_g\sigma_e\big(N_2(t) - N_1(t)\big)S(t) - v_g(\alpha_{lo} + \alpha_{ex})S(t)\right] \tag{3.8}$$

3.2.2 Model Simulation and Validation

Both 4-level and 2-level models were programmed in Matlab and numerical solutions were obtained by solver 'ode45'. Model parameters were set according to experimental ASE data and assume zero losses (Appendix 3A) [14,16]. In order to test when the 2-level picture becomes invalid, ground state density is set to $N_0 = 10^{16}\ cm^{-3}$ – 5 orders lower than the average value in molecular semiconductor materials (i.e. polymers) [14,15]. All initial state conditions are zero at $t = 0$. The simulation ran for $10\ ns$ under constant pump intensity with a step size of $10^{-4}\ ns$, thus the temporal evolution in ps remains accurate. It was confirmed that the simulation results do not change if the pump was replaced by a Gaussian pulse with the same energy [11]. Figure 3.2 compares the temporal response of state densities $N_1(t), N_2(t)$ and the photon density $S(t)$ for a 4-level and 2-level model at a pump intensity $u_p = 10^{17}\ cm^{-2}\ ns^{-1}$, well above ASE threshold. Within the first $100\ ps$, both state densities increase linearly to build up population inversion, which then vanishes after ASE is turned on. As a result, the photon density has an S-shape on a log-log scale. At $10\ ns$, the model has already reached its steady state as both ASE and PL lifetime are shorter than excitation. Note that it is the time integrated photon density that is collected by a charge-coupled device (CCD) in ASE measurement. Although the temporal response 4-level and 2-level differ slightly when $t < 1\ ns$, this does not affect the validity of simulation results in steady state in Figure 3.2.

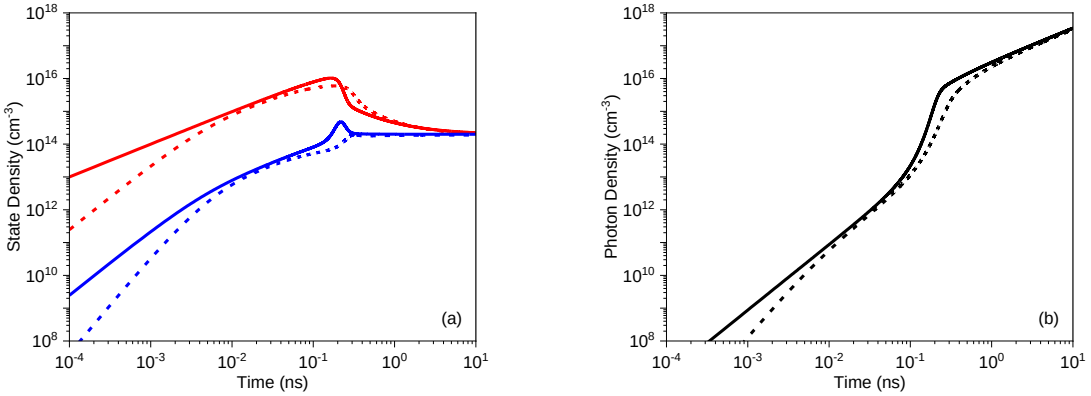


Figure 3.2 – Temporal response of state density (a) ($N_1(t)$ in blue, $N_2(t)$ in red) and photon density (b) ($S(t)$ in black) calculated by rate equation model at pump intensity $u_p = 10^{17}\ cm^{-2}\ ns^{-1}$. Results from 2-level model Equation (3.6 – 3.8) plotted in solid lines and 4-level model (Equation (3.1 – 3.5) in dashed lines. When $t < 1\ ns$, 2-level model has faster response (faster in all transitions – absorption, PL, ASE) due to the lack of internal relaxation. For longer t, both models reach the steady state and become undistinguishable. Note a small $N_0 = 10^{16}\ cm^{-3}$ is applied while it is actually around $10^{21}\ cm^{-3}$.

To further compare the two models, Figure 3.3 plots electronic state and photon state densities after $10\ ns$ against a wide range of pump intensity (also energy per area per pulse). Only when the ground state $N_0(t)$ starts to depopulate and break the assumption of $dN_0/dt \to 0$ would the 4-level model become essential – this means when pump energy is higher than $10^6\ \mu J\ cm^{-2}$. Since the laser used in this study never reaches $10^6\ \mu J\ cm^{-2}$ and the actual $N_0 \approx 10^{21}\ cm^{-3}$ is 5 orders larger than simulation in Figure 3.3, ground state depopulation is unlikely and the 2-level model is a good estimation.

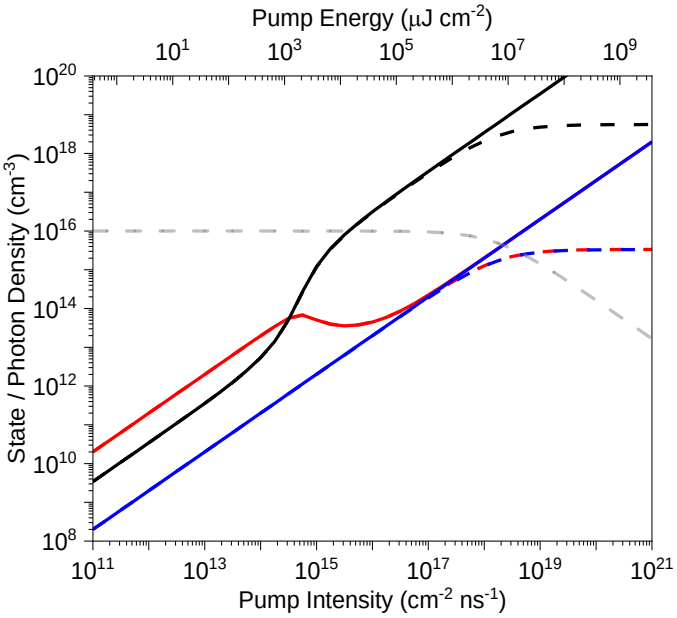


Figure 3.3 – Energy response of 2-level model (solid) and 4-level model (dashed) at steady state ($t = 10\,ns$). N_0 plotted in grey, N_1 in blue, N_2 in red and S in black. Up to $u_p = 10^{18}\ cm^{-2}\ ns^{-1}$, both models do not show any difference. However, ground state density N_0 depopulation arises once pump intensity is higher. As a result, N_1, N_2 and S stop increasing with pump, making 2-level model invalid. Note a small $N_0 = 10^{16}\ cm^{-3}$ is applied while it is actually around $10^{21}\ cm^{-3}$. Pump energy is converted from pump intensity at $685\ nm$.

The 2-level model was then used to fit ASE energy response measured with a RedF sample [16]. Fitting parameters are the two losses α_{lo} and α_{ex}, as they have greater dependence on sample quality and measurement conditions [17]. Here, material loss α_{lo} was varied between 0 and 10 cm^{-1} while photon cavity loss α_{ex} is taken to be inversely proportional to excitation stripe length L – assuming 90% to 99% of travelling photons exit the stripe without being reflected back, then α_{lo} is roughly between $1/L$ and $2/L$ [14]. For $\alpha_{lo} = 3.2\ cm^{-1}$ and $\alpha_{ex} = 1.6/L$, the modelling achieved a very good fit to the experimental data, especially the S-shaped response with different stripe length L (Figure 3.4). Therefore, the 2-level rate equation model provides a solid and reliable base to understand ASE of molecular semiconductor materials in thin-film structures.

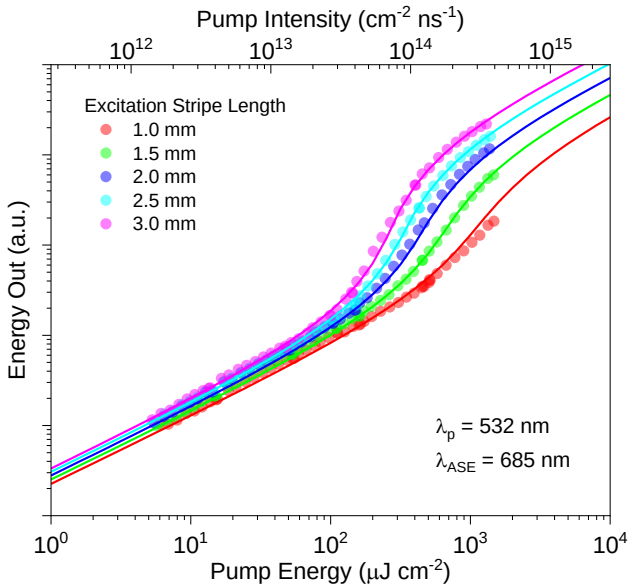


Figure 3.4 – ASE data of RedF thin-film sample excited with different stripe length (circle dots) fitted by steady state energy response of the 2-level rate equation model (solid lines). RedF data is from [16] pumped at $532\ nm$ with ASE peak at $685\ nm$. The change of stripe length L is implemented as change of photon cavity loss α_{ex} inversely proportional to L. The successful fit proves that the 2-level model is a good estimation of ASE in thin-film structures. Note here ASE threshold in dependent on excitation stripe length (see Chapter 4.3.1 for detail).

3.2.3 Identifying Key Material Parameters for Amplified Spontaneous Emission

With the validated 2-level model, the effect of each parameter on the overall ASE performance can be accessed. In this section, the investigation focuses on material parameters that have potential effects on ASE – absorption cross-section σ_p, stimulated emission cross-section σ_e, excited state lifetime τ_2 and spontaneous emission factor β. Figure 3.5 plots the calculated energy response when each of the parameters changes its value while all other parameters remain unchanged. It is clear that larger σ_p and σ_e, longer τ_2, smaller β are all beneficial for ASE, but in different ways. Recall stimulated emission $R_{se} = v_g\sigma_e(N_2 - N_1)S$ – larger σ_{se} directly increases R_{se}; longer τ_2 helps population inversion thus larger $(N_2 - N_1)$; larger σ_p contributes to more R_p thus larger S. However, the effect of β is tricky as it does not change

ASE threshold but has significant impact on the slope of S-shape (gain). This will be discussed in detail in Chapter 5.4. Apart from material parameters, pump efficiency is also worth mentioning – ASE measurements from different excitation pulse width are not comparable (Appendix 3B).

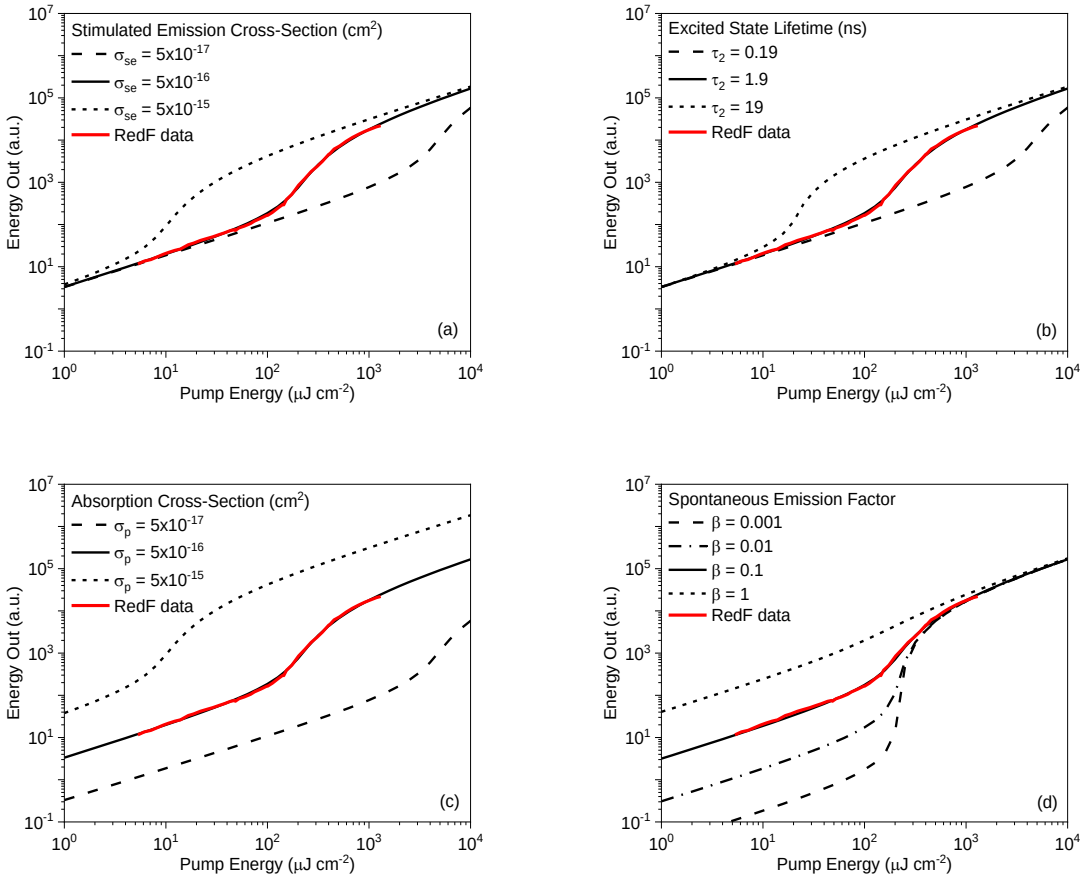


Figure 3.5 – Steady state energy response of the 2-level rate equation model in Figure 3.4. For each curve, one of the parameter values is changed to check its effect on ASE. The model, which fits RedF data (red) at $L = 3\ mm$, is used as reference (solid black). Larger stimulated emission cross-section σ_e (a), longer excited state lifetime τ_2 (b), larger absorption cross-section σ_p (c) and smaller spontaneous emission factor β (d) are all beneficial for ASE, providing all other parameters remain the same.

3.3 Modelling Thin Film Structures

3.3.1 Modal Property of Thin-film Planar Structures

As mentioned in Chapter 3.2.1, the spin-coated samples prepared in Chapter 2.2 effectively form an asymmetric air/film/substrate slab waveguide, where the modal property has to be considered. Figure 3.6 shows the schematic of sample cross-section in a Cartesian coordinate system. Once the gain media is excited by a stripe in yz plane, the emitted and confined photons can travel along the excitation stripe from 0 to L in gain-guided waveguide modes. Depending on material refractive index and film thickness, TE and TM modes may compete when propagating. Moreover, photons travelling in $+z$ and $-z$ directions may also increase the competition. Therefore, it is essential to consider these in the 2-level rate equation model – modal property is studied in this section and spatial propagation will be investigated in Chapter 3.3.2.

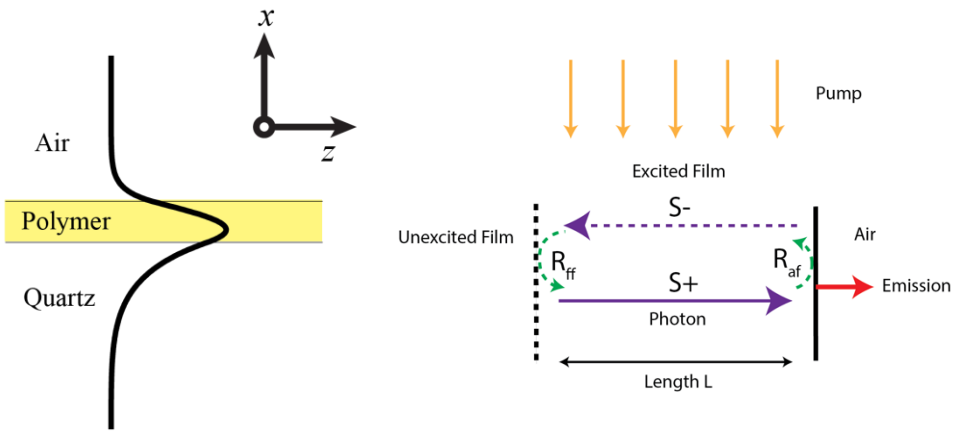


Figure 3.6 – Schematic of ASE propagation in polymer thin-film structures in Cartesian coordinate system, which is effectively a weakly guided slab waveguide. Excitation is via a laser stripe, which supports ASE in yz plane by gain guiding. Within the active gain media, photons can travel in both $+z$ and $-z$ directions and are subject to transmission/reflection at both ends. Modelling thin-film structures should consider both waveguide confinement and competing travelling-waves.

Modes TE (E_y, H_x, H_z) and TM (E_x, E_z, H_y) in slab waveguide can be obtained by solving

Maxwell's equations (Appendix 3C). In Matlab simulation, the intensities of electromagnetic field and effective index n_{eff} were calculated numerically by a mode solver with 1 nm spatial resolution [18]. The waveguide confinement factor, which represents the power distribution in x axis, can be written as [19-21]

$$\Gamma_{TE} = \frac{\int_0^d n(x)\left|E_y\right|^2 dx}{n_{\text{eff}} \int_{-\infty}^{+\infty}\left|E_y\right|^2 dx} \approx \frac{\int_0^d \left|E_y\right|^2 dx}{\int_{-\infty}^{+\infty}\left|E_y\right|^2 dx} \tag{3.9}$$

$$\Gamma_{TM} = \frac{n_{\text{eff}} \int_0^d (|E_x|^2+|E_z|^2) dx}{\int_{-\infty}^{+\infty} n(x)|E_x|^2 dx} \approx \frac{\int_0^d |E_x|^2 dx}{\int_{-\infty}^{+\infty}|E_x|^2 dx} \tag{3.10}$$

where assumption $n_{\text{eff}} \approx n$ and $|E_z|^2 \ll |E_x|^2$ is based on weakly guided scenario, which is the case for slab waveguides consist of air, quartz ($n = 1.4755$ from a Cauchy's description) and molecular semiconductor materials ($n < 2$). Figure 3.7 shows an example of calculated effective index and field distribution in PFO thin-film sample. To minimise modal competition, the method used in this thesis is to make a single longitudinal mode slab waveguide by controlling the thickness of the gain media in an optimised range, ideally where Γ_{TE} is relatively high and Γ_{TM} is relatively low (details in Chapter 4).

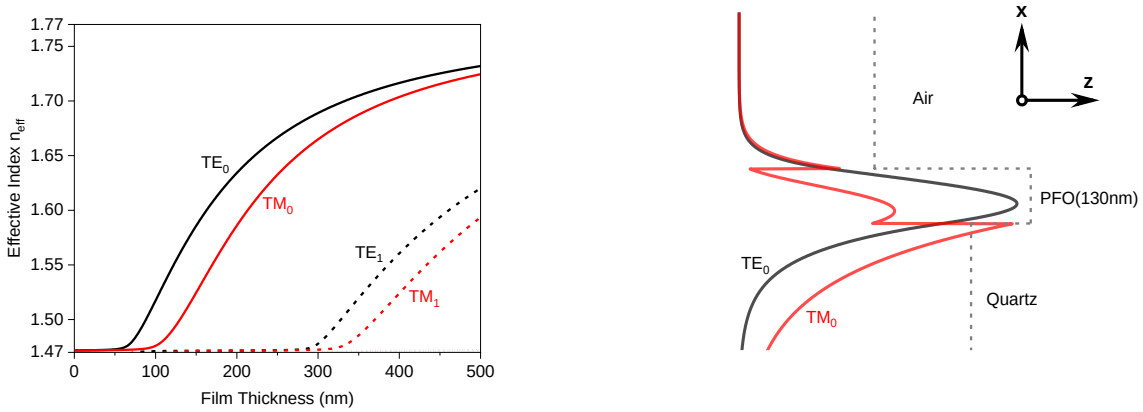


Figure 3.7 – Calculated waveguide mode effective index n_{eff} in air/polymer/quartz thin-film structures. Calculation based on PFO with emission at 450 nm thus the refractive indices for the structure is 1.0000/1.7690/1.4755 illustrated in dashed grey (polymer index from unpublished PFO report, quartz index from Cauchy's equation). n_{eff} has to be higher than 1.4755 to support a guided mode, and thicker films can accommodate more modes with higher n_{eff}. In order to minimise modal competition, preferred thickness when Γ_{TE} is relatively high and Γ_{TM} is relatively low – an example of power distribution ($|E_y|^2$ for TE and $|E_x|^2$ for TM) is shown in 130 nm sample.

3.3.2 Spatial Dependence of State Density and Photon Density

Regarding propagating photons inside the slab waveguide, the spatial dependence was also included to the 2-level rate equation model. The photon density S now varies in both time and distance.

$$\frac{dS(t)}{dt} = \frac{\partial S(t,z)}{\partial t} + v_g \frac{\partial S(t,z)}{\partial z} \tag{3.11}$$

Similarly, the state densities $N_1(t,z), N_2(t,z)$ also become spatially dependent. Assuming the slab waveguide is single mode (TE_0), the modified rate equation model with photons propagating in both $+z$ and $-z$ directions can be written as

$$\frac{dN_2(t,z)}{dt} = \sigma_p u_p N_0 - \frac{N_2(t,z)}{\tau_2} - R_{se}(t,z) + R_{lo}(t,z) \tag{3.12}$$

$$\frac{dN_1(t,z)}{dt} = -\frac{N_1(t,z)}{\tau_1} + \frac{N_2(t,z)}{\tau_2} + R_{se}(t,z) - R_{lo}(t,z) \tag{3.13}$$

$$\frac{\partial S_+(t,z)}{\partial t} + v_g \frac{\partial S_+(t,z)}{\partial z} = \Gamma\left(\beta \frac{N_2(t,z)}{\tau_2} + R_{se+}(t,z) - R_{lo+}(t,z)\right) \tag{3.14}$$

$$\frac{\partial S_-(t,z)}{\partial t} - v_g \frac{\partial S_-(t,z)}{\partial z} = \Gamma\left(\beta \frac{N_2(t,z)}{\tau_2} + R_{se-}(t,z) - R_{lo-}(t,z)\right) \tag{3.15}$$

where S_+ propagates from $z = 0$ to $z = L$ and S_- in the opposite way; $R_{se}(t,z)$ and $R_{lo}(t,z)$ are the sum of the values in both directions. The spatial dependence model was applied for three scenarios with different initial boundary conditions of photon density, while always keeping $N_1(0,z) = N_1(0,z) = 0$.

1. Single-pass: Photons propagate in $+z$ direction only – no Equation (3.15).

   Initial conditions: $S_+(0,z) = 0$, $S_+(t,0) = 0$.

2. Double-pass: Photons propagate equally in both directions without any interaction.

   Initial conditions: $S_+(0,z) = S_-(0,z) = 0$, $S_+(t,0) = S_-(t,L) = 0$

3. Double-pass with reflection: Consider reflection at both ends of excitation stripe – R_{af} at film/air interface and R_{ff} at excited/unexcited film interface.

   Initial conditions: $S_+(0,z) = S_-(0,z) = 0$, $S_+\big((t+dt),0\big) = R_{ff}S_-(t,0)$,

   $S_-\big((t+dt),L\big) = R_{af}S_+(t,L)$.

The three scenarios were simulated in Matlab as in Chapter 3.2.2. To save calculation time, the

model assumed zero loss and increased step size $\Delta t = 10^{-3}\ ns$, so $\Delta z = v_g \Delta t$. The results are interesting – the spatial distribution of population inversion ($N_2(z) - N_1(z)$) against pump intensity is plotted in Figure 3.8 and the photon density $S(z) = S_+(z) + S_-(z)$ is plotted in Figure 3.9. The key observation is that population inversion, or gain, has an inverse relationship with photon density – a large S could depopulate N_2 via stimulated emission once ASE is active. While the single-pass has a decreasing gain from 0 to L, the used of the double-pass reveals a symmetric distribution with highest point in the centre [3,7]. This is further shifted towards $z = L$ when reflection is included. It is also noted that the single-pass has the highest gain and photon density at film edge ($z = L$). However, both double-pass and reflection increase photon competition and thus lower the gain and photon density. The main conclusion is that a model based on single-pass of travelling wave may overestimate ASE energy out in the thin-film structures, which is worth keeping in mind.

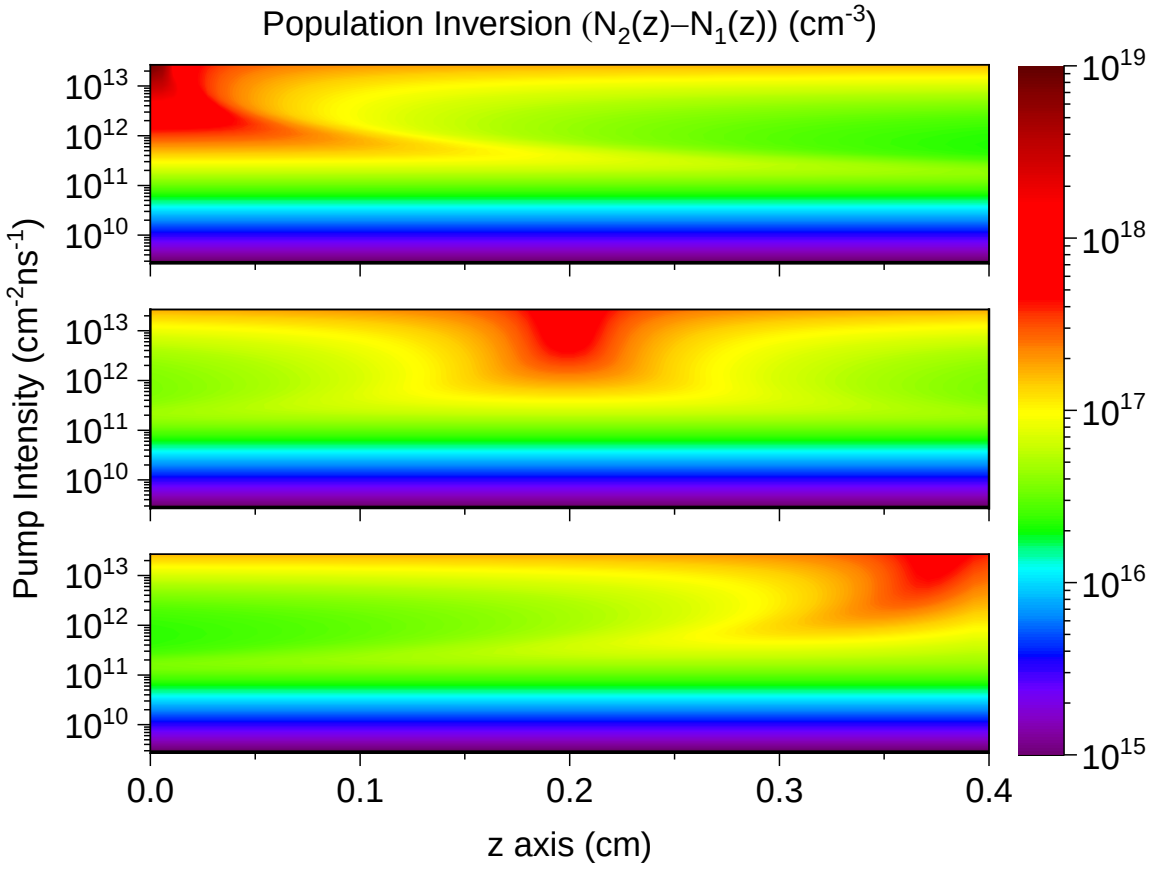


Figure 3.8 – Distribution of population inversion ($N_2(z) - N_1(z)$) in a 0.4 cm stripe against pump intensity calculated by the spatial-temporal model (Equation (3.12 – 3.15)) in three scenarios of travelling wave – single-pass (top), double-pass (middle) and double-pass with reflection (bottom, where $R_{af} = 0.06$, $R_{af} \to 0$). The population inversion does not increase with pump intensity when ASE is turned on, because N_2 can be depopulated by stimulated emission with high photon density. The photon competition determines that the gain is always decreasing in single-pass, is symmetric in double-pass, and further shifts with reflection.

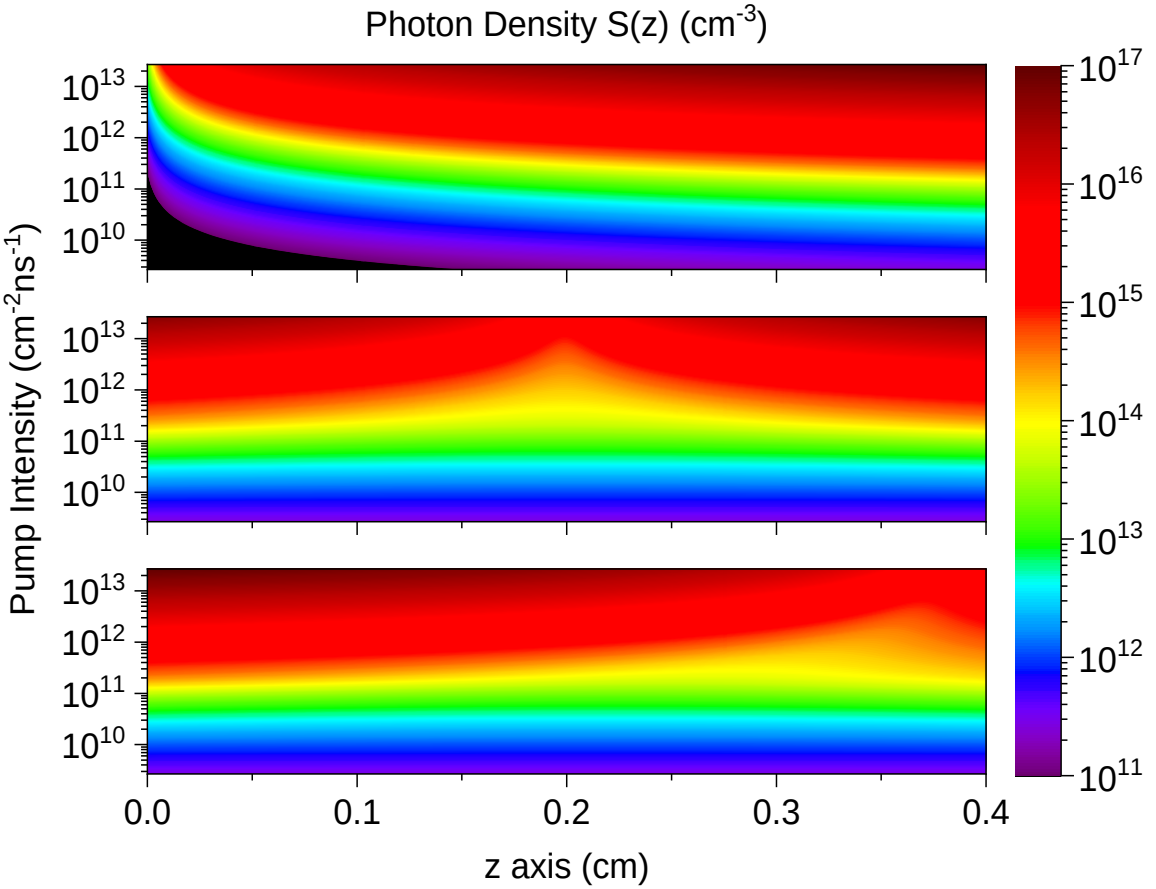


Figure 3.9 – Distribution of photon density $S(z) = S_+(z) + S_-(z)$ in a 0.4 cm stripe against pump intensity calculated by the spatial-temporal model (Equation (3.12 – 3.15)) in three scenarios of travelling wave – single-pass (top), double-pass (middle) and double-pass with reflection (bottom, where $R_{af} = 0.06$, $R_{af} \to 0$). Compare with Figure 3.9, photon density is always inverse proportional to population inversion. Since photons are collected at film edge in ASE measurement (i.e. $S(z = 0.4\ cm)$), using the single-pass method which overestimate the energy out would underestimate the extracted gain.

3.3.3 Effect of Gain Saturation

Equation (3.14) and (3.15) can be regarded as general equations for ASE, as they include both temporal and spatial evolution. However, gain characterisation from experiment requires data of photon intensity at variable length $I(z)$ at steady state $\frac{\partial}{\partial t} = 0$. Since $I = v_g S$, the photon equation can be written as (using single-pass travelling wave as an example)

$$\frac{dI(z)}{dz} = \Gamma\left[\beta\frac{N_2(z)}{\tau_2} + \sigma_e\big(N_2(z) - N_1(z)\big)I(z) - \alpha_{lo}I(z)\right] \tag{3.16}$$

Defining $\mathrm{A}_{PL}(\mathrm{z}) = \Gamma\beta N_2(z)/\tau_2$ and $\langle g(z)\rangle = \Gamma\big[\sigma_e\big(N_2(z) - N_1(z)\big) - \alpha_{lo}\big]$, Equation (3.16) becomes the general equation for single-pass gain.

$$\frac{dI(z)}{dz} = \mathrm{A}_{PL}(\mathrm{z}) + \langle g(z)\rangle I(z) \tag{3.17}$$

where $\mathrm{A}_{PL}(\mathrm{z})$ represents the PL component in ASE and $\langle g(z)\rangle$ is the net modal gain.

While the single-pass approach is widely used since it is easy to analyse and is reasonably valid for conventional pump-probe experiment, its applicability for ASE measurements in thin-film structures needs to be re-assessed [3,5,22]. This section compares the spatial dependent gain $\langle g(z)\rangle$ calculated from spatial temporal rate equation models of single-pass, double-pass and double-pass with reflection. Since $\langle g(z)\rangle = \Gamma\big[\sigma_e\big(N_2(z) - N_1(z)\big) - \alpha_{lo}\big]$ and loss is assumed to be zero, population inversion $\big(N_2(z) - N_1(z)\big)$ is always proportional to the gain. Figure 3.10 shows that gain values vary significantly at different stripe positions for all three scenarios. The cause is gain saturation, as excited states are depopulated by stimulated emission. The effect of both double-pass and reflection lowers ASE intensity as additional sources of saturation. Therefore, $\langle g(z)\rangle$ in Equation (3.17) cannot be used to fit a constant gain value and saturation must be included. While there is no practical way to fit with double-pass with/without reflection, without assuming a homogeneous gain distribution [3], this thesis uses the single-pass equation to extract gain, which inevitably produces underestimated results. More details of gain extraction and characterisation are discussed in Chapter 4.

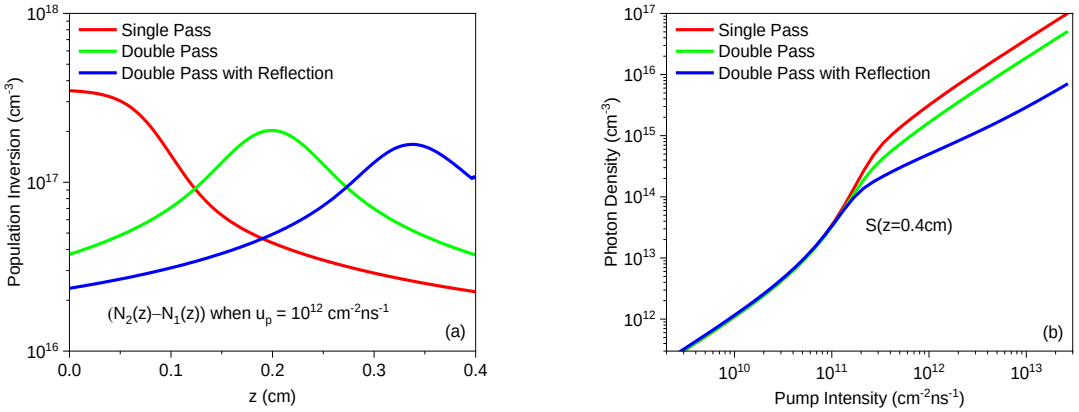


Figure 3.10 – (a) Distribution of population inversion $(N_2(z) - N_1(z))$ at pump intensity $u_p = 10^{12}\ cm^{-2}\ ns^{-1}$ from Figure 3.8. It is clear that single-pass has the highest average effective gain for the whole stripe length, while the intrinsic material gain is the same in all three scenarios. (b) Energy response of photon density $S(z = 0.4\ cm)$ (i.e. energy out) from Figure 3.9. Using the single-pass method would underestimate the effect of gain saturation and fit a higher gain value to the same set of data.

3.3.4 Further Considerations

Although the spatial temporal rate equation model provides a solid base to closely simulate ASE in molecular semiconductor thin-film structures, there could be improvements in several aspects, some of which may be important in certain cases.

1. The model does not explicitly include thickness dependence. Molecules in different positions of x axis in Figure 3.6 absorb different excitation intensities according to Beer-Lambert law. In thicker samples, molecules near substrate may experience incomplete absorption from pump, which may in turn re-absorbs ASE emission from molecules in upper regions. The thickness dependence is more important in samples with two or more emission layers and/or feedback structures.

2. The model does not include spectral dependency and parameters are set to the value at 0-1 peak in PL spectrum – assuming the line shape of stimulated emission does not

change, which is not true. Besides, while most ASE in molecular semiconductor materials are at 0-1 peak, there could be competition between two peaks, especially in donor-acceptor blends with energy transfer (Chapter 5.4.1). An ASE model with spectral dependency has been reported recently [3].

3. The model ignores triplet and polaron states known to be present and does not assess the loss due to here [23]. Triplet management is important for the gain media, and thermally activated delayed fluorescence (TADF) materials are starting to show stimulated emission [24-26].

3.4 Summary

This chapter presented numerical simulation of stimulated emission in thin-film structures. A 2-level rate equation model was proposed and verified against experimental data. The temporal evolution and steady-state response helped identifying key material parameters for ASE – large stimulated emission cross-section and longer PL lifetime are beneficial, while loss and spontaneous emission factor should be kept to a minimum. Moreover, the effect of waveguide geometry and modal propagation was also considered by the modified spatial-temporal model, which revealed that the actual emission from the thin-film structure is much less than single-pass amplification due to competition of travelling waves in both directions. The calculation in this chapter gave better understanding of ASE threshold and saturation and provided important guidance for measurement and analysis in the following chapters.

References

[1] Samuel, I. D. W., & Turnbull, G. A. (2007). Organic semiconductor lasers. *Chemical Reviews*, *25*(7), 1272–1295.

[2] Voss, D. (2000). Cheap and cheerful circuits. *Nature*, *407*, 442–444.

[3] Cerdán, L. (2020). Simultaneous retrieval of optical gains , losses , and threshold in active waveguides. *Optics and Laser Technology*, *121*, 105814.

[4] Allen, L., & Peters, G. I. (1971). Amplified spontaneous emission III. Intensity and saturation. *Journal of Physics A: General Physics*, *4*(4), 564–573.

[5] Shaklee, K. L., Nahory, R. E., & Leheny, R. F. (1973). Optical gain in semiconductors. *Journal of Luminescence*, *7*(C), 284–309.

[6] Linford, G. J., Peressini, E. R., Sooy, W. R., & Spaeth, M. L. (1974). Very Long Lasers. *Applied Optics*, *13*(2), 379.

[7] Ganiel, U., Hardy, A., Neumann, G., & Treves, D. (1975). Amplified Spontaneous Emission and Signal Amplification in Dye-Laser Systems. *IEEE Journal of Quantum Electronics*, *11*(11), 881–892.

[8] Siegman, A. E. (1986). Lasers. *University Science Books*.

[9] Yokoyama, H., & Brorson, S. D. (1989). Rate equation analysis of microcavity lasers. *Journal of Applied Physics*, *66*(10), 4801–4805.

[10] BjÖrk, G., & Yamamoto, Y. (1991). Analysis of Semiconductor Microcavity Lasers Using Rate Equations. *IEEE Journal of Quantum Electronics*, *27*(11), 2386–2396.

[11] Xia, Y. (2014). MRes thesis. *Imperial College London.*

[12] Lakowicz, J. R. (2006). Principles of fluorescence spectroscopy, 3rd edition. *Springer*.

[13] Gärtner, C., Karnutsch, C., Lemmer, U., & Pflumm, C. (2007). The influence of annihilation processes on the threshold current density of organic laser diodes. *Journal of Applied Physics*, *101*(2), 023107.

[14] Xia, R., Heliotis, G., Hou, Y., & Bradley, D. D. C. (2003). Fluorene-based conjugated polymer optical gain media. *Organic Electronics*, *4*(2–3), 165–177.

[15] Yap, B. K., Xia, R., Campoy-Quiles, M., Stavrinou, P. N., & Bradley, D. D. C. (2008). Simultaneous optimisation of charge-carrier mobility and optical gain in semiconducting polymer films. *Nature Materials*, *7*(5), 376–380.

[16] Yoon, H. (2011). PhD thesis. *Imperial College London.*

[17] Mogensen, P. C., Smowton, P. M., & Blood, P. (1997). Measurement of optical mode loss in visible emitting lasers. *Applied Physics Letters*, *71*(14), 1975–1977.

[18] Fallahkhair, A. B., Li, K. S., & Murphy, T. E. (2008). Vector Finite Difference Modesolver for Anisotropic Dielectric Waveguides. *Journal of Lightwave Technology, Vol. 26, Issue 11, Pp. 1423-1431*, *26*(11), 1423–1431.

[19] Haes, J., Demeulenaere, B., Baets, R., Lenstra, D., Visser, T. D., & Blok, H. (1997). Difference between TE and TM modal gain in amplifying waveguides: Analysis and assessment of two perturbation approaches. *Optical and Quantum Electronics*, *29*(2), 263–273.

[20] Visser, T. D., Blok, H., Demeulenaere, B., & Lenstra, D. (1997). Confinement factors and gain in optical amplifiers. *IEEE Journal of Quantum Electronics*, *33*(10), 1763–1766.

[21] Huang, Y.-Z. (2001). Comparison of modal gain and material gain for strong guiding slab waveguides. *IEE Proceedings - Optoelectronics*, *148*(3), 131-133(2).

[22] Dal Negro, L., Bettotti, P., Cazzanelli, M., Pacifici, D., & Pavesi, L. (2004). Applicability conditions and experimental analysis of the variable stripe length method for gain measurements. *Optics Communications*, *229*(1–6), 337–348.

[23] Clark, J., & Lanzani, G. (2010). Organic photonics for communications. *Nature Photonics*, *4*(7), 438–446.

[24] Nakanotani, H., Furukawa, T., & Adachi, C. (2015). Light Amplification in an Organic Solid-State Film with the Aid of Triplet-to-Singlet Upconversion. *Advanced Optical Materials*, *3*(10), 1381–1388.

[25] Nakanotani, H., Furukawa, T., Hosokai, T., Hatakeyama, T., & Adachi, C. (2017). Light Amplification in Molecules Exhibiting Thermally Activated Delayed Fluorescence. *Advanced Optical Materials*, *5*(12), 1700051.

[26] Jiang, Y., Lv, P., Pan, J., Li, Y., Lin, H., Zhang, X., … Huang, W. (2019). Low-Threshold Organic Semiconductor Lasers with the Aid of Phosphorescent Ir(III) Complexes as Triplet Sensitizers. *Advanced Functional Materials*, *29*(19), 1806719.

4 Measurements of Amplified Spontaneous Emission

4.1 Introduction

To characterise lasing materials, amplified spontaneous emission (ASE) in organic thin-films has been extensively studied in recent years but electrically pumped molecular semiconductor lasers have not yet been confirmed [1-4]. While a wide variety of materials and devices have been reported, results are often inconsistent and incomparable, especially for extracted gain values [5-11]. Therefore, standardising ASE and gain characterisation becomes one of the main focus in the field [12]. This chapter critically explains the experimental set-up built specifically to measure ASE in thin-film structures. Effort has been made to improve measurement reliability, but certain limitations still exist. Then methods for data processing and gain extraction are discussed in detail, including travelling-wave equations with and without saturation term. Emphasis has been made to determine the applicability of each method, and results are checked against parameters in ASE rate equation model (Chapter 3.2.3). Furthermore, new metrics, which assess material property and device performance but are independent of measurement set-ups, have been proposed to better evaluate potential gain media. The method has been applied to different polyfluorenes (blue and green), all showing competent gain characteristics linked to the property of materials.

4.2 Experimental Set-up

4.2.1 Calibration and Measurement Procedures

Although ASE is useful and essential to investigate any gain media, the measurement on solid state thin-film structures is still challenging. Firstly, the sub-wavelength film thickness makes it difficult to confine photons in an air/polymer/quartz asymmetric slab waveguide; the polymer layer must be at least $80 - 120\ nm$ thick to support a propagating mode, depending on emission wavelength (Chapter 3.3.1). However, the film that is too thick would cause self-absorption and turn off the gain. This is due to the high absorption coefficient (usually $10^5\ cm^{-1}$) in conjugated polymers, which results in incomplete pumping in thick films. Secondly, as photons are confined in the waveguide structure, ASE signal has to be collected from film edge where the guided photons emit into the air, which requires a flat film surface from centre to the edge. This is hard to achieve in polymer thin-films, as films spin-coated on quartz substrate generally have non-uniform edges. Increasing spin-speed would improve the uniformity but would also reduce film thickness. Finally, when recording signals, collection optics has to be carefully designed to focus on guided ASE emission but eliminate the majority of Lambertian photoluminescence (PL), which emits from both edge and surface of the film.

Despite the above limitations, a semi-automatic ASE set-up was built to systematically study the gain properties in thin-film structures. Figure 4.1 and 4.2 show the schematic of ASE measurement, where the thin-film is placed on a metal sample holder and can be finely adjusted in y and z axis. Excitation source is a diode-pumped Q-switched YAG laser at $355\ nm$ with pulse width fixed at $8.1\ ns$ and repetition rate (adjustable) at $10\ Hz$. In focusing optics, pump energy is controlled by a set of ND filters and a shutter, both of which are connected to a PC

and are automatically controlled in LabView. The incoming laser beam is polarised in z axis and shaped into a rectangular stripe $L \times W$ through a series of spherical and cylindrical lenses. The stripe length is cut out by a manual slit, while its width can be adjusted by a beam rotator, which also helps aligning the stripe to z axis. During optical calibration, every effort was made to ensure the stripe intensity is uniformly distributed. Stripe image and its top-hat intensity is recorded by a beam profiler. The typical stripe dimension in ASE measurement is $L \times W = 4\ mm \times 0.1\ mm$. Its top-hat profile was checked by fitting a horizontal line to the measured stripe, which recorded adjusted $R^2 \geq 0.93$ in length and ≥ 0.85 in width (Appendix 4A). Once the film is excited by pump pulses and emits PL photons, part of the emission is confined in the waveguide and gain-guided along the stripe in both $+z$ and $-z$ directions, as shown in Figure 4.3 (Chapter 3.3.1). Since one end of the excitation stripe is aligned to the film edge, the ASE emission in $+z$ direction can be collected. The collection optics comprises a microscope objective, a Glan-Thompson polariser and a multi-mode fibre fed into a charge-coupled device (CCD) spectrometer. The microscope objective has 0.35 numerical aperture (NA) with minimum resolution about $2\ \mu m$, which eliminates most but not all PL emission from the film surface. The polariser is used to selectively filter TE or TM mode (Chapter 3.3.1), while the CCD records its full spectrum.

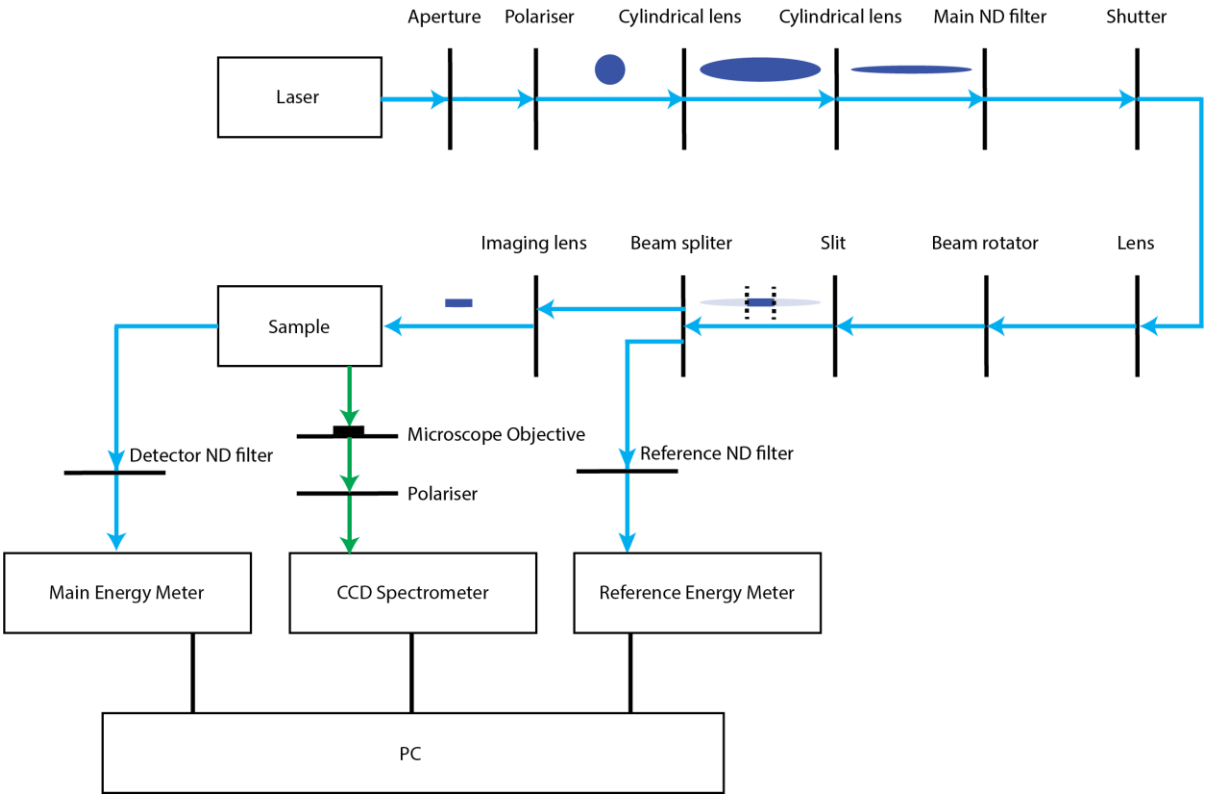


Figure 4.1 – Schematic diagram of ASE measurement set-up. The shutter and neutral density filter are automatically controlled by PC, as well as energy meters and CCD spectrometer. Full optical path is presented in sky blue arrows. Laser beam shaping is illustrated in dark blue.

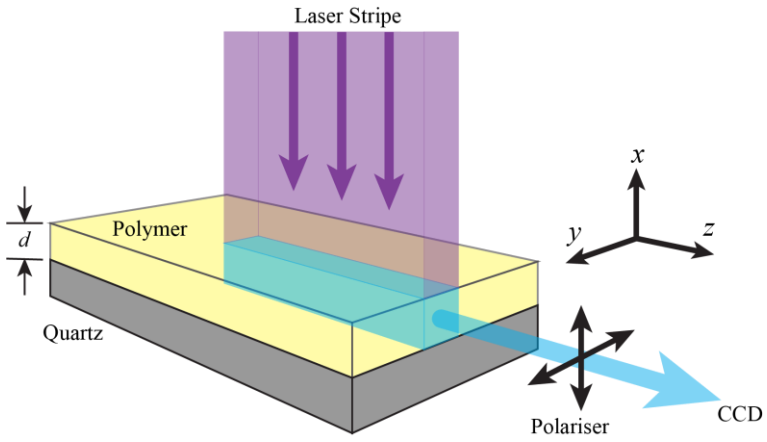


Figure 4.2 – Schematic of ASE sample excitation, emission and collection. Laser pulses are pumped into a rectangular $4\,mm \times 0.1\,mm$ stripe area, which forms a gain-guided air/polymer/quartz slab waveguide. Photons emitted from polymer are coupled into the waveguide propagating in z axis and are collected at the film edge by a multi-mode optical fiber fed into a CCD.

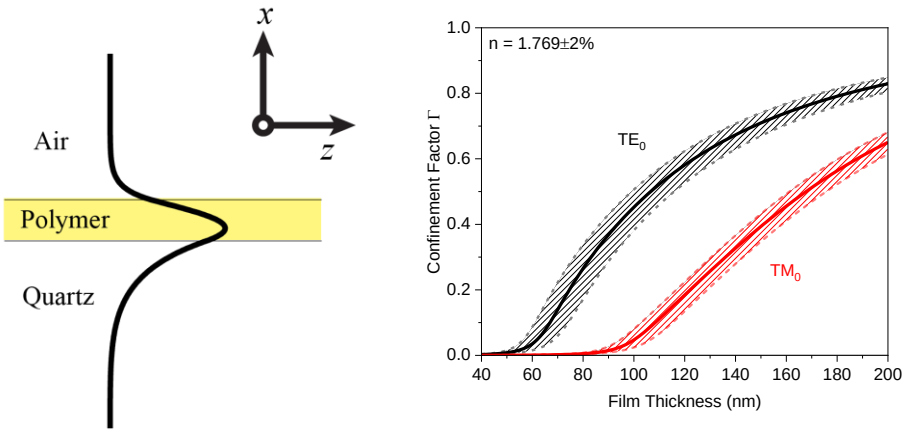


Figure 4.3 – Schematic of ASE modal propagation in the film. The air/polymer/quartz waveguide can be calculated by solving Maxwell's equations – E_y, H_x, H_z for TE modes and H_y, E_x, E_z for TM modes. TE and TM modes are collected separately in experiment via a Glan-Thompson polariser. The result of mode calculation is also plotted (spatial resolution $1\ nm$). Emission wavelength fixed at $450\ nm$ and refractive indices set at 1.0000/1.7690/1.4755 (polymer index from unpublished PFO report, quartz index from a Cauchy's description). The polymer film has to be thick enough to support a propagation mode but not too thick to involve modal competition. The optimised thickness is around $120\ nm$, where Γ_{TE} is relatively high and Γ_{TM} is relatively low as mentioned in Chapter 3.3.1. This can be used for most blue polyfluorenes with similar refractive indices and ASE at 0-1 vibronic peak.

4.2.2 Experimental Error and Reliability

There are several sources of error, which has significant impact on measurement reliability; appropriate measures are in place to ensure that experimental results are accurate and repeatable. Firstly, ASE intensity is highly sensitive to pump energy – the stimulated emission changes exponentially while pump energy varies linearly. The laser beam in the set-up has a small pulse-to-pulse variation of less than 10% in standard deviation – measured at the end of optical path. To accurately monitor pump pulses, a beam splitter on the optical path reflects about 8% of pump energy to a reference energy metre, which records the energy of every single pulse during experiment. Secondly, some polymer thin-films, for example blue polyfluorenes, are easily oxidised and shift to green-band emission when pumped in air. By using fully automated neutral density filters and shutters to scan a series of pump energy in a row, the thin-

film sample would only be exposed to pump when signal is recorded, and total experimental time can be shorter than measuring manually. Thirdly, on the collection side, the intensity of PL emission at low pump can be $3-4$ orders of magnitude less than the intensity of saturated ASE at high pump, and it is challenging for a CCD to record both spectra without changing the slit width. To tackle this issue, the measurement routine is designed to scan from lowest pump energy all the way to the highest as defined by user input. Starting with a relatively long $10-30$ seconds CCD exposure time for low intensity PL, the measurement programme would halve the exposure time every time CCD is saturated, which not only maintains good spectral signal-to-noise ratio for all energy levels, but also shortens the pump duration at high energy when thin-films are vulnerable. Finally, the sample holder may be slightly adjusted in y axis between scans, if necessary, to further prevent excessive pumping in the same area of the sample. The reliability of ASE measurement was tested by measuring the same SC5A thin-film in two consecutive days, during which the sample was stored in air. The decrease of intensity in the second measurement is negligible in PL region and less than 10% in saturated ASE region, which is very stable in blue polyfluorenes.

ASE measurement produces two sets of data – pump energies and emission spectra. In data processing, incident energy is defined as average pulse energy, which is then divided by the area of excitation stripe to obtain energy density (per pulse per area). The 'Pump Energy $\mu J\ cm^{-2}$' used in this thesis only accounts for energy absorbed – energy density times thin-film absorption (%), which is estimated as $(1-T\%)$, unless otherwise specified. On the other hand, spikes in raw spectra are eliminated by a third-order one-dimensional median filter (fitting algorithm 'medfilt1' Matlab). ASE intensity ($a.u.$) is defined as peak intensity of the corresponding vibronic peak (usually 0-1) without spectral integration. This is based on that

stimulated emission always has a fixed full-width-half-maximum (FWHM) regardless of intensity. An average over 1 nm (5 data points) is taken at the peak to produce more stable results. By varying pump energies (automatic scan) and excitation stripe lengths (manual adjustment), ASE intensity can be collected as a two-dimensional matrix $I(I_p, z')$, where pump energy $0 < I_p \leq I_{max}$ and excitation stripe length $0 < z' \leq L_{max}$. Around 40 steps are typically recorded in each dimension – neutral density filters ranging from 2 to 0 with step size 0.05 for pump energy and 0.1 to 4 mm excitation stripe length with step size 0.1 mm. It is worth mentioning that pump energy is adjusted in log scale while stripe length is limited to linear scale.

4.3 Characterisation of Amplified Spontaneous Emission

4.3.1 ASE Threshold and Modal Effect

As an example, one of the blue polyfluorenes F8DP2 was chosen to show step-by-step ASE measurement and analysis (Figure 4.4). Solutions were prepared in Chlorobenzene with concentration $5, 10, 20\ mg/ml$ (Appendix 4B). Thin-films were made by spin-coating at 2000rpm from solution onto 1.5 $cm \times 1.5\ cm$ quartz substrate. The first step is to check film quality – both surface and edge – under cross-polarised microscope, which should show featureless images. The $5\ mg/ml$ film, which is about $60\ nm$ thick, was used for basic photo-physics characterisation in Chapter 2.3 & 2.4 (UV-Vis, PL, PLE, PLQE, PL lifetime). As detailed in Chapter 4.2.1, ASE was measured on the $10\ mg/ml$ film, which is about $110\ nm$ thick and optimum for a strong single TE mode emission as seen in Figure 4.3. This is to ensure the samples for ASE measurement were at their best conditions without any potential

destructive exposure. The $20\ mg/ml$ film, which is about $210\ nm$ thick, has worse ASE as it not only gets more self-absorption from incompletely pumped area but also has two competing modes (TE and TM), which reduces the maximum amplification one can achieve (Chapter 3.3).

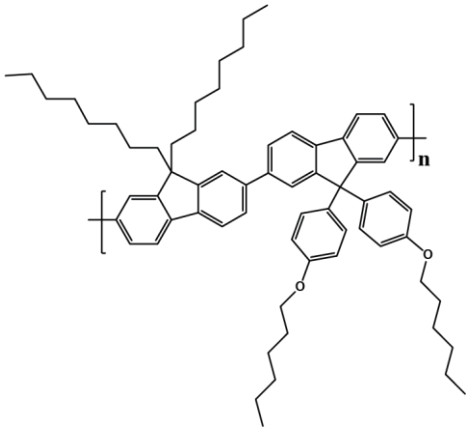


Figure 4.4 – Chemical structure of F8DP2 blue polyfluorenes.

With the two-dimensional ASE data, energy response is analysed by plotting $I(I_p)$ at fixed excitation stripe $z = 4\ mm$. Figure 4.5 plots the energy response – measured in TE and TM mode respectively – of F8DP2 film, which is $130\ nm$ thick and supports two guided modes (TE_0 and TM_0) at 0-1 vibronic peak ($449\ nm$). While both curves are S-shaped divided into PL, ASE and saturation regions, TE mode always has higher intensity than TM. The difference in PL region is due to the better optical confinement of TE mode, which then has more advantage as modes start competing in ASE region. Since most stimulated photons are emitted in TE mode, all ASE and gain analysis are focused on TE mode only. Figure 4.5 also plots the spectra of selected data points to show the non-linear spectral change of 0-1 peak from PL to ASE, in contrast to linearly increasing 0-0 and 0-2 peaks.

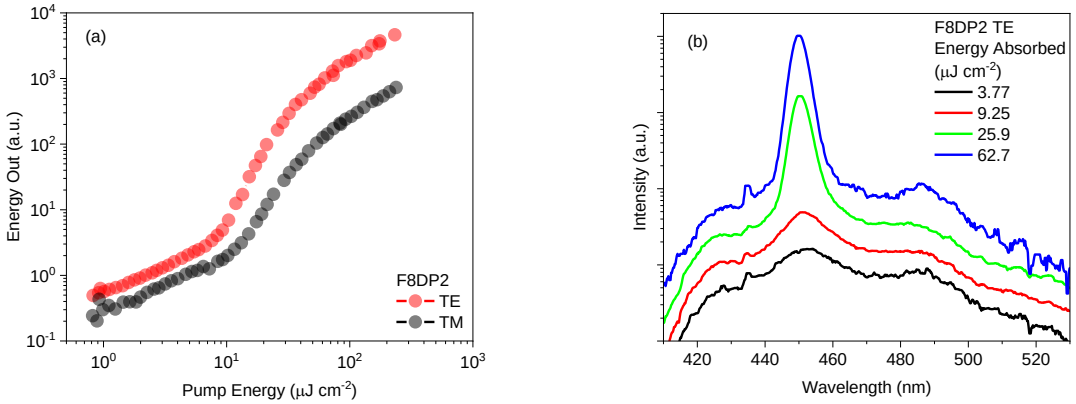


Figure 4.5 – (a) Energy response of F8DP2 film. 'Pump Energy' is energy per pulse absorbed per film area. 'Energy Out' (ASE intensity) is 0-1 vibronic peak intensity in 1 nm spectral width. The energy curve features an S-shape with PL, ASE and saturation regions. TE modes always confine more photons than TM modes, and the difference increases after ASE is turned on, because TE is superior in mode competition. The ASE characterisation mainly focuses on TE_0 mode. (b) Spectra collected from F8DP2 film in TE mode. ASE comes from 0-1 vibronic peak at 449 nm, which increases exponentially with the pump. While 0-0 and 0-2 peaks increases linearly as normal PL.

ASE threshold accounts for the minimum energy required to exhibit ASE in experiment and is commonly used as the first evaluation of lasing materials [13]. It can be extracted in two ways – either by energy response (at the intersection of liner PL and exponential ASE) or by spectra (when the FWHM narrows to half of PL at low pump). Figure 4.6 extracts the ASE threshold of F8DP2 film in TE mode – 8.7 $\mu J\ cm^{-2}$ by energy response and 10.2 $\mu J\ cm^{-2}$ by spectra. It is important to note that the energy response method is more accurate than FWHM. While the intensity/energy only accounts for the 0-1 peak, the calculated FWHM can be influenced by 0-0 and 0-2 peaks depending on how sharp and close the vibronic peaks are. It is not always possible to isolate the FWHM of the 0-1 peak (usually $25 - 30nm$ for blue polyfluorenes). Furthermore, the energy response method also extracts spontaneous emission factor β – the difference between PL and saturation ($\beta = \Omega\eta$, Chapter 3.2.3), which is a key parameter in gain analysis later on.

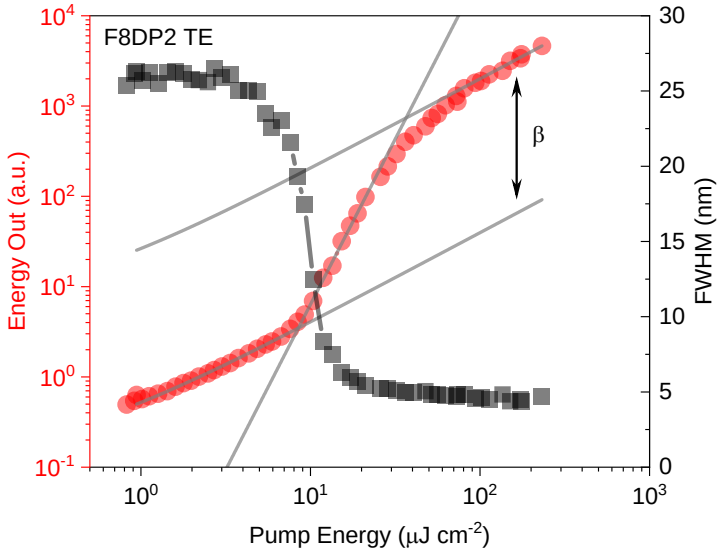


Figure 4.6 – F8DP2 ASE threshold extracted from energy response and FWHM. Threshold in energy response (8.7 $\mu J\ cm^{-2}$) is the intersection of linear PL and exponential ASE (grey lines). Threshold in FWHM (10.2 $\mu J\ cm^{-2}$) is defined as half of FWHM in PL spectrum. For spectra with multiple peaks, threshold extracted from energy response is more accurate than FWHM. The difference between PL and saturation β is extracted to be 0.0197.

To study gain, which describes exponential amplification of signal intensity per length, ASE intensity $I(z)$ is plotted against variable excitation stripe length at fixed pump energy. Figure 4.7 plots $I(z)$ of F8DP2 film measured at various pump energies, as an example for gain extraction. In log-log scale, $I(z)$ has the same S-shape as $I(I_p)$ in Figure 4.5 with clear regions of PL, ASE and saturation. Here ASE threshold is proved to be largely determined by experimental conditions, not a material parameter. Changing excitation stripe length can change ASE threshold dramatically as dotted grey line between PL and ASE region indicates in Figure 4.7 (the same observed in Figure 3.4). Apart from excitation stripe length, ASE threshold also depends on film thickness, film roughness, pump pulse width, excitation stripe width, collection optics etc, some of which have been quantitatively studied in ASE rate Equation (Chapter 3.2.3). Therefore, ASE threshold only judges the presence of ASE under certain experimental conditions and should not be used to characterise materials for lasers and

amplifiers.

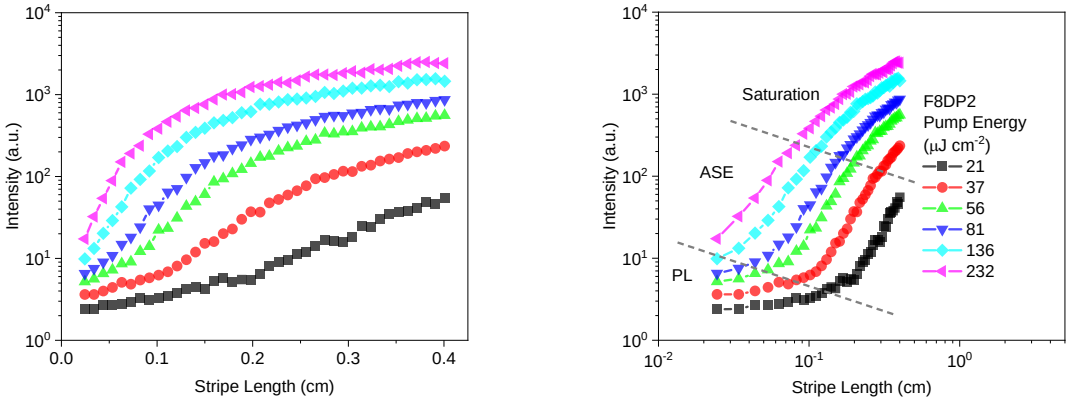


Figure 4.7 – ASE intensity of F8DP2 measured with various stripe length, which then plotted as ASE intensity versus variable stripe length ($I(z)$). Data is plotted on both semi-log and log-log scales. The exponential ASE region is linear on a semi-log scale, while PL and saturation regions are linear on a log-log scale. Measurements at higher pump show ASE at shorter length.

4.3.2 Simplified Gain Equation – Limitations and Applicability

Theoretically, ASE intensity $I(z)$ at a fixed pump energy I_p may be interpreted by travelling-wave equation in a single-pass approach as Equation (3.17) [14-17]

$$\frac{dI(z)}{dz} = \mathrm{A}_{PL}(\mathrm{z}) + \langle g(z)\rangle I(z) \tag{4.1}$$

assuming photons only propagating in $+z$ direction from 0 to L. Here $\langle g(z)\rangle = \frac{g_0}{(1+I(z)/I_s)^x}$ ($x = 1$ for homogeneous saturation and $x = 1/2$ for inhomogeneous saturation) is the net modal gain – the effective gain in a device, while material gain $g(z) = \langle g(z)\rangle\Gamma^{-1}$ is modal gain divided by waveguide confinement factor. In this thesis, all extracted gains (g_0, g_m) are net modal unless otherwise specified. g_0 is net modal gain in small signal regime when $I(z) \leq I_s$. A larger saturation intensity I_s is always better as it allows higher photon intensity in the guided waveguide and also a longer corresponding saturation length L_s, which provides more

flexibility in device dimensions. The gain analysis usually focuses on the fundamental TE_0 mode. $A_{PL}(z)$ is spontaneous emission that contributes to ASE. In polymer thin-films, A_{PL} is independent of z as spontaneous emission is governed by waveguided confinement instead of geometrical structure, thus the z dependent observer-based solid angle does not apply (Appendix 4C). Saturation intensity I_s is a material property defined as the inverse of product of stimulated cross section and excited state lifetime $I_s = (\sigma_e \tau_2)^{-1}$ [13]. $x = 1$ for homogeneous saturation while $x = 0.5$ for inhomogeneous saturation. Here homogeneous saturation is chosen for ASE in polymer thin-films, because all stimulated photons are the same species and the shape (FWHM) of ASE spectrum does broaden in saturation region. When $I(z) \ll I_s$, the effect of saturation is negligible and Equation (4.1) can be simplified to

$$\frac{dI(z)}{dz} = A_{PL} + g_m I(z) \tag{4.2}$$

$$I(z) = \frac{A_{PL}}{g_m}(e^{g_m z} - 1) \tag{4.3}$$

where g_m is small signal net modal gain without saturation term. When $g_m z \ll 1$, Equation (4.3) can be further simplified to

$$I(z) = A_{PL} z \tag{4.4}$$

Equation (4.4) is only valid in PL region as ASE threshold is calculated as $g_m z = 1.256$ [18].

Fitting $I(z)$ to Equation (4.3) where A_{PL} and g_m are floating parameters is the most common method for gain extraction in polymer thin-films [19-21]. However, it has limited applicability and can include large error raised from both PL and saturation regions [22]. The single fitting equation is also highly sensitive to the range of data selected and would only work if there are

sufficient data points in both PL and ASE regions but not in saturation region, which also makes it difficult to compare results from different experimental set-ups. Moreover, the method does not utilise the relationship among different pump energies but fits each curve as isolate data. On the contrary, this chapter proposes a new approach to systematically fit the whole data step-by-step where the overall fitting error is shared among equations and steps, which extracts the net modal gain in a more accurate and meaningful way.

4.3.3 Gain Extraction (g_m) not including Saturation

The first step is to extract the value of A_{PL} by fitting Equation (4.4) in PL region $0 \leq z \leq L_{PL}$ (fitting algorithm 'polyfit' in Matlab). As mentioned in measurement limitations, there are some background noise (e.g. film surface PL emission) apart from waveguided edge emission. The actual fitting function is $I(z) = A_{PL}z + b$, where b is expected to be small. The key to fit Equation (4.4) is to determine the upper limit of L_{PL} and ensure $I(z)$ is always below ASE threshold. The valid range of L_{PL} may be defined as where $I(z)$ looks linear in Figure 4.7, but the more effective way is where the spectral FWHM remains relatively the same as the spectrum measured in PL region (i.e. at the lowest pump energy in ASE set-up). The FWHM starts narrowing at higher pump energy and/or at longer stripe length when ASE is turned on (Appendix 4D). Figure 4.8 compares different choices of L_{PL} ranging from $0.3mm$ to $2.5mm$ at 21 $\mu J\ cm^{-2}$ pump energy. The extracted individual $A_{PL}(L_{PL})$ is sensitive to the choice L_{PL} – large error when L_{PL} is too short and overestimation when L_{PL} is too long (into the ASE region). Hence the upper limit of L_{PL} is when individual $A_{PL}(L_{PL})$ starts to increase, and the overall A_{PL} at 21 $\mu J\ cm^{-2}$ is determined by the median of all individual $A_{PL}(L_{PL})$ extracted below the upper limit of L_{PL}, which can also be double checked later once g_m is extracted.

Since ASE threshold is defined as $g_m L_{th} = 1.256$, the stripe length at the threshold L_{th} can be calculated and considered as the maximum L_{PL}. The validity of L_{PL} is checked at 21, 37, 56, 81 $\mu J\ cm^{-2}$, and its upper limit always stays below L_{th} (Appendix 4D). When fitting Equation (4.4), b is found to be much smaller than A_{PL} both in value and derivative, thus its error is likely to be small (Appendix 4D). For the two highest pump energies 136, 232 $\mu J\ cm^{-2}$, the respective L_{th} is too short ($0.3 - 0.4\ mm$) to define a reliable range of L_{PL} due to stripe length limitation ($L_{min} \approx 0.2mm$ and $dz \approx 0.1mm$). However, spontaneous emission is proportional to excited state density (assuming PLQE does not change with I_p), which is also proportional to pump energy as $A_{PL}(I_p) \propto I_p$ (except the highly unlikely ground state depopulation). Therefore, A_{PL} at high pump energies can be linearly projected from the obtained $A_{PL}(I_p)$ at lower pump energies, linking data at different pump energies (Figure 4.9).

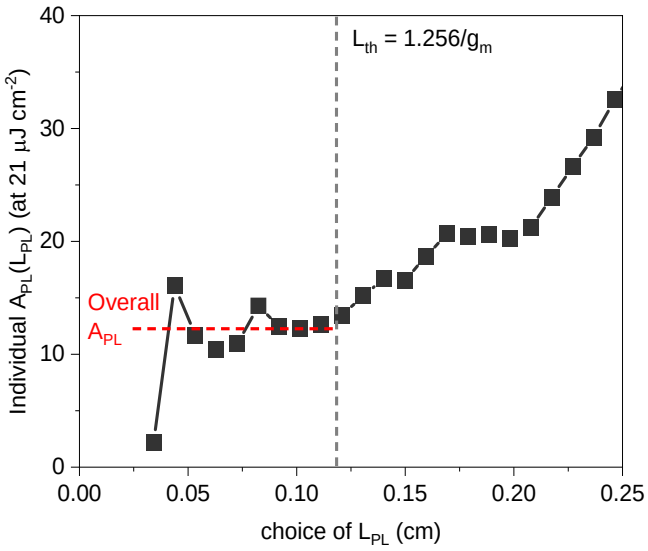


Figure 4.8 – At 21 $\mu J cm^{-2}$, individual $A_{PL}(L_{PL})$ is extracted by fitting $I(0 < z \leq L_{PL})$ to Equation (4.4) and the overall A_{PL} (red) is the median within range $0 < L_{PL} < L_{th}$. The upper limit L_{th} is subject to ASE threshold $g_m L_{th} = 1.256$ and is where $A_{PL}(L_{PL})$ starts to increase.

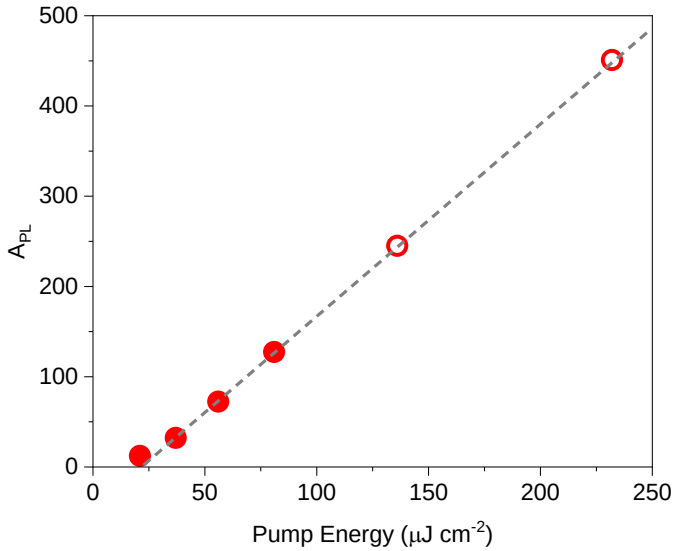


Figure 4.9 – Extracted A_{PL} in Figure 4.8 linearly increases with pump, as expected in Equation (4.4). Linear projection is used at high pump where PL cannot be observed.

The next step is to extract g_m by fitting Equation (4.3) in PL and ASE regions $0 \leq z \leq L_s$, where L_s is saturation length when $I(z) = I_s$ (fitting algorithm 'lsqnonlin' in Matlab, minimising $\sum_0^{L_s}\left(\ln I_{fit}(z) - \ln I(z)\right)^2$). As the saturation length is an estimation in this step, L_{si} is used for this initial value instead of L_s. Unlike the commonly used method discussed in 4.3.2, here A_{PL} is fixed at the value previously extracted, which largely reduces fitting error. The actual fitting function $I(z) = \frac{A_{PL}}{g_m}(e^{g_m z} - 1) + b$ also accounts for background noise while b is limited to the value previously fitted with a $\pm 30\%$ range. Again, the key to fit Equation (4.3) is to find the correct L_{si} and exclude any points in saturation region. Unlike L_{PL}, L_{th} which can be judged by the change of spectrum, L_{si} is very difficult to estimate because the saturation process is more gradual than threshold, and spectral FWHM almost remain unchanged (Figure 4.6). Although L_{si} can still be roughly defined by the S-shaped $I(z)$, the error is large due to the lack of quantitative control. Here the strategy is to try fitting with every possible length as a guess, then L_{si} can be estimated in the region where g_m is most

stable and usually the highest. The corresponding $I_{si} = I(L_{si})$ is the initial estimation of saturation length I_s. As an example, Figure 4.10 plots the extracted g_m and L_{si} of F8DP2 film at 56 $\mu J\ cm^{-2}$. Applying the same method, Equation (4.3) is used to fit F8DP2 data from Figure 4.7. Once the saturation occurs, the fitted line always has a higher unsaturated intensity. However, the disadvantage of this method is that most data would be wasted at high pump energy where saturation takes places at a very short length, which makes the result unreliable and misleading.

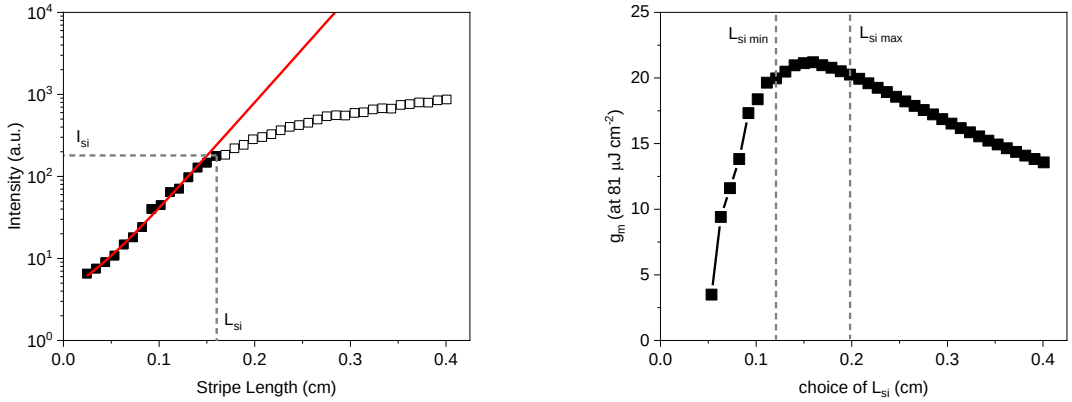


Figure 4.10 – Gain extraction not including saturation for $I(z)$ at 56 $\mu J cm^{-2}$. g_m is extracted by fitting $I(0 < z \leq L_{si})$ regime to Equation (4.3) using the extracted overall A_{PL} in Figure 4.9. Saturation length L_{si} is estimated to a range with best fit (adjusted $R^2 \geq 0.95$), which also has the highest gain. With L_{si}, the corresponding I_{si} can be obtained.

4.3.4 Gain Extraction (g_0) including Saturation

The final step is to include saturation term, which allows fitting globally up to the maximum stripe length L_{max} [12,23,24]. Homogenous saturation is preferred as stimulated emission photons are the same species which does not change the shape of gain spectrum when saturated [13,25]. Experimental results also confirm that the FHWM does not change in saturation region (Figure 4.6). Nevertheless, both homogeneous and inhomogeneous saturation were tested in a

set of experimental data. Not only the data fits homogeneous saturation better, but the extracted homogenous gain distribution follows closer to calculated values from spatial-temporal model in Chapter 3.3.3 (Appendix 4E). Therefore, only homogenous saturation is applied in this thesis. Rewrite Equation (4.1) with homogeneous saturation

$$\frac{dI(z)}{dz} = \frac{\mathrm{A}_{PL}}{1 + I(z)/I_s} + \frac{g_0 I(z)}{1 + I(z)/I_s} \tag{4.5}$$

where both A_{PL} and g_0 are saturated by the depopulation of the excited state, which decreases spontaneous and stimulated emission to the same extent. Equation (4.5) cannot be solved analytically to obtain $I(z)$, however, $\frac{dz(I)}{dI}$ can be solved for $z(I)$ instead [26-28].

$$z(I) = \frac{I/I_s}{g_0} + \frac{(g_0 - \mathrm{A}_{PL}/I_s)\ln(1 + g_0 I/\mathrm{A}_{PL})}{{g_0}^2} \tag{4.6}$$

Gain can be extracted by fitting Equation (4.5) to a grey-box model containing a linear ordinary differential equation (fitting algorithm 'idgrey' in Matlab, initial condition $I(0) = b$ as in 4.3.3). Alternatively, data $z(I)$ can be fitted to Equation (4.6) directly (fitting algorithm 'lsqnonlin' in Matlab, minimising $\sum_{I_{min}}^{I_{max}} \left(\ln z_{fit}(I) - \ln z(I)\right)^2$). Both methods produce the same result ($\pm 3\%$), and Equation (4.6) is chosen for simplicity and faster running time. Again, A_{PL} is fixed from Figure 4.9. Both g_0 and I_s are initially extracted in one optimisation with initial guess from previous result as $g_0 = g_m, I_s = I_{si}$. Although I_s is a material property thus independent of pump energy, the reason not to fix its value is that previous estimation I_{si} has large error – it is a secondary estimation from L_{si}, which is not quantitatively derived. Instead, I_{si} is limited in a range of $I_s \pm 30\%$. In this way, the values of I_s at 56, 81, 136, 232 $\mu J\ cm^{-2}$ are found to be within $\pm 10\%$, and $I_s = 115$ is finally chosen to be the value extracted at the

highest pump 232 $\mu J\ cm^{-2}$, because saturation is more recognisable and reliable at high pump energies and more data points would extract a more accurate I_s. Then Equation (4.6) is fitted to F8DP2 data from Figure 4.7 with fixed I_s and A_{PL} (Appendix 4D), while I_s is also used to find the corresponding L_s. Both L_s and previously estimated L_{si} follow an inverse proportional shape while L_s is a little shorter than L_{si} (Figure 4.11). Similarly, I_s also sits on the lower end of I_{si} (Figure 4.12). This suggests that saturation occurs inside the stripe before it can be visually observed in figures, and g_m may be underestimated and may have lower value than g_0. It is worth to note that although $I_s = (\sigma_e \tau)^{-1}$ is a material constant, its arbitrary value is determined by waveguide confinement and collection optics thus cannot be compared in different measurements.

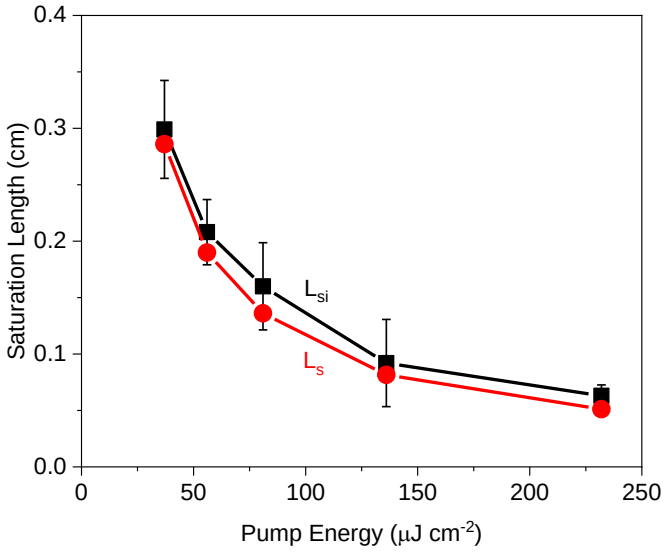


Figure 4.11 – Saturation length L_s extracted in Equation (4.6) is similar but a little shorter than L_{si} estimated in Figure 4.10 where saturation is not included.

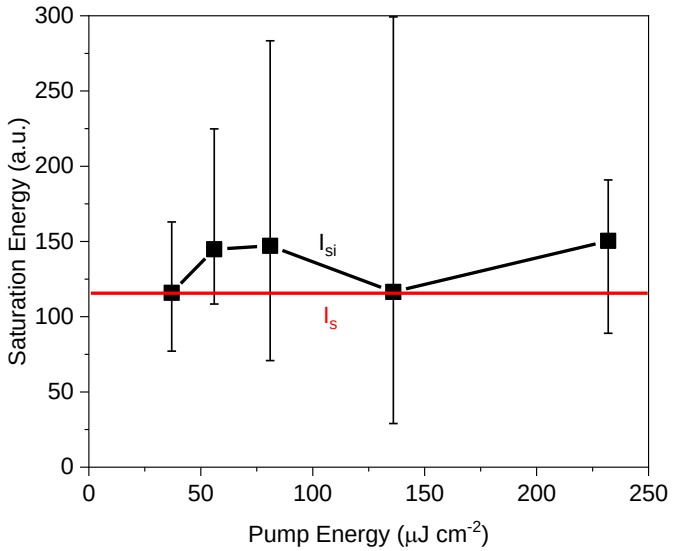


Figure 4.12 – Saturation intensity I_s extracted in Equation (4.6) is within the estimated range of I_{si}. I_s is a material constant defined as $I_s = (\sigma_e \tau_2)^{-1}$ but its experimental value varies on waveguide confinement and collection optics.

4.4 New Metrics for ASE in Thin-film Structures

4.4.1 Material Aspect – Gain versus Pump

Once curve fitting is completed, gain values extracted from Chapter 4.3.3 and 4.3.4 are plotted against pump energy as $g_m(I_p)$ and $g_0(I_p)$, which are both net modal gains (Figure 4.13). At low pumping regime, g_m and g_0 have similar values and increase linearly with the pump. When pump is high, however, g_m starts to bend down while g_0 still maintains its linearity, which confirms that g_m is underestimated due to ASE saturation. Although extra care is taken when selecting data for Equation (4.3), the effect of saturation cannot be eliminated. Even at saturation threshold $I(z) = I_s$, the method not including saturation would still underestimate by 50% as $\frac{g_0 I(z)}{1+I(z)/I_s} = \frac{1}{2} g_0$. Therefore, only method including saturation should be used when

there is a clear saturation region in the data, and $g_0(I_p)$ should always be linear, which can be derived from rate equation as (Chapter 3.3.3)

$$g_0 = \Gamma[\sigma_e(N_2 - N_1) - \alpha_{lo}] \tag{4.7}$$

where loss α_{lo} is negligible and population inversion $N_2 - N_1 \approx N_2$. σ_e is material property, Γ is constant for the same sample and pumping efficiency is constant for the same laser source so that $N_2 \propto I_p$. Then Equation (4.7) becomes

$$g_0 \propto \sigma_e I_p \tag{4.8}$$

Equation (4.8) is consistent with Figure 4.13 and suggests that higher stimulated cross-section σ_e is beneficial to gain media. More importantly, once modal gain is divided by waveguide confinement factor Γ to obtain material net gain, dg/dI_p can be comparable as a material property and does not change with device structure (e.g. film thickness) or measurement set-up.

Apart from the intensity at ASE peak, gain g_0 is also extracted at different wavelength by Equation (4.6). The extracted gain values for the full 0-1 vibronic peak of F8DP2 film was also investigated (Appendix 4F). The shape of gain follows ASE spectrum exactly, which confirms that ASE in gain-guided thin-films is a self-seeding process at the maximum gain position. However, by carefully designing device structure, the F8DP2 material would be capable to show gain in a much broader spectral range.

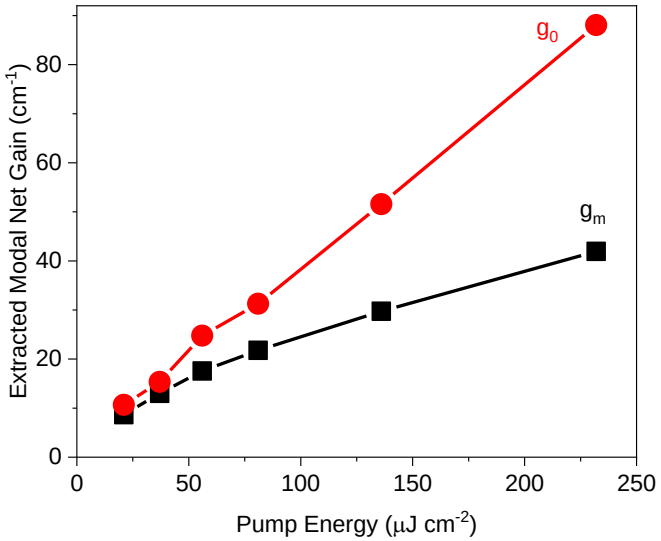


Figure 4.13 – Compare small signal net modal gain g_m extracted in Equation (4.3) and global net modal gain g_0 extracted in Equation (4.6). g_0 is believed to be the real net modal gain in TE mode because it increases linearly with pump. The slope of g_0 is independent of experimental set-up and can be used to screen materials for laser or amplifiers. Although data range is carefully selected to eliminate saturation, g_m underestimates net modal gain by up to 50%. Saturation is a gradual effect with no clear onset (unlike threshold), which should be always considered in gain extraction.

4.4.2 Device Aspect – Gain Length Product

Although $\frac{dg}{dI_p}$ describes the gain potential of a material, it is still essential to know the expectation of actual device performance. The gain length product $(gL)_{max} = g_0 L_s$ represents the maximum amplification that can be achieved in a particular device – a thin-film in case of ASE measurement [1]. $g_0 L_s$ depends on device structure but is independent of how it is measured. Since ASE threshold can be expressed as $g_0 L_{th} = 1.256$ [18], there should be another value for ASE saturation, between which the actual gain can be measured. Rewrite Equation (4.6) at saturation threshold

$$L_s = z(I = I_s) = \frac{1}{g_0} + \frac{(g_0 - \mathrm{A}_{PL}/I_s)\ln(1 + g_0 I_s/\mathrm{A}_{PL})}{{g_0}^2} \tag{4.9}$$

Equation (4.9) can be simplified as follows. Referring to Chapter 3.2.3, $\mathrm{A}_{PL} = \Gamma\Omega\eta N_2/\tau_2$, $I_s = (\sigma_e\tau_2)^{-1}$ and $g_0 \approx \Gamma\sigma_e N_2$ when population inversion $N_2 \gg N_1$, thus $(\mathrm{A}_{PL}/g_0 I_s)_{approx.} = \Omega\eta$ which is in the order of 10^{-2}. Substitute $\mathrm{A}_{PL}/I_s \ll g_0$ into Equation (4.9)

$$(L_s)_{approx.} = {g_0}^{-1}[1 + \ln(1 + g_0 I_s/\mathrm{A}_{PL})] \tag{4.10}$$

Then substitute $(g_0 I_s/\mathrm{A}_{PL})_{approx.} = \Omega\eta = \beta$ (Chapter 3.2.3)

$$(g_0 L_s)_{approx.} = 1 + \ln(1 + \beta^{-1}) \tag{4.11}$$

As the nature of logarithmic function, when $\beta^{-1} \gg 1$

$$(g_0 L_s)_{approx.} = 1 + \ln(\beta^{-1}) \tag{4.12}$$

where $\beta = \Omega\eta$ can either be interpreted as the product of spontaneous emission factor and PLQE η or be measured as the difference between PL and saturation when extracting ASE threshold from energy response. Experimentally $g_0 L_s$ is around $4 - 5$ (~ 20 dB) for polyfluorenes as results from F8DP2 film are plotted in Figure 4.14. Similar value of $g_0 L_s$ was observed in other conjugated polymers [1]. As expected, the product of linearly increasing g_0 and inverse proportional L_s is almost constant at different pump energies. However, $g_m L_{si}$ by the method not including saturation shows a decrease, which is again due to underestimated g_m. This further confirms that including saturation is necessary in gain extraction.

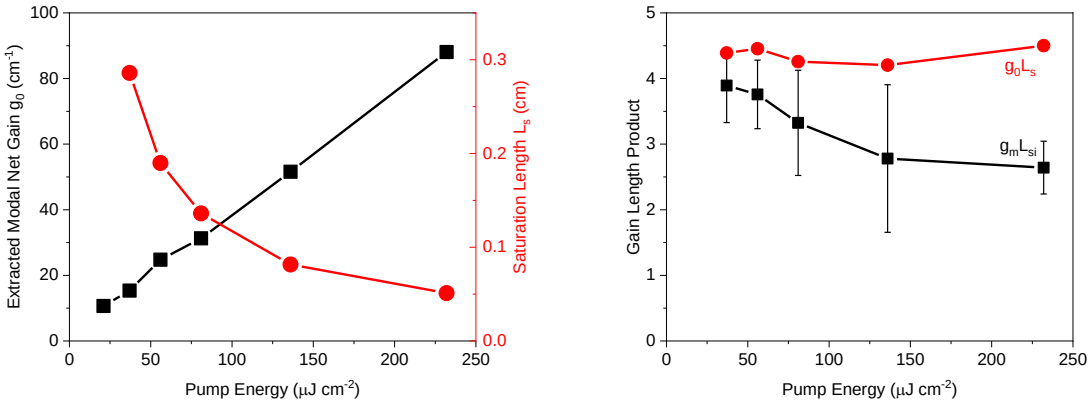


Figure 4.14 – While net modal gain increases linearly, saturation length is inverse proportional to the pump. Then the gain length product should be constant, as expected in Equation (4.12). The product represents the maximum amplification that can be achieved in the given sample, irrespective of experimental set-up. Again, $g_0 L_s$ follows the constant line ($4.4 \pm 5\%$) while $g_m L_{si}$ decreases by 40% due to saturation. This metric suggests the F8DP2 sample is capable of applications within 19.5 dB.

4.5 Material Comparison and Discussion

4.5.1 Materials

Apart from F8DP2, other conjugated polymers SC5A, PFO glassy and F8BT were also studied (Figure 4.15, Table 4.1, Appendix 4B). It is useful to compare the three blue polyfluorenes F8DP2, SC5A and PFO glassy, which share the same backbone structure, with F8BT, which has red-shifted absorption and also PL and ASE emission (Figure 4.16 and 4.17). The differences in materials would help understand the potential key aspects for gain media and promote better chemical designs specifically for lasing applications. Thin-films were made by spin-coating at 2000rpm from solution onto $1.5\ cm \times 1.5\ cm$ quartz substrate. The solution concentration ($10 - 20\ mg/ml$) was tuned to achieve desired film thickness for ASE – around $120\ nm$ thick for blue-emitting F8DP2, SC5A, PFO glassy (Figure 4.3), and around $250\ nm$ thick for green-emitting F8BT – measured with a Dektak Surface Profilometer once all other

measurements were completed. Like F8DP2, thinner films with half the thickness were also made separately from each material for basic photo-physics characterisation in Chapter 2.3 and 2.4 (UV-Vis, PL, PLE, PLQE, PL lifetime). All films were checked under cross-polarised microscope to have flat film quality and reasonably clear film edge. ASE and gain measurements were performed and analysed as in Chapter 4.3 and 4.4.

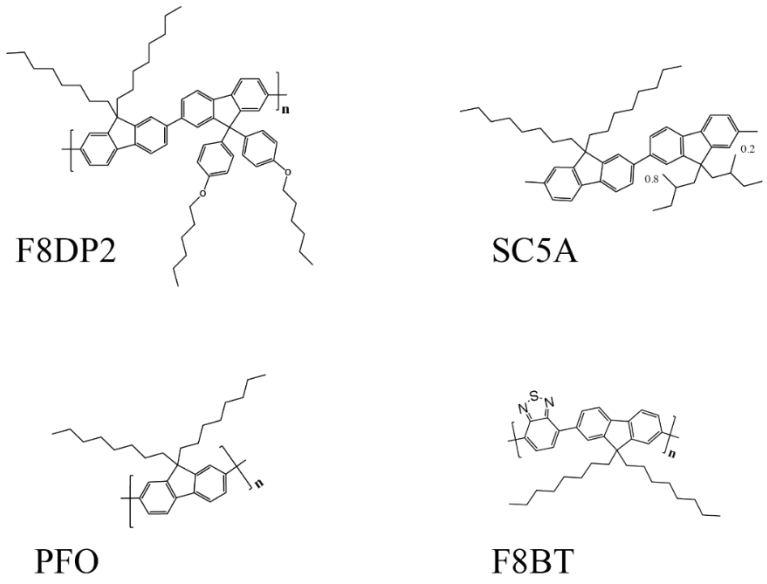


Figure 4.15 – Chemical structures of conjugated polymers studied as gain media.

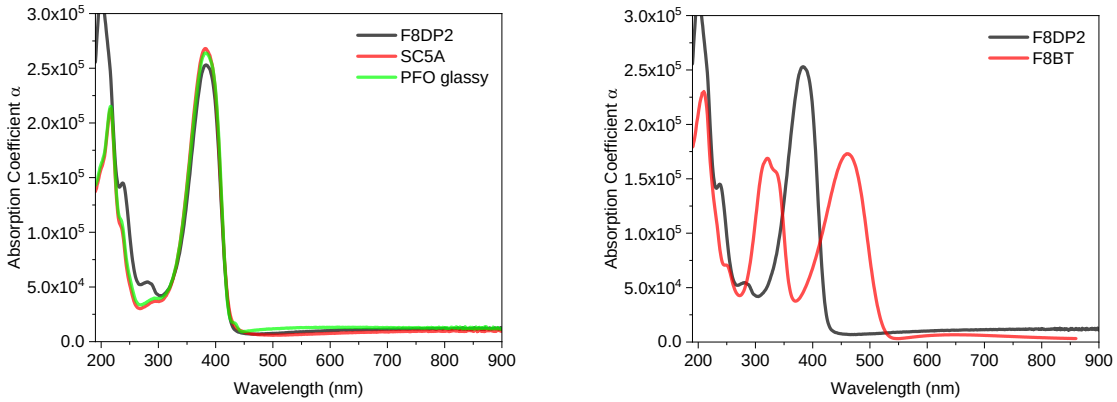


Figure 4.16 – Absorption coefficient calculated from Beer-Lambert law. Raw data from thin film UV-Vis transmittance measurement (Chapter 2.3.1). While F8DP2, SC5A and PFO glassy all have similar absorption peak at about 380 nm due to the same chemical backbone, F8BT has double peaks at about 320 and 460 nm.

Table 4.1 – Basic photo-physics parameters of polyfluorenes: F8DP2, SC5A, PFO glassy and F8BT, including film thickness (d), absorption peak (λ_{Abs}), absorption coefficient (α), PL 0-1 vibronic peak (λ_{PL}), refractive index (n), PLQE (η), PL lifetime (τ). ASE parameters measured in TE mode from $4\ mm\ \times 0.1\ mm$ stripe and pumped at $355\ nm$ are also listed: ASE peak (λ_{ASE}), ASE threshold (I_{th}), minimum FWHM, spontaneous factor (β)

Polymers	F8DP2	SC5A	PFO glassy	F8BT
$d\ (nm)$ [a]	110 ± 10	130 ± 10	135 ± 10	260 ± 20
$\lambda_{Abs}\ (nm)$	383	383	382	460
$\alpha(\lambda_{Abs})\ (cm^{-1})$ [b]	2.53×10^5	2.68×10^5	2.64×10^5	1.73×10^5
$\lambda_{PL}\ (nm)$	448	447	448	572
$n(\lambda_{PL})$ [c]	1.77	1.77	1.77	1.69
η (%) [d]	36 ± 3	36 ± 3	38 ± 3	35 ± 3
$\tau\ (ns)$ [e]	0.23 ± 0.02	0.21 ± 0.02	0.21 ± 0.02	1.9 ± 0.1
$\lambda_{ASE}\ (nm)$	449	449	451	575
$I_{th}\ (\mu J\ cm^{-2})$ [f]	8.7	18.9	17.1	33.5
FWHM (nm)	4.4	4.3	4.2	10
β [g]	0.0197	0.0266	0.0360	< 0.0489

a. Thin-film thickness measured using a Dektak surface profilometer. Each film was measured at $5 - 6$ different positions.
b. Absorption coefficient calculated from Beer-Lambert law.
c. Refractive index at 0-1 peak.
d. Photoluminescence quantum efficiency (PLQE) measured at λ_{Abs} and calculated from de Mello method as in Chapter 2.3.3.
e. Photoluminescence lifetime (τ) measured using a Streak Camera and extracted by single/double exponential method (Chapter 2.4.5). τ is constant across spectrum.
f. ASE threshold in TE mode, extracted by energy response as in Figure 4.6.
g. Spontaneous emission factor $\beta = \Omega\eta$, extracted as in Figure 4.6. F8BT data does not show complete linear saturation region due to short of pump energy, thus an estimated higher limit is listed.

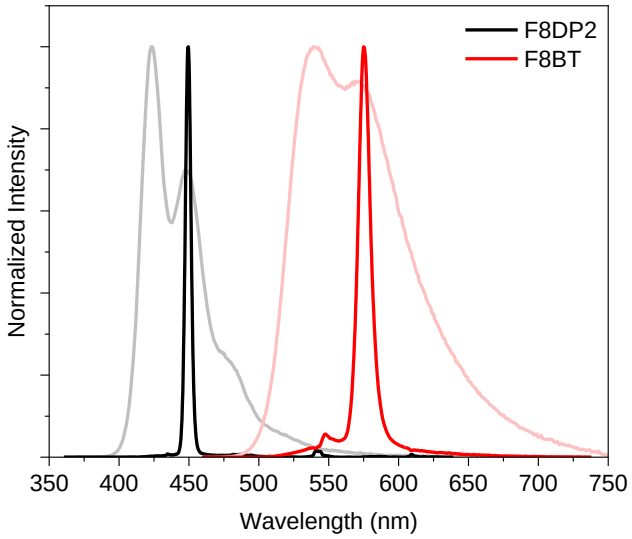


Figure 4.17 – PL and saturated ASE spectra of F8DP2 and F8BT pumped at 355 nm and measured in TE mode (details in Table 4.1). For both PL and ASE, while F8DP2 has blue and narrower spectra (at 450 nm with FWHM up to about 50 nm), F8BT emission is green-yellow and broader (at 570 nm with FWHM up to about 100 nm).

4.5.2 Blue Polyfluorenes F8DP2, SC5A, PFO glassy

Following Chapter 4.5.1, ASE and gain results were compared among blue polyfluorenes F8DP2, SC5A and PFO glassy. They share the same chemical backbone, which governs the main optical properties including spontaneous and stimulated emissions, while the modified side chains alter the material processing such as solubility and packing (Table 1) [6]. Figure 4.18 shows net modal gain g_0 versus pump energy extracted in Equation (4.6). As expected, all blue polyfluorenes have similar slope about 0.4, which means they are the same kind of gain media. Moreover, as the samples all have film thickness about 130 nm thus similar waveguide confinement, the actual material gain is also similar. However, the ASE threshold varies several times (F8DP2 8.77 $\mu J cm^{-2}$, SC5A 18.1 $\mu J cm^{-2}$, PFO glassy 21.2 $\mu J cm^{-2}$). This confirms experimentally that ASE threshold cannot be used to evaluate materials for lasing applications. Extracted saturation length L_s is also plotted in Figure 4.19.

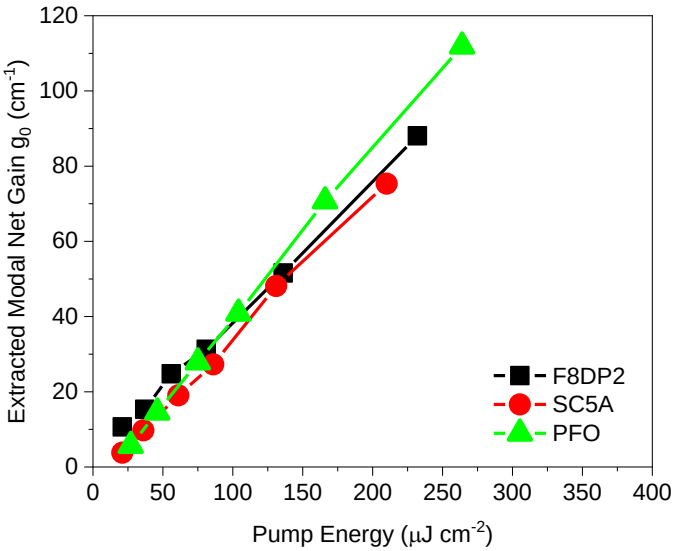


Figure 4.18 – Compare net modal gain versus pump in TE mode extracted in Equation (4.6). All 3 polymers have similar slopes despite different ASE threshold (F8DP2 8.77 $\mu J cm^{-2}$, SC5A 18.1 $\mu J cm^{-2}$, PFO glassy 21.2 $\mu J cm^{-2}$). In this case the longer PL lifetime of F8DP2 contributes to a lower ASE threshold. The slope of gain is a better metric than ASE threshold for accessing gain media.

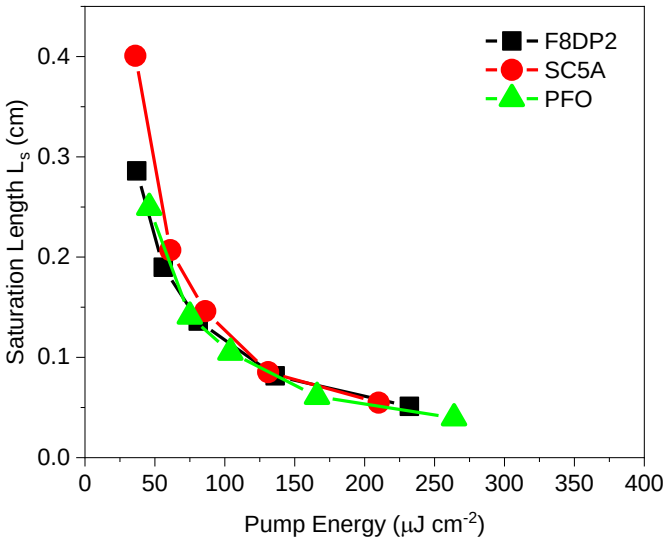


Figure 4.19 – Compare saturation length L_s in TE mode extracted in Equation (4.6). Again, all 3 polymers show similar results due to similar optical properties.

Then the gain length product $g_0 L_s$ is compared in Figure 4.20. Since both g_0 and L_s are similar, the 3 blue polyfluorenes also have $g_0 L_s$ about $4 - 4.5$, which has $18 - 20$ dB amplification.

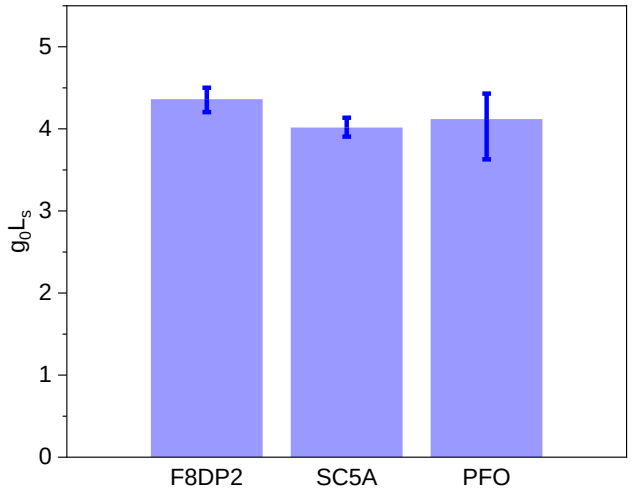


Figure 4.20 – Compare gain length product $g_0 L_s$ in TE mode. All 3 polymers have a maximum amplification between $4 - 4.5$, which are capable of applications within $18 - 20$ dB. This is as expected in Equation (4.12) where all polyfluorenes have similar PLQE, refractive index and film thickness.

4.5.3 Green-yellow F8BT

ASE and gain results from blue emission F8DP2 and green-yellow emission F8BT were compared. Basic characterisations are listed in Table 4.1. Again, net modal gain g_0 versus pump energy extracted in Equation (4.6) are plotted in Figure 4.21. F8BT has much smaller slope – about $20 - 25\%$ of F8DP2. On the contrary, saturation length L_s is extracted to be $4 - 5$ times longer for F8BT than F8DP2 (Figure 4.22). Therefore, for gain length product $g_0 L_s$, F8BT and F8DP2 have similar values (Figure 4.23, Table 4.2). Both materials can achieve about 19 dB amplification but in different device dimensions, which fits different types of application designs.

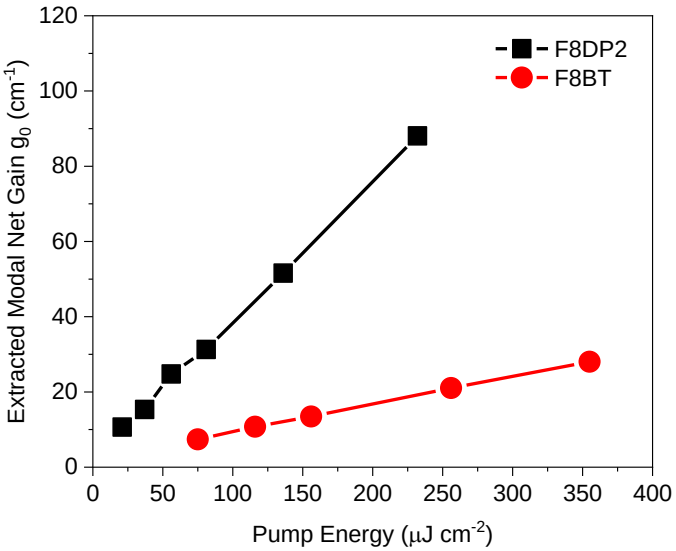


Figure 4.21 – Compare net modal gain versus pump in TE mode extracted in Equation (4.6). F8DP2 has much higher gain ($4-5$ times) than F8BT. The possible reason is F8DP2 has higher stimulated emission cross-section.

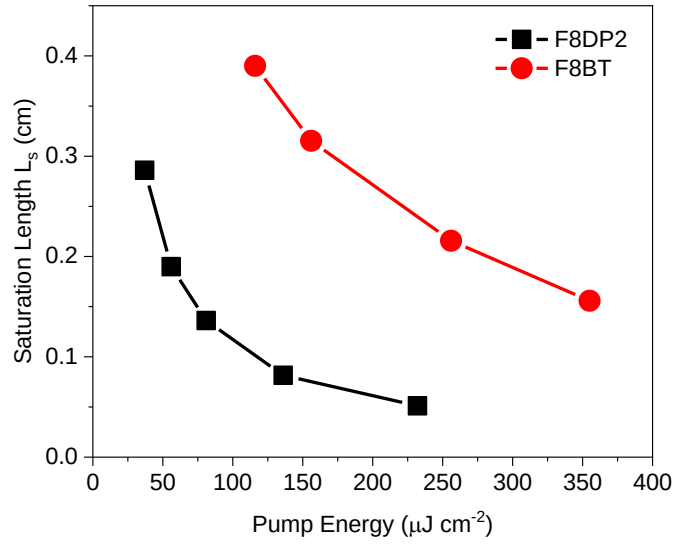


Figure 4.22 – Compare saturation length L_s in TE mode extracted in Equation (4.6). F8BT has much longer L_s ($4-5$ times) than F8DP2.

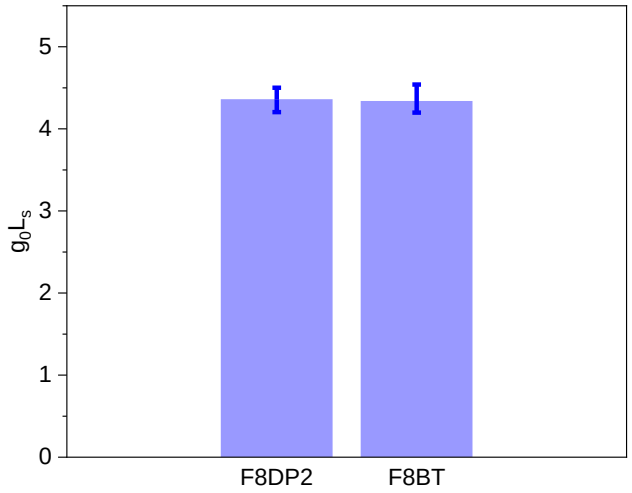


Figure 4.23 – Compare gain length product g_0L_s in TE mode (F8DP2 4.41 ± 0.19, F8BT 4.36 ± 0.14). Longer saturation length of F8BT compensates the lower gain, resulting in similar gain length product g_0L_s for both materials.

Table 4.2 – New metric for gain materials – comparing polyfluorenes: F8DP2, SC5A, PFO glassy and F8BT. All results are extracted by curve fitting including saturation term in Equation (4.6). $\frac{dg_0}{dI_p}$ is the slope obtained by the linear fit of $g_0(I_p)$. Although the actual gain values differ, all materials have similar g_0L_s, which represents the maximum amplification can be achieved in a thin-film device.

Polymers	F8DP2	SC5A	PFO	F8BT
$\frac{dg_0}{dI_p}$ $(cm\,\mu J^{-1})$	0.366	0.382	0.450	0.0735
g_0L_s	4.36 ± 0.15	4.02 ± 0.15	4.12 ± 0.35	4.34 ± 0.20
$(g_0L_s)_{approx.}$ [a]	4.93	4.63	4.32	> 4.02

a. Approximate value of g_0L_s as $1 + \ln(\beta^{-1})$ in Equation (4.12). β is extracted experimentally as in Table 4.1.

4.6 Summary

This chapter presented an accurate and reliable characterisation scheme for ASE in polymer thin-films. The measurement and analysis techniques were discussed in detail under certain limitations, which makes ASE threshold inadequate for assessing material properties. Emphasis was made on including saturation in gain extraction, which is the primary reason that gain values were underestimated. New metrics were also proposed to compare different gain media – net modal gain versus pump $g_0(I_p)$ represents the ability to produce gain and gain length product $g_0 L_s$ provides the maximum amplification to be fitted in thin-films – both of which can potentially help promote better materials and devices towards electric pumped lasers and amplifiers in organic thin-film structures.

References

[1] McGehee, M. D., Gupta, R., Veenstra, S., Miller, E. K., Díaz-García, M. A., & Heeger, A. J. (1998). Amplified spontaneous emission from photopumped films of a conjugated polymer. *Physical Review B - Condensed Matter and Materials Physics*, *58*(11), 7035–7039.

[2] Heliotis, G., Bradley, D. D. C., Turnbull, G. A., & Samuel, I. D. W. (2002). Light amplification and gain in polyfluorene waveguides. *Applied Physics Letters*, *81*(3), 415–417.

[3] Aimono, T., Kawamura, Y., Goushi, K., Yamamoto, H., Sasabe, H., & Adachi, C. (2005). 100% fluorescence efficiency of 4, 4′ -bis[(N-carbazole)styryl] biphenyl in a solid film and the very low amplified spontaneous emission threshold. *Applied Physics Letters*, *86*(7), 071110.

[4] Sandanayaka, A. S. D., Matsushima, T., Bencheikh, F., Terakawa, S., Potscavage, W. J., Qin, C., … Adachi, C. (2019). Indication of current-injection lasing from an organic semiconductor. *Applied Physics Express*, *12*(6), 061010.

[5] Xia, R., Heliotis, G., Hou, Y., & Bradley, D. D. C. (2003). Fluorene-based conjugated polymer optical gain media. *Organic Electronics*, *4*(2–3), 165–177.

[6] Yap, B. K., Xia, R., Campoy-Quiles, M., Stavrinou, P. N., & Bradley, D. D. C. (2008). Simultaneous optimisation of charge-carrier mobility and optical gain in semiconducting polymer films. *Nature Materials*, *7*(5), 376–380.

[7] Tsiminis, G., Wang, Y., Shaw, P. E., Kanibolotsky, A. L., Perepichka, I. F., Dawson, M. D., … Samuel, I. D. W. (2009). Low-threshold organic laser based on an oligofluorene truxene with low optical losses. *Applied Physics Letters*, *94*(24), 243304.

[8] Kim, H., Schulte, N., Zhou, G., Müllen, K., & Laquai, F. (2011). A high gain and high charge carrier mobility indenofluorene-phenanthrene copolymer for light amplification and organic lasing. *Advanced Materials*, *23*(7), 894–897.

[9] Bourdakos, K. N., Cury, L. A., & Monkman, A. P. (2011). The dependence of the amplified spontaneous emission on the waveguide excitation length for high quantum efficiency conjugated polymers. *Organic Electronics: Physics, Materials, Applications*, *12*(7), 1142–1145.

[10] Sandanayaka, A. S. D., Matsushima, T., Bencheikh, F., Yoshida, K., Inoue, M., Fujihara, T., … Adachi, C. (2017). Toward continuous-wave operation of organic semiconductor lasers. *Science Advances*, *3*(4), e1602570.

[11] Kim, D.-H., D'Aléo, A., Chen, X.-K., Sandanayaka, A. D. S., Yao, D., Zhao, L., … Adachi, C. (2018). High-efficiency electroluminescence and amplified spontaneous emission from a thermally activated delayed fluorescent near-infrared emitter. *Nature Photonics*, *12*(2), 98–104.

[12] Cerdán, L. (2020). Simultaneous retrieval of optical gains , losses , and threshold in active waveguides. *Optics and Laser Technology*, *121*, 105814.

[13] Siegman, A. E. (1986). Lasers. *University Science Books*.

[14] Shaklee, K. L., Nahory, R. E., & Leheny, R. F. (1973). Optical gain in semiconductors. *Journal of Luminescence*, *7*(C), 284–309.

[15] Ganiel, U., Hardy, A., Neumann, G., & Treves, D. (1975). Amplified Spontaneous Emission and Signal Amplification in Dye-Laser Systems. *IEEE Journal of Quantum Electronics*, *11*(11), 881–892.

[16] Lange, C., Schwalm, M., Chatterjee, S., Rühle, W. W., Gerhardt, N. C., Johnson, S. R., … Zhang, Y. H. (2007). The variable stripe-length method revisited: Improved analysis. *Applied Physics Letters*, *91*(19), 191107.

[17] Ghani Moghadam, G., & Farahbod, A. H. (2016). General formula for calculation of amplified spontaneous emission intensity. *Optical and Quantum Electronics*, *48*(4), 227.

[18] Cerdán, L., Costela, A., & García-Moreno, I. (2010). On the characteristic lengths in the variable stripe length method for optical gain measurements. *Journal of the Optical Society of America B*, *27*(9), 1874.

[19] Amyot-Bourgeois, M., Keshmarzi, E. K., Hahn, C., Tait, R. N., & Berini, P. (2017). Gain optimisation, bleaching, and e-beam structuring of IR-140 doped PMMA and integration with plasmonic waveguides. *Optical Materials Express*, *7*(11), 3963.

[20] Lattante, S., De Giorgi, M. L., Pasini, M., & Anni, M. (2017). Low threshold Amplified Spontaneous Emission properties in deep blue of poly[(9,9-dioctylfluorene-2,7-dyil)-alt- p -phenylene] thin films. *Optical Materials*, *72*, 765–768.

[22] Lampert, Z. E., Papanikolas, J. M., Lappi, S. E., & Reynolds, C. L. (2017). Intrinsic gain and gain degradation modulated by excitation pulse width in a semiconducting conjugated polymer. *Optics & Laser Technology*, *94*, 77–85.

[22] Cerdán, L. (2017). Variable Stripe Length method: influence of stripe length choice on measured optical gain. *Optics Letters*, *42*(24), 5258.

[23] Silvestre, I., Marques, P. W. B., Valadares, M., & Cury, L. A. (2008). Gain coefficient method for amplified spontaneous emission in thin waveguided film of a conjugated polymer. *Applied Physics Letters*, *93*(16), 163307.

[24] Hariri, A., & Sarikhani, S. (2015). Application of the geometrically dependent gain coefficient model to describe amplified spontaneous emission behavior in organic solid laser materials: Theoretical considerations. *Journal of Modern Optics*, *62*(10), 822–829.

[25] Kobayashi, T., Flämmich, M., Jordan, G., D'Arcy, R., Rüther, M., Blau, W. J., … Kaino, T. (2006). Blue-green small-signal gain and saturation in a luminescent polymer gain medium. *Applied Physics Letters*, *89*(13), 131119.

[26] Costela, a, García, O., Cerdán, L., García-Moreno, I., & Sastre, R. (2008). Amplified spontaneous emission and optical gain measurements from pyrromethene 567--doped polymer waveguides and quasi-waveguides. *Optics Express*, *16*(10), 7023–7036.

[27] Chénais, S., & Forget, S. (2009). Comment on "Gain coefficient method for amplified spontaneous emission in thin waveguided film of a conjugated polymer" [Appl. Phys. Lett. 93, 163307 (2008)]. *Applied Physics Letters*, *94*(10), 106101.

5 Energy Transfer and Blend Study

5.1 Motivation

As mentioned in Chapter 1, molecular materials, especially conjugated polymers, have the potential to produce lasers and amplifiers for miniaturised optoelectronic applications. While optically pumped devices have been widely demonstrated, however, the major challenge still remains as electrical pumped organic lasing has not been confirmed yet and the key device specifications not directly linked to material properties [1-3]. One of the key issues is combining optical and electronic properties – efficient light emission and current injection. Conventional organic based devices are normally tuned in one aspect – organic light-emitting diodes (OLEDs) have superior light emission while organic field-effect transistors (OFETs) need outstanding charge transport. It is difficult to achieve both simultaneously as high carrier mobility usually quenches exciton luminescence due to cofacial π-electron system to π-electron system interactions [4]. Moreover, tuning electronic properties of conjugated polymers would change the highest occupied and lowest unoccupied molecular orbitals (HOMO and LUMO), which are coupled with emission wavelength and would affect optical gain property [5]. One of the more sensible approaches is to use Förster resonance energy transfer (FRET) in donor-acceptor blends, where donor and acceptor are optimised for transport and emission respectively [5-8]. Electronic properties can be tuned in the donor while leaving the optical properties of the acceptor unaltered. With established experimental techniques and data analysis from Chapter 2 to Chapter 4, a study of donor-acceptor blends would also produce a large scale of comparable data, which is essential to reveal and understand the underlying relationships between material parameter and device performance.

5.2 Energy Transfer Modelling

5.2.1 Donor-acceptor Energy Transfer

There are two common types of energy transfer that may occur in donor-acceptor blends of molecular materials, both of which transfer excited states from donor to acceptor. The first type is radiative energy transfer, where photons emitted by the donor are re-absorbed by the acceptor. The process requires the spectral overlap of the emission spectrum of the donor and the absorption spectrum of the acceptor, and its transfer efficiency depends solely on PLQE of donor and absorption of acceptor – there is no actual interactions between donor and acceptor molecules. In contrast, the second type – resonance energy transfer is an electrodynamic phenomenon without the appearance of a photon, where dipole-dipole interactions between donor molecule in excited state and acceptor molecule in ground state [9-12]. The theory of resonance energy transfer is based on an isolating dipole exchange energy with another dipole with a similar resonance frequency, which requires the same extend of spectral overlap as radiative transfer but also depends upon other material properties such as refractive index, PLQE, excited state lifetime. However, the resonance energy transfer rate is also dependent on the relative orientation of the donor and acceptor transition dipoles, and the distance r between the donor and acceptor molecules. For simplicity, Förster distance R_0 (typically in nm) is defined as the distance at which 50% of donor excited state is transferred to acceptor, and the transfer efficiency is proportional to $(R_0/r)^6$. Distance r can be fine-tuned by varying blend concentration ratios while R_0 remains constant for a donor-acceptor pair. Since resonance energy transfer is competing with PL of the donor, a shorter r gives faster transfer rate thus shorter donor lifetime. To comprehensively study energy transfer in transient regime, research

work in this chapter encompass the methodology from Chapter 2 to Chapter 4 – photo-physics measurements, rate equation model and ASE measurements. Note Dexter energy transfer is not considered in this thesis as it requires very small intermolecular distance (in Å) [13].

Materials used in this chapter are F8BT, RedF, SC5A and SpL (Figure 5.1). SpL is a ladder-type monodisperse oligo(*p*-phenylene) that can also be solution processed just as the other conjugated polymers [14,15]. Normalised UV-Vis absorbance and PL emission are plotted in Figure 5.2. F8BT and RedF have very similar chemical structures thus similar absorption peak, but RedF has an additional absorption peak at $550\ nm$, which is right at F8BT emission peak. It should be noted that both F8BT and RedF molecules are excited together when pumping the blend, thus emission from RedF comes from both direct excitation and energy transfer. This effect is negligible when RedF concentration is small. On the other hand, SC5A and SpL are completely different materials. The SC5A emission between $400 - 450\ nm$ overlaps with SpL absorption. Meanwhile pumping SC5A at $350 - 380\ nm$ would hardly excite SpL molecules. Overall, both pairs have the required overlap to achieve energy transfer. In practical analysis, F8BT:RedF should be easier to separate emission while SC5A:SpL is better at separating excitation.

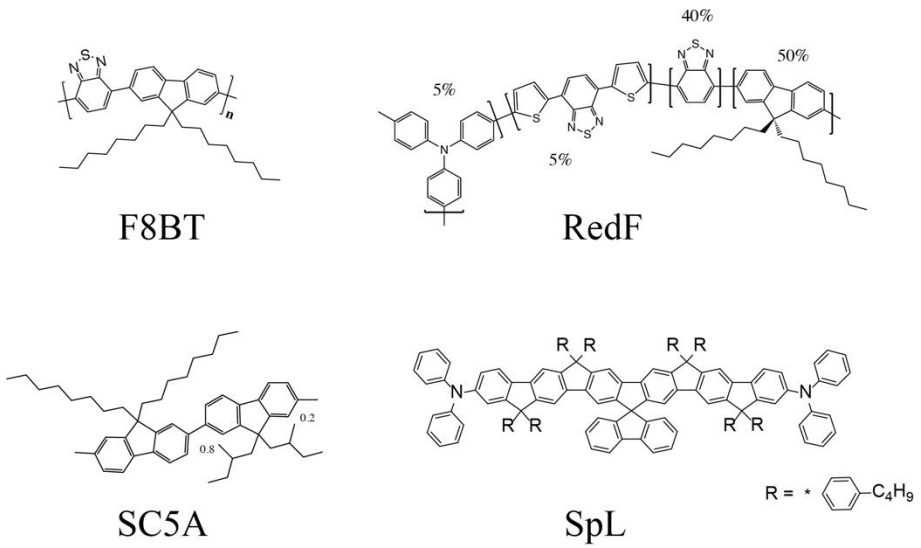


Figure 5.1 – Chemical structures of conjugated polymers studied as donor-acceptor blends.

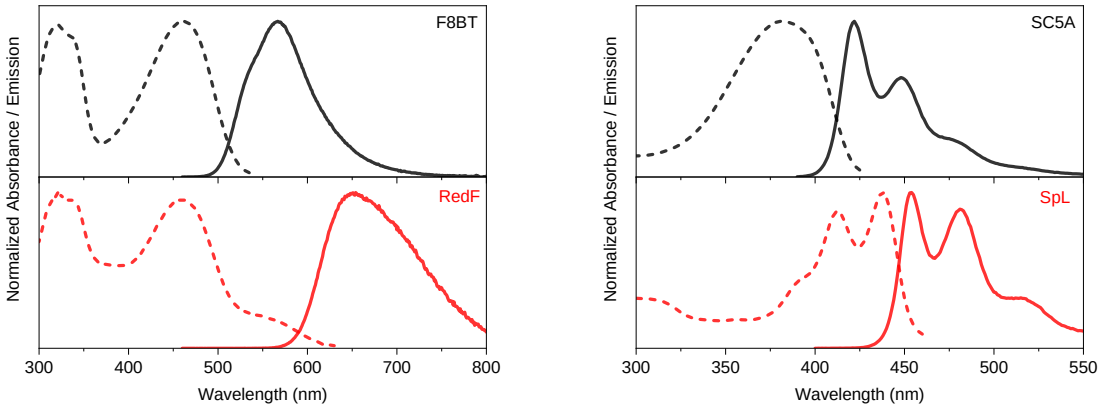


Figure 5.2 – Normalised absorbance (dashed) and photoluminescence (solid) spectra of two pairs of donor-acceptor blends – F8BT:RedF and SC5A:SpL. The PL measurement used the following excitation wavelength – F8BT and RedF at 450 nm, SC5A and SpL at 380 nm.

5.2.2 Rate Equation Model – 2-Level System

This section uses model simulation to help understand the possible effect of donor-acceptor energy transfer may have on molecular thin-film samples. Since radiative energy transfer does not affect transient dynamics of materials, only resonance energy transfer is considered here. With donor-acceptor blend, the excited state decay mechanism in Equation (2.4) becomes

$$\frac{dN_D(t)}{dt} = -k_D N_D(t) - k_{DA} N_D(t) + k_{AD} N_A(t) \tag{5.1}$$

$$\frac{dN_A(t)}{dt} = -k_A N_A(t) + k_{DA} N_D(t) - k_{AD} N_A(t) \tag{5.2}$$

where $k_D = 1/\tau_D$ and $k_A = 1/\tau_A$ are intrinsic excited state decay rates without energy transfer, k_{DA} and k_{AD} are forward and reverse energy transfer rates. Substitute Equation (5.1) and (5.2) into the 2-level rate equation model in Chapter 3.2, the new model with forward and reverse resonance energy transfer can be written as

$$\begin{aligned}\frac{dN_{D2}(t,z)}{dt} = \sigma_{pD} I_p N_{D0} - \frac{N_{D2}(t,z)}{\tau_{D2}} - k_{DA} N_{D2}(t,z) + k_{AD} N_{A2}(t,z) \\ - v_g \sigma_{eD} (N_{D2}(t,z) - N_{D1}(t,z)) S_D(t,z)\end{aligned} \tag{5.3}$$

$$\frac{dN_{D1}(t,z)}{dt} = \frac{N_{D2}(t,z)}{\tau_{D2}} + v_g \sigma_{eD} \big(N_{D2}(t,z) - N_{D1}(t,z)\big) S_D(t,z) - \frac{N_{D1}(t,z)}{\tau_{D1}} \tag{5.4}$$

$$\begin{aligned}\frac{\partial S_D(t,z)}{\partial t} + v_g \frac{\partial S_D(t,z)}{\partial z} \\ = \Gamma \left[\beta_D \frac{N_{D2}(t,z)}{\tau_2} + v_g \sigma_{eD} (N_{D2}(t,z) - N_{D1}(t,z)) S_D(t,z) \right]\end{aligned} \tag{5.5}$$

$$\begin{aligned}\frac{dN_{A2}(t,z)}{dt} = \sigma_{pA} I_p N_{A0} - \frac{N_{A2}(t,z)}{\tau_{A2}} + k_{DA} N_{D2}(t,z) - k_{AD} N_{A2}(t,z) \\ - v_g \sigma_{eA} (N_{A2}(t,z) - N_{A1}(t,z)) S_A(t,z)\end{aligned} \tag{5.6}$$

$$\frac{dN_{A1}(t,z)}{dt} = \frac{N_{A2}(t,z)}{\tau_{A2}} + v_g \sigma_{eA} \big(N_{A2}(t,z) - N_{A1}(t,z)\big) S_A(t,z) - \frac{N_{A1}(t,z)}{\tau_{A1}} \tag{5.7}$$

$$\frac{\partial S_A(t,z)}{\partial t} + v_g \frac{\partial S_A(t,z)}{\partial z}$$

$$= \Gamma \left[\beta_A \frac{N_{A2}(t,z)}{\tau_{A2}} + v_g \sigma_{eA} (N_{A2}(t,z) - N_{A1}(t,z)) S_A(t,z) \right] \tag{5.8}$$

For simplicity, this model assumes single-pass travelling wave in photon equation and all losses are not considered here. Comparing this model with the one in Chapter 3.2, the only difference appears in excited state rate equation (both donor N_{D2} and acceptor N_{A2}). Therefore, it is the change of excited state lifetime that affects stimulated emission in a donor-acceptor blend (assuming absorption is sufficient) and solving Equation (5.3) and (5.6) becomes the key to understand the effect of energy transfer. Unfortunately, neither resonance energy transfer nor stimulated emission is a linear process and it is hard to find solutions to with two nonlinear terms. As a result, excited state equation is solved in PL without stimulated emission – both numerical simulation and analytical solution are obtained, and double checked. Note that the model used here also carries the same assumptions that applied in Chapter 3.2 – for example, triplets and polarons are not considered, which may have more complicated effects in blends, but the model is still a first approximation.

5.2.3 Donor-Acceptor Resonance Energy Transfer Analytical Solution

The rate equation model of donor-acceptor blends (Equation (5.1) and (5.2)) can be solved numerically just as the 2-level model in Chapter 3.2, it can also be estimated by convolution approach [17]. In Matlab simulation, both numerical and analytical solutions give the same result of excited state density thus deemed valid (Appendix 5A). For materials used in this Chapter, as in Figure 5.2, the spectral overlap of reverse energy transfer is minor, and it is appropriate to assume $k_{AD} = 0$. Consider forward transfer rate $k_{DA}(t) = \mathrm{A}_{DA} t^{-\frac{1}{2}}$ where

$A_{DA} \propto r^{-6}$ is governed by blend concentration in a given donor-acceptor pair [10,16]. Then Equation (5.1) and (5.2) become

$$\frac{dN_D(t)}{dt} = -k_D N_D(t) - A_{DA} t^{-\frac{1}{2}} N_D(t) \tag{5.9}$$

$$\frac{dN_A(t)}{dt} = -k_A N_A(t) + A_{DA} t^{-\frac{1}{2}} N_D(t) \tag{5.10}$$

Assuming only donor is pumped directly, initial conditions are set to $N_D(0) = 1$ and $N_A(0) = 0$. Then Equation (5.9) and (5.10) can be solved as

$$N_D(t) = e^{-k_D t} e^{-2A_{DA} t^{\frac{1}{2}}} \tag{5.11}$$

$$N_A(t) = \int_0^t e^{-k_A(t-t')} \left[A_{DA} t'^{-\frac{1}{2}} N_D(t') \right] dt' \tag{5.12}$$

Equation (5.11) shows that lifetime of the donor must become shorter when energy transfer is present, while Equation (5.12) suggests acceptor lifetime does not change (term $\left[A_{DA} t'^{-\frac{1}{2}} N_D(t') \right]$ can be considered as pump $g(t')$ in Equation (2.6)). Therefore, the transient response of excited states density would be a useful indicator to check whether resonance energy transfer is resonance.

5.3 Photo-physics and Energy Transfer of Polymer Blends

5.3.1 Sample Preparation

As mentioned in Chapter 5.2.1, F8BT:RedF and SC5A:SpL polymer blends were studied in thin-film structures. All samples are spin-coated thin-films made inside a fume hood in a high

pressure semi-clean room as detailed in Chapter 2.2. Materials were used as received and solved in Chlorobenzene as follows – F8BT 2.4 ml at 30 mg/ml, RedF 0.9 ml at 30 mg/ml, SC5A 2.5 ml at 20 mg/ml, SpL 0.3 ml at 40 mg/ml. Solutions were stirred and heated overnight and were then diluted down for blending (stirred and heated for 2 hours). For F8BT:RedF blends, solutions F8BT 2.4 ml at 30 mg/ml, RedF 0.8 ml at 30 mg/ml, RedF 0.2 ml at 6 mg/ml, RedF 1 ml at 1.2 mg/ml were blended in weight as $(1-x)$F8BT:xRedF where x = 0%, 0.1%, 0.2%, 0.4%, 0.8%, 1%, 2%, 4%, 8%, 10%, 20%, 40%, 80%, 100%. For SC5A:SpL blends, solutions SC5A 2.5 ml at 20 mg/ml, SpL 0.25 ml at 40 mg/ml, SpL 0.1 ml at 10 mg/ml, SpL 0.1 ml at 1 mg/ml were blended in weight as $(1-x)$SC5A:xSpL where x = 0%, 0.1%, 0.2%, 0.4%, 0.8%, 1%, 2%, 4%, 8%, 10%, 100%. Unlike F8BT:RedF which has a continuous set, SC5A:SpL has a gap between 10% and 100% due to limited amount of SpL material. Therefore, all spectra of 100% SpL sample are plotted in a different colour for clarity. All solutions were again stirred and heated overnight before cooling down to room temperature for spin-coating. For both blends, thin-films were formed by solution spun at 2000rpm for 1 minute. While an additional set of thin samples (5000rpm) were made as a backup, all measurements presented in this Chapter were based on 2000rpm samples.

Film quality was checked by atomic force microscope (AFM) and optical microscope to ensure a flat surface and minimal roughness. AFM measurements were measured in tapping mode with a resolution of 0.5 nm in relative height. All samples show a uniform morphology and the standard deviation in height is about 1 nm (Appendix 5B). This is also confirmed by images captured under an optical microscope with resolution of 2 μm – the films have plain surface and are featureless at cross-polarisation (Appendix 5C).

5.3.2 Photo-physics Characterisation

Since the first photo-physics measurement, UV-Vis spectroscopy was recorded as in Chapter 2.3.1. Transmittance was measured directly, and absorbance was calculated by Equation (2.1). The absorbance spectra of blends should equal the superposition of the two constituents, i.e.

$$A_{blend} = (1 - x)A_{donor} + xA_{acceptor} \tag{5.13}$$

Figure 5.3 shows transmittance and absorbance spectra of F8BT:RedF thin-films. The transmittance has clear Fabry-Pérot oscillations ($> 550\ nm$) and touches the spectra of quartz, ensuring good film quality with no scattering as explained in Figure 2.3. While F8BT and RedF have absorption peaks at $210, 330, 450nm$, the RedF exclusive peak at $540nm$ is changing proportionally with the increasing x. It is noted that in this case RedF is significantly thicker than F8BT under the same conditions, probably due to different molecular weights. However, it is appropriate to assume that all $(1 - x)$F8BT:xRedF thin-films have the same thickness when $x \leq 10\%$. The thickness is estimated to be $200 - 220\ nm$ by Equation (2.2). The absorbance spectra of $x =$ 10%, 20%, 40%, 80% is also checked against Equation (5.13) as $A_{blend} = (1 - x)A_{F8BT} + xA_{RedF}$. The height of absorption peak is matched by calculated ones, which means this set of samples are reliable (Appendix 5D).

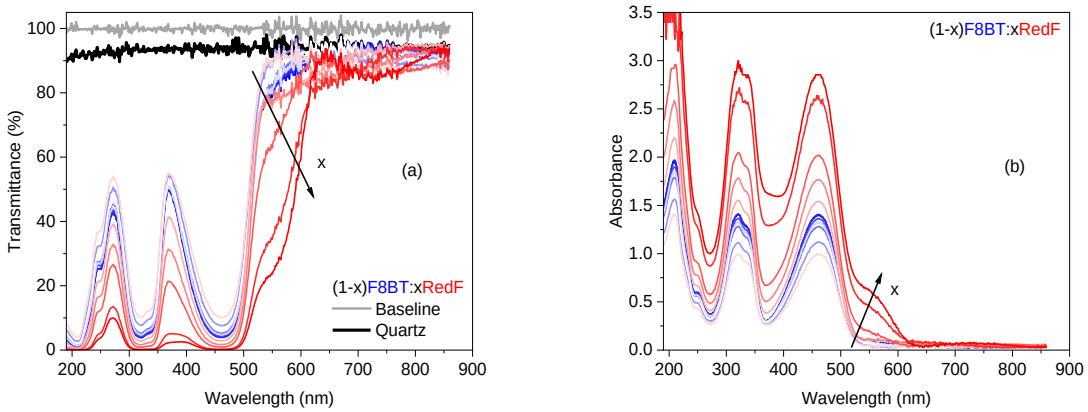


Figure 5.3– (a) UV-Vis transmittance of F8BT:RedF thin-films. Fabry-Pérot oscillation ($> 550\,nm$) shows good film quality. F8BT and RedF have almost identical absorption peaks (except $540\,nm$ for RedF) as most of their chemical structures are the same. (b) Calculated absorbance of F8BT:RedF by Equation (2.1). The RedF peak at $540\,nm$ is increasing with RedF concentration. Film thicknesses estimated by Equation (2.2) range from $200\,nm$ to $400nnm$, with the majority around $200 - 220\,nm$ (when $x \leq 10\%$).

Figure 5.4 plots transmittance and absorbance spectra of SC5A:SpL thin-films. Again, the Fabry-Pérot oscillations ($> 480\,nm$) indicates good film quality. SC5A shows typical polyfluorene spectrum with main absorption peaked at $380\,nm$. On the other hand, SpL, as a ladder-type macro-molecule, features sharp and distinct vibronic absorption peaks due to its rigid structure. Comparing with SC5A, the absorption of SpL is red-shifted by about $50nm$. Since the highest acceptor concentration is $x = 10\%$, all samples can be assumed to have the same thickness about $170 - 210\,nm$, estimated by Equation (2.2). Superposition of absorbance also works in this case – the absorbance spectrum for $x = 10\%$ equals to the calculated $A_{blend} = (1 - x)A_{SC5A} + xA_{SpL}$ (Appendix 5D). It is noted that the SC5A film here is thicker than the one in Chapter 4.5.1 where the solvent is P-xylene instead of Chlorobenzene – Chlorobenzene tend to produce thicker film than P-xylene (as in Appendix 4B SC5A(a)). They were also prepared in different set-ups. Apart from difference in thickness, both films have good optical quality and can produce reliable ASE results.

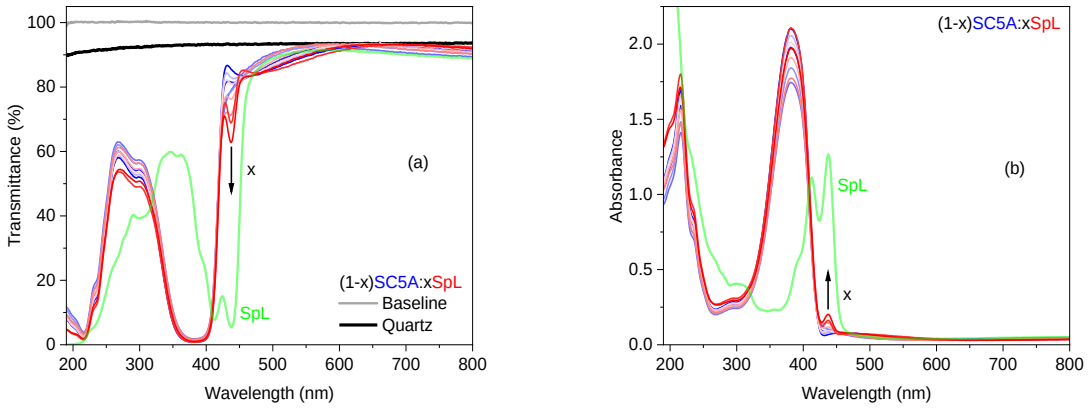


Figure 5.4 – (a) UV-Vis transmittance of SC5A:SpL thin-films. Fabry-Pérot oscillation ($> 480nm$) shows good film quality. SC5A (polymer) and SpL (macro-molecules) have very different absorption peaks with SpL having sharper vibronic peaks mirroring emission as seen in Figure 5.2, while SC5A shows typical polyfluorene spectrum. (b) Calculated absorbance of SC5A:SpL by Equation (2.1). The SpL peak at $438nm$ is increasing with SpL concentration. Film thickness of blends estimated by Equation (2.2) is $170 - 210\ nm$, which is thicker than the SC5A sample used in Chapter 4.5.1. This is because solvent Chlorobenzene tend to produce thicker film than P-xylene (as in Appendix 4B SC5A(a)).

Photoluminescence (PL) spectroscopy was measured and presented as in Chapter 2.3.2. Figure 5.5 shows the evolution of PL spectra of both blends. Excitation wavelength were chosen at absorption peak of donors respectively (F8BT and SC5A). F8BT:RedF blends were pumped at $450\ nm$ and SC5A:SpL blends were pumped at $380\ nm$. Both spectra show a gradual shift from donor emission to acceptor emission and the trend is confirmed by the set of thin samples. Employing a Jacobian conversion from wavelength to energy scale, the spectra were fitted to multiple Gaussian peaks and emission percentages of donor and acceptor were plotted in Figure 5.6. The percentage seems to be increasing linearly versus acceptor concentration on a semi-log scale. For F8BT:RedF, acceptor dominates over 90% of total emission when acceptor concentration $x \geq 4\%$ while for SC5A:SpL the energy transfer is faster and the equivalent just needs $x \geq 2\%$. Since the emission is clearly not proportional to blend concertation, energy transfer from donor to acceptor is likely to be the key. At this stage, it is not evident whether

radiative and/or resonance energy transfer plays the role here.

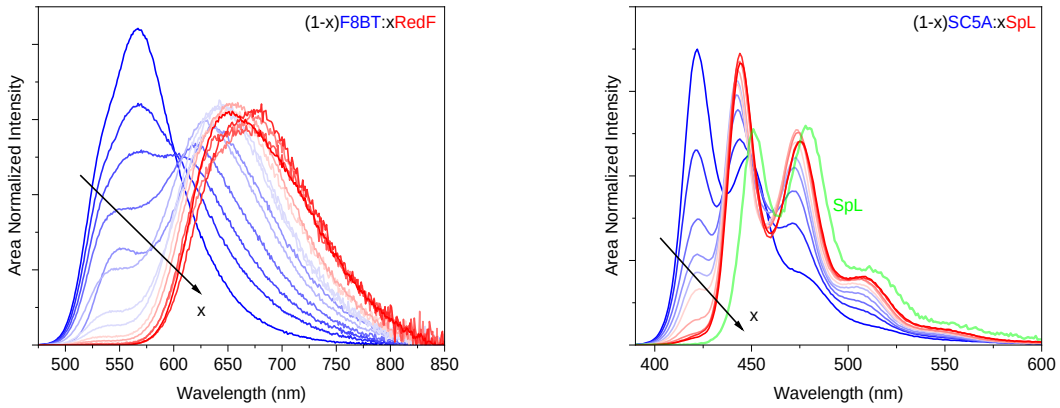


Figure 5.5 – Area normalised PL spectra of F8BT:RedF (pumped at 450 nm) and SC5A:SpL (pumped at 380 nm) measured as in Chapter 2.3.2. Since acceptor concentration increases, PL spectrum gradually shifts from donor (F8BT, SC5A) to acceptor (RedF, SpL). Note the change of PL is faster than change of UV-Vis in Figure 5.4, indicating energy transfer is taking place from donor to acceptor.

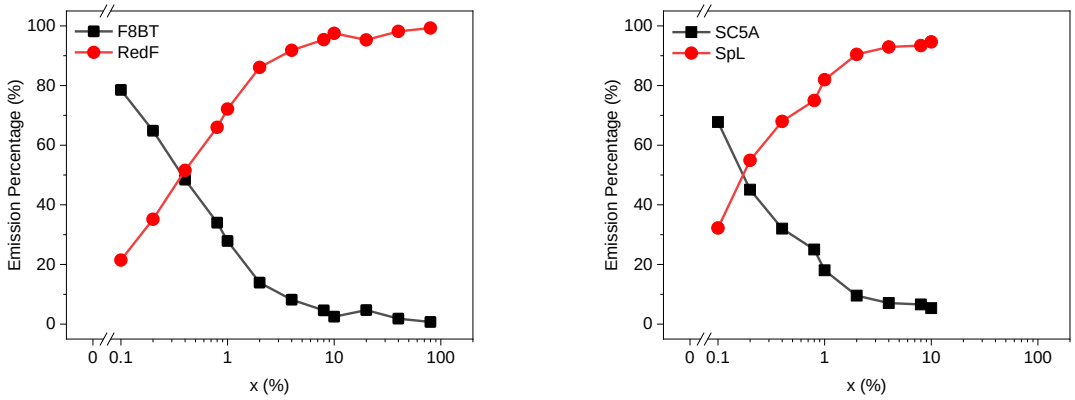


Figure 5.6 – Emission percentages of two species (donor and acceptor) extracted from curve fitting in Figure 5.5. SC5A:SpL blends have faster energy transfer than F8BT:RedF blends.

Photoluminescence quantum efficiency (PLQE) of both blends was measured using the de Mello method as in Chapter 2.3.3. Excitation wavelength was kept the same as PL measurement. In Figure 5.7, F8BT:RedF samples show a linear trend of PLQE – F8BT is 37%, RedF is 20% and the blend samples linearly distribute between the two constituents on a semi-log scale. However, for SC5A:SpL samples, while SC5A is 38% and SpL is 5%, the highest

PLQE is 52% when $x = 1\%$ – higher than both constituents. The PLQE figures were double-checked with a set of thin samples. This observation indicates that energy transfer is resonance, since radiative energy transfer would only decrease the overall PLQE as absorption and emission happen twice. Figure 5.7 proves that resonance energy transfer is an effective way to fine-tune PLQE without altering the emission spectrum.

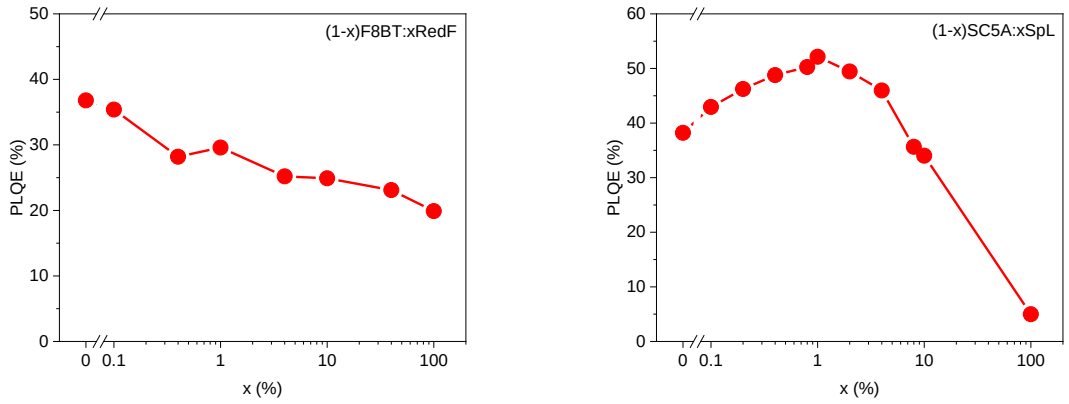


Figure 5.7 – PLQE measured and calculated as in Chapter 2.3.3. F8BT:RedF blends pumped at 450 nm and SC5A:SpL blends pumped at 380 nm. In F8BT:RedF, PLQE of blends sit linearly between the two constituents while SC5A:SpL blends can have higher PLQE than both donor and acceptor.

5.3.3 Photoluminescence Lifetime Characterisation

Transient photoluminescence spectroscopy was employed using the streak camera as in Chapter 2.4. Again, the excitation wavelength was chosen as the donor absorption peak. F8BT:RedF blends were pumped by 465 nm laser and measured in a 288 nm spectral range. Signals were collected in a 5 ns window, which is much shorter than the 20 ns used for F8BT in Figure 2.13. This was chosen because energy transfer is expected to be much faster than photoluminescence of F8BT itself. As in Equation (5.11), the shortening of donor lifetime is the key to study resonance energy transfer, the shorter time range is necessary to quantitatively determine the transfer rate. Similarly, SC5A:SpL blends were pumped at 379 nm and

measured over a 96 nm spectral range. The signal collection time range for this pair is 2 ns, which suits the fast decay of blue polyfluorenes and the even faster energy transfer. Figure 5.8 shows the area normalised streak camera spectra of both blends. Despite the short time range, the spectra are very similar to the steady state PL spectra in Figure 5.5, which means the $5/2$ ns time range is sufficient to collect most photons. The spectra once again confirm that emission from acceptor species is disproportionally more than its absorption. It is very efficient for a small amount of acceptor to receive a large fraction of excitons from the donor in a very short time.

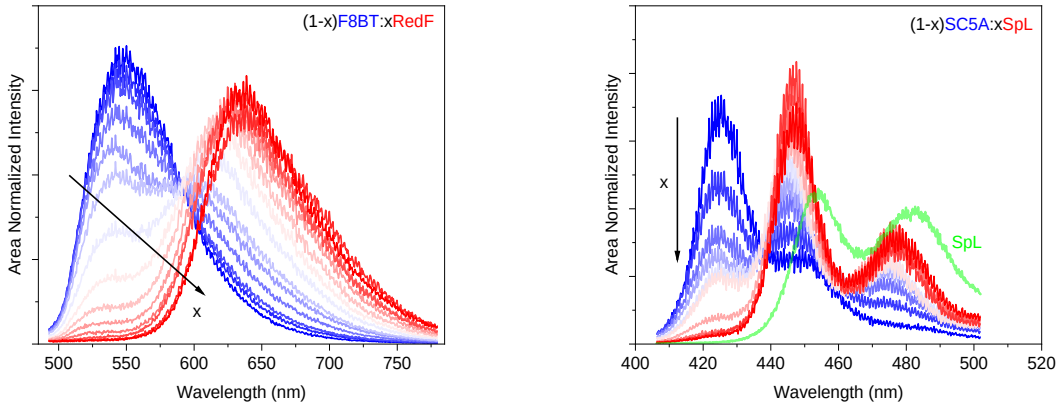


Figure 5.8 – Area normalised spectra measured from streak camera as in Chapter 2.4.2. F8BT:RedF blends pumped at 465 nm and collected in 5 ns, and SC5A:SpL blends pumped at 379 nm and collected in 2ns. The spectra show similar trend as in Figure 5.5 indicating energy transfer from donor to acceptor.

From the spectra, donor and acceptor emission regions can be identified respectively, which provides a way to decouple the donor and acceptor transient response. For F8BT:RedF blends, the signal at 542 nm is considered as pure F8BT emission while the 658 nm is for RedF (although still with a little emission from the other). The decay was extracted from a 40 nm width binned wavelengths range, which has enough signal but not too much noise from other emitting species. Figure 5.9 plots the fluorescent decay for F8BT (542 nm) and RedF (658 nm)

respectively. Since acceptor concentration (RedF) increases, donor lifetime (F8BT) becomes substantially shorter, approaching the response of excitation beam (laser signal). Moreover, the acceptor lifetime does not show any significant change except the onset is quicker for higher concentration. Consider energy transfer as a secondary pump to the acceptor, this means that higher acceptor concentration gives faster energy transfer. With evidence from time resolved decay curves, energy transfer in F8BT:RedF blends is confirmed to be resonance.

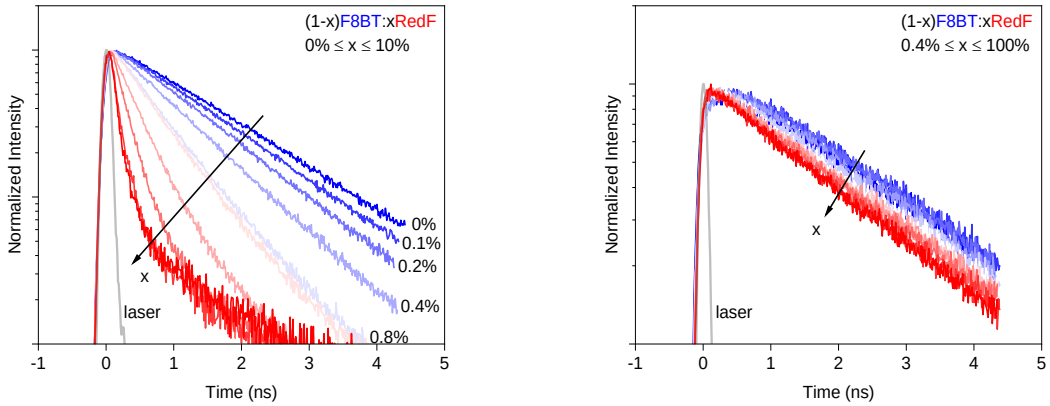


Figure 5.9 – F8BT:RedF blends normalised decay at $542\ nm$ and $658\ nm$, binned with $40\ nm$ width from streak camera data. F8BT peak ($542\ nm$) has shorter lifetime with increasing RedF concentration while RedF peak ($658\ nm$) shows faster onset, both of which indicates energy transfer from F8BT to RedF.

For SC5A:SpL blends, binned wavelengths at $420\ nm$ is considered as the pure SC5A emission and $480\ nm$ as SpL emission. The width of binned wavelengths is adjusted to $20\ nm$ to suit the narrow emission peaks. Figure 5.10 plots the fluorescent decay for SC5A ($420\ nm$) and SpL ($480\ nm$) respectively. Again, the donor lifetime (SC5A) is shortened by the presence of acceptor (SpL), indicating resonance energy transfer. However, the acceptor lifetime is tricky to analyse as the $480\ nm$ band contains a significant fraction of SC5A emission. What can be confirmed is that the lifetime of SpL in blends is longer than pure SpL thin-film (also longer than pure SC5A thin-film). This is consistent with PLQE result in Figure 5.7 – assuming

non-radiative rate does not change, the fluorescent lifetime $\tau_{blends} > \tau_{SC5A} > \tau_{SpL}$ implies $\eta_{blends} > \eta_{SC5A} > \eta_{SpL}$. Streak camera measurements were also taken on the set of thin samples, which confirmed the results.

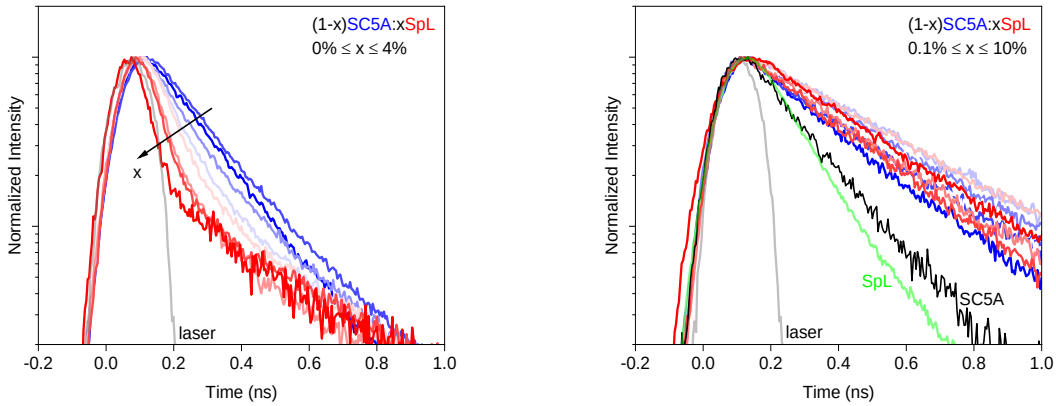


Figure 5.10 – SC5A:SpL blends normalised decay at $420\,nm$ and $480\,nm$, binned with $20\,nm$ width from streak camera data. SC5A peak ($420\,nm$) has shorter lifetime with increasing SpL concentration, showing energy transfer from SC5A to SpL. However, the SpL peak ($480\,nm$) also has a significant fraction of SC5A peak and its trend is tricky. The only confirmation for this peak is that $\tau_{blends} > \tau_{SC5A} > \tau_{SpL}$ is consistent with $\eta_{blends} > \eta_{SC5A} > \eta_{SpL}$.

In both Figures 5.9 and 5.10, the donor decay shows a clear trend and better reliability. The donor lifetime was extracted by curve fitting using single exponential method in Chapter 2.4.5. Note the decay is not single exponential as energy transfer is a non-linear process. The extracted lifetime is the explicit (average) donor lifetime, which has already included the effect of energy transfer. It would give an idea of how fast energy transfer is comparing with photoluminescence. Figure 5.11 plots the extracted donor lifetime for F8BT:RedF and SC5A:SpL. Both F8BT and SC5A lifetime decreases dramatically from their intrinsic lifetimes – energy transfer is the dominant process taking place in the ps time scale – much shorter than the ns photoluminescence.

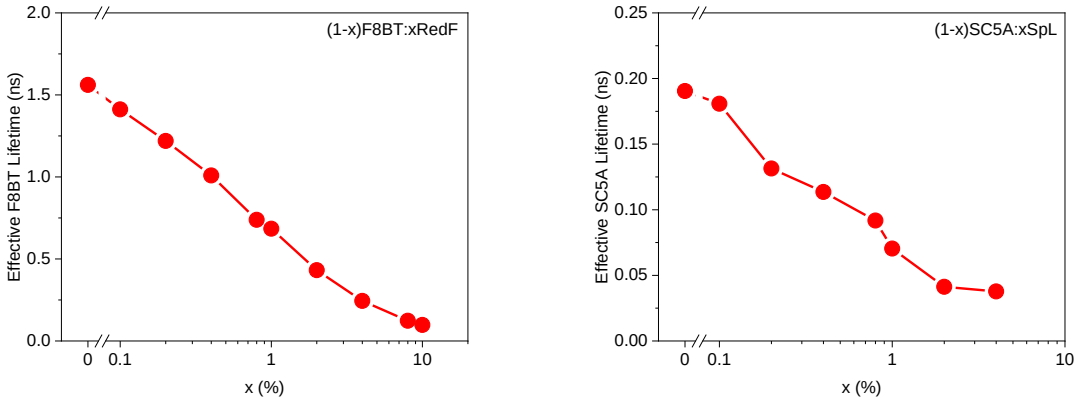


Figure 5.11 – Binned donor lifetime in blends extracted by single exponential method in Chapter 2.4.5. Note the lifetime is subject to energy transfer rate and is not single exponential, which is the average expression of effective donor lifetime. The fitting is restricted in the 'single exponential' region of the raw data. The shortening indicates that the energy transfer is resonance, not radiative.

5.3.4 Energy Transfer Rate

Donor decays in Figure 5.9 and 5.10 can also be used to extract energy transfer rates. The donor rate equation solved as Equation (5.11) is more appropriate to replace the single exponential decay in Chapter 2.4.5 and extract energy transfer rate A_{DA}. Since different blends have very different lifetime, the actual data for curve fitting was cropped within the time range to maintain the same orders of magnitude in decay for each curve. Only in this way can the extracted lifetime be compared with each other. Furthermore, to ensure the reliability of extracting lifetime from these very fast decays that approach the limit of streak camera set-up, curve fitting was tried for several rounds using different orders of decay using the method in Chapter 2.4, and the final result is an average of all good fits with error bars. Figure 5.12 plots extracted energy transfer rate A_{DA} in F8BT:RedF blends against acceptor concentration. The rate increases with acceptor concentration in a non-linear pace and seems to saturate at 2.5 when $x = 10\%$. Similarly, Figure 5.13 plots A_{DA} in SC5A:SpL blends, which again increases

with acceptor concentration in a non-linear pace and seems to saturate at 3.5 when $x = 2\%$. Note that the rate at $x = 4\%$ is not reliable as the resolution may be limited by the 379 nm laser (FWHM $0.12ns$). Nevertheless, this is consistent with results from PL spectra (Figure 5.5) that energy transfer in SC5A:SpL is faster than F8BT:RedF and lower acceptor concentration is needed. More work needs to be done to fully understand the link between transfer rate and material properties.

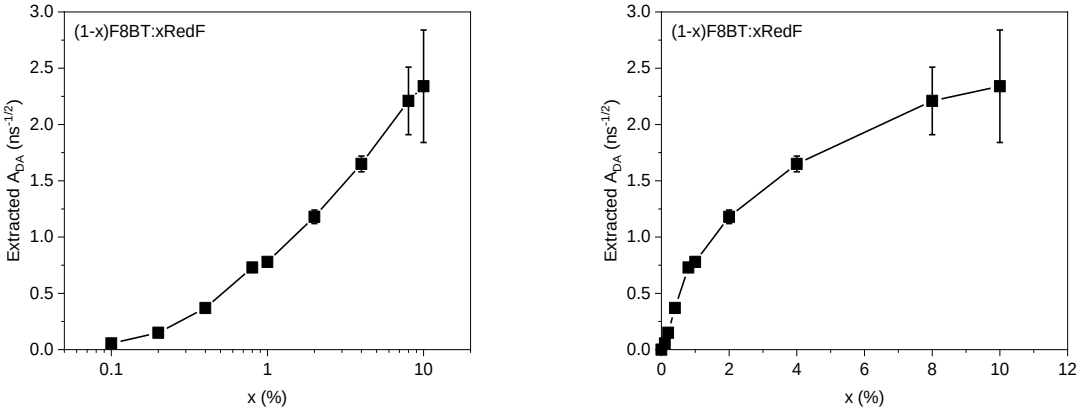


Figure 5.12 – Extracted energy transfer rate A_{DA} of F8BT:RedF blends by fitting decay of F8BT peak to Equation (5.11). Result plotted on both semi-log and linear scales. Higher RedF concentration results in higher energy transfer rate, which seems to be saturated at 2.5 when $x = 10\%$.

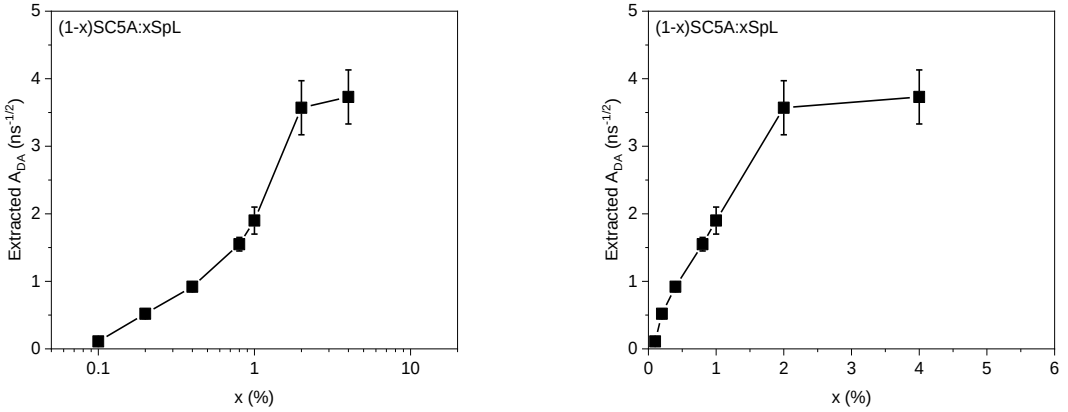


Figure 5.13 – Extracted energy transfer rate A_{DA} of SC5A:SpL blends by fitting decay of SC5A peak to Equation (5.11). Result plotted on both semi-log and linear scales. Higher SpL

concentration results in higher energy transfer rate, which seems to be saturated at 3.5 around $x = 2\%$ but also can be limited by the set-up.

5.4 ASE and Gain Characterisation of Polymer Blends SC5A:SpL

5.4.1 ASE Energy Response

Amplified spontaneous emission (ASE) was performed as in Chapter 4.2. Due to the availability of the $355\ nm$ laser, only SC5A:SpL blends were measured. First, ASE energy response $I(I_p)$ were investigated using a fixed rectangular laser stripe of $4mm \times 0.1mm$ for all samples (Appendix 4A). Figure 5.14 plots normalised ASE spectra (TE mode) and peak positions of all samples pumped at $200\ \mu J\ cm^{-2}$. When SpL concentration is low ($x \leq 0.4\%$), ASE peak is SC5A 0-1 peak near $450\ nm$. When SpL concentration becomes higher ($x \geq 0.8\%$), ASE peak is SpL 0-1 peak near $480\ nm$. This is due to energy transfer from SC5A to SpL, which moves most population inversion to the 0-1 peak of SpL. The change of emission peak in the ASE requires higher SpL concentration than PL where $0.1\% - 0.2\%$ SpL is enough to activate energy transfer. The reason is that ASE requires energy transfer to happen in a short time (in ps as in Chapter 3.2), while PL lifetime is typically in ns for these molecular materials. Therefore, higher concentration of SpL is essential to achieve the required higher energy transfer rate for ASE. Note the 0.4% blend has ASE from both peaks, which will be investigated later.

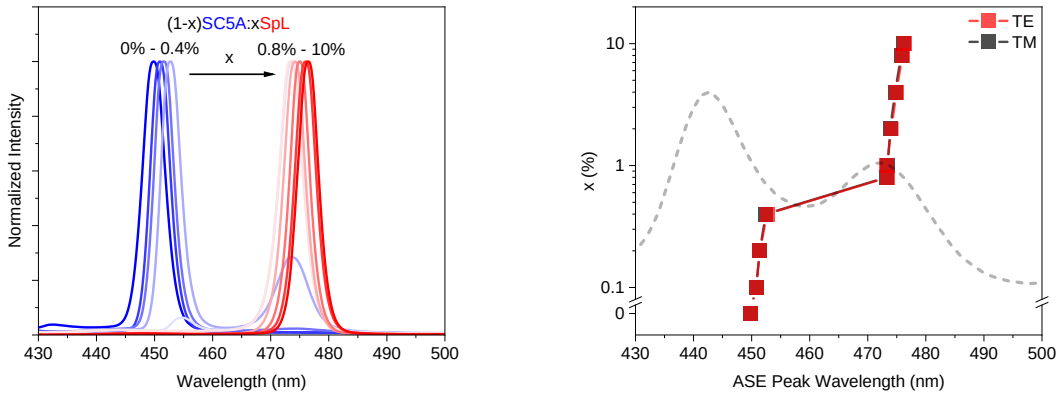


Figure 5.14 – SC5A:SpL blends normalised ASE spectra in TE mode (collected at 200 $\mu J\ cm^{-2}$ pump energy). Most stimulated emission moves from SC5A 0-1 peak to SpL 0-1 peak between 0.4% and 0.8%, which is later than the similar move in PL between 0.1% and 0.2%. Note the 0.4% blend has ASE from both peaks and its PL spectrum is plotted in dashed grey for reference.

As mentioned in Chapter 4.3.1, ASE threshold is determined by fitting the linear PL region and exponential ASE region, and spontaneous emission factor β is extracted by the difference of PL and saturation. Figure 5.15 plots the energy response of SC5A:2%SpL in TE mode at SpL 0-1 peak as an example and then compares the threshold of all samples. For SC5A 0-1 peak, the threshold is always increasing with SpL concentration x due to the decrease of SC5A lifetime as a donor (Figure 5.11) as well as SC5A emission being absorbed by SpL (Figure 5.2). As discussed in Chapter 3.2, both shorter PL lifetime and absorption contribute to a higher ASE threshold. For SpL 0-1 peak, the threshold reaches its lowest value 9.75 $\mu J\ cm^{-2}$ at 2% blend. Both TE and TM modes have the same trend. Note ASE threshold is comparable here as all samples were measured under the same conditions. Figure 5.16 compares spontaneous emission factor β of all samples. β is studied in the fundamental TE mode only as TM mode requires higher pump energy to achieve saturation and is highly unstable as it loses out to TE mode in saturation region (On the contrary, ASE thresholds for both TE and TM modes are reliable as mode competition is not intense when ASE is just turned on). For SC5A 0-1 peak,

β increases with SpL concentration x – similar to ASE threshold. For SpL 0-1 peak, β shows the opposite trend as ASE threshold – 1% blend has the highest β of 0.0183 and 10% blend has the lowest β of 0.0602. However, only β from SpL 0-1 peak is useful where both PL and ASE are from SpL molecules, while β from SC5A 0-1 peak is complicate to analyse – take the 0.2% blend as an example, most of its PL is from SpL but ASE from SC5A. Note β cannot be extracted for 0.4% blend, which will be explained later. Combining Figure 5.15 and 5.16, PLQE η (measured in steady state in Figure 5.7) is found to be proportional to β but inversely proportional to ASE threshold. This is consistent with the definition $\beta = \Omega\eta$ in the rate equation model (Chapter 3.2.1) – the fraction of guided spontaneous emission Ω for SpL 0-1 peak is constant as SpL lifetime does not change noticeably in different blends (Figure 5.10) and all other physical parameters (e.g. sample thickness, refractive index, absorption) do not change much either when SpL is the minority less than 10%. Note there is a slight shift between the highest PLQE at 1% and the lowest ASE threshold at 2%. This is because PLQE integrating sphere (Chapter 2.3.3) measures the sample face emission in steady state (spectrum similar to isolated single molecule emission) while ASE set-up measures guided emission in ps time scale (Chapter 3.2.2), which has a red-shifted spectrum (Appendix 5E). For a similar reason, the β curve is not as stable or precise as PLQE η because guided emission is extremely sensitive to both film quality and experimental set-up, especially in PL region where the less directional emission requires more accurate collection optics. In conclusion, higher PLQE (in guided and transient conditions) is desired for lower ASE threshold. By blending 2% SpL with SC5A, ASE threshold is reduced by more than 50%.

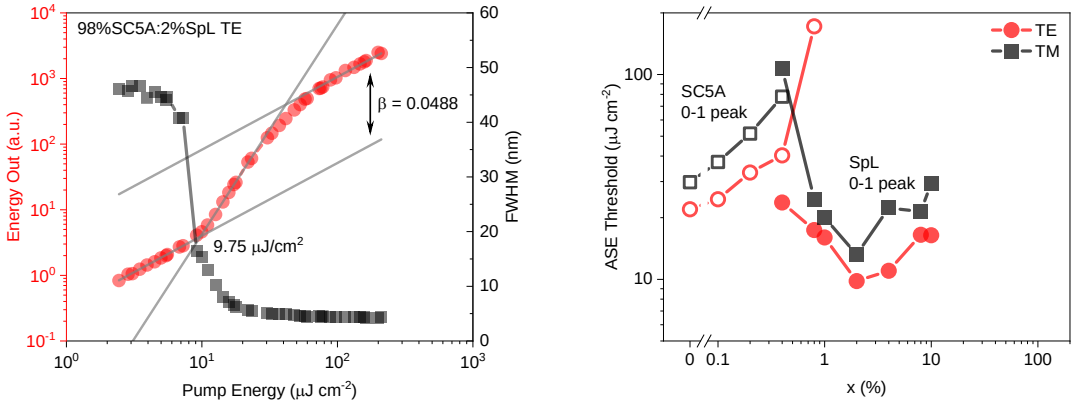


Figure 5.15 – ASE energy response of 2% blend at SpL 0-1 peak, which has lowest ASE threshold in TE mode. Spontaneous emission factor β is also extracted. By comparing ASE threshold in different blends, as SpL concentration increases, the SC5A peak always has higher threshold while the SpL peak has the minimum threshold at 2% for both TE and TM modes.

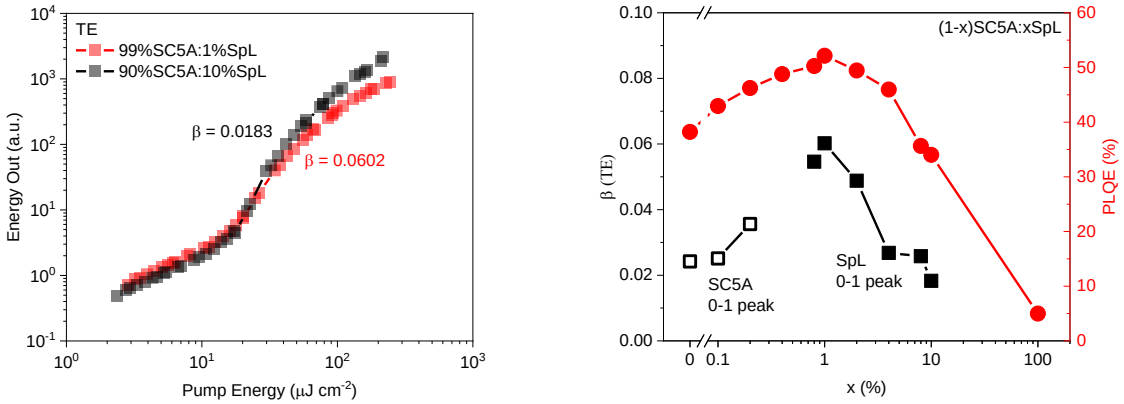


Figure 5.16 – Compare energy response of 1% and 10% blends at SpL 0-1 peak in TE mode. Although they have similar ASE threshold, the spontaneous emission factor β of 1% blend is over 3 times higher than 10% blend. β is also compared with PLQE in different blends, where they share the same trend $\beta \propto \eta$.

The energy response of SC5A:0.4%SpL is specially analysed in Figure 5.17 by comparing the emission from SC5A and SpL 0-1 peaks. Both energy and spectra show a severe competition between the two, making it difficult to extract spontaneous emission factor β. When pump energy is low, there is only PL emission and photons emitted from both molecules do not affect each other. Increasing pump energy activate ASE on SpL first, followed by SC5A. In both PL and ASE regions, SpL emits more photons than SC5A. However, at about 60 $\mu J\ cm^{-2}$, SpL

emission suddenly reaches its saturation while SC5A emission is not affected and keeps increasing. When ASE intensity is high, the lifetime of SC5A is shortened by stimulated emission, which is competing with donor-acceptor energy transfer for available excited states in SC5A. Since stimulated emission increases exponentially, it wins the competition and blocks the source of excited states for SpL. The key is that the 0.4% SpL cannot support an energy transfer rate that would be high enough to block ASE in SC5A at the first place, which is why blends with higher SpL concentrations have ASE in SpL only.

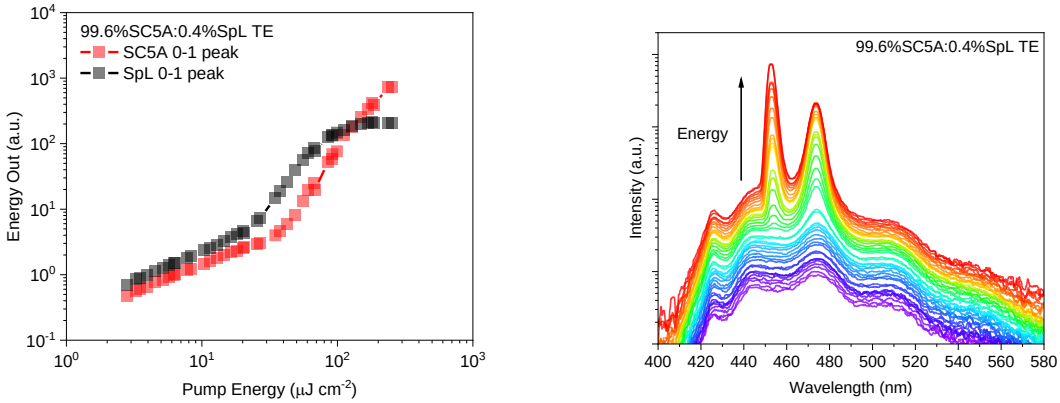


Figure 5.17 – Energy and spectral response of 0.4% blend, where both SC5A and SpL have ASE. Although SpL has lower ASE threshold, ultimately SC5A wins the competition by completely turning off SpL emission. When ASE is turned on in SC5A, it continuously shortens its excited state lifetime due to fast stimulated emission. Once the stimulated emission rate becomes higher than energy transfer rate, it would block the source of excited state for SpL. The depopulation of excited state stops both PL and ASE in SpL.

5.4.2 Optical Gain Characterisation

To study gain properties in SC5A:SpL blends, variable stripe length ASE intensity $I(z)$ is plotted at fixed pump energy in Figure 5.18. Only data from TE mode is used for optical gain characterisation. 2% and 10% blends were chosen as they have distinct properties at SpL 0-1 peak – 2% blend has the lowest ASE threshold of 9.75 $\mu J\ cm^{-2}$, near highest PLQE of 49.5 and relatively large spontaneous emission factor β of 0.0488, while 10% blend has a higher

ASE threshold of 16.5 $\mu J\ cm^{-2}$, smallest β of 0.0183 and lower PLQE of 34.0. Both samples were pumped at similar fixed energies as absorption of the donor SC5A does not change much when SpL concentration is low.

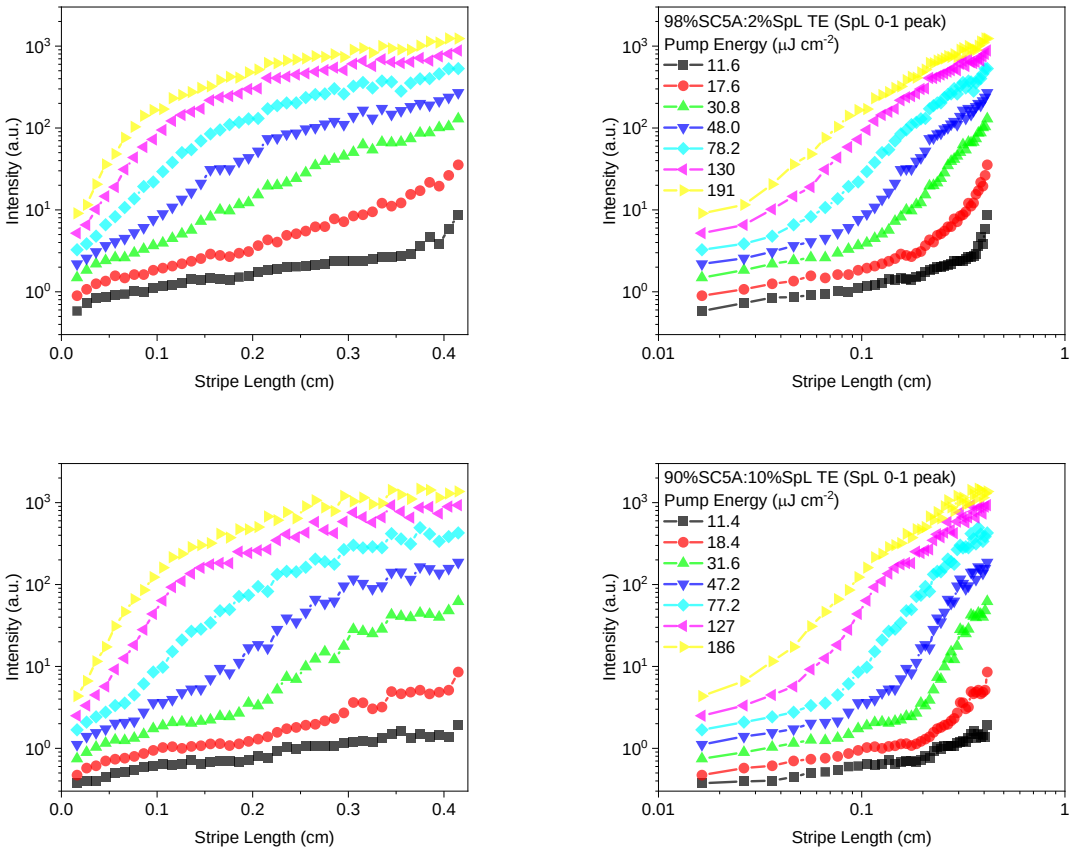


Figure 5.18 – ASE intensity of 2% and 10% blends in TE mode measured with variable stripe length and plotted as ASE intensity versus variable stripe length ($I(z)$). In the figure, 2% blend has higher intensities in PL region while 10% blend has higher amplification (the difference in intensities between lowest PL region and highest saturation region).

From the experimental data in Figure 5.18, the 10% blend is showing higher amplification as the change of intensity among different pump energies is more significant than the 2% blend (the gap between black curve and yellow curve). Method described in Chapter 4.3.3 was used to extract net modal gain g_0 and saturation length L_s, plotted in Figure 5.19. First, both blends have the same gain values. Recall Equation (4.7) for g_0 – when waveguide confinement factor

Γ should be similar for samples with similar thickness and refractive index, and stimulated emission cross section σ_e is unchanged for the same emitting specie SpL, the population inversion $(N_2 - N_1)$ must not change either (assuming loss α_{lo} is unchanged and negligible). This can be explained as both 2% and 10% blends have sufficient energy transfer rate, which is fast enough and is either saturated or beyond the limit of measurement in Figure 5.13. Then the SpL molecules in both blends would be pumped (indirectly by SC5A) in a time much shorter than ASE thus the difference is negligible. Apart from excitation, the spontaneous emission rate of SpL as acceptor also remains unchanged as in Figure 5.10, Therefore the population inversion is believed to be identical for both blends when ASE is activated (before gain saturation). Meanwhile, Figure 5.19 also shows that 2% blend has shorter saturation length than 10% at all pump energies. While Equation (4.10) for L_s is not straightforward to analyse, Equation (4.12) for $g_0 L_s$ is used instead as g_0 remains unchanged. Shorter saturation length and smaller $g_0 L_s$ imply larger spontaneous emission factor β, which is tied with the higher PLQE of 2% blend – consistent with values extracted from ASE energy response in Figure 5.16. To fully study the nature of $g_0 L_s$, Figure 5.20 compares extracted gain length product for both SpL 0-1 peak ($x = 2\%, 10\%$) and SC5A 0-1 peak ($x = 0\%, 0.2\%, 0.4\%$, extracted g_0 and L_s in Appendix 5F). It shows again that $g_0 L_s$ is a reliable metric independent of pump energy. For SpL 0-1 peak, $g_0 L_s$ is 3.83 ± 0.07 (16.6 dB) for 2% and 4.93 ± 0.14 (21.4 dB) for 10%, while $g_0 L_s$ calculated from Equation (4.12) using measured β in Figure 5.16 is 4.02 for 2% and 5.00 for 10%. The values extracted from two different sets of data coincide, which confirms the validity of Equation (4.12) $g_0 L_s \approx 1 + \ln(\beta^{-1})$. For SC5A 0-1 peak, $g_0 L_s$ is decreasing from 3.91 ± 0.15 (17.0 dB) for $x = 0\%$ to 3.15 ± 0.05 (13.7 dB) for 0.2% and 2.40 ± 0.04 (10.4 dB) for 0.4%, while its PLQE and β are increasing with x as

in Figure 5.16. Note Equation (4.12) cannot be used to estimate $g_0 L_s$ for SC5A 0-1 peak because the change of β is also affected by the competition and spectral overlap between SC5A and SpL. In conclusion, although higher PLQE lowers ASE threshold, it also decreases gain length product, which represents maximum amplification of the sample. Figure 5.21 plots the average $g_0 L_s$ in bar chart for $x = 0\%, 0.2\%, 0.4\%, 2\%, 10\%$. By blending 10% SpL with SC5A, the maximum amplification increases from 17.0 dB to 21.4 dB. As mentioned in Chapter 4.4, the gain length product $g_0 L_s$ is a useful metric to evaluate a gain media in a device aspect along with gain versus pump $g_0(I_p)$. While both $g_0(I_p)$ and gain length product $g_0 L_s$ are independent of measurement conditions (unlike ASE threshold), $g_0(I_p)$ is material property and is determined with the materials provided (SC5A and SpL), it is $g_0 L_s$ that can be tuned. The donor-acceptor blends reported here are able to change the saturation length while maintaining a constant net gain, which could provide more flexibility in device design of amplifiers [18-20].

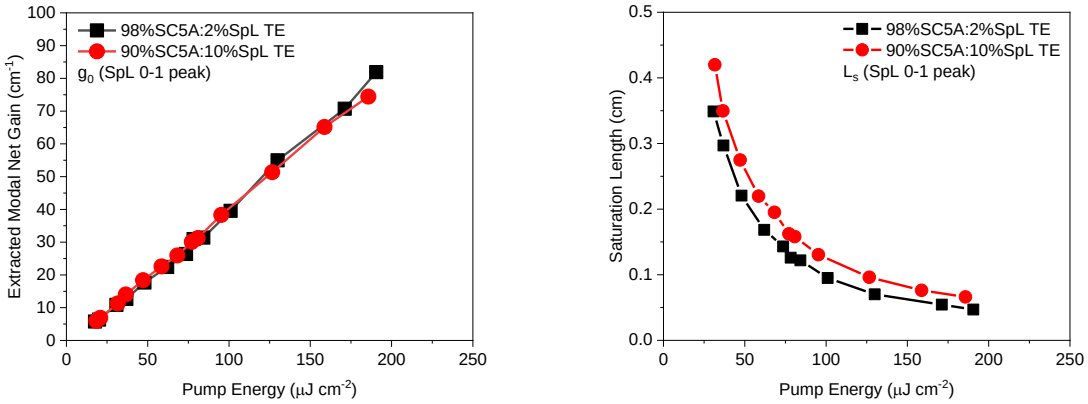


Figure 5.19 – Extracted net modal gain g_0 and saturation length L_s from Figure 5.18 using method in Chapter 4.3.3. Both blends have the same gain values, however, the 2% blend has shorter L_s, which is due to its high PLQE thus high spontaneous emission factor β.

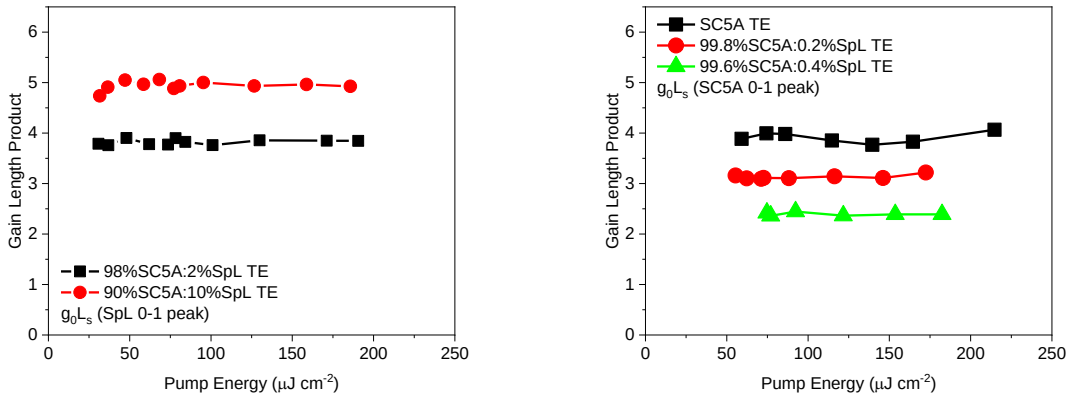


Figure 5.20 – SC5A:SpL blends extracted gain length product $g_0 L_s$ (Chapter 4.4.2). For SC5A peak ASE, $g_0 L_s$ decreases in the same way as threshold increases. For SpL peak ASE, however, 10% blend has higher threshold but also has higher $g_0 L_s$, which means lower threshold, even on a comparable like-for-like basis, does not necessarily give better ASE.

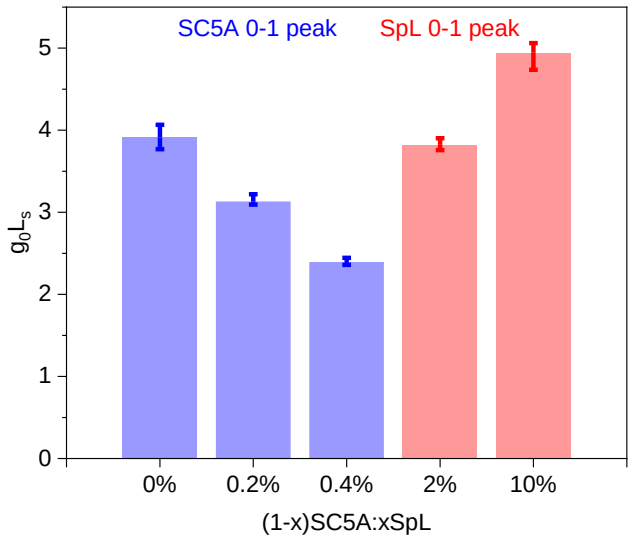


Figure 5.21 – SC5A:SpL blends gain length product $g_0 L_s$. Among these samples, the 10% blend has the highest amplification, which is 25% higher than SC5A, thanks to efficient energy transfer from SC5A to SpL. Note the 10% blend has neither highest PLQE or lowest threshold, thus neither of which should be used to judge a gain media in thin-film structures.

5.4.3 Linking ASE/lasing and Photo-physics

One of the most promising advantages of organic molecular materials is the ability to synthesise and tune the chemical and physical properties to accommodate different types of

applications. In recent years, materials for most plastic electronic devices such as OLEDs and OPVs are tailor made due to the widely understood link between material property and device performance. However, this does not apply to applications involving stimulated emission – even the characterisation of ASE/lasing has not been standardised in literature. While Chapter 4 introduces a reliable method to assess ASE in thin-film structures, this chapter presents the experimental data from a complete set of samples, which also went through photo-physics measurements (UV-Vis, PL, PLQE, PL lifetime). It is now possible to link ASE/lasing performance to the desired photo-physics parameters, which can be tuned by synthetic chemists. It is worth to mention that there is no single answer of 'best material' for ASE/lasing because it depends highly on device design. Under same or comparable experimental conditions, assuming all other parameters are the same (or differences are negligible), and when net gain is positive, the following relationships have been found, both in calculation and in experiment.

- Higher PLQE gives lower ASE threshold.
- Longer PL lifetime gives lower ASE threshold.
- Higher PLQE gives shorter saturation length, thus lower gain length product.
- Larger stimulated emission cross-section gives higher gain.
- Waveguide mode confinement is important. Sample cannot be too thin (not guided) or too thick (mode competition).

All of above have to be considered in device design and are determined by device dimensions, pumping conditions, required amplification etc. There are still many other links not revealed

as the work in this thesis is based on a simplified ASE model (Chapter 3.3) and a fixed experimental condition (Chapter 4.2). For example, all calculations presented here did not account any loss – it is very difficult to measure loss when sample is excited, and even more challenging to separate and analyse material loss and waveguide loss. Besides, the gain equation based on single-pass travelling wave is just an approximation of the actual double pass scenario, which makes a difference in saturation region by adding competition. Moreover, this thesis does not investigate the effect of varying excitation pulse widths and repetition rates, which are essential towards continuous-wave operation. Overall, the method described in this thesis provides a general guidance for synthesising optical gain materials and could be further improved to apply in specific applications.

5.5 Summary

This chapter presented a comprehensive study of Förster resonance energy transfer and its effect on stimulated emission in polymer blends. Firstly, by adding energy transfer terms to the rate equation model (Chapter 3.3), the temporal evolution of excited state density of donor and acceptor were solved, showing a shortened donor lifetime and a delay in acceptor emission. Secondly, two sets of samples F8BT:RedF and SC5A:SpL were prepared and characterised. Photo-physics measurements indicated both pairs have efficient energy transfer with transfer rate up to $2-4\ ns^{-1/2}$. Then, ASE and gain properties of SC5A:SpL were studied using the method in Chapter 4. The result reliably links ASE/lasing with material properties obtained in photo-physics measurements. One of the key observations is that higher PLQE can potentially lower ASE threshold but also lower the gain length product $(gL)_{max}$.

References

[1] Samuel, I. D. W., & Turnbull, G. A. (2007). Organic semiconductor lasers. *Chemical Reviews*, *25*(7), 1272–1295.

[2] Kuehne, A. J. C., & Gather, M. C. (2016). Organic Lasers: Recent Developments on Materials, Device Geometries, and Fabrication Techniques. *Chemical Reviews*, *116*(21), 12823–12864.

[3] Sandanayaka, A. S. D., Matsushima, T., Bencheikh, F., Terakawa, S., Potscavage, W. J., Qin, C., … Adachi, C. (2019). Indication of current-injection lasing from an organic semiconductor. *Applied Physics Express*, *12*(6), 061010.

[4] Yap, B. K., Xia, R., Campoy-Quiles, M., Stavrinou, P. N., & Bradley, D. D. C. (2008). Simultaneous optimisation of charge-carrier mobility and optical gain in semiconducting polymer films. *Nature Materials*, *7*(5), 376–380.

[5] Zhang, Q., Wei, Q., Guo, X., Hai, G., Sun, H., Li, J., … Cabanillas-Gonzalez, J. (2019). Concurrent Optical Gain Optimisation and Electrical Tuning in Novel Oligomer:Polymer Blends with Yellow-Green Laser Emission. *Advanced Science*, *6*.

[6] Gupta, R., Stevenson, M., & Heeger, A. J. (2002). Low threshold distributed feedback lasers fabricated from blends of conjugated polymers: Reduced losses through Förster transfer. *Journal of Applied Physics*, *92*(9), 4874–4877.

[7] Perissinotto, S., Garbugli, M., Fazzi, D., Bertarelli, C., Carvelli, M., Srimath Kandada, A. R., … Lanzani, G. (2011). Optical modulation of amplified emission in a polyfluorene-diarylethene blend. *ChemPhysChem*, *12*(18), 3619–3623.

[8] Xia, R., Stavrinou, P. N., Bradley, D. D. C., & Kim, Y. (2012). Efficient optical gain media comprising binary blends of poly(3-hexylthiophene) and poly(9,9-dioctylfluorene-co-benzothiadiazole). *Journal of Applied Physics*, *111*(12), 123107.

[9] Lakowicz, J. R. (2006). Principles of Fluorescence Spectroscopy, 3rd edition. *Springer*.

[10] Powell Zoltán, G., & Richard, C. (1975). Singlet Exciton Energy Transfer in Organic Solids. *Journal of Luminescence*, *11*(1–2), 1–45.

[11] Yu, J. W., Kim, J. K., Cho, H. N., Kim, D. Y., Kim, C. Y., Song, N. W., & Kim, D. (2000). Long-range energy migration in photoexcited polymers. *Macromolecules*, *33*(15), 5443–5447.

[12] Yu, J. W., Kim, J. K., Kim, D. Y., Kim, C., Song, N. W., & Kim, D. (2006). Prediction of efficient energy transfer in emissive polymer blends based on Förster radius and the excited state lifetime of acceptors. *Current Applied Physics*, *6*(1), 59–65.

[13] Murphy, C. B., Zhang, Y., Troxler, T., Ferry, V., Martin, J. J., & Jones, W. E. (2004).

Probing Förster and Dexter energy-transfer mechanisms in fluorescent conjugated polymer chemosensors. *Journal of Physical Chemistry B*, *108*(5), 1537–1543.

[14] SpL (unpublished material) supplied by Dr. Yi Jiang and Prof. Wen-Yong Lai, Nanjing University of Posts and Telecommunications, P. R. China.

[15] Jiang, Y., Fang, M., Chang, S. J., Huang, J. J., Chu, S. Q., Hu, S. M., … Huang, W. (2017). Towards Monodisperse Star-Shaped Ladder-Type Conjugated Systems: Design, Synthesis, Stabilized Blue Electroluminescence, and Amplified Spontaneous Emission. *Chemistry - A European Journal*, *23*(23), 5448–5458.

[16] Sienicki, K., & Winnik, M. A. (1988). Donor-acceptor kinetics in the presence of energy migration. Forward and reverse energy transfer. *Chemical Physics*, *121*(2), 163–174.

[17] Twardowski, R., & Kuśba, J. (1988). Reversible Energy Transfer and Fluorescence Decay in Solid Solutions. *Zeitschrift für Naturforschung A*, *43*(7), 627-632.

[18] Siegman, A. E. (1986). Lasers. *University Science Books*.

[19] Dal Negro, L., Bettotti, P., Cazzanelli, M., Pacifici, D., & Pavesi, L. (2004). Applicability conditions and experimental analysis of the variable stripe length method for gain measurements. *Optics Communications*, *229*(1–6), 337–348.

[20] Milonni, P. W., & Eberly, J. H. (2010). Laser Physics. *Wiley*.

6 Conclusions

6.1 Thesis Summary

Following the extensive and successful research and application of organic light-emitting diodes (OLEDs), organic photovoltaics (OPVs) and organic field-effect transistors (OFETs), molecular semiconductor materials, primarily conjugated polymers, appear to be a fascinating class of gain media with the potential to offer an alternative for tunable and flexible lasers or amplifiers. The manufacturing of thin-film structures, required in most organic devices, offer ease of large-scale fabrication. However, challenges remain; achieving continuous-wave operation and electrical pumping continue to be one a main focus. Intimately tied to this is the current characterisation of polymeric materials and how it can be linked to stimulated emission performance. To address this, the thesis has comprehensively investigated stimulated emission processes (i.e. amplified spontaneous emission (ASE)) in molecular thin-film structures.

Amorphous and glassy thin-film samples were prepared by spin-coating from solutions and examined. Film quality (i.e. surface roughness) was checked by microscopes and Fabry-Pérot oscillations in UV-Vis spectroscopy, which measures transmittance and estimates film thickness. Standard photoluminescence (PL) measurements including quantum efficiency (PLQE) were recorded. In particular, time-resolved PL measured using a streak camera – the two-dimensional wavelength-time data were carefully processed and fitted to a convolution of excitation and fluorescent decay to extract reliable and possibly spectrally resolved excited state lifetimes.

A rate equation model was introduced to simulate ASE properties in thin-film structures. The

2-level model proved to yield a good estimation and was validated against experimental data. For the material aspect, the calculated temporal evolution revealed the effect of basic material parameters on ASE performance, i.e. absorption and stimulated emission cross-sections, excited state lifetime and the PLQE. To simulate the actual emission out of a thin-film sample, which is effectively a slab waveguide, the model incorporated accurate modal propagation of travelling waves (single-pass, double-pass and double-pass with reflection) to study the spatial dependency of both electronic state and photon state densities. The results suggested that population inversion (i.e. gain) was not evenly distributed, as implicitly assumed in the majority of previous reports, and gain saturation must be considered. The modelling provided initial ideas of what to expect in ASE measurement, which factors are determinant and how to avoid misleading gain characterisation.

ASE measurements were examined in detail from experimental set-up to data analysis, seldom reported in the literature. ASE from thin-film structures was gain-guided to the film edge, and spectra taken for TE/TM modes at varying pump intensities and varying excitation stripe lengths. The energy response at different stripe lengths showed that ASE threshold is heavily dependent on experimental conditions and, while ubiquitously reported, is therefore not generally suitable to assess materials – except for a given set-up. For the gain characterisation, a modified variable stripe length method was implemented. Homogeneous saturation proved to be more adequate for amorphous polymer thin-films and was verified using both numerical and experimental observations. Net modal gain was then extracted by a carefully designed fitting procedures that extracted one parameter at a time to improve reliability. New metrics, which are independent of experimental conditions, were introduced to evaluate gain media. Specifically, the rate of increase of gain with pump energy, dg/dI_p, showing the maximum

potential gain, which is linear and proportional to pump energy; and the gain-length product $(gL)_{max}$ representing the device capability for maximum amplification. The latter is capped by gain saturation and governed by both material and thin-film structure. Both these metrics appear to be independent of the set-up used and are important parameters from which different materials may be assessed. As an example, blue polyfluorenes (SC5A, PFO, F8DP2) have much higher dg/dI_p than F8BT but their $(gL)_{max}$ are similar, implying that they are both useful gain media but for different applications.

Further investigation focused on the ASE properties from donor-acceptor blend thin-films with the help of resonance energy transfer. Adopting the new metrics and methods detailed above, two complete sets of samples (F8BT:RedF and SC5A:SpL) with efficient resonance energy transfer, but different excited state lifetime and PLQE were prepared and characterised. In particular, ASE measurement on SC5A:SpL samples verified findings obtained from our rate equation model – PLQE is inversely proportional to both ASE threshold and 'gain length product' $(gL)_{max}$, while it does not affect 'gain versus pump' dg/dI_p; excited state lifetime is inversely proportional to ASE threshold but itself does not affect dg/dI_p or $(gL)_{max}$. To our knowledge, this is the first time that molecular material's photo-physics property has been unambiguously linked to stimulated-device performance. It is hoped from here that materials can be targeted for applications.

In conclusion, this work introduced a reliable and straightforward method to characterise ASE in molecular thin-films. ASE threshold is not material property while gain saturation must be considered. Instead, 'gain versus pump' and 'gain length product' are not only independent of experimental conditions but also directly linked to material's photo-physics property. With these new metrics, ASE results from different labs are comparable and materials specifically

designed for lasing can be synthesised, which should be the correct way towards continuous wave operated and electrically pumped organic lasers.

6.2 Outlook for Future Work

With a standardised ASE measurement and analysis in Chapter 4, a large range of materials can be tested on thin-film samples in the future, and more insights can be found on enhancing stimulated emission from material aspect. One possible strategy would be modifying polymer side chains while the main backbone remains the same. For example, ASE characterisation of blue polyfluorenes with additional branches for better charge injection could be an interesting comparison, which would complement the link between materials and devices [1].

Following the work in Chapter 5, utilising energy transfer in donor-acceptor blends is also a promising direction to optimise stimulated emission in molecular thin-films. Efforts can be made on tuning the spectral gap between donor and acceptor and investigate its influence on the charge state. This could potentially help to better understand polaron absorption in an active and transient environment with a large set of comparable data.

Another attracting aspect would be molecular thin-film alignment for polarisation dependent absorption/emission [2,3]. By aligning the molecules in liquid crystal phase to the same angle and introduces birefringence, absorption and emission of the thin-film sample strongly favours one polarisation axis while suppresses the other, and ASE may be enhanced in one direction. With the possibility to align molecules in spatial patterns, it would be of great interest to see how this affects feedback structures for lasing.

There are also plans to make organic lasers with resonators. It would be beneficial to fabricate

a device that can receive both optical excitation and charge injection. Optically pump the device above its ASE/lasing threshold, then inject additional electrical pump and record the change of emission. Since the energy response is much more sensitive when stimulated emission is turned on, it would be better to study the effect of electrical pumping in this region than the PL region below threshold.

References

[1] Unpublished series of fluorene-based polymers with added side chains favouring charge transport and also affecting molecular packing.

[2] Grell, M., Bradley, D. D. C., Inbasekaran, M., & Woo, E. P. (1997). A glass-forming conjugated main-chain liquid crystal polymer for polarised electroluminescence applications. *Advanced Materials*, *9*(10), 798–802.

[3] Martini, I. B., Craig, I. M., Molenkamp, W. C., Miyata, H., Tolbert, S. H., & Schwartz, B. J. (2007). Controlling optical gain in semiconducting polymers with nanoscale chain positioning and alignment. *Nature Nanotechnology*, *2*(10), 647–652.

Appendix 2A

Spectral fast Fourier transform

A fast Fourier transform (FFT) was used to eliminate background noise and unwanted oscillations in photoluminescence spectra $I(\lambda)$. The process is performed numerically in Matlab (function 'fft' and 'ifft') as follows.

1. Convert raw spectrum $I(\lambda)$ to energy $I(E)$ scale by Jacobian conversion.
2. Use FFT to convert the spectrum $I(E)$ to frequency domain $f(\omega)$.
3. Shortpass filter the frequency domain signal to eliminate high frequency noise and oscillations (for example $f(\omega > 40) = 0$).
4. Use inverse FFT to obtain $I'(E)$, then Jacobian conversion to convert back to noise eliminated spectrum $I'(\lambda)$.

Example – SC5A streak camera spectrum from Figure 2.16 (a)

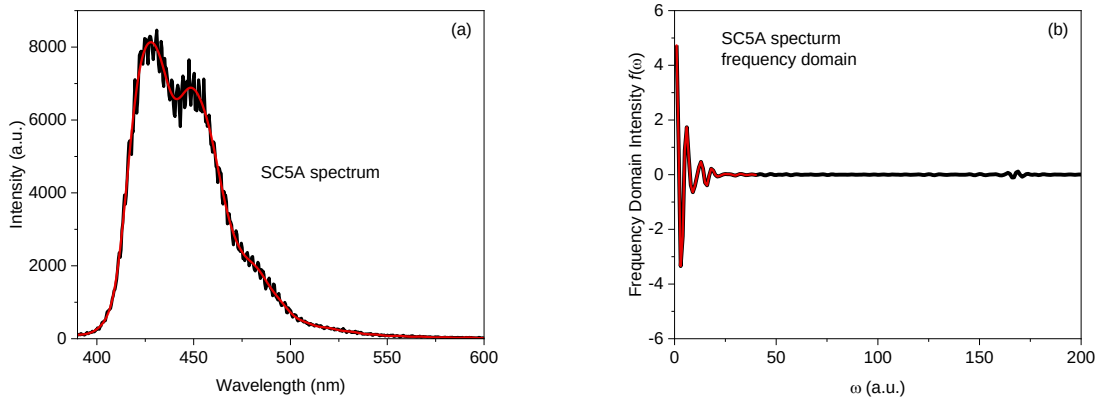


Figure 2.A1

(a) SC5A streak camera spectrum. Raw spectrum $I(\lambda)$ (black) is from Figure 2.16 (a). Noise eliminated spectrum $I'(\lambda)$ (red) is obtained by FFT described above.
(b) SC5A frequency domain intensity $f(\omega)$ by FFT (black), which is then shortpass filtered by $f(\omega > 40) = 0$ (red).

Appendix 2B

Convolution of Gaussian function and single exponential decay

To find an analytical solution of the convolution of excitation and decay signals. Recall Equation (2.6)

$$I(t) = \int_0^t g(t')f(t-t')dt' \tag{2.B1}$$

where $g(t) = \frac{1}{\sigma\sqrt{2\pi}} e^{-\frac{(t-t_0)^2}{2\sigma^2}}$ and $f(t) = \mathrm{A}e^{-\frac{t}{\tau}}$. Then Equation (2.B1) becomes

$$\begin{aligned} I(t) &= \frac{\mathrm{A}}{\sigma\sqrt{2\pi}} \int_0^t e^{-\frac{(t'-t_0)^2}{2\sigma^2}} e^{-\left(\frac{t-t'}{\tau}\right)} dt' \\ &= \frac{\mathrm{A}}{\sigma\sqrt{2\pi}} e^{\left(\frac{-2\tau t+\sigma^2+2\tau t_0}{2\tau^2}\right)} \int_0^t e^{-\frac{\left[t'-\left(t_0+\frac{\sigma^2}{\tau}\right)\right]^2}{2\sigma^2}} dt' \end{aligned} \tag{2.B2}$$

According to integral calculus [B1]

$$\int_a^b e^{-x^2} dx = \frac{\sqrt{\pi}}{2}[erf(b) - erf(a)] \tag{2.B3}$$

where $x = \frac{t'-\left(t_0+\frac{\sigma^2}{\tau}\right)}{\sqrt{2}\sigma}$ and $dx = \frac{dt'}{\sqrt{2}\sigma}$. Substituting Equation (2.B3) into Equation (2.B2)

$$I(t) = \frac{1}{2}\mathrm{A}e^{\left(\frac{-2\tau t+\sigma^2+2\tau t_0}{2\tau^2}\right)}\left[erf\left(\frac{t\tau - t_0\tau - \sigma^2}{\sqrt{2}\sigma\tau}\right) - erf\left(\frac{-t_0\tau - \sigma^2}{\sqrt{2}\sigma\tau}\right)\right] \tag{2.B4}$$

Equation (2.B4) is the solution presented as Equation (2.9).

[B1] Varberg, D., Purcell, E. J., & Rigdon, S. E. (2007). Calculus with Differential Equations, 9th edition. *Pearson*.

Appendix 2C

Power-like decay – lifetime distribution models

When the excited state lifetime is not a fixed value but in a form of a probability distribution, the decay function can be written as

$$f(t) = \int_0^\infty P(\tau)\, exp\left(-\frac{t}{\tau}\right) d\tau \tag{2.C1}$$

where $P(\tau)$ is normalised probability distribution of each individual lifetime. Decay function $f(t)$ in Equation (2.C1) is the Laplace transform of $P(\tau)$. Unlike symmetric Gaussian and Cauchy distributions, the power-like decay is designed for systems with heterogeneity and long tail distributions, and is defined as the distribution function of decay rate $P(k = 1/\tau)$ that maximise the entropy [C1]

$$H = -\int P(k)\, ln\, P(k) dk \tag{2.C2}$$

The distribution P(k) is solved in the form of gamma function [C2]

$$P(k) = \frac{1}{\Gamma(1/(q-1))}\left(\frac{\tau_0}{q-1}\right)\left(\frac{k\tau_0}{q-1}\right)^{\left(\frac{2-q}{q-1}\right)} exp\left(-\frac{k\tau_0}{q-1}\right) \tag{2.C3}$$

where q is a heterogeneity parameter describing the relative variance ω of fluctuations of γ with $q = 1 + \omega$, and τ_0 is the mean value of lifetime distribution with $\tau_0 = 1/\langle k \rangle$. Substitute Equation (2.C3) into (2.C1), the power-like decay function is [C3]

$$f(t) = \mathrm{A}\left(\frac{2-q}{\tau_0}\right)\left[1 + (q-1)\frac{t}{\tau_0}\right]^{-\left(\frac{1}{q-1}\right)} \tag{2.C4}$$

The actual lifetime is increasing with time as

$$\tau(t) = \frac{\tau_0 + (q-1)t}{q} \tag{2.C5}$$

There are two common types of power-like decays – compressed hyperbola and stretched exponential. Compressed hyperbola function is often used to describe luminescent decays with

trapping and re-trapping processes when there are both localised and interactive luminescent centres [C4]. The decay equation is

$$\frac{dN(t)}{dt} = -(k_r + k_{nr})N(t)^{1+\mathrm{c}} \tag{2.C6}$$

$$f(t) = \mathrm{A}N(t) = \mathrm{A}\left(1 + \mathrm{c}\frac{t}{\tau_0}\right)^{-\frac{1}{\mathrm{c}}} \tag{2.C7}$$

where $0 < \mathrm{c} < 1$ describes how dispersive the system is. By taking the inverse Laplace transform, the probability distribution is

$$P(k) = \frac{1}{\Gamma(1/\mathrm{c})}\frac{\tau_0}{\mathrm{c}}\left(\frac{k\tau_0}{\mathrm{c}}\right)^{\left(\frac{1-\mathrm{c}}{\mathrm{c}}\right)} exp\left(-\frac{k\tau_0}{\mathrm{c}}\right) \tag{2.C8}$$

And the actual time dependent lifetime can be calculated

$$\tau(t) = \tau_0 + \mathrm{c}t \tag{2.C9}$$

Although compressed hyperbola has the same mathematical form as power-like decay but is derived from different basis. They have identical distribution function – parameter c in compressed hyperbola is the same as relative variance ω in power-like decay, but the definitions of τ_0 is different. When $\mathrm{c} = 0$, the decay is single exponential, while $\mathrm{c} = 1$, the decay is purely second order. Therefore, it is more convenient to use compressed hyperbola distribution in transient spectroscopy analysis.

Another widely used power-like decay is stretched exponential with decay function [C5].

$$f(t) = \mathrm{A}e^{-\left(\frac{t}{\tau_0}\right)^{\beta}} \tag{2.C10}$$

where $0 < \beta < 1$. Again, the probability distribution and actual lifetime are calculated [C5,C6].

$$P(k) = \frac{\tau_0}{\pi}\int_0^{\infty} e^{-k\tau_0 u} e^{\left[-u^{\beta}cos(\beta\pi)\right]} sin\left[u^{\beta}\sin(\beta\pi)\right] du \tag{2.C11}$$

$$\tau(t) = \frac{\tau_0}{\beta}\left(\frac{\tau_0}{t}\right)^{(\beta-1)} \tag{2.C12}$$

where the definitions of τ_0 allows $\tau(t = 0) = 0$. This characteristic of stretched exponential has no physical meaning for photoluminescence in molecular materials. Therefore, it cannot be used to describe lifetime distributions.

[C1] Montroll, E. W., & Shlesinger, M. F. (1983). Maximum entropy formalism, fractals, scaling phenomena, and 1/f noise: A tale of tails. *Journal of Statistical Physics*, *32*(2), 209–230.

[C2] Kierdaszuk, B. (2010). From discrete multi-exponential model to lifetime distribution model and power law fluorescence decay function. *Spectroscopy*, *24*(3–4), 399–407.

[C3] Włodarczyk, J., & Kierdaszuk, B. (2003). Interpretation of fluorescence decays using a power-like model. *Biophysical Journal*, *85*(1), 589–598.

[C4] Berberan-Santos, M. N., Bodunov, E. N., & Valeur, B. (2005). Mathematical functions for the analysis of luminescence decays with underlying distributions: 2. Becquerel (compressed hyperbola) and related decay functions. *Chemical Physics*, *317*(1), 57–62.

[C5] Berberan-Santos, M. N., Bodunov, E. N., & Valeur, B. (2005). Mathematical functions for the analysis of luminescence decays with underlying distributions 1. Kohlrausch decay function (stretched exponential). *Chemical Physics*, *315*(1–2), 171–182.

[C6] Lindsey, C. P., & Patterson, G. D. (1980). Detailed comparison of the Williams-Watts and Cole-Davidson functions. *The Journal of Chemical Physics*, *73*(7), 3348–3357.

Appendix 3A

Simulation parameters of rate equation model

Table 3.A1 – Parameters used when running simulation of rate equation model in Matlab unless otherwise stated. The values are from data of RedF thin-film.

Symbol	Description	Value
N_0	Initial ground state density	$10^{21}\ cm^{-3}$
σ_p	Absorption cross-section	$5 \times 10^{-16}\ cm^2$
σ_e	Stimulated cross-section	$5 \times 10^{-16}\ cm^2$
τ_2	Excited state lifetime	$1.9\ ns$
τ_1, τ_3	Internal relaxation lifetime	$1.9 \times 10^{-2}\ ns$
η	Photoluminescence quantum efficiency (PLQE)	40%
β	Spontaneous emission factor	0.04
Γ	Waveguide confinement factor	0.35
n	Material refractive index	1.65
L	Excitation stripe length	$4\ mm$
α_{lo}	Re-absorption loss	$3.2\ cm^{-1}$
α_{ex}	Photon cavity loss	$1.6/L$

Appendix 3B

Pumping efficiency and its effect on ASE

Examine the effect of varying excitation pulse widths – how excited state density and ASE intensity are affected. Note that although constant pump intensity (square pulse) is used in the calculation, Gaussian pulse would lead to the same result. Firstly, define pumping efficiency in the 2-level rate equation model as

$$\eta_p(t) = \frac{N_2(t)}{R_\mathrm{p} t} = \frac{N_2(t)}{\sigma_p u_p N_0 t} \tag{3.B1}$$

where longer excitation pulse has longer time t, which may change $\eta_p(t)$. Since the focus is pumping efficiency when emission is small, it is appropriate to assume $S \to 0$, thus the temporal evolution of excited state in Equation (3.6) becomes

$$\frac{dN_2(t)}{dt} = R_\mathrm{p} - \frac{N_2(t)}{\tau_2} \tag{3.B2}$$

which can be solved as

$$N_2(t) = R_p \tau_2 (1 - e^{-t/\tau_2}) \tag{3.B3}$$

Substitute Equation (3.B3) into Equation (3.B1)

$$\eta_p(t) = (1 - e^{-t/\tau_2})(t/\tau_2)^{-1} \tag{3.B4}$$

When $t \gg \tau_2$, pumping efficiency $\eta_p(t)$ increases when t/τ_2 decreases. Higher η_p results in higher N_2 with the same pump energy, thus larger population inversion and higher gain. To confirm the relationship between t/τ_2 and ASE, the 2-level rate equation model in Chapter 3.2 were simulated in Matlab while t and τ_2 were assigned different values $t/\tau_2 = 1, 10, 100$. Figure 3.B1 plots the steady state energy response of photon density S, and t/τ_2 is clearly the dominant factor –ASE performance would remain unchanged as long as the ratio between t and τ_2 does not change and lower t/τ_2 is beneficial as in Equation (3.B4). In conclusion, pumping efficiency has significant impact on ASE, and results from different pulse width are

not comparable. Efforts should be made to achieve ASE at longer excitation pulse or continuous-wave operation, which are much more useful in applications.

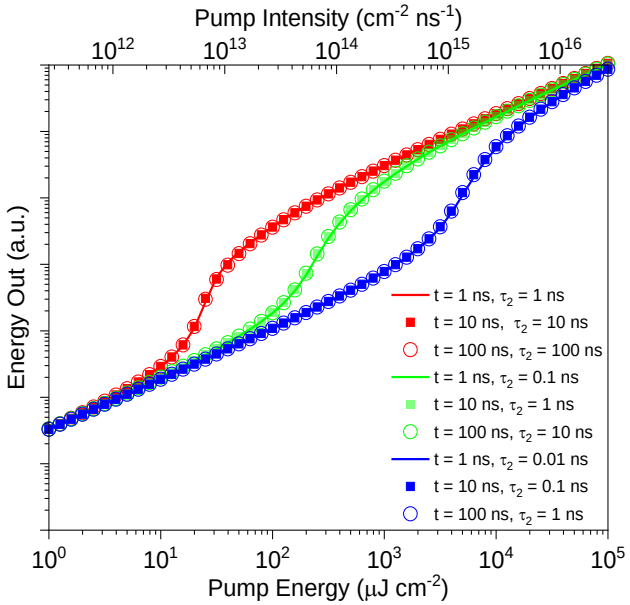


Figure 3.B1 – Steady state energy response of photon density $S(t)$ calculated by the 2-level rate equation model in Figure 3.5 with changing excitation pulse width t and excited state lifetime τ_2. The result does not change as long as the ratio of t/τ_2 stays the same. Smaller t/τ_2 reduces ASE threshold, however, longer t is desired towards continuous-wave operation. Materials with longer τ_2 may be beneficial to ASE.

Appendix 3C

Slab waveguide modes

Solve guided modes for the slab waveguide in the Cartesian coordinate system shown in Figure 3.6. Maxwell's equations describe the electric and magnetic fields as

$$\nabla \times \vec{E} = i\mu\omega\vec{H} \tag{3.C1}$$

$$\nabla \times \vec{H} = i\varepsilon\omega\vec{E} \tag{3.C2}$$

$$\nabla \cdot \vec{E} = 0 \tag{3.C3}$$

$$\nabla \cdot \vec{H} = 0 \tag{3.C4}$$

Solve E_x, E_y and n_{eff} to calculate waveguide confinement factor Γ as in Equation (3.9) and (3.10). Since the molecular semiconductor thin-film is coated on yz plane, assume $\varepsilon_y = \varepsilon_z \neq \varepsilon_x$.

$$\begin{bmatrix} D_x \\ D_y \\ D_z \end{bmatrix} = \begin{bmatrix} \varepsilon_x & 0 & 0 \\ 0 & \varepsilon & 0 \\ 0 & 0 & \varepsilon \end{bmatrix} \begin{bmatrix} E_x \\ E_y \\ E_z \end{bmatrix} \tag{3.C5}$$

For TE mode, non-zero components are E_y, H_x, H_z.

$$ikE_y = -i\mu\omega H_x \tag{3.C6}$$

$$\frac{\partial E_y}{\partial \mathrm{x}} = -i\mu\omega H_z \tag{3.C7}$$

$$-ikH_x - \frac{\partial H_z}{\partial x} = i\varepsilon\omega E_y \tag{3.C8}$$

$$\frac{\partial^2 E_y}{\partial x^2} + (\mu\varepsilon\omega^2 - k^2)E_y = 0 \tag{3.C9}$$

where $k = n_{eff}k_0$. Solve Equation (3.C9) in air/film/quartz layers to obtain n_{eff} and E_y.

For TM mode, non-zero components are E_x, E_z, H_y.

$$ikH_y = i\varepsilon_x\omega E_x \tag{3.C10}$$

$$\frac{\partial H_y}{\partial \mathrm{x}} = i\varepsilon\omega E_z \tag{3.C11}$$

$$-ikE_x - \frac{\partial E_z}{\partial x} = -i\mu\omega H_y \tag{3.C12}$$

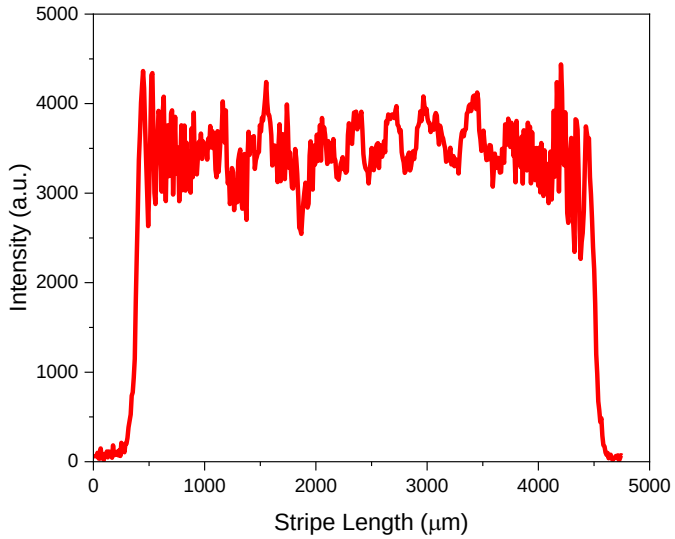
$$\frac{\partial^2 H_y}{\partial x^2} + \left(\mu\varepsilon\omega^2 - \frac{\varepsilon}{\varepsilon_x}k^2\right)H_y = 0 \tag{3.C13}$$

where $k = n_{eff}k_0$. In practice, assume $\varepsilon_x = \varepsilon$. Solve Equation (3.C13) in air/film/quartz layers to obtain n_{eff} and H_y. Then substitute into Equation (3.C10) to obtain E_x.

When the film is thick enough, solutions of n_{eff} can be found higher than refractive index of quartz substrate (1.4755), which means the waveguide supports guided modes.

Appendix 4A

Excitation stripe profile for ASE measurement



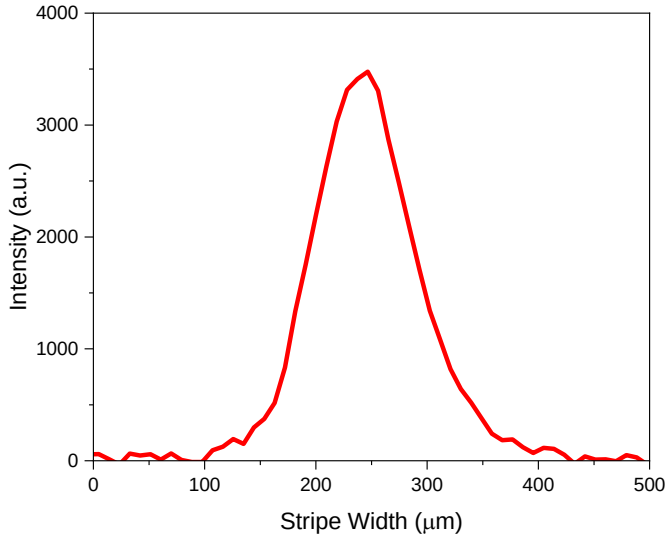
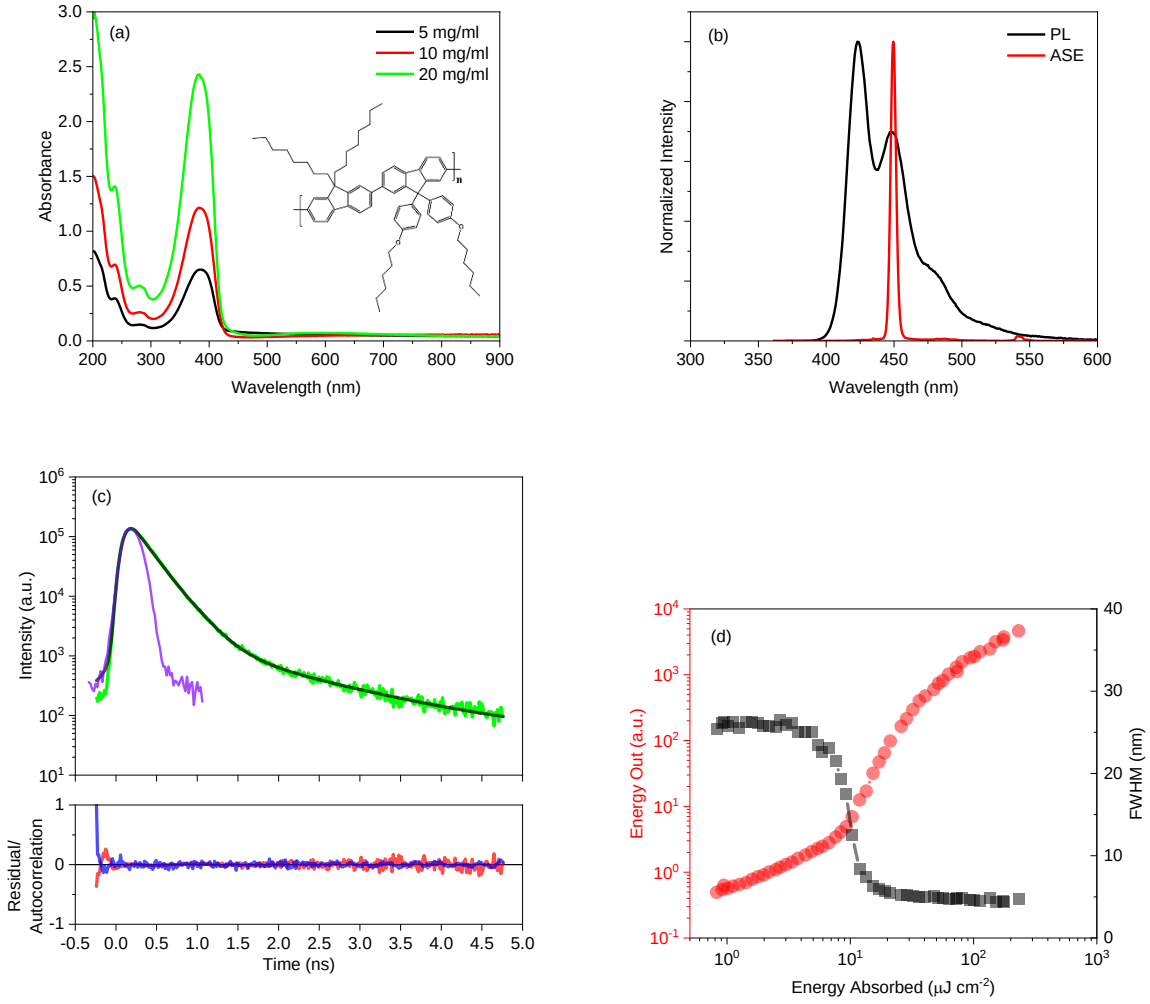


Figure 4.A1 – Dimensions of 355 nm laser stripe measured using a CCD beam profiler. Based on full-width-half-maximum (FWHM), the stripe has a length of 4120 μm (top-hat adjusted $R^2 = 0.94$) and a width of 101.9 μm (top-hat adjusted $R^2 = 0.86$), which were ten used to calculate energy density per area. The beam profile intensities were measured as moving average of 5 seconds (50 pulses in case of 10 Hz).

Appendix 4B

F8DP2

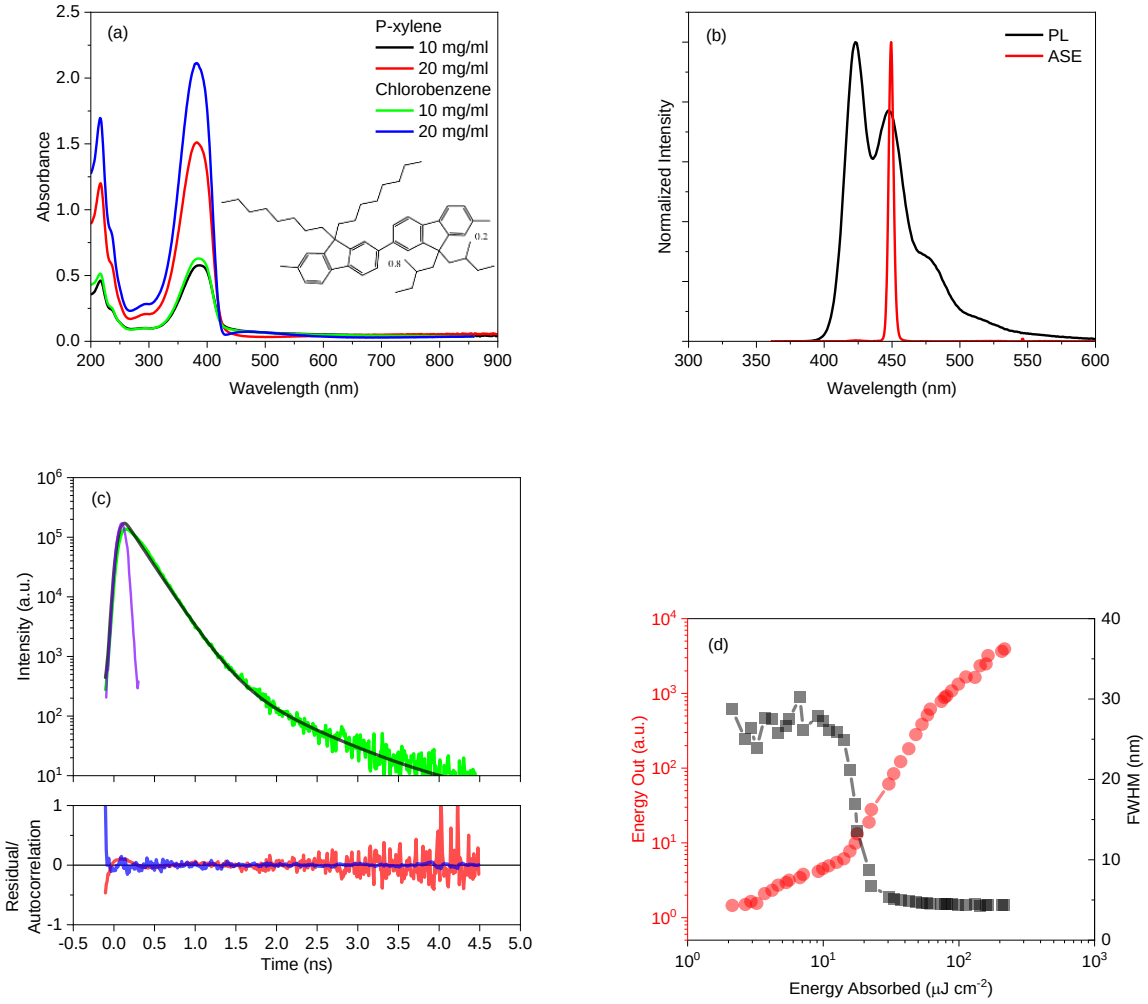
Material was dissolved in Chlorobenzene with concentration $5, 10, 20\ mg/ml$. Solutions were stirred at 700rpm and heated at 100C, before spin-coating into thin-film on quartz substrate at 2000rpm for 60s.



(a) F8DP2 chemical structure and UV-Vis absorbance calculated from transmittance as $Abs = -\log_{10}(T)$.
(b) Normalised PL spectrum (pumped at 380 nm) and saturated ASE spectrum in TE mode (pumped at 355 nm) of 10 mg/ml F8DP2 film.
(c) Transient PL measured using the Streak Camera (pumped at 379 nm) and fitted with laser signal convolved with double exponential decay (Chapter 2.4.5). The lifetime 10 mg/ml of F8DP2 (excludes the less than 10% green band) is $0.23 \pm 0.02\ ns$.
(d) ASE energy response in TE mode of 10 mg/ml F8DP2 film. Pumped at 355 nm and measured with $4\ mm \times 0.1\ mm$ stripe.

SC5A

Material was dissolved in P-xylene and Chlorobenzene separately with concentration $10, 20\ mg/ml$. Solutions were stirred at 700rpm and heated at 100C, before spin-coating into thin-film on quartz substrate at 2000rpm for 60s.



(a) SC5A chemical structure and UV-Vis absorbance calculated from transmittance as $Abs = -\log_{10}(T)$.

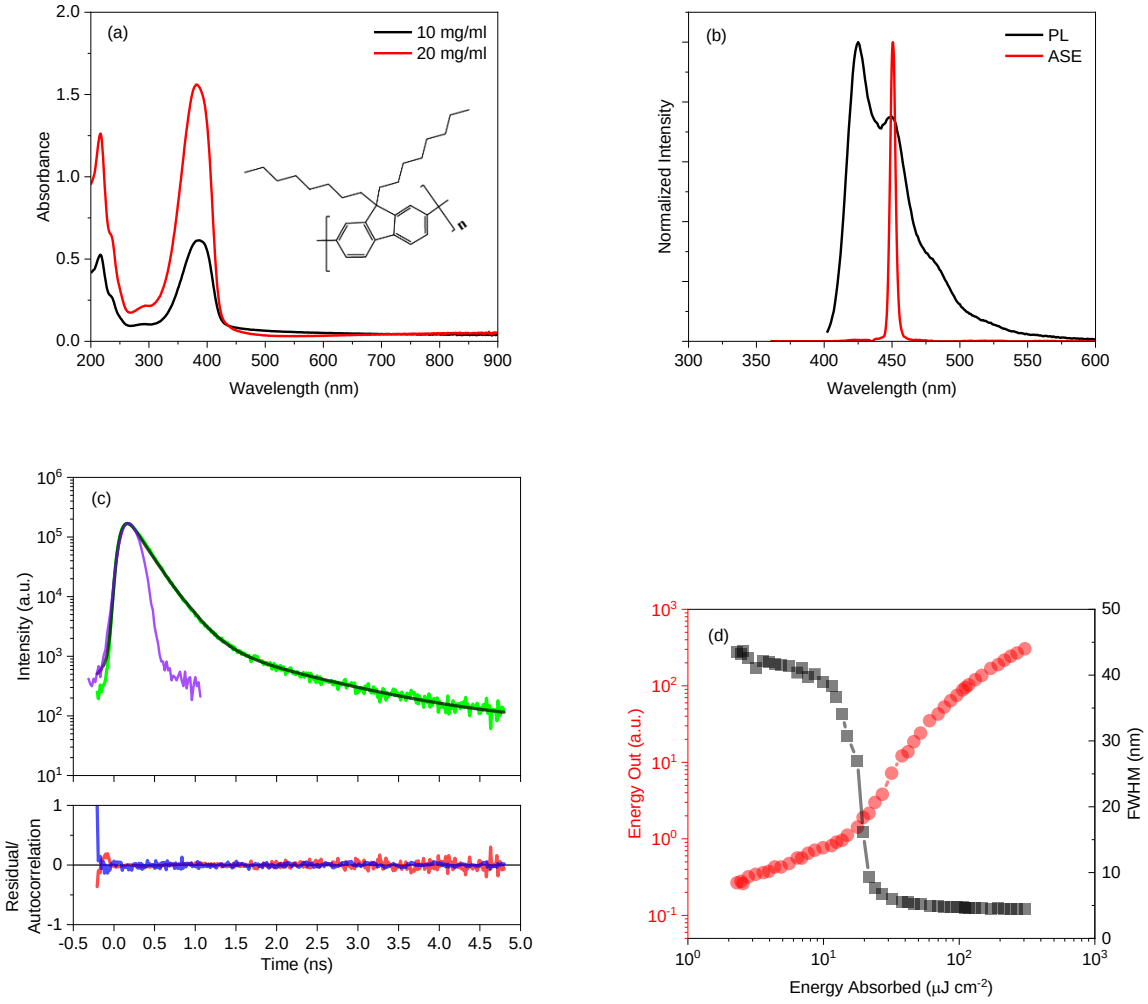
(b) Normalised PL spectrum (pumped at 380 nm) and saturated ASE spectrum in TE mode (pumped at 355 nm) of 20 mg/ml P-xylene SC5A film.

(c) Transient PL measured using the Streak Camera (pumped at 379 nm) and fitted with laser signal convolved with double exponential decay (Chapter 2.4.5). The lifetime 20 mg/ml of Chlorobenzene SC5A (excludes the less than 10% green band) is $0.21 \pm 0.02\ ns$.

(d) ASE energy response in TE mode of 20 mg/ml P-xylene SC5A film. Pumped at 355 nm and measured with $4\ mm \times 0.1\ mm$ stripe.

PFO glassy

Material was dissolved in P-xylene with concentration $10, 20\ mg/ml$. Solutions were stirred at 700rpm and heated at 100C, before spin-coating into thin-film on quartz substrate at 2000rpm for 60s.



(a) PFO chemical structure and UV-Vis absorbance calculated from transmittance as $Abs = -\log_{10}(T)$.

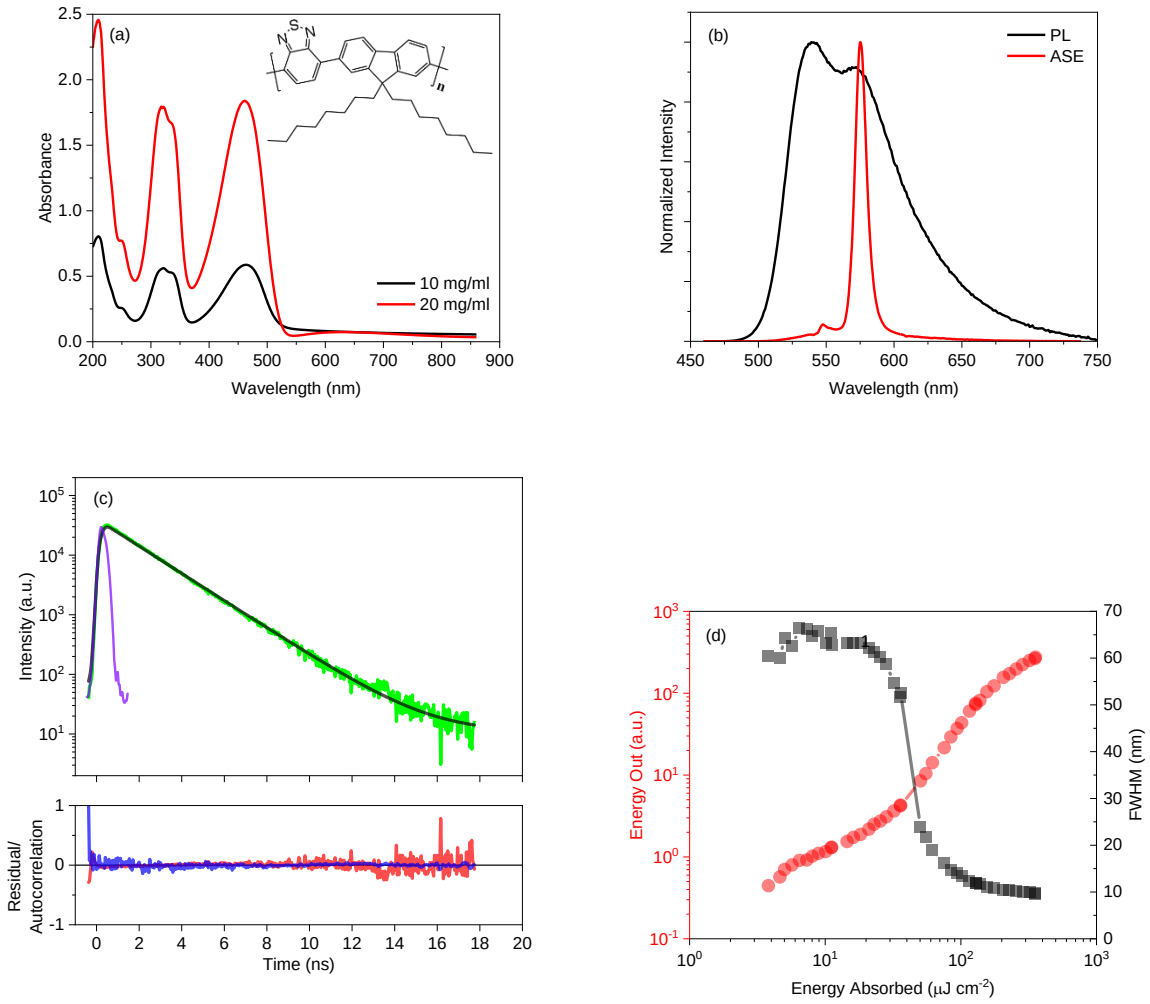
(b) Normalised PL spectrum (pumped at 380 nm) and saturated ASE spectrum in TE mode (pumped at 355 nm) of 20 mg/ml PFO glassy film.

(c) Transient PL measured using the Streak Camera (pumped at 379 nm) and fitted with laser signal convolved with double exponential decay (Chapter 2.4.5). The lifetime 20 mg/ml of PFO glassy (excludes the less than 10% green band) is $0.21 \pm 0.02\ ns$.

(d) ASE energy response in TE mode of 20 mg/ml PFO glassy film. Pumped at 355 nm and measured with 4 $mm \times 0.1\ mm$ stripe.

F8BT

Material was dissolved in Chlorobenzene with concentration $5, 10, 20\ mg/ml$. Solutions were stirred at 700rpm and heated at 100C, before spin-coating into thin-film on quartz substrate at 2000rpm for 60s.



(c) F8BT chemical structure and UV-Vis absorbance calculated from transmittance as $Abs = -\log_{10}(T)$.

(d) Normalised PL spectrum (pumped at $450\ nm$) and (not saturated) ASE spectrum in TE mode (pumped at $355\ nm$) of $20\ mg/ml$ F8BT film.

(e) Transient PL measured using the Streak Camera (pumped at $379\ nm$) and fitted with laser signal convolved with single exponential decay (Chapter 2.4.5). The lifetime $20\ mg/ml$ of F8BT is $1.9 \pm 0.1\ ns$.

(f) ASE energy response in TE mode of $20\ mg/ml$ F8BT film. Pumped at $355\ nm$ (ideally $440 - 450\ nm$) and measured with $4\ mm \times 0.1\ mm$ stripe.

Appendix 4C

Waveguided spontaneous emission in thin-film structures

ASE photon equation from 2-level (or 4-level) rate equation model (Chapter 3.2)

$$\frac{\partial S(t,z)}{\partial t} + v_g \frac{\partial S(t,z)}{\partial z} = \Gamma\left(\Omega(\mathrm{z})\eta R_{sp}(t) + R_{se}(t,z) - R_{lo}(t,z)\right) \tag{4.C1}$$

η is PLQE, Ω is the fraction of guided spontaneous emission, Γ is waveguide confinement factor, spontaneous emission factor $\beta = \Omega\eta$. $\Gamma\Omega(\mathrm{z})\eta R_{sp}(t)$ is the rate of photoluminescence (PL) that can be collected in ASE measurement. $\Omega(\mathrm{z})$ is widely considered as the solid angle subtended by the stripe edge cross-section (defined as the product of stripe width and film thickness) as seen by the differential element dz in the excitation stripe, which was originated from cylindrically shaped active media [C1-C2] but also applied in solid state thin films [C3]. The solid is valid in conventional cylindrical amplifiers as all PL photons are non-directional and the number of PL photons reaching the exit (edge) mainly depends on the geometry of the media. However, thin film structures form a loosely confined planar waveguide (substrate/gain media/air). The waveguide trapped some of PL photons [C4], which are directed to the end of excitation stripe, which is more prominent than the fraction of PL photons through solid angle. Since waveguide confinement is solely determined by the sample structure, it is appropriate to assume Ω is a constant independent of propagation axis z. Figure 4.B1 compares PL spectrum measured using the Fluoromax (face emission) and ASE set-up (edge emission). Face emission is dominant by 0-0 vibronic peak while edge emission is dominant by 0-1 vibronic peak. The difference confirms that the majority of PL photons in edge emission are guided by the planar waveguide, which favours 0-1 peak (longer wavelength, lower self-absorption) than 0-0 peak (shorter wavelength, higher self-absorption).

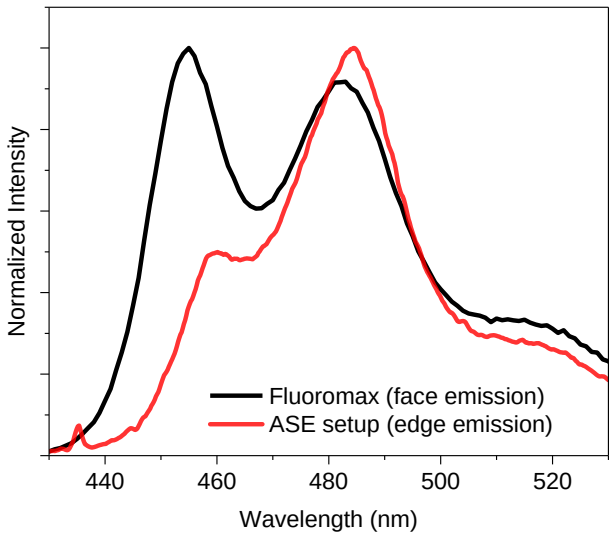


Figure 4.C1 – Photoluminescence of SpL-1 thin film collected from Fluoromax (face emission) and ASE set-up (edge emission). Edge emission favours longer wavelength 0-1 vibronic peak, which is guided by planar waveguide.

[C1] Linford, G. J., Peressini, E. R., Sooy, W. R. & Spaeth, M. L. (1974). Very long lasers. *Applied Optics*, *13*, 379-390.
[C2] Svelto, O., Taccheo, S., & Svelto, C. (1998). Analysis of amplified spontaneous emission: Some corrections to the Linford formula. *Optics Communications*, *149*(4–6), 277–282.
[C3] Dal Negro, L., Bettotti, P., Cazzanelli, M., Pacifici, D., & Pavesi, L. (2004). Applicability conditions and experimental analysis of the variable stripe length method for gain measurements. *Optics Communications*, *229*(1–6), 337–348.
[C4] Cerdán, L., Costela, A., & García-Moreno, I. (2010). On the characteristic lengths in the variable stripe length method for optical gain measurements. *Journal of the Optical Society of America B*, *27*(9), 1874.

Appendix 4D

Detailed curve fitting figures

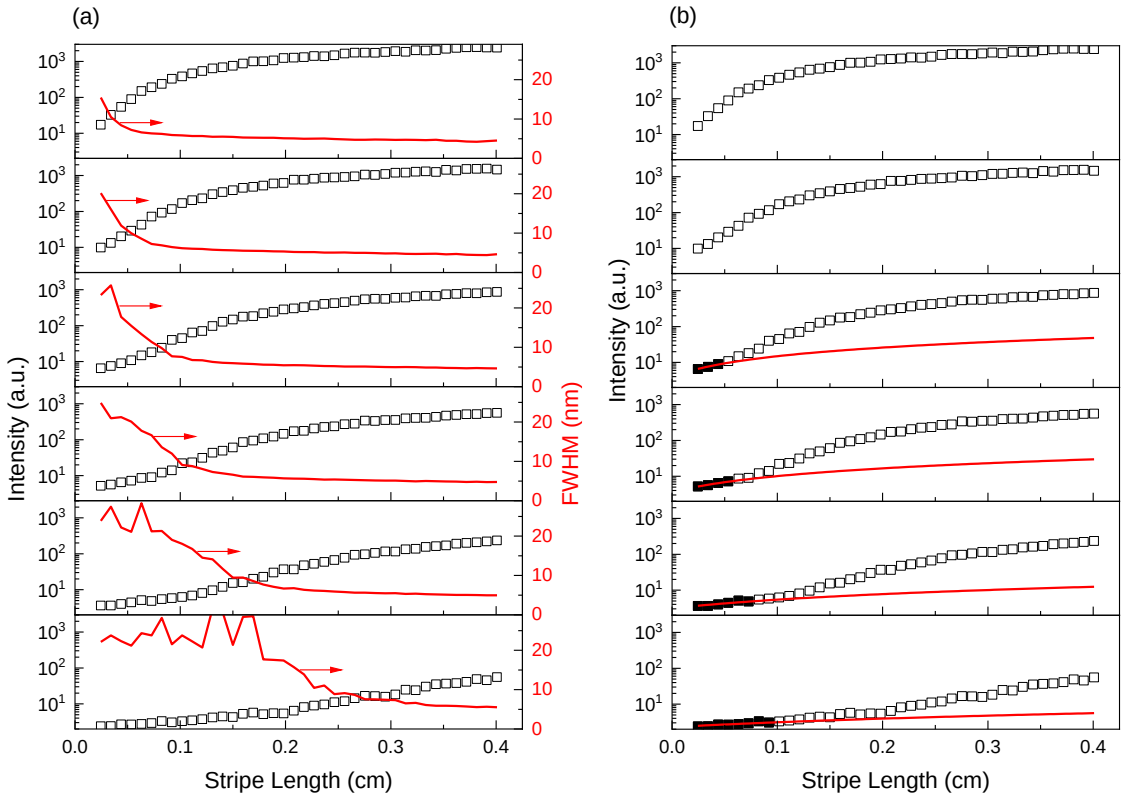


Figure 4.D1

(a) F8DP2 ASE intensity and FWHM plotted in variable stripe length. The maximum FWHM in PL is around 25 nm, which is the FWHM of a single vibronic peak, thus the drop of FWHM is a good indication of ASE threshold at different absorbed pump energies.

(b) F8DP2 data PL region fitted to Equation (4.4). At 136 and 232 $\mu J cm^{-2}$, PL region cannot be clearly defined thus A_{PL} cannot be extracted directly.

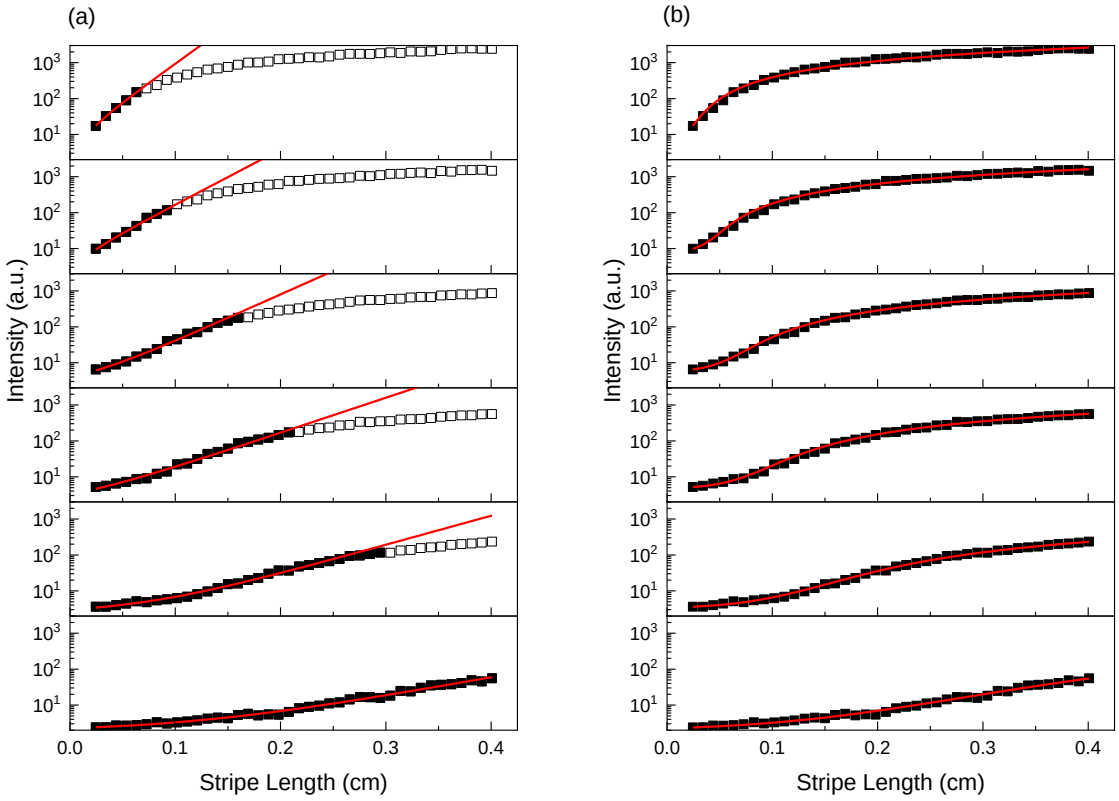


Figure 4.D2

(a) F8DP2 data in PL and ASE regions fitted to Equation (4.3) using A_{PL} extracted in Figure 4.9 and L_{si} defined in Figure 4.10. The fitted curve has higher intensity when $z > L_{si}$ because no saturation is included. The extracted g_m is small signal net gain.

(b) F8DP2 data fitted globally to Equation (4.6) with initial guess $g_0 = g_m, I_s = I_{si}$. A_{PL} is fixed as extracted in Figure 4.9, while I_s is constrained in the range $I_{si} \pm 30\%$. The value of I_s for the whole set is then determined as the best fit at 232 $\mu J cm^{-2}$ where $I_s = 115$.

Fit PL region $I(z) = A_{PL}z + b$ $(0 \leq z \leq L_{PL})$

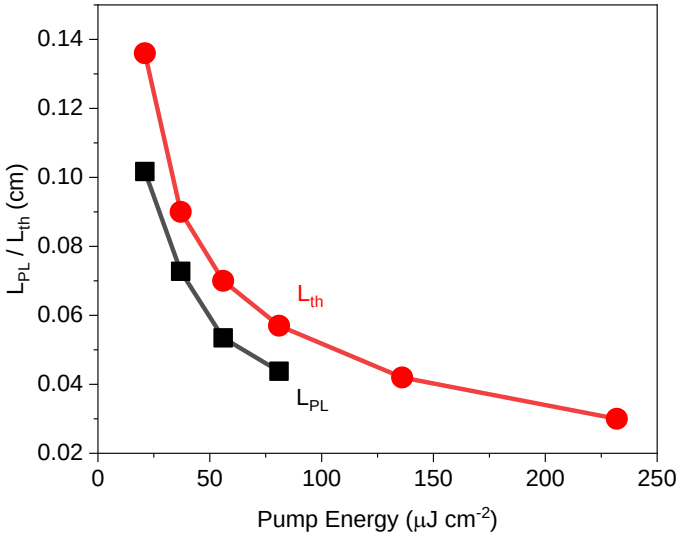


Figure 4.D3 – F8DP2 data stripe length at the threshold L_{th} calculated from $g_m L_{th} = 1.256$ and the chosen L_{PL} for fitting Equation (4.4) in PL region $0 \leq z \leq L_{PL}$. Since L_{PL} is always less than L_{th}, the defined PL region is valid to extract A_{PL} as $I(z) = A_{PL}z$.

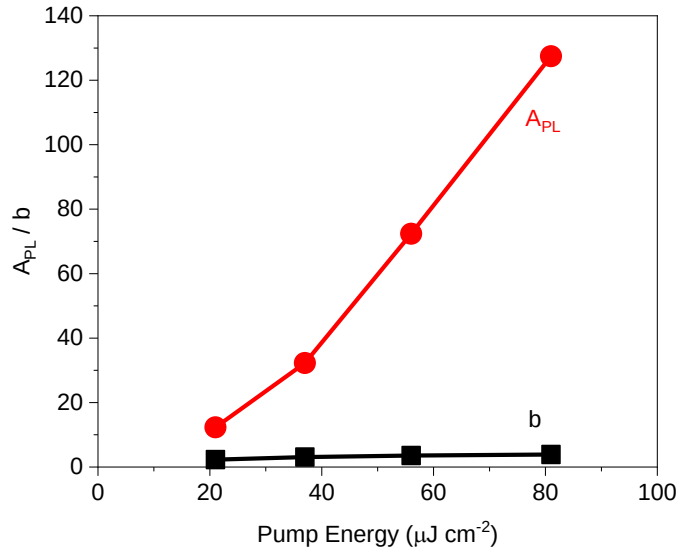


Figure 4.D4 – F8DP2 data fitted PL region $I(z) = A_{PL}z + b$. Since the value of b is much smaller than A_{PL}, it can be neglected and A_{PL} is considered as linear.

Appendix 4E

Homogeneous and inhomogeneous saturation

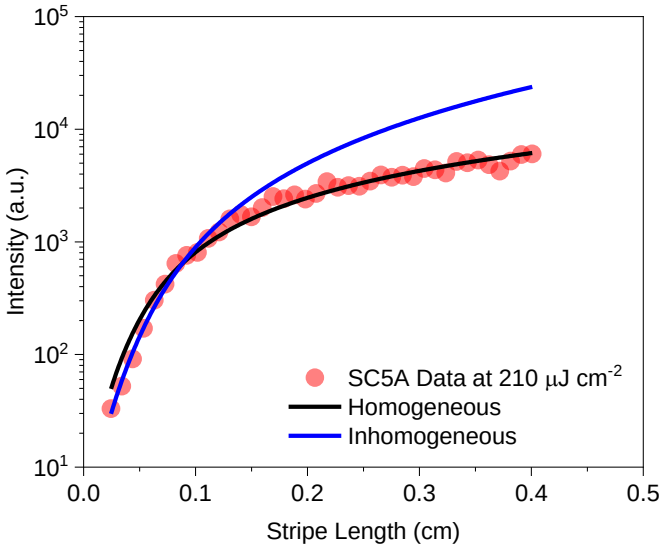


Figure 4.E1 – Data $I(z)$ of SC5A sample (Appendix 4B) measured at $210\ \mu J\ cm^{-2}$ in TE mode, fitted by single-pass approach with homogeneous saturation $(1+I(z)/I_s)^{-1}$ and inhomogeneous saturation $(1+I(z)/I_s)^{-1/2}$. Homogenous saturation fits much better, especially in saturation region when $I(z)$ becomes nonlinear on a semi-log scale.

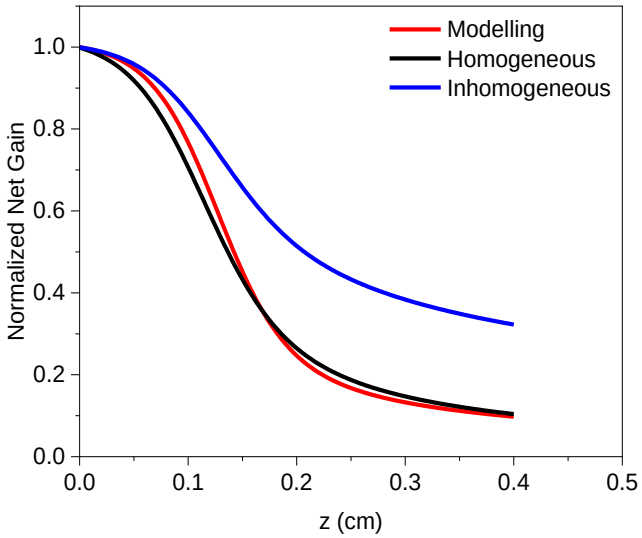


Figure 4.E2 – Compare measured homogeneous and inhomogeneous gain (net modal gain extracted in Figure 4.E1) with normalised population inversion (which is proportional to gain) calculated by the spatial-temporal model in Chapter 3.3. The modelling follows the homogeneous curve closely, while the inhomogeneous pattern cannot catch saturation effect.

Appendix 4F

Spectral gain distribution

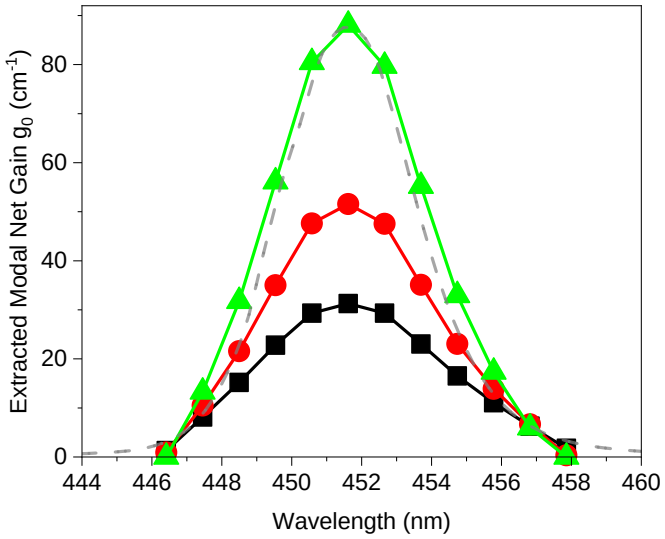


Figure 4.F1 – Spectral gain dependence is investigated by extracting g_0 in Equation (4.6) using F8DP2 TE data $I(z)$ in different wavelength. Pump energy (absorbed) is 81 (black), 136 (red), 232 (green) $\mu J cm^{-2}$. The FWHM of gain is about 5 nm – close to saturated ASE spectrum (dashed grey). The narrow gain is due to self-seeding in this sample, while the potential gain of F8DP2 is much broader (in different devices).

Appendix 5A

Energy transfer calculation – numerical vs. analytical solutions

Equations to be solved

$$\frac{dN_D(t)}{dt} = -k_D N_D(t) - k_{DA} N_D(t) + k_{AD} N_A(t) \tag{5.1}$$

$$\frac{dN_A(t)}{dt} = -k_A N_A(t) + k_{DA} N_D(t) - k_{AD} N_A(t) \tag{5.2}$$

Initial conditions $N_D(0) = 1$ and $N_A(0) = 0$. Numerical solution is obtained from Matlab solver 'ode45' with step size $\Delta t = 10^{-4}\ ns$. For analytical solution, convolution approach is used. Assume energy transfer as an indirect pump/decay – for donor, $k_{AD} N_A(t)$ is the pump term, $k_D N_D(t)$ and $k_{DA} N_D(t)$ are decay terms; for acceptor, $k_{DA} N_D(t)$ is the pump term, $k_A N_A(t)$ and $k_{AD} N_A(t)$ are decay terms. The excited state population

$$N(t) = (pump) * (decay) \tag{5A.1}$$

When both forward and reverse transfers are present, the whole process can be considered in sequence as $D_1 \rightarrow A_1 \rightarrow D_2 \rightarrow A_2 \rightarrow \cdots \rightarrow D_x \rightarrow A_x$ where D for donor and A for acceptor. The excited state density is the sum of all associations.

$$N_D(t) = N_{D1}(t) + N_{D2}(t) + \cdots N_{Dx}(t) \tag{5A.2}$$

$$N_A(t) = N_{A1}(t) + N_{A2}(t) + \cdots N_{Ax}(t) \tag{5A.3}$$

where

$$N_{D1}(t) = e^{-k_D t} e^{-k_{DA} t} \tag{5A.4}$$

$$N_{A1}(t) = \int_0^t e^{-k_A (t-t')} e^{-k_{AD} (t-t')} [k_{DA} N_{D1}(t')]\, dt' \tag{5A.5}$$

$$N_{D2}(t) = \int_0^t e^{-k_D(t-t')} e^{-k_{DA}(t-t')} [k_{AD} N_{A1}(t')]\, dt' \tag{5A.6}$$

$$N_{A2}(t) = \int_0^t e^{-k_A(t-t')} e^{-k_{AD}(t-t')} [k_{DA} N_{D2}(t')]\, dt' \tag{5A.7}$$

$$\vdots$$

$$N_{Dx}(t) = \int_0^t e^{-k_D(t-t')} e^{-k_{DA}(t-t')} \left[k_{AD} N_{A(x-1)}(t')\right] dt' \tag{5A.8}$$

$$N_{Ax}(t) = \int_0^t e^{-k_A(t-t')} [k_{DA} N_{Dx}(t')]\, dt' \tag{5A.9}$$

As in Chapter 5.2.3, assume $k_{DA} = \mathrm{A}_{DA} t^{-\frac{1}{2}}$ and $k_{AD} = 0$, then $N_D(t) = e^{-k_D t} e^{-2\mathrm{A}_{DA} t^{\frac{1}{2}}}$ (5.11) and $N_A(t) = \int_0^t e^{-k_A(t-t')} \left[\mathrm{A}_{DA} t'^{-\frac{1}{2}} N_D(t')\right] dt'$ (5.12) can be obtained. Set $k_D = k_A = 1\, ns^{-1}$, compare numerical and analytical solutions when $\mathrm{A}_{DA} = 0.1$ (Figure 5.A1) and $\mathrm{A}_{DA} = 1$ (Figure 5.A2) respectively. Both solutions are confirmed to be same.

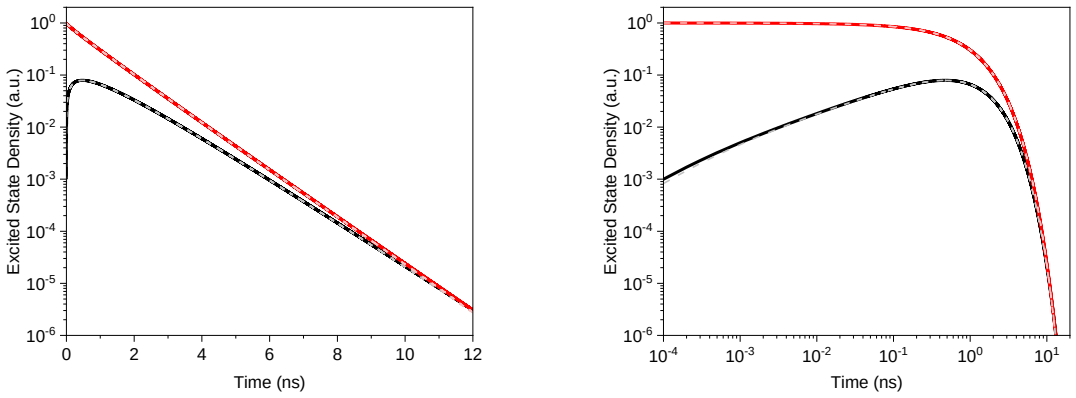


Figure 5.A1 – Calculated excited state density in donor-acceptor blend when $\mathrm{A}_{DA} = 0.1$, $k_{AD} = 0$ and $\tau_D = \tau_A = 1\, ns$. $N_D(t)$ (red) and $N_A(t)$ (black) are plotted on semi-log and log-log scales. Numerical solution (dashed) and analytical solution (solid) are the same. Since A_{DA} is small, only a minority of donor excited states are transferred to acceptor.

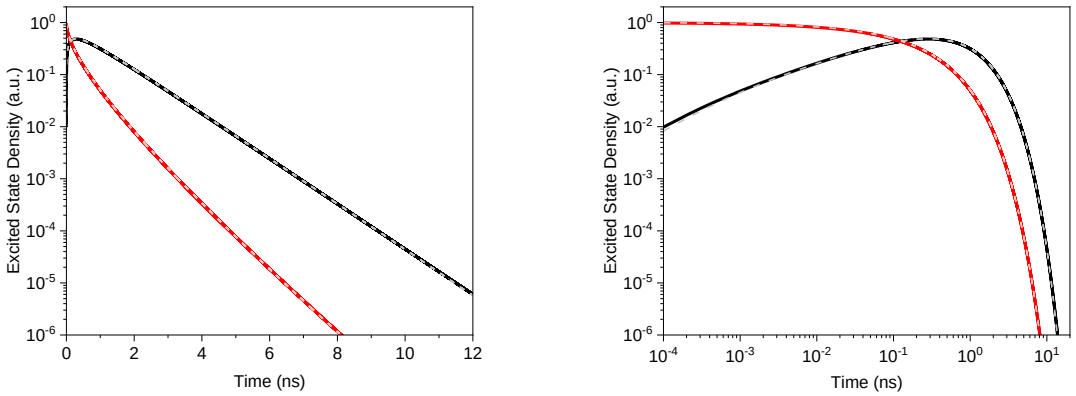
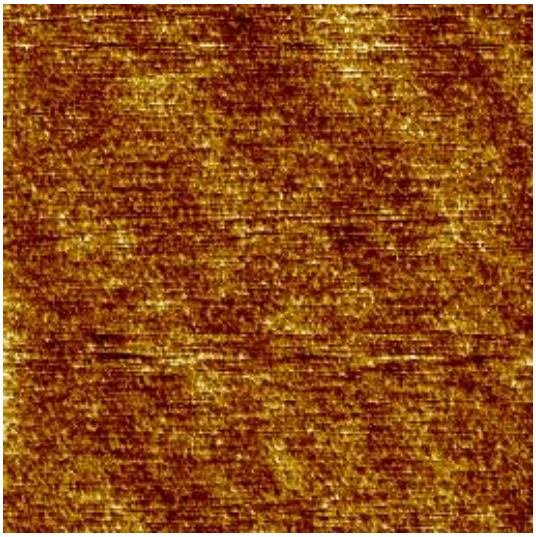


Figure 5.A2 – Calculated excited state density in donor-acceptor blend when $A_{DA} = 1$, $k_{AD} = 0$ and $\tau_D = \tau_A = 1\,ns$. $N_D(t)$ (red) and $N_A(t)$ (black) are plotted on semi-log and log-log scales. Numerical solution (dashed) and analytical solution (solid) are the same. Since A_{DA} is 10 times larger than Figure 5.A1, the majority of donor excited states are transferred to acceptor, and donor lifetime shortens significantly.

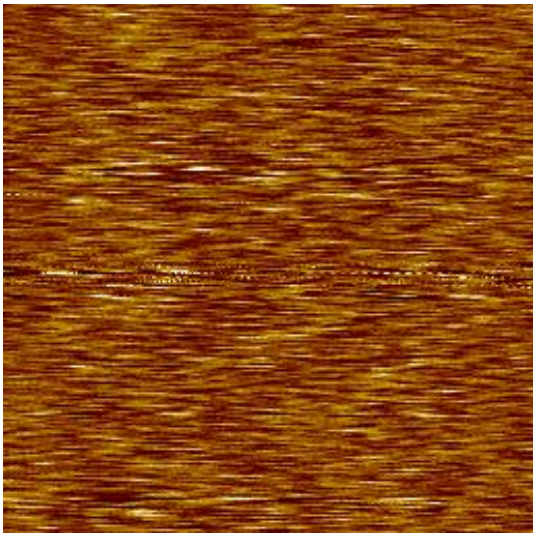
Appendix 5B

Atomic force microscope (AFM) images

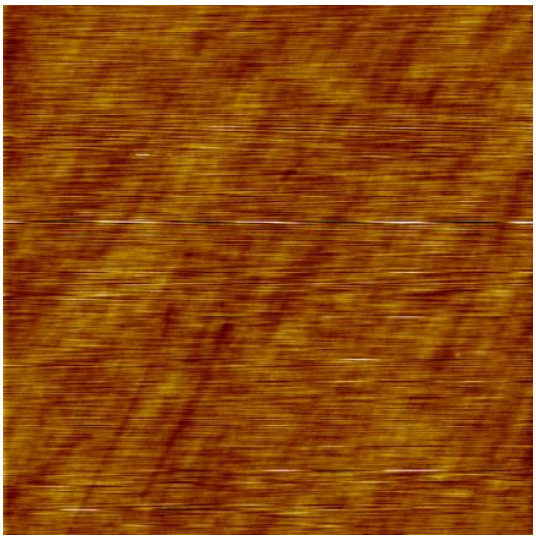
Examples of AFM images (2000rpm blend samples) taken by Nanosurf CoreAFM in tapping mode. Each image was scanned in an area $A = 2.5\ \mu m\ \times\ 2.5\ \mu m$ with 256×256 data points. $s_q = \sqrt{A^{-1} \iint Z^2(x,y)dxdy}$ (root mean square height) is used to access surface roughness, where $Z(x,y)$ is measured relative height on the xy surface.



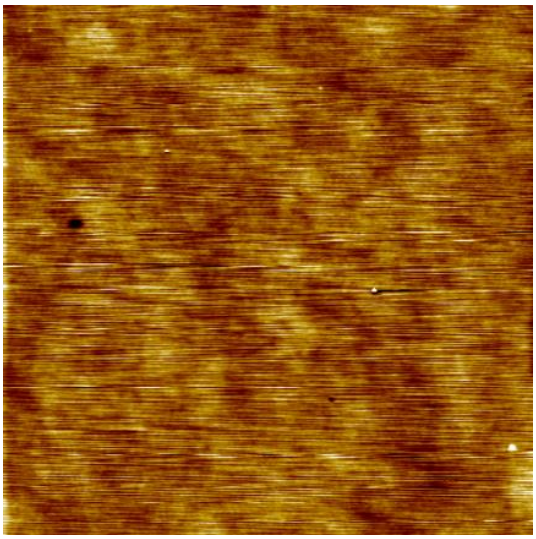
F8BT
$s_q = 1.13\ nm$



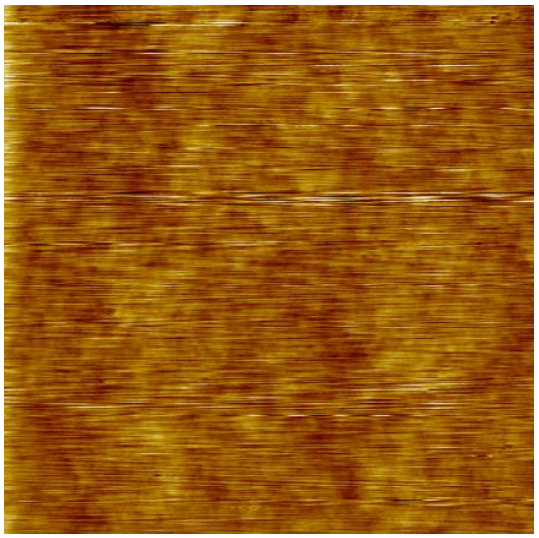
90%F8BT:10%RedF
$s_q = 0.909\ nm$



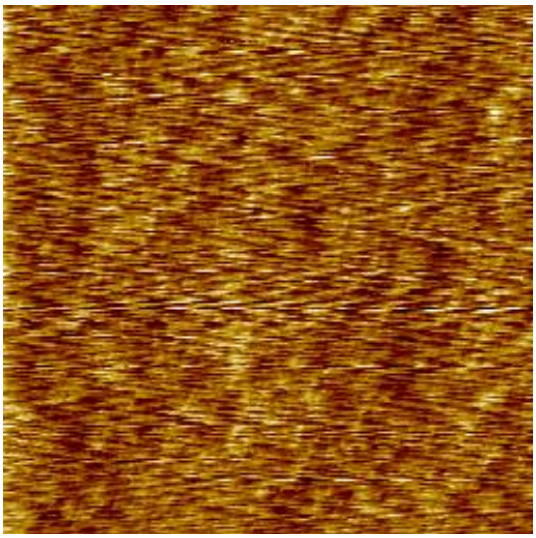
RedF
$s_q = 0.950\ nm$



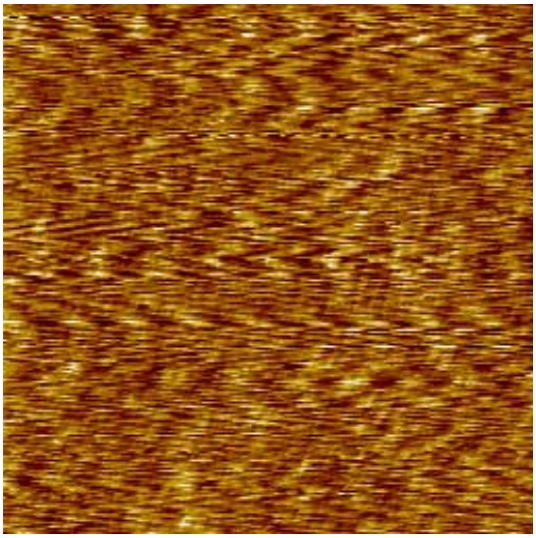
SC5A
$s_q = 0.747\ nm$



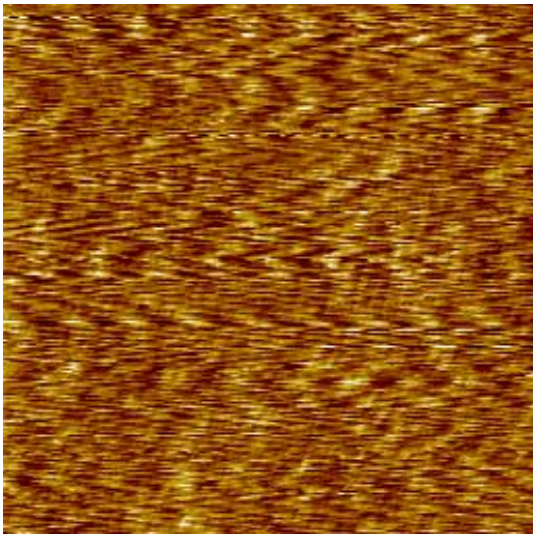
99.6%SC5A:0.4%SpL
$s_q = 0.656\ nm$



98%SC5A:2%SpL
$s_q = 0.947\ nm$



90%SC5A:10%SpL
$s_q = 0.822\ nm$

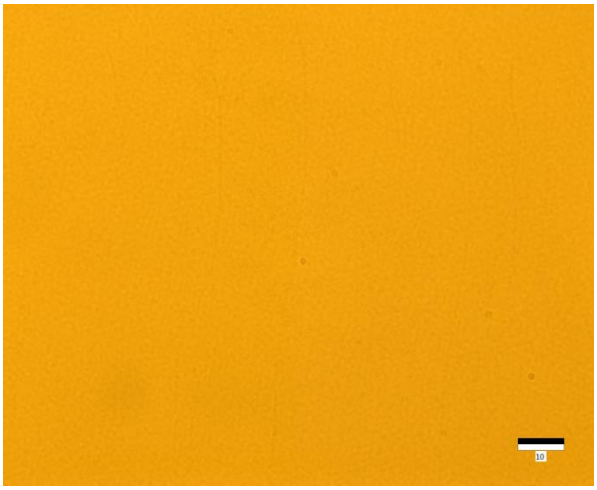


SpL
$s_q = 0.883\ nm$

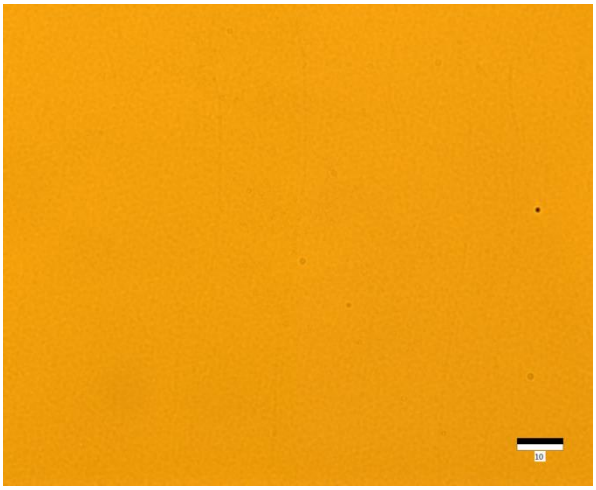
Appendix 5C

Optical microscope images

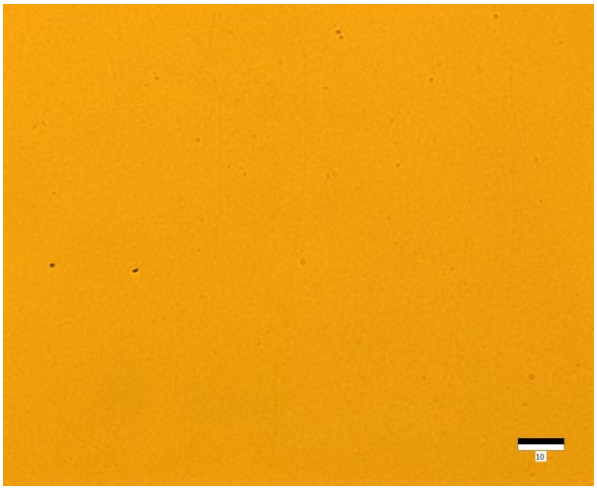
Examples of optical microscope images (2000rpm blend samples) taken by a 50X Olympus microscope without any polarisation. The scale bar is 10 μm. When cross-polarisation was applied, it recorded a black background without any signal. Apart from SpL sample, which naturally form rougher film than polymers, all other samples have flat and featureless surfaces.



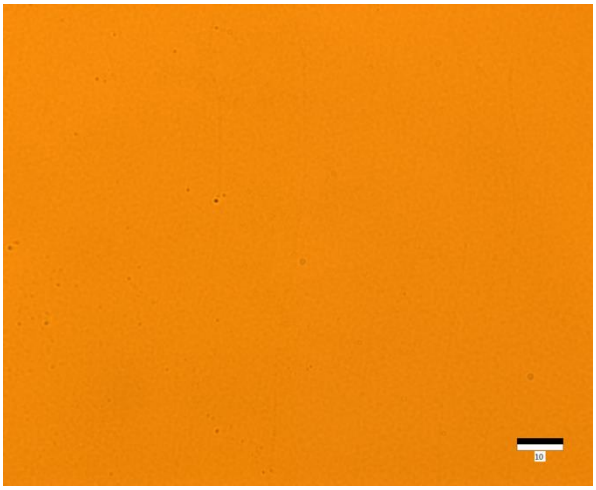
F8BT



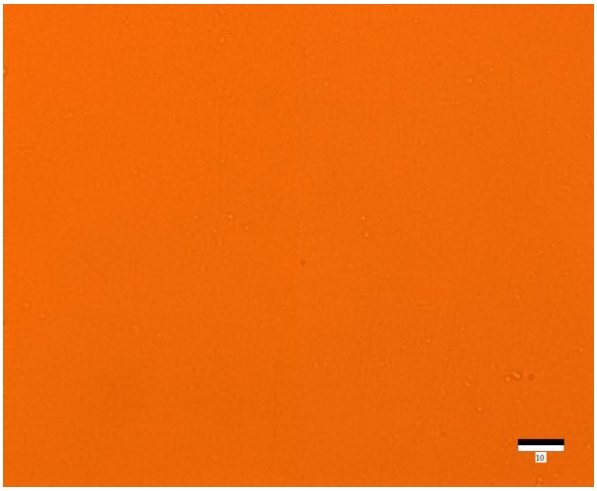
99%F8BT:1%RedF



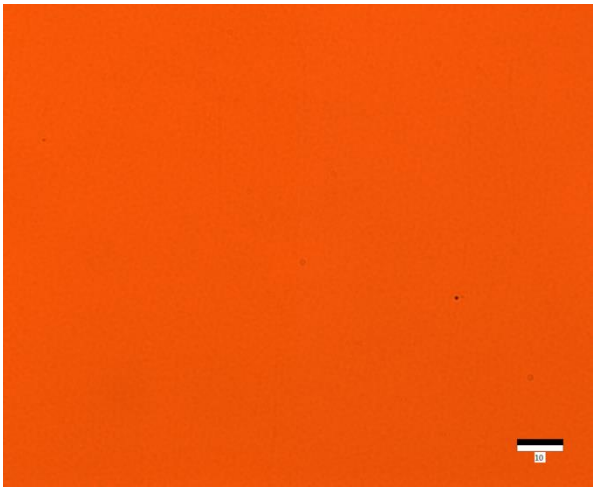
90%F8BT:10%RedF



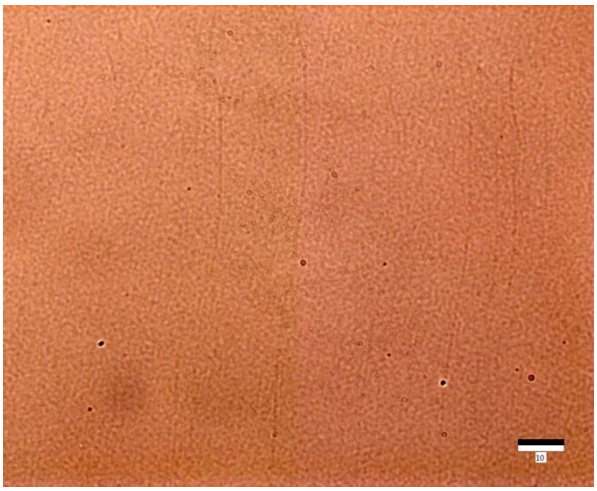
60%F8BT:40%RedF



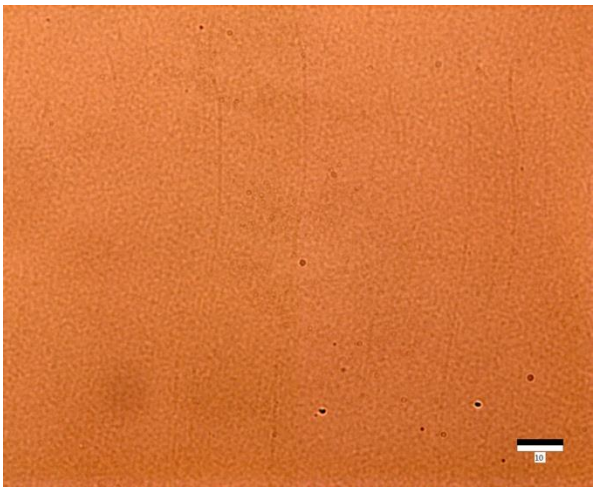
20%F8BT:80%RedF



RedF



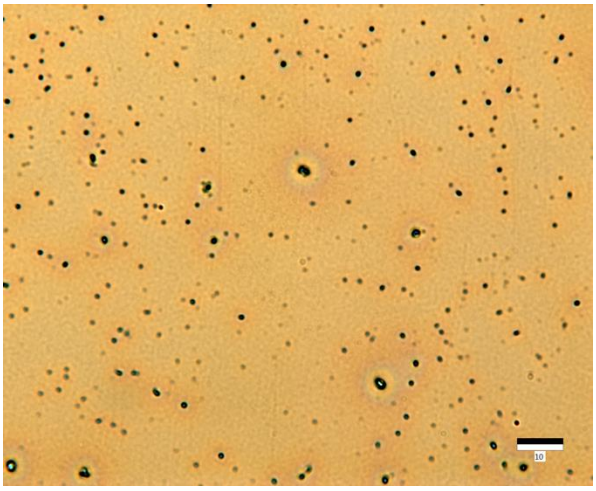
SC5A



99%SC5A:1%SpL



90%SC5A:10%SpL



SpL

Appendix 5D

Absorbance of donor-acceptor blends – calculation vs. measurement

Compare absorbance measured directly from blends and calculated from Equation (5.13).

$$A_{blend} = (1 - x)A_{donor} + xA_{acceptor} \tag{5.13}$$

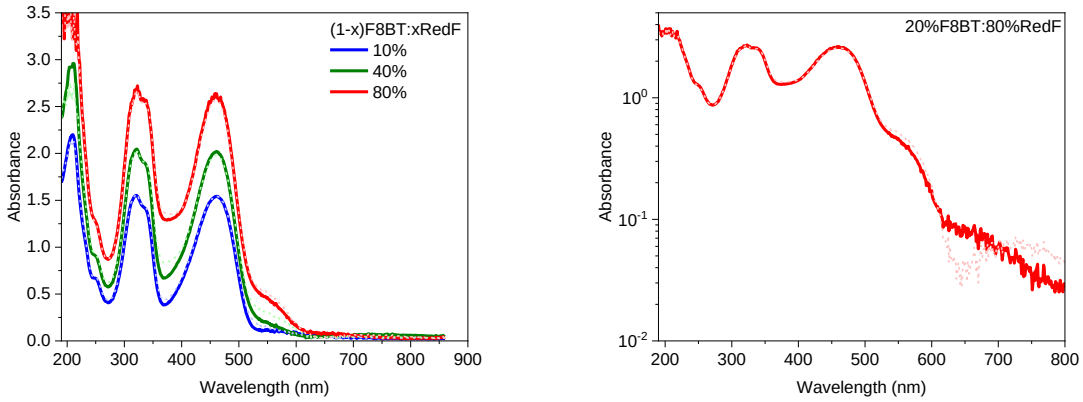


Figure 5.D1 – Absorbance of F8BT:RedF samples obtained from direct UV-Vis measurement (solid) and from Equation (5.13) (dashed). The height of absorbance peaks for blends matches the superposition of the two constituents (linear scale). However, differences occur in longer wavelength with Fabry-Pérot oscillations (semi-log scale) because sample thicknesses vary (as RedF film is thicker than F8BT, the blend samples follow the same trend).

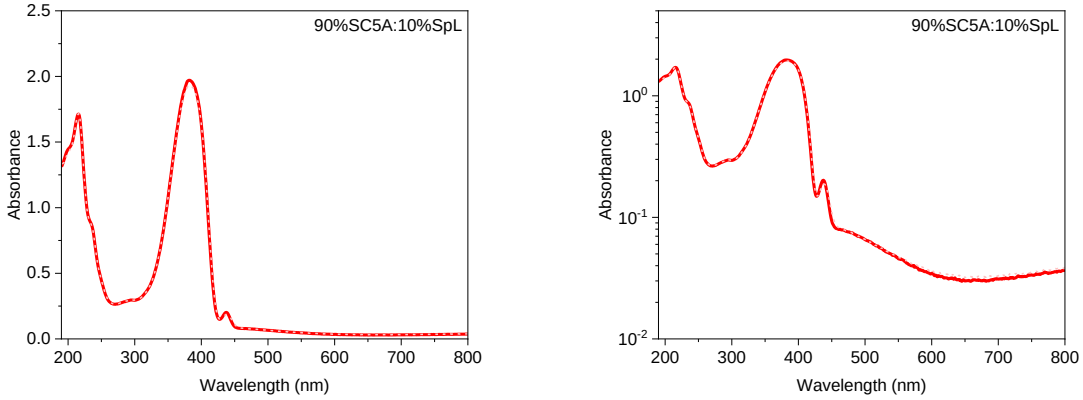


Figure 5.D2 – Absorbance of the SC5A:10%SpL sample obtained from direct UV-Vis measurement (solid) and from Equation (5.13) (dashed). 10% is the highest SpL concentration in blends. Both the height of absorbance peaks (linear scale) and Fabry-Pérot oscillation (semi-log scale) matches the superposition of the two constituents, because SC5A and SpL films have the same thickness as all blend samples.

Appendix 5E

Photoluminescence in waveguided thin-film structures

Photoluminescence (PL) collected in ASE set-up (TE mode) is not the same as measured in FluoroMax (Chapter 2.3.2). Figure 5.E1 reveals that PL spectrum is red-shifted in waveguided thin-film structures, which has more self-absorption at shorter wavelength and more confinement at longer wavelength (Chapter 3.3.1). Transient effect also plays a part – FluoroMax uses a lamp for steady state excitation while ASE is pumped by a 8.1 ns pulsed laser with ASE onset in ps time scale. Therefore, the low PLQE required for low ASE threshold represents the quantum efficiency in a short transient response and in waveguided thin-film structures, which may differ from PLQE measured in the integrating sphere (attached to FluoroMax).

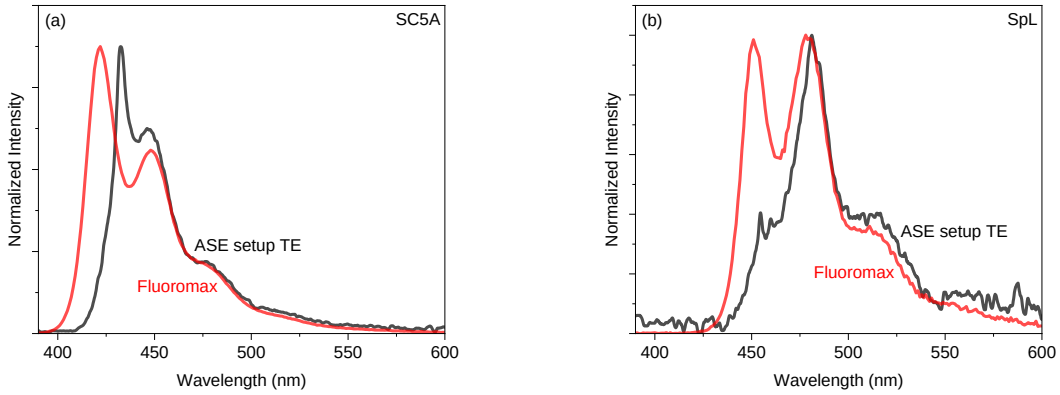


Figure 5.E1 – SC5A (a) and SpL (b) peak normalised PL spectra measured in FluoroMax (Chapter 2.3.2) and ASE set-up (Chapter 4). The spectrum from FluoroMax shows the emission from sample surface under steady state excitation, while the spectrum from ASE set-up, collected in TE mode in PL region when pump energy is 4 $\mu J\ cm^{-2}$, shows guided emission from thin-film edge under 8.1 ns pulsed excitation. As a result, the spectrum from ASE set-up is red-shifted and does not show 0-0 peak.

Appendix 5F

SC5A:SpL gain characterisation for SC5A 0-1 peak

Figure 5.F1 plots the extracted net modal gain g_0 and saturation length L_s for SC5A emission in SC5A:SpL blends. Since SpL concentration increases, PLQE of SC5A peak is decreasing (despite PLQE of the whole sample including SpL emission is increasing). Unlike SpL 0-1 peak in Figure 5.19, the decreasing PLQE results in lower g_0 and L_s. This is due to energy transfer and the competition of SpL emission, which limit the available SC5A excited states $N_D(t,z)$ both in time and space.

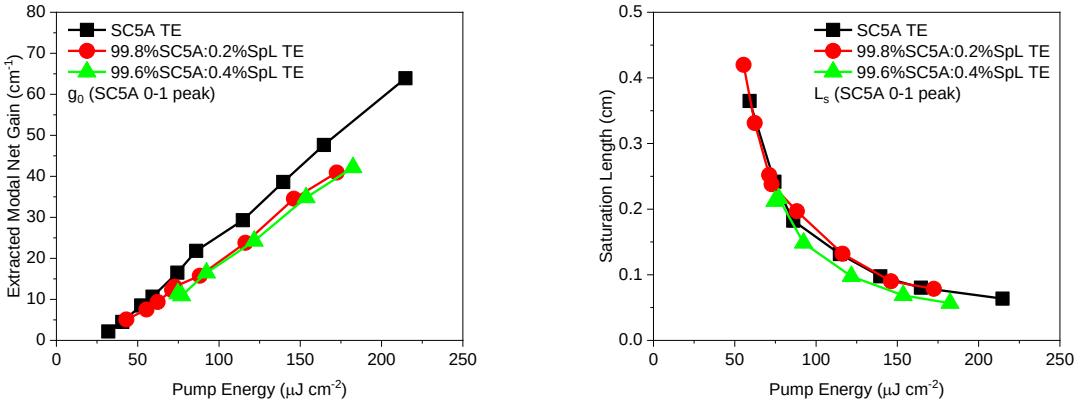


Figure 5.F1 – Extracted net modal gain g_0 and saturation length L_s for SC5A 0-1 peak from $I(z)$ data using method in Chapter 4.3.3. Compared with SC5A sample, the blends have lower values for both parameters, contributing to lower $g_0 L_s$ in Figure 5.20.